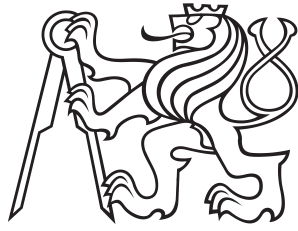


Dissertation Thesis



Czech
Technical
University
in Prague

F6

Faculty of Transportation Sciences
Department of Mechanics and Materials

Numerical modelling of auxetic structures

Petr Koudelka

Supervisor: prof. Ing. Ondřej Jiroušek, Ph.D.

Field of study: Technology in Transportation and Telecommunication

Subfield: Transportation Systems and Technology

August 2020

Acknowledgements

I would like to thank my supervisor prof. Ondřej Jiroušek for his patient guidance, useful advice, and kind helpful approach during the completion of this thesis. I would also like to thank Michaela Neuhäuserová and Radim Dvořák for their kind help with the experiments and numerical simulations during their studies at FTS, CTU in Prague. I was delighted to cooperate with Daniel Kytýř, Petr Zlámal, Tomáš Fíla, Tomáš Doktor, whom I would like to express my thanks for their patient help with the application of the experimental and numerical methods, the realisation of this thesis, and for keeping good spirits at our workplace on both a professional and personal level.

I would also like to thank to my wife Veronika, my daughter Jana, close relatives, and friends for their moral encouragement during my studies.

The research work was supported by:

- projects of the Czech Science Foundation
 - P105/12/0824
 - 15-15480S
 - 19-23675S
- institutional support of the Academy of Sciences of the Czech Republic, Institute of Theoretical and Applied Mechanics - RVO: 68378297
- projects of the Grant Agency of the Czech Technical University in Prague
 - SGS10/218/OHK2/2T/16

- SGS12/205/OHK2/3T/16
- SGS15/225/OHK2/3T/16

- the research plan of the Ministry of Education, Youth and Sports MSM6840770043
- the Operational Programme Research, Development and Education in the project INAFYM (CZ.02.1.01/0.0/0.0/1816_019/0000766)

All financial support is gratefully acknowledged.

Declaration

I hereby submit, for the evaluation, and defence, the doctoral thesis elaborated upon the CTU in Prague, Faculty of Transportation Sciences.

I have no relevant reason against using this schoolwork in the sense of paragraph 60 of Act No. 121/2000 Coll. on the Copyrights and Rights Related to Copyright and on the Amendment to Certain Acts (the Copyright Act).

I declare I have accomplished my final thesis by myself and I have named all the sources used in accordance with the Guideline on the ethical preparation of university final theses.

In this thesis, the selected results, images, and parts of the texts from the contributions listed as references no. [1–13] were used. In all the cases, I am the corresponding author of the contributions or one of the main authors and there is no conflict in copyright agreements for them to be published as a part of the dissertation thesis.

Petr Koudelka

Prague, 31. August 2020

Abstract

The dissertation thesis is focused on the numerical modelling of the mechanical response of auxetic structures to uniaxial compressive loading. According to the primary application of auxetics in terms of deformation energy mitigation, where their unique characteristics arising from the negative Poisson's ratio of the structure, high strain rate response is emphasised. Additionally, quasi-static characteristics are assessed to obtain reference data for the evaluation of the strain-rate dependency induced particularly by micro-inertia effects. Mechanical properties are studied using stress-strain characteristics, whereas the microstructural response is evaluated based on the function of Poisson's ratio. In the thesis, three auxetic unit-cells having uni- or biaxial auxetic characteristics are considered. The structures are developed by a periodic assembly of unit-cells in the respective spatial directions. Due to the complex deformation response of the auxetic structures, the reference data for the development of numerical simulations are obtained from the experiments with the samples of structures manufactured using 3D printing. Dynamic loading is performed using a Split Hopkinson Pressure Bar (SHPB) apparatus, while an approach to the numerical simulations consisting of the development of a full-scale virtual SHPB for an explicit time integration scheme in LS-DYNA was selected. In the dynamic simulations, geometrical models of the lattices precisely corresponding to the geometry of the structures for the 3D printing are used. The numerical aspects of the simulations together with the influence of the 3D printing quality on the reliability of the results

are discussed. The ability of the numerical simulations to describe the deformation response of the investigated auxetic lattices is assessed based on the numerical stress-strain curves and the graphs of the strain-dependent Poisson's ratio.

Keywords: auxetic materials, meta-materials, uni-axial compression, quasi-static response, dynamic loading, Split-Hopkinson Pressure bar (SHPB), finite element method (FEM), strain-rate sensitivity, digital image correlation (DIC), additive manufacturing (AM)

Supervisor:

prof. Ing. Ondřej Jiroušek, Ph.D.
Department of Mechanics and Materials,
FTS CTU in Prague,
Na Florenci 25,
110 00 Prague 1,
Czech Republic

Abstrakt

Dizertační práce je zaměřena na numerické modelování mechanické odezvy auxetických struktur, porézních meta-materiálů s negativním Poissonovým číslem, při namáhání jednoosým tlakem. Vzhledem k použití těchto struktur zejména jako součástí absorberů deformační energie je důraz kladen na analýzu jejich deformačního chování za vysokých rychlostí deformace. Vedle toho je provedena analýza při kvazi-statických podmínkách pro získání referenčních dat pro vyhodnocení vlivu jevů souvisejících s vysokou rychlostí deformace, jakými jsou např. efekty mikro-setrvačnosti. Mechanické vlastnosti jsou sledovány na křivkách napětí-deformace, přičemž mikrostrukturální odezva struktur je studována s využitím funkce Poissonova čísla v závislosti na rychlosti deformace. Práce je zaměřena na studium chování tří typů auxetických jednotkových buněk s jedno- a dvouose negativním Poissonovým číslem, z nichž jsou výsledné struktury generovány jejich periodickým opakováním s různým počtem buněk v jednotlivých směrech souřadného systému. Významná část práce je věnována právě testování vzorků struktur vyrobených různými metodami 3D tisku, protože referenční data pro kalibraci a verifikaci numerických simulací lze vzhledem ke složitosti chování studovaných struktur obdržet pouze provedením příslušných experimentů. Dynamická odezva na tlakové zatížení je studována metodou dělené Hopkinsonovy tyče (Split Hopkinson Pressure Bar - SHPB), přičemž numerické simulace jsou provedeny řešičem LS-DYNA s explicitní časovou integrací. Je vytvořen virtuální model sestavy SHPB a inverzní simulace využívají geometrii

struktur přesně odpovídající vyrobeným vzorkům. Diskutovány jsou numerické aspekty simulací i vliv kvality 3D tisku na spolehlivost výsledků. S využitím křivek napětí - deformace a grafů funkce Poissonova čísla studována mechanická odezva struktur z hlediska schopnosti vytvořených numerických simulací popsat deformační chování uvažovaných auxetických struktur.

Klíčová slova: auxetické materiály, meta-materiály, jednoosý tlak, kvazi-statické vlastnosti, dynamické zatěžování, dělená Hopkinsonova tyč (SHPB), metoda konečných prvků, citlivost na rychlost deformace, digitální korelace obrazu, aditivní výroba

Překlad názvu: Numerické modelování auxetických struktur

Contents

Abbreviations	1		
1 Introduction	3		
1.1 Aims and objectives	15		
Quasi-static loading	16		
Dynamic loading	17		
1.2 Structure of the thesis	17		
1.3 Limitations	18		
1.4 Collaboration	20		
2 Auxetics	21		
2.1 Important mechanical characteristics	23		
2.1.1 Resistance to indentation	23		
2.1.2 Shear resistance	24		
2.1.3 Fracture resistance	24		
2.2 Investigated auxetic lattices	26		
2.2.1 Production methods and materials	27		
2.2.2 Specimen geometry	29		
3 Quasi-static response	31		
3.1 Introduction	31		
3.2 Experimental methods	32		
3.2.1 Experimental setups	32		
3.2.2 Digital Image Correlation of the Quasi-Static Experiments	34		
3.3 Numerical methods	37		
3.4 Results	40		
3.4.1 Polymeric samples	40		
3.4.2 Steel samples	53		
3.5 Discussion	60		
3.6 Summary - quasi-static regime	65		
4 Dynamic response	67		
4.1 Introduction	67		
4.2 Experimental methods	68		
4.2.1 SHPB setup	68		
4.2.2 SHPB experiments	71		
4.3 Numerical methods	75		
4.3.1 Explicit dynamics	80		
4.3.2 Mesh development - bars	105		
4.3.3 Mesh development - auxetic lattices	109		
4.3.4 SS316L material model	113		
4.4 Results	123		
4.4.1 Experimental results	123		
4.4.2 Numerical results	136		
4.5 Discussion	153		
4.6 Summary - dynamic regime	166		
5 Summary	167		
A Bibliography	173		
B SEM micrographs - steel constructs	191		

Figures

1.1 Principle of the SHPB apparatus.	8
1.2 Signals measured during a typical SHPB experiment (left) and a space-time diagram of the propagating waves (right).	8
1.3 The principles of auxetic lattices in structural applications.	11
2.1 Multi-jet modelling printed specimens for quasi-static testing: 2D missing-rib (left), 2D re-entrant honeycomb (middle), 3D re-entrant honeycomb (right).	28
2.2 SLS printed specimens for dynamic testing: 2D missing-rib (left), 2D re-entrant honeycomb (middle), 3D re-entrant honeycomb (right).	29
2.3 SLS printed specimens with RVE number of unit-cells for dynamic testing: 2D missing-rib (left), 2D re-entrant honeycomb (middle), 3D re-entrant honeycomb (right).	29
3.1 Loading setup used in the experiments with the polymeric samples.	33
3.2 Loading setup used in the experiments of the SLS printed samples.	33
3.3 Loading scene captured using a CCD camera during the experiment - missing-rib specimen with a sprayed surface for the DIC strain evaluation (left), visualisation of the optically determined displacements (right).	35
3.4 Example of the correlation pattern (green colour) generated on the 2D re-entrant honeycomb specimen showing the inner (red) and outer part used for the DIC evaluation of the results.	36
3.5 Visualisation of the FE-model unit-cells used in the numerical simulations with details of the unit-cells: a) missing-rib structure, b) 2D re-entrant honeycomb, and c) 3D re-entrant honeycomb.	39
3.6 FE model of the missing-rib structure and the 2D re-entrant honeycomb. Detailed view of the elements inside the periodic unit-cell in the upper right corner.	39
3.7 FE model of the 3D re-entrant structure: side view of the FE mesh (left), isometric view (right) with a detailed view of the elements inside the periodic unit-cell in the lower right corner.	40
3.8 Comparison of the experimental stress-strain curve and the numerically calculated curve for the missing-rib structure.	41
3.9 Comparison of the experimental stress-strain curve and the numerically calculated curve for the 2D re-entrant structure.	42
3.10 Comparison of the experimental stress-strain curve and the numerically calculated curve for the 3D re-entrant honeycomb structure.	43

<p>3.11 Comparison of the experimental stress-strain curve and the numerically calculated curve for the 2D re-entrant structure. 44</p> <p>3.12 Comparison of the experimental stress-strain curve and the numerically calculated curve for the 3D re-entrant honeycomb structure. 45</p> <p>3.13 Overall stiffness plotted against the relative density for the <i>missing-rib structure</i> - the difference in the small/finite strain theory and the elastic/elasto-plastic material models. 47</p> <p>3.14 Overall stiffness plotted against the relative density for the <i>2D re-entrant structure</i> - the difference in the small/finite strain theory and the elastic/elasto-plastic material models. 48</p> <p>3.15 Overall stiffness plotted against the relative density for the <i>3D re-entrant structure</i> - the difference in the small/finite strain theory and the elastic/elasto-plastic material models. 49</p> <p>3.16 Calculated Poisson's ratio plotted against the relative density for the <i>missing-rib structure</i> showing the importance of taking geometrical non-linearity into account. 50</p> <p>3.17 Calculated Poisson's ratio plotted against the relative density for the <i>2D re-entrant structure</i> showing the importance of taking geometrical non-linearity into account. 51</p>	<p>3.18 Calculated Poisson's ratio plotted against the relative density for the <i>3D re-entrant structure</i> showing the importance of taking geometrical non-linearity into account. 52</p> <p>3.19 Comparison of the experimental quasi-static stress-strain curve - 2D missing-rib lattice with a different number of unit-cells. 53</p> <p>3.20 Comparison of the experimental quasi-static stress-strain curve - 2D re-entrant honeycomb lattice with a different number of unit-cells. 54</p> <p>3.21 Comparison of the experimental quasi-static stress-strain curve - 3D re-entrant honeycomb lattice with a different number of unit-cells. 55</p> <p>3.22 Comparison of the experimental quasi-static function of Poisson's ratio - 2D missing-rib lattice with a different number of unit-cells and the standard deviation for the 6×6 lattice. 57</p> <p>3.23 Comparison of the experimental quasi-static function of Poisson's ratio - 2D re-entrant honeycomb lattice with a different number of unit-cells and the standard deviation for the 6×7 lattice. 58</p> <p>3.24 Comparison of the experimental quasi-static function of Poisson's ratio - 3D re-entrant honeycomb lattice a with different number of unit-cells and the standard deviation for the 6×7 lattice. 59</p>
---	---

3.25 Details of the strut joints of the re-entrant lattice acquired using the SEM-SE imaging.	61	4.6 Orientation of the specimens during production: a) vertical, b) horizontal, and c) tilted.	117
3.26 Unit-cell of a 3D re-entrant honeycomb with spheres generated at the strut-joints.	62	4.7 Dimensions of the dog bone shaped specimen used for the dynamic experiments.	118
3.27 Comparison of the stress concentrations inside one unit-cell of the 3D re-entrant structure: a beam model with a rectangular cross-section (left), a beam model with a circular cross-section (middle), and an enhanced model with solid spheres at the joints (right).	63	4.8 Orientation of the specimens during production: a) vertical, b) horizontal, and c) tilted.	118
3.28 SEM-SE micrographs of the SLS printed re-entrant lattices: 3D assembly with the 3×3 cells (left), 2D assembly with RVE dimensions (right).	64	4.9 Quasi-static averaged stress-strain curves for the cylindrical and dog bone specimens.	119
4.1 Hopkinson bar experimental setup used for the dynamic compression of the specimens. [14]	71	4.10 Averaged results for the specimens printed at an angle of 45 degrees.	120
4.2 Principle of the virtual SHPB.	76	4.11 The yield stress (a) and the plastic hardening modulus (b) used in the MAT 12 material model plotted against the strain-rate.	122
4.3 Meshed cross-section of the bar used in the FEA.	108	4.12 Comparison of the 3×3 samples in an intact state, structures collapsed in the quasi-static experiment, and structures collapsed in the SHPB experiments, (a) 2D re-entrant honeycomb, (b) 3D re-entrant honeycomb, (c) 2D missing rib.	123
4.4 Strain plotted against time showing the numerical strain waves for the different element formulations representing the auxetic lattice.	112	4.13 Comparison of the RVE sized samples during the dynamic crushing in the SHPB experiments, (a) 2D re-entrant honeycomb, (b) 3D re-entrant honeycomb, (c) 2D missing rib.	124
4.5 Strain plotted against time showing the numerical strain waves for the different number of elements within the cross-section of the microstructure.	113	4.14 Experimental stress-strain curves - 2D missing-rib lattice composed of the 3×3 unit-cells, the dynamic and quasi-static response.	125

4.15 Experimental stress-strain curves - 2D re-entrant honeycomb lattice composed of the 3×3 unit-cells, dynamic and the quasi-static response.	126	4.23 Experimental function of Poisson's ratio - 2D missing-rib lattice composed of the 6×6 unit-cells, the dynamic and quasi-static response.	134
4.16 Experimental stress-strain curves - 3D re-entrant honeycomb lattice composed of the 3×3 unit-cells, the dynamic and quasi-static response.	127	4.24 Experimental function of Poisson's ratio - 2D re-entrant honeycomb lattice composed of the 6×7 unit-cells, the dynamic and quasi-static response.	135
4.17 Comparison of the experimental stress-strain curves - the RVE sized 2D missing-rib lattice, the dynamic and quasi-static response.	128	4.25 Experimental function of Poisson's ratio - 3D re-entrant honeycomb lattice composed of the 6×7 unit-cells, the dynamic and quasi-static response.	136
4.18 Comparison of the experimental stress-strain curves - the RVE sized 2D re-entrant honeycomb, the dynamic and quasi-static response.	129	4.26 Comparison of the 3×3 samples - visualisation of the FE results using the resultant displacement showing the intact specimens (first row), the plateau stress region (middle row), and the maximum achieved compression (bottom row).	137
4.19 Comparison of the experimental stress-strain curves - the RVE sized 3D re-entrant honeycomb, the dynamic and quasi-static response.	130	4.27 Comparison of the RVE sized samples during high strain rate loading - visualisation of the FE results using the resultant displacement showing the intact specimens (first row), the plateau stress region (middle row), and the maximum achieved compression (bottom row).	138
4.20 Experimental function of Poisson's ratio - 2D missing-rib lattice composed of the 3×3 unit-cells, the dynamic and quasi-static response.	131	4.28 Comparison of the numerical and experimental stress-strain curves - 2D missing-rib lattice composed of the 3×3 unit-cells, dynamic and quasi-static response.	139
4.21 Experimental function of Poisson's ratio - 2D re-entrant honeycomb lattice composed of the 3×3 unit-cells, the dynamic and quasi-static response.	132		
4.22 Experimental function of Poisson's ratio - 3D re-entrant honeycomb lattice composed of the 3×3 unit-cells, the dynamic and quasi-static response.	133		

4.29 Comparison of the numerical and experimental stress-strain curves - 2D re-entrant honeycomb lattice composed of the 3×3 unit-cells, the dynamic and quasi-static response.	140	4.36 Numerical and experimental function of Poisson's ratio - 3D re-entrant honeycomb lattice composed of the 3×3 unit-cells, the dynamic and quasi-static response.	148
4.30 Comparison of the numerical and experimental stress-strain curves - 3D re-entrant honeycomb lattice composed of the 3×3 unit-cells, the dynamic and quasi-static response.	141	4.37 Comparison of the numerical and experimental function of Poisson's ratio for the RVE sized 2D missing-rib lattice: (a) low strain rate, (b) high strain rate, (c) all the experiments and the FE results.	149
4.31 Comparison of the numerical and experimental stress-strain curves for the RVE sized 2D missing-rib lattice: (a) low strain rate, (b) high strain rate, (c) all the experiments and the FE results.	142	4.38 Comparison of the numerical and experimental function of Poisson's ratio for the RVE sized 2D re-entrant honeycomb: (a) low strain rate, (b) high strain rate, (c) all the experiments and the FE results.	151
4.32 Comparison of the numerical and experimental stress-strain curves for the RVE sized 2D re-entrant honeycomb: (a) low strain rate, (b) high strain rate, (c) all the experiments and the FE results.	143	4.39 Comparison of the numerical and experimental function of Poisson's ratio for the RVE sized 3D re-entrant honeycomb: (a) low strain rate, (b) high strain rate, (c) all the experiments and the FE results.	152
4.33 Comparison of the numerical and experimental stress-strain curves for the RVE sized 3D re-entrant honeycomb: (a) low strain rate, (b) high strain rate, (c) all the experiments and the FE results.	145	4.40 Slices in the reconstructed 3D image of the SLS printed 3D re-entrant lattice: front view in the axis of symmetry of the struts (top), front view showing the unsintered surface of the struts (middle), and side view showing the porosity within the struts (bottom).	162
4.34 Numerical and experimental function of Poisson's ratio - 2D missing-rib lattice composed of the 3×3 unit-cells, the dynamic and quasi-static response.	146	B.1 Microstructure at the printed surface.	191
4.35 Numerical and experimental function of Poisson's ratio - 2D re-entrant honeycomb lattice composed of the 3×3 unit-cells, the dynamic and quasi-static response.	147	B.2 Microstructure at the printed surface of the strut joint.	192
		B.3 Microstructure at the printed surface in the strut joint area.	193
		B.4 Microstructure at the printed surface of the strut joint.	194

B.5 Polished surface of the 6×7 2D re-entrant honeycomb.....	195
B.6 Polished surface of the 6×7 2D re-entrant honeycomb - detail of the strut joints.	196
B.7 Polished surface of the 6×7 2D re-entrant honeycomb.....	197
B.8 Polished surface of the 6×7 2D re-entrant honeycomb - detail of the strut joints.	198
B.9 Polished surface of the 3×3 3D re-entrant honeycomb.....	199
B.10 Polished surface of the 3×3 3D re-entrant honeycomb - detail of the strut joints.	200

Tables

2.1 Properties of the VisiJet EX200 material.....	27
2.2 Properties of the wrought SS316L-0407 steel.	28
3.1 Material properties of the EX200 material used in the FE simulations. ...	38
4.1 Properties of the FE-mesh representing the SHPB bars in the numerical simulations.	108
4.2 Number of elements and nodes required for the numerical representation of the studied auxetic lattices.....	114
4.3 Relevant mechanical properties of the components additively manufactured from SS316L-0407 provided by Renishaw....	116
4.4 Constants of the MAT 12 material model of the SLS printed steel used for the initial study of the dynamic FEA.....	120



Abbreviations

Al-Ep Aluminium foam filled with Epoxy.

Al-LDPE Aluminium foam filled with Low-density Polyethylene.

Al-PA6 Aluminium foam filled with Nylon 6.

Al-PE Aluminium foam filled with Polyethylene.

AM Additive Manufacturing.

ASTM American Society for Testing and Materials.

CCD Charge-coupled Device.

CMOS Complementary Metal Oxide Semiconductor.

CNC Computer Numerical Control.

CPU Central Processing Unit.

CT Computed Tomography.

DIC Digital Image Correlation.

DOF Degree of Freedom.

DPI Dots per Inch.

FDM Fused Deposition Modelling.

FE Finite Element.

FEA Finite Element Analysis.

FEM Finite Element Method.

FPA Focal Plane Array.

FPS Frames per Second.

IPC Interpenetrating Phase Composite.

LED Light-emitting Diode.

LWIR Long-wave Infrared.

MPPC Metal Porous Polymer Composite.

MWIR Mid-wave Infrared.

NCC Normalised Cross-Correlation.

Ni/PU Aluminium foam coated with Nickel.

NPR Negative Poisson's Ratio.

P/M Powder Metallurgy.

PC Personal Computer.

PECS Pulsed Electric Current Sintering.

PMMA Polymethyl Methacrylate.

RVE Representative Volume Element.

S/R Selective Reduced (integration).

SEM Scanning Electron Microscope.

SEM-SE Scanning Electron Microscopy - Secondary Electrons.

SHPB Split Hopkinson Pressure Bar.

SLM Selective Laser Melting.

SLS Selective Laser Sintering.

SWIR Short-wave Infrared.

ZNSSD Zero-mean Normalised Sum-of-square Differences.



Chapter 1

Introduction

In light of the current trend of extensive optimisation efforts in many fields of knowledge, complementary solutions to legacy engineering practices or substitutes for standard construction materials are also being sought in the field of structural materials for the absorption of deformation energy. One of the possible solutions on how to increase the efficiency of structures is the utilisation of structural cellular solids. Such materials, in the form of structural metal foams, were developed in the last decades of the 20th century and, to a certain extent, revolutionised design practices in vibration damping and the crash-worthiness of vehicles.

Metal foams are typical representatives of bio-mimicking materials, materials that imitate models, systems, and elements of nature to solve complex human problems. As such, either form of the metal foams' microstructure (i.e., open-cell or closed-cell microstructure) is, in terms of its microgeometry, similar to various naturally developed materials. The natural counterpart in the case of the closed-cell metal foam is typically wood, whereas, interestingly, the typical natural counterpart of the open-cell foams is a trabecular bone. The response of metal foams to different types of mechanical loading has been studied intensively using various approaches leading to a relatively thorough understanding of the related constitutive laws. Following advances in the production methods, microstructural analysis and assessment of the

mechanical properties, cellular materials have been widely used in various applications including protective structures, packaging, structural functions, due to their good energy-absorption capacity, high strength/weight ratio, and the outstanding tailor-made ability [15, 16]. Particular attention has been paid to the assessment of their effective (overall) mechanical characteristics to facilitate their use in engineering practice by omitting the geometry of their internal structure [2, 3]. The cellular material can be then equally represented by a combination of solid geometry and an appropriate (homogenised) material model. The material model itself can be obtained based on both analytical (i.e., modulus-porosity relations, homogenisation schemes, etc.) and numerical methods (finite element modelling using either real microgeometry or geometrical analogies, numerical homogenisation, and others).

Metal foams, particularly aluminium foams, are materials suitable for applications requiring significant mass reduction and simultaneous high impact energy absorption. This is given by the foams' low specific weight and thus high specific stiffness. However, for certain applications (including blast protection), it may be necessary to use materials with a relatively high compressive strength, which disqualifies the usage of most types of aluminium foams [17]. To improve the strength and energy absorption capacity without increasing the mass of the construction elements, a new type of material had to be found. Recently, there were efforts to improve the mechanical properties of metal foams by coating light-alloy foams with hard materials, such as hybrid nickel/aluminium foams [18–21]. Ni/Al hybrid foams combine a standard open-cell aluminium skeleton with a coating of nanocrystalline nickel. Here, the combination of three design strategies is skillfully utilised: cellular lightweight construction, nanotechnology, and composites. When these strategies are cleverly coupled and the synergies are used, nanocrystalline coated hybrid foams have become an innovative and multifunctional nano-material for future applications in the fields of lightweight construction and energy absorption [5].

An alternative solution has been found in a new class of composite materials - interpenetrating phase composites (IPC) or specifically metal porous polymer composites (MPPC) and open-cell hybrid foams consisting of a coated metallic skeleton. MPPC materials have an interpenetrating microstruc-

ture, where both phases form a topologically continuous network through a three-dimensional mutual interconnection [22]. Liu [23] considered aluminium-polyethylene (Al-PE) and Aluminium-Epoxy (Al-Ep) composites manufactured using the infiltration method (vacuum-assisted low negative pressure moulding process). Two important characteristics were revealed during the experimental compressive testing. The Al-Ep with 63% of a polymer exhibited a multifold increase in the plateau stress compared to the pure aluminium foam. The Al-PE specimen with the same volumetric polymer content showed a slightly higher plateau stress compared to the pure foam, but the plateau was extended up to 75% of the strain before densification begun. Compared to the pure foam, both MPPC materials were also superior in terms of the energy absorption capabilities. Regarding the flexural characteristics, Dukhan et al. [24] tested aluminium-polypropylene foam samples with different pore densities and concentrated their work on the determination of the flexural stiffness and strength. Comparison with either of the base foam materials showed superior properties of the MPPC and higher flexural stiffness with a decreasing pore size. It has been also shown that moderate strain-rate loading induced by a drop-tower causes insignificant changes in the deformation curves in the case of the open-cell foam, while an increased energy-absorption capacity can be observed in the case of the samples equipped with the polymeric filling [4]. Additionally, impact testing of polymer-filled auxetics at high strain-rate using SHPB showed that polyurethane filling increases the specific absorbed energy by a factor of 1.05 – 1.4, whereas the effect of gelatine leads to an increase of only 5 – 10%. Analysis of the strain-dependent Poisson's ratio revealed the influence of filling on the achievable (negative) values of Poisson's ratio, when compared to the unfilled specimens. The results for the function of Poisson's ratio apparently yielded different values as the assessed minima of the quasi-static Poisson's ratio in small deformations are constrained by a factor of 15 [8]. To fully utilise the potential of the MPPC, accurate and reliable methods for the prediction of their properties have to be developed. Here, finite element parametric modelling is used as a powerful tool to perform a large set of simulations to find the best computational representation of this type of material. Su [25] has already shown that mechanical characteristics of various aluminium MPPCs (Al-PA6 and Al-LDPE) can be computationally determined using microscopic models composed of periodic patterns of spherical or Kelvin's cells and also at different temperatures. Jhaver [26] also introduced a numerical modelling scheme based on Kelvin's cell and

demonstrated the possibility to cure the open-cell network using silane to increase the adhesion between the metallic network and the polymer foam.

■ Artificial porous constructs

According to the fact that the internal structure of metal foams can be controlled to a certain extent only, their microgeometry can still be considered 'natural'. This follows from the available set of parameters controllable during the manufacturing process, which include the porosity, cell-size, cell-wall thickness, pore orientation, and shape of the pores in general (i.e., spherical or polyhedral). All of these parameters, or even a single one, may significantly influence the resulting effective characteristics of the material. However, the final characteristics are still a result of only the marginally controlled natural physical processes occurring during the foaming process, hence, the term 'natural' microgeometry. The characteristics of the manufacturing process, thus, limits the application potential of the metal foams, which is further accentuated by recent advancements in other fields of material science. Among others, direct manufacturing methods comprised of additive manufacturing techniques, such as 3D printing including fused deposition modelling, stereolithography, selective laser melting/sintering, and CNC machining have received increasing attention. Independently from the method used for production, it has now become possible to literally construct porous materials with a pore-size even on a sub-millimetric scale [27, 28]. The resulting products are then artificial constructs, whose micro-geometry can be pre-determined in detail by an arbitrary modelling tool, and which can be subjected to relatively simple (compared to metal foams) optimisation routines. Therefore, the properties of the produced material are limited only by the capabilities of the production device's instrumentation.

3D printing or additive manufacturing (AM) is a technology used extensively for the production of prototypes and, more recently, for the final product development. There are many different production processes used in AM. The most common one is a material extrusion technique called fused deposition modelling (FDM), which is, by far, the least expensive and most often used technique. However, the first additive technology that has been used since the

early 1980s is stereolithography, in which the desired object is produced by cross-linking, i.e., by generating inter-molecular bonds in polymers. The last group of methods uses a high-power laser to fuse a powdered base material into solid 3D objects and is called laser sintering [29]. Two basic methods can be distinguished - Selective Laser Sintering (SLS) and Selective Laser Melting (SLM). The notable advantage of using AM methods lies in a large variety of powdered materials suitable for sintering - from plastics (nylon, polyamides, etc.) to metals and alloys (stainless steel, aluminium, nickel alloys, titanium, cobalt, chromium, copper) [30]. However, especially for the case of the SLS of metal alloys, there are several open questions. Particularly the behaviour of the printed parts and structures under high strain-rate loading, the failure mechanisms, and energy absorption remain insufficiently researched areas.

■ Split Hopkinson Pressure Bar

Many engineering applications subject structural materials to an extreme environment of dynamic loading. Components designed for defence, aerospace, automotive, and even industrial applications can experience high stresses and high strain rate loading conditions that are characteristic for impact or shock loading [31]. This kind of loading is accomplished by the stress wave propagation. Most research activities in the given area have been focused on the dynamic behaviour of metallic materials studied since the middle of the last century. Among the various experimental techniques developed over the past century, the Kolsky Bar system, as presented by Kolsky in 1949, which is more frequently denoted as the Split Hopkinson Pressure Bar (SHPB) test, is the most straightforward and simple technique as far as its use and data reduction are concerned. Figure 1.1 depicts a typical configuration of the SHPB consisting of an impacting striker bar, an input incident bar, an output transmission bar, a damper for the absorption of the residual energy, and a specimen placed between the incident and transmission bars.

The loading of a sample using the SHPB is performed by the strain waves formed at the impact of the striker bar onto the incident bar with the purpose of inducing a high strain-rate within the sample. During the experiment, the incident, reflected, and transmitted pulses are recorded with strain-gauges.

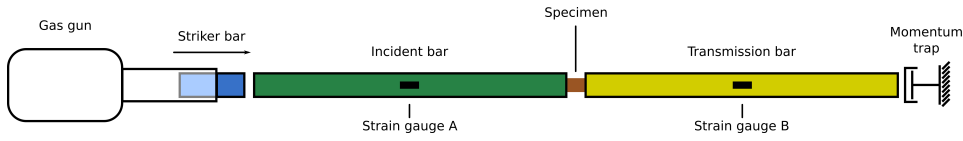


Figure 1.1: Principle of the SHPB apparatus.

The recorded strain-gauge signals and known properties of the experimental setup (e.g., bar dimensions, Young's modulus, density, wave propagation velocity, etc.) are used for the evaluation of the stress-strain diagram of the specimen for the given strain-rate. For a valid experiment, two crucial requirements have to be fulfilled - the satisfactory dynamic stress equilibrium and the approximately constant strain-rate. In the specimen, the wave is also reflected on the interface of the specimen with the transmission bar. Therefore, a defined number of reflections has to pass through the specimen before the dynamic stress equilibrium is reached. The dynamic equilibrium condition in the experiment is crucial as the standard mathematical methods for the evaluation of the specimen response are valid only in the equilibrium state. Figure 1.2 shows the pulses measured using the strain-gauges and the space-time diagram of the propagating waves; t is time, x is spatial coordinate, ε is strain, σ is stress, ε_I is incident strain, ε_T is transmitted strain, and ε_R is reflected strain.

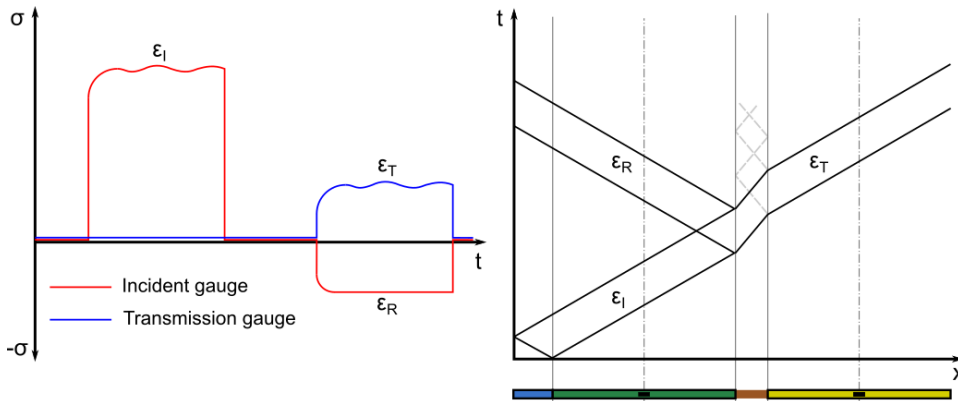


Figure 1.2: Signals measured during a typical SHPB experiment (left) and a space-time diagram of the propagating waves (right).

Chen and Song [32] reviewed the different versions of this technique, under which the specimen is deformed at uniaxial stress conditions (compression, tension, or shear) at various strain rates. The use of viscoelastic bars for

testing low mechanical impedance specimens, which is important for testing porous solids, was demonstrated by, e.g., Zhao et al. [33]. Other high-rate loading techniques include plate impacts, both normal and inclined, in which the specimens are subjected to high pressures and temperatures, as well as high strain rates. The overall picture, which these techniques outline is that the flow stresses of the metals (and their alloys) increase with the rate of strain they experience. The dynamic yield stress of a metal can be generally described by a function of the plastic strain, strain rate, temperature, and internal state variables related to the structural evolution of the material. Generally, there are two types of constitutive models - the first one is a high-pressure type and the other one a regular-pressure type. The high-pressure type considers the pressure effect of a strong shock, which is established in one-dimensional strain experiments like a pressure-shear plate impact test. The other is the regular-pressure type, which does not need to include the pressure state variable and is established on the one-dimensional stress experiments like the SHPB test. The distinct states of stress and strain in the two types of experiments may result in different plastic deformation mechanisms since the deviatoric stress and pressure induce different microstructural responses in the materials [34]. Additionally, the Taylor test consisting of the impact of a cylinder against the rigid wall or on other specimen is often used in the dynamics of materials to investigate crushing up to high compressive strains [35]. From the point of constitutive modelling, high-pressure models, as reviewed in [36], include the Steinberg-Guinan model, the Steinberg-Lund model, and the Preston-Tonks-Wallace model. Regular-pressure models, as reviewed by Chaboche [37] and Lin and Chen [38], include the widely used Johnson-Cook model [39], the Khan-Huang-Liang model [40, 41], and the Hollomon/Voce model [42].

Although there are other issues and open questions in SLS/SLM produced parts, most of the research that has been done so far was aimed at the quasi-static properties and quasi-static behaviour. However, considering the utilisation in deformation energy mitigation applications, the dynamic behaviour also needs to be described properly not only for the bulk material and related to the intrinsic properties (e.g., the change from ductile behaviour at lower strain rates to brittle above a certain level), but also in relation to the structures and the particular type of loading. While under quasi-static conditions, the deformation of printed structures and lattices has been

studied in many papers [43–45], the papers dealing with the behaviour of printed structures under dynamic loading and especially impact conditions are more scarce. Research has been performed on 3D printed cellular materials, such as ultralight metallic micro lattices [46], cellular composites [47], auxetic cellular structures [48], polymer-derived ceramics structures, octet truss lattice materials [49] and many others. These structures exhibit, e.g., outstanding absorption capacity to blast loading [50]. Research has also been focused on 3D printed sacrificial honeycomb cladding [51]. This technology may also lead to an improvement in the ballistic resistance of Al alloys, e.g., [52]. Owing to this fact, research on the dynamic mechanical properties of the 3D printed materials is still desirable [53]. In dynamic testing, special attention is being paid to the investigation of additively manufactured bulk materials like steel [54], titanium [55], Al alloys [40, 56, 57], lattices [58, 59] and the coupled thermomechanical effects in the materials [60].

■ Auxetic metamaterials

The introduction of direct production methods opens up the possibilities to introduce conceptually new types of materials with unique mechanical properties highly optimised with respect to their application. One such interesting material property is the negative Poisson’s ratio (NPR) of the so-called auxetic materials [61]. The NPR is, among natural materials, a rather unique phenomenon seen for the first time in crystals of iron pyrites and followed only by isolated reports in the 1970’s and 1980’s. The first artificially prepared auxetic polymeric foam was reported by Lakes et al. in 1987 [62], when the commercially available foam was modified in a process involving 30 % volumetric compression and heating of the samples to the polymer’s softening temperature followed by cooling, whilst remaining under compression. Although research involving microstructures prepared by various similar techniques from existing materials has continued, the investigation into auxetic-based materials for deformation energy absorption has closely followed advances in direct production methods. Application-wise, artificial auxetic constructs have the potential to outperform the current types of metal foams in terms of the specific absorbed deformation energy, the ability to be used as ballistic protection, to mitigate effects of blasts and to exhibit

strain-rate dependent deformation characteristics (Figure 1.3).

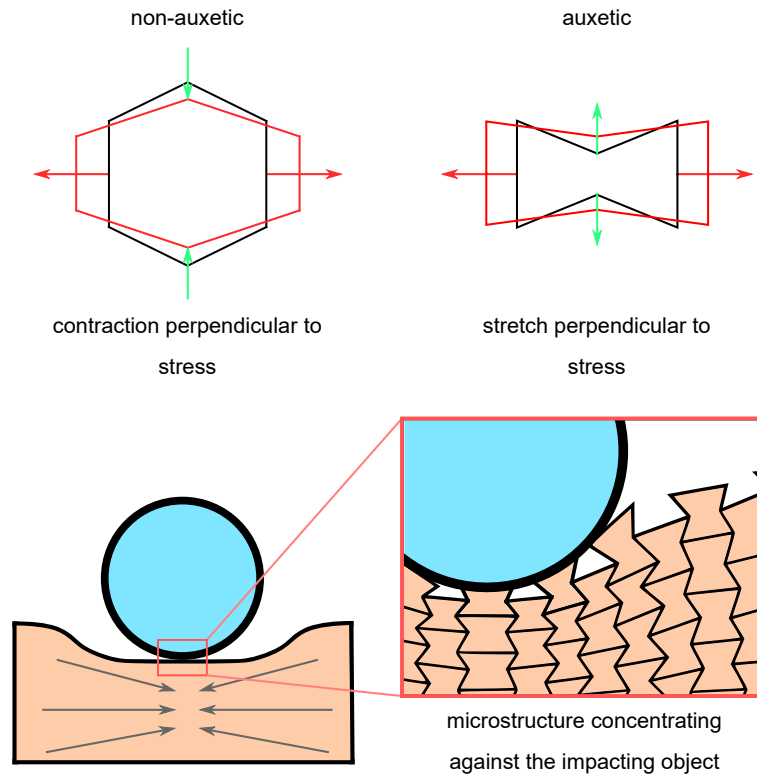


Figure 1.3: The principles of auxetic lattices in structural applications.

However, to fully utilise the aforementioned properties in the field of construction design, the detailed description of the deformation characteristics must be given. This involves, in particular, experimentally verified computational methods as a technique for the necessary parametric predictive and optimisation procedures. The high strain-rate loading of foams has been extensively studied in many works that comprised both polymeric [63–66] and metal foams [67, 68] including papers concentrated on the dynamic crushability of foams and early cell-collapse response [69]. Similarly, high strain-rate testing and the related numerical simulations concerning 3D printed structures including auxetics is a very complex problem from the point of view of theoretical mechanics, thermodynamics, material science, and the numerical solution itself [61]. Several phenomena have to be included in the correct modelling of such scenarios including inertia effects, wave propagation in solid bodies, contact constraints on the boundaries and inside the objects including friction, nonlinear geometrical effects of large displacements, and large rotation kinematics. In the case of the structures, the stability problems

of slender beams together with the related bifurcation behaviour is also an important issue. At the level of constitutive models, the response of the materials with respect to large elastoplastic deformation including strain-rate effect, fracture properties, internal material friction, and damping, and the effect of temperature due to the dissipation of deformation energy into heating have to be taken into account. For these reasons, the accurate and robust numerical solution of the impact problems of metal foams and 3D printed structures is not a trivial task. Here, the explicit time integration in finite element analysis (FEA) is preferred due to the possibility of dealing with the problems concerning the fast impact response of the materials and to consider the wave propagation phenomena [70, 71]. Although an intensive effort has been concentrated on developing new methods in FEA including the dispersion and stability analyses [72], treatment of contact interfaces [73], local and global searching algorithms, or explicit methods for time integration [74, 75], commercial software packages such as LS-DYNA are suitable for modelling the contact-impact problems related to the SHPB testing.

■ Numerical modelling of dynamic compression

Along with the development of the experimental testing using a SHPB apparatus, the analytical and simulation methods have been sought to enable the prediction of the materials' behaviour and the development of constitutive material models. Initially, only the analytical methods based on the physics of materials and the interpretation of the experimental data were developed due to the limitations of contemporary simulation methods. The recent development of numerical methods including FEA with explicit time integration complemented by advances in the performance of the computer hardware enabled development of accurate numerical representations of the SHPB tests in various fields of material science. Significant attention has been paid, in SHPB testing and simulations, to the investigation of geological materials such as rocks [76] and artificial building materials including concrete [77–79]. Similarly, FEA with explicit time integration has proved to be a powerful tool in the case of high strain-rate dynamics and contact-impact problems of lattice structures [80] and auxetics. For instance, Novak et. al demonstrated simulations of an inverted tetrapod unit-cell [81] up to a strain

rate of $1 \cdot 10^4 \text{ s}^{-1}$ [82], while Qiao showed the numerical results for a double arrowhead auxetic unit-cell [83]. Furthermore, Hou et al. presented results on the bending of auxetic and non-auxetic sandwich composites subjected to a low-velocity impact, which can be used for the development of constitutive models incorporating material failure and erosion in different crushing modes observed in the porous core of the panels [84]. Since the high strain-rate compression of materials and structures is a complex problem involving material characteristics including damage and thermomechanical characteristics, various constitutive models have been considered in the literature. In the group of regular-pressure constitutive models, the Johnson-Cook material model is commonly used [85–87] together with, e.g., the Ogden constitutive model [86] and the Cowper-Symonds constitutive model [87]. However, interesting results have also been obtained using much simpler material models with an incorporated plasticity and damage model [88] or a piecewise linear plasticity model with Cowper-Symonds strain-rate effects [80–82]. Depending on the sample geometry considered in the numerical simulations, either the axisymmetric representation of the loading apparatus is commonly used for geological materials and solid metal samples (having, in all cases, a cylindrical geometry) [76, 78, 89] or a fully 3D model for other sample geometries [90, 91]. When the full-scale numerical representation of the SHPB setup is considered, it has been shown that both the three-bar model, where the loading is performed by a strain wave generated by the simulated impact of the striker bar onto the incident bar [79], or the defined strain-history representing the stress wave propagating in the incident bar can be effectively used [77]. In several cases though, it is not necessary to include the numerical representation of the experimental setup itself in the simulations, if appropriate boundary and initial conditions are used depending on the type of loading. Here, several possible combinations of both conditions are available: a constant velocity rigid-wall on the impact face and a fixed rigid wall on the distal face [83, 85], an initial velocity rigid-wall on the impact face and a fixed rigid wall on the distal face [82, 88], an initial velocity elastic-plate on the impact face and a fixed elastic-plate on the distal face [81], a direct stress loading mode for problems involving the advanced shaping of the incident wave (where the pulse duration and stress amplitude can be represented by, e.g., a rectangular waveform and a half-sine waveform to simulate spindle striker) [76], and a constant velocity prescribed to the nodes on the impact face with a simple support prescribed to the nodes of the distal face [92]. In the case of the

contact definitions, many problems referenced herein before involve a significant mismatch in the stiffness of the sample and the bars and/or mismatch in the element size, which can result in an hourglass deformation mode and the non-physical energy dissipation, particularly during late stages of the simulated experiments. This phenomenon can be overcome, depending on the FE code used in the simulations, basically by three means. For the case of element-size difference, the obvious solution may consist in a homogeneous mesh density in all of the bodies [79], which, however, results in a possible low critical time step and the high computational cost of the simulation. The other option is to refine the mesh in the volume close to the vicinity of the contact, including a gradual mesh refinement, where a lower mesh size in the contact region reduces the undesirable numerical energy dissipation to an acceptable level. Such an approach can be found in [90], or [77], while even the mesh transition from hexahedra to tetrahedra can be found [78]. Nevertheless, the LS-DYNA software used in this work offers an effective tool to counter the material and element related contact numerical problems by using a 'soft' option for the contact interfaces. In this formulation, the contact stiffness is based on stability considerations taking the time step size into account as the contact, which is similar in this formulation to a group of spring-mass systems, each with a Courant number matched to the actual time step used in the simulation.

Concerning the approach used in this work, a further two factors have to be considered in the simulations. The first one is the geometrical representation of the auxetic lattice, where it is possible to use either a beam analogy to model its microstructure or a geometrically precise model identical to the geometry prescribed for the AM production of the samples. While the majority of the authors use the discretisation based on the beam analogy (e.g., [82, 83]), Xiao et al. [85] used a hexahedral voxel model based on the micro-tomography of a sample. This is an interesting approach, which, however, also brings significant disadvantages in the required number of elements and their low size. This is overcome in the beam analogy formulation of the problem, but significant discrepancies between geometry of the real specimen and its model representation, particularly in the joints of struts, may result in a different deformation behaviour and have a questionable influence on the micro-inertia effects. This is further exaggerated, when correlation with the experimental SHPB data is sought as the true shape of the incident

stress wave and variable strain-rate is considered. The second factor is the numerical aspects related to the modelling of the stress wave propagation, where the Courant number and the bandwidth of the mesh have to be taken into account for the precise modelling of the physics of the SHPB testing. In the full-scale representation of the SHPB setups, a common factor found in the literature is the missing mesh sensitivity considerations of the bars particularly resulting in omitted frequency characteristics [86] influencing the extracted strain-histories at the virtual strain-gauges including the behaviour related to the Pochhammer-Chree oscillations [89]. It will be shown in this work that a combination of the full-scale numerical representation of the SHPB setup with the evaluated frequency characteristics coupled with the precise geometry of the AM produced auxetic samples represented by a simple elastoplastic constitutive model can be used for the estimation of both their overall stress-strain response and the function of Poisson's ratio with reasonable precision.

1.1 Aims and objectives

The aim of the dissertation is to investigate of the mechanical behaviour of auxetic materials using a combination of experimental testing and numerical FE modelling techniques with an emphasis put on the dynamic response of the lattices. The studied auxetic constructs are intended to be used as a core in modular panels for ballistic protection and the mitigation of deformation energy of blasts. Thus, the analyses are primarily focused on the development of modelling schemes for the reliable prediction of the materials' mechanical properties under dynamic loading. From the scientific context and according to the development of methods used in this thesis, the compressive stress-strain characteristics of the considered constructs and experimentally determined functions of Poisson's ratio are also shown also for the quasi-static response. Particular attention is, in the numerical studies, paid to the evaluation of the influence of the numerical aspects of the modelling methods including the development of a virtual SHPB apparatus for analysis in a dynamic field.

The research related to the auxetic lattices builds upon the methods developed

for the investigation of metal foams and the results acquired from respective experiments and numerical simulations. For this reason, a brief overview of the author's contribution to the research of metal foams including modelling using beam discretisation and strain-rate sensitive foams is given in the chapter devoted to the state-of-the-art porous solids for deformation energy absorption. The methods developed for the inverse estimation of the effective mechanical properties of the metal foams are shown as they were used as the basis for the development of a simulation framework for the auxetic structures in both the quasi-static and dynamic field. The core of the dissertation is then aimed at the analyses of three auxetic structures exhibiting both in-plane NPR and fully 3D structures with volumetric NPR characteristics. In the quasi-static analyses, the stiffness and yield criteria are studied for the individual constructs since these parameters are important, when the auxetic lattices are used as structural elements in the constructions. The explicit dynamic simulations are then used to develop a full-scale virtual SHPB apparatus used in the experiments and to assess the structural and mechanical characteristics of the investigated constructs under a high-strain rate, large deformation conditions. The achievement of the goal will then enable to continue with the development of structurally optimised sandwich panels with the auxetic core as a solution for the mitigation of the deformation energy during impact loading. Simultaneously, the results obtained from the sensitivity studies related to the development of the virtual SHPB and determination of the numerical aspects influencing the explicit dynamics analysis to enhance the high strain-rate experiments with the ability to predict and select the appropriate parameters of the measurements.

Several sub-tasks are performed to achieve the objective:

■ Quasi-static loading

- experimental investigation of the compressive properties of the constructs for validation of the numerical simulations
- employment of DIC for the evaluation of the stress-strain characteristics and the function of Poisson's ratio

- development of the FE simulations for the inverse estimation of the effective mechanical characteristics of the constructs based on metal-foam discretisation schemes
- development of parametric models of the auxetic constructs for the additive manufacturing

■ Dynamic loading

- experimental investigation of the compressive properties of the constructs for validation of the numerical simulations
- employment of DIC for the evaluation of the function of Poisson's ratio from high-speed camera data
- development of the virtual SHPB apparatus of the device used in the experiments
- development of explicit FE simulations for the estimation of the mechanical characteristics and the function of Poisson's ratio of the constructs using the virtual SHPB
- verification of the numerical results

■ 1.2 Structure of the thesis

Chapter 1 introduces the topic of the doctoral thesis including a review of the state-of-the-art techniques in the field of metal foams, additive manufacturing, dynamics of materials at a high strain-rate and the related FE modelling; the sub-tasks and objectives are additionally defined.

Chapter 2 provides an introduction to the auxetic materials together with the fundamental NPR induced effects on the overall mechanical characteristics. Additionally, the auxetic lattices investigated in this thesis are presented together with a detailed description of the additively manufactured samples

used in the experiments and the FE simulations. The chapter also covers the methods of the specimen production using AM from a polymeric material and powdered stainless steel.

Chapter 3 deals with the quasi-static response of the auxetic constructs. The chapter covers the fields of the experimental investigation using DIC, numerical simulations, and comparison of the numerical and experimental results. According to the sub-objectives necessary during the development of the research methods, this chapter includes the analysis of the polymeric samples using both the experiments and the FEA. The experimental analysis of the steel samples is then performed as a reference for the dynamic results.

Chapter 4 deals with the dynamic response of the auxetic constructs. The chapter covers the fields of the experimental investigation using DIC, the fundamentals of the explicit FE analysis, the development of the virtual SHPB apparatus including sensitivity studies to reveal the numerical aspects of the simulations, and a comparison of the numerical and experimental results.

Chapter 5 summarises the work performed in the doctoral thesis and concludes the possibilities of using a combination of experimental and numerical procedures to predict the compressive characteristics of auxetic lattices.

■ 1.3 Limitations

The presented work is concentrated on the use of a virtual SHPB apparatus for simulation of the dynamic compressive response of periodic auxetic lattices based on three different unit-cell geometries. For this reason, the outcomes of the thesis do not have the ambition of evaluating the performance of the considered lattices, nor the formulation of the trends or recommendations in the development of auxetic lattices for specific applications and with specific NPR characteristics. Additionally, the structure of the thesis follows historical context in terms of research activities concerning NPR structures, where the goal, according to the applications in the deformation energy mitigation, is

their dynamic response. Thus, the primary purpose of the chapter concentrated on the quasi-static response of the lattices is to provide data acquired at a low strain rate for comparison with the dynamic loading. The related numerical simulations based on the beam analogy modelling of the lattices are then only a demonstration of the capabilities of parametric numerical simulations to reveal the microstructural, mechanical, and numerical influences to the effective mechanical characteristics and Poisson's ratio of the structures. This is also an explanation for the use of polymeric samples in the quasi-static analysis as the AM of the PMMA is significantly easier, provides a better resolution, and guarantees a higher reliability in terms of quality and conformity of the constructs. In contrast, the PMMA is prone to shock response during the dynamic compression and that is why all the remaining experiments and simulations are performed only using the steel specimens. In the dynamic FEA, a relatively simple material model is considered, which is a known limitation. However, this selection was performed deliberately due to its numerical stability and possibility for the easy calibration using the experimental data. The additional effects of the strain rate hardening and thermal softening of the AM steel are being evaluated as a part of the ongoing research. Unlike the SHPB experiments, the presented numerical simulations do not include the pulse shaper, which is typically a piece of soft material inserted between the striker and the incident bar. Its purpose is changing the incident wave shape to reduce the wave dispersion effects by the generation of smoother pulses that guarantee the faster equilibrium of the dynamic forces during the test. However, this is a very complex problem from the perspective of numerical simulations, the related tasks are being solved in parallel for the future integration in the virtual SHPB apparatus, and has been solved in the Master's thesis of Radim Dvorak under the author's supervision [93]. As a result, a difference in the slope of an incident wave's rising and falling edge can be observed between the numerical and experimental test, which has implications on the strain rate in the specimen and on the oscillations in the strain waves. The resulting impact on the calculated response of the specimen consists in a difference of the simulated behaviour up to the initial parts of the plateau stress region and in the late stages of the compression in the densification region.

■ 1.4 Collaboration

Due to the complexity of the studied topic, the realisation of the presented thesis would not be possible without collaboration with scientific partners having possession of state-of-the-art testing and computational equipment:

- The Czech Academy of Sciences, Institute of Theoretical and Applied Mechanics, v. v. i.
 - mechanical experiments
 - scanning electron microscopy
 - processing of tomographical data
- The Czech Academy of Sciences, Institute of Geonics, v. v. i.
 - microfocus X-ray tomography



Chapter 2

Auxetics

It has already been shown that cellular solids are able to absorb large amounts of deformation energy during impacts with the possibility to introduce strain-rate dependent characteristics into their deformation response. However, certain applications, such as blast and flying debris protection systems, may require a material with a relatively high strength in addition to the excellent deformation absorption capabilities. Such complex mechanical characteristics can be achieved without altering existing lightweight alloys (such as aluminium-based materials) used for the material's production, when the microstructure is constructed in such a way to exhibit NPR behaviour, forming a so-called auxetic material.

Auxetic structures are metamaterials that possess NPR due to the deformation response of their internal structure to the applied loading. As a result, they expand in a transverse direction when loaded in tension and shrink when compressed. The example of a material with NPR was described by Kolpakov in 1985 [94]. This behaviour can be achieved artificially due to the special design of the internal structuring, but examples of naturally occurring materials with the same property also exist, such as mineral rods, zeolites, silicates, and a few biological tissues [95]. The first cellular materials with NPR were designed and synthesised in 1987 by Lakes et al. from conventional low-density open-cell polymer foams by tri-axial compression and the sub-

sequent placing in a mould causing the ribs of each cell to protrude inward permanently [62]. The word 'auxetic' referring to a material with NPR was first used by Evans in 1991 [96]. With the advancement of material science and especially with the emergence of computer-aided design together with additive manufacturing technologies, different structures with 2D and 3D auxetic behaviour have been designed, produced, and tested [97–99]. Currently, there are generally eight types of common auxetic structures that can be classified as: (a) rigid node rotation, (b) chiral, (c) re-entrant lattice, (d) elastic instability, (e) kirigami fractal cut, (f) origami, (g) star shape connected, and (h) missing-rib [100–103]. Design optimisation and improvements to the deformation characteristics have been also investigated [104–106] including the out-of-plane deformation characteristics and bending behaviour [107, 108]. Owing to their specific properties, many interesting applications of auxetic materials have been described as potentially rendering use in different application areas, ranging from the medical (foldable devices, angioplasty, or oesophageal stents) [109, 110] to the automotive, aerospace, sport, or defence industries. Due to the possible increase in the strain energy absorption, special attention has been paid to the application of auxetic materials for energy absorption purposes during a crash, blast, and other impact loading situations [111–113]. Advancements in additive manufacturing and particularly the introduction of SLS/SLM, powder metallurgy (P/M) sintering, and pulsed electric current sintering (PECS) has enabled one to use metals as the base material for the production of the structures [114]. This has broadened the application area of auxetic materials in impact protector devices [115] and increased the energy absorption capability through the possibility of using lighter and thinner components. These new technologies are still rather expensive, but with their increasing accessibility and their potential utilisation in mass production leading to a reduction in the final price, the application of 3D printing in this area is expanding.

The deformation behaviour, both elastic and plastic, of such an auxetic construct is determined by the concurrent effects of the intrinsic behaviour of the material used for its production, cell topology, and connectivity. To optimise its microstructure to suit the intended application and to achieve a stable NPR up to high strains, control over the pore structure is required. Here, the use of additive manufacturing is favourable as all the intended geometrical characteristics can be attained deterministically, satisfying the

need for the high mechanical integrity of the construct during deformation and the possibility for the precise tuning of the overall stiffness and plastic properties [116]. The mechanical characteristics of such auxetic lattices are given not only by the overall geometrical arrangement of struts in the unit-cell and their connectivity, but by the deformation properties of the strut joints as well. The influence of all these factors on the effective mechanical properties, in both an elastic and plastic regime, has to be thoroughly evaluated and taken into account in the analytical and numerical prediction of their mechanical characteristics [117, 118].

2.1 Important mechanical characteristics

2.1.1 Resistance to indentation

The load applied by the indenter locally compresses the material, when a conventional non-auxetic material is subjected to indentation. As a result, the material spreads in the direction perpendicular to the applied load to compensate for the localised pressure [119]. However, a local contraction against the penetrating object is observed, when an indentation loading is applied to a microstructure of an isotropic auxetic material. The material accumulates under the indenter due to a connectivity-induced displacement of the unit-cells and an area of denser material with higher resistance to the indentation is created [120]. This mechanism improves the indentation resistance of auxetic materials, when compared to conventional materials [121, 122]. Here, the increase in the indentation resistance can be justified by the theory of elasticity. The material hardness H is correlated to Poisson's ratio by the equation [123]

$$H \propto \left[\frac{E}{(1 - \nu^2)} \right]^\gamma, \quad (2.1)$$

where E is Young's modulus, ν is Poisson's ratio of the base material, and

γ is the constant that assumes the value 1 or $2/3$ in the case of a uniform pressure distribution or Hertzian indentation, respectively. It can be inferred that for 3D isotropic materials and Poisson's ratio decreasing to extreme values near -1 , the hardness of the material tends towards infinity [124].

■ 2.1.2 Shear resistance

Auxetic materials are more resistant to shear forces [123]. The classical theory of elasticity for 3D isotropic solids implies that the elastic behaviour of a body can be described by two of four constants among Young's modulus E , the shear modulus G , the bulk modulus K , and Poisson's ratio ν [125]. The relationship between these constants is given by the following equations in 3D

$$G = \frac{3K(1-2\nu)}{2(1+\nu)}, \quad (2.2)$$

$$G = \frac{E}{2(1+\nu)}. \quad (2.3)$$

It can be observed that the value of the shear modulus and the shear resistance increases, when Poisson's ratio decreases. Furthermore, for stable unconstrained solids, the shear modulus must be positive [126]. This implies that Poisson's ratio has values between -1 and the isotropic solid limit of 0.5 . This relationship causes that the shear modulus tends to lean towards infinity at the extreme negative values of Poisson's ratio.

■ 2.1.3 Fracture resistance

It has been shown that auxetic materials exhibit increased resistance to fracturing [127, 128] as well as having high crack propagation resistance [129] yielding a fragile fracture behaviour. Maiti demonstrated, in the work on crack growth, that the stress intensity factor for conventional foams (K_{IC}^*)

is proportional to the normalised density and can be described by the equation [130]

$$\frac{K_{IC}^*}{\sigma_f \sqrt{\pi l}} = 0.19 \left(\frac{\rho^*}{\rho_S} \right), \quad (2.4)$$

where σ_f is the fracture stress of the cell strut, l is the strut length, ρ^* is the foam density, and ρ_S is the density of the base material used for the foam production. Later, the work by Choi and Lakes showed that in the case of re-entrant foams, Equation (2.4) was not applicable and that the stress intensity factor for these foams (K_{IC}^r) can be expressed by the equation [127]

$$\frac{K_{IC}^r}{\sigma_f \sqrt{\pi l}} = 0.1 \frac{\sqrt{1 + \sin\left(\frac{\pi}{2} - \varphi\right)}}{1 + \cos(2\varphi)} \frac{\rho^*}{\rho_S}, \quad (2.5)$$

where φ is the re-entrant angle of the unit-cell. In the same work, Choi observed that for the analysed re-entrant foam, the relationship between the stress intensity factors could be established according to the equation [120]

$$\frac{K_{IC}^r}{K_{IC}^*} = 0.53 \frac{\sqrt{1 + \sin\left(\frac{\pi}{2} - \varphi\right)}}{1 + \cos(2\varphi)}. \quad (2.6)$$

The experimental results also showed that re-entrant foams achieve an increased fracture toughness at higher values of volumetric compression. This behaviour can be explained using the dimensional growth of the auxetic material, if it is subjected to tensile loading, which can be easily verified macroscopically. As the growth is an inevitable result of the dimensional growth of each individual unit-cell, whenever a crack is formed, the expansion of the cell naturally tends to close it. As a result, while taking other macroscopic characteristics into account, auxetic materials have the potential to significantly improve the state-of-the-art in deformation energy mitigation and particularly their resistance to impact loading.

2.2 Investigated auxetic lattices

In this work, three different types of unit-cell geometries have been investigated: i) the two-dimensional cut missing-rib, ii) the two-dimensional re-entrant (inverted) honeycomb, and iii) the three-dimensional re-entrant honeycomb. These unit-cells were periodically arranged so that a predictable (determinate) in-plane or volumetric negative strain-dependent Poisson's ratio was achieved in the case of the two-dimensional and three-dimensional geometries, respectively. Constructs of the two-dimensional geometries were generated by extruding a planar (single layer) arrangement of the unit-cells, whereas the three-dimensional construct was created by generating a three-dimensional pattern of the fully three-dimensional unit-cells along all spatial directions.

Three different groups of specimens having the aforementioned unit-cell geometries were created in a parametric modeller and produced using two additive manufacturing technologies. To obtain the initial estimation on the stiffness, yield, and failure behaviour of the auxetic lattices during quasi-static compression, the specimens were first printed using a polymeric material. Then, to be able to assess the dynamic characteristics of the lattices, SLS using powdered stainless steel was used to manufacture samples conforming with the properties of the SHPB device used in the experiments. The SLS printed specimens were divided into two sub-groups according to the number of unit-cells in the periodic assembly. The initial experiments and numerical simulations were performed with lattices having 3 unit-cells along every relevant spatial direction to gain experience with the SHPB testing, the repeatability of the SLS printing, and the numerical simulations with the FE models having a modest number of elements. Then, the same types of unit-cells were used to generate lattices satisfying the requirements on the RVE of cellular solids as defined by Ashby et al. [15] by generating a periodic assembly of 6×6 or 6×7 unit-cells depending on a specific type of lattice. SolidWorks (Dassault Systèmes SolidWorks Corp., France) and Inventor (Autodesk, USA) parametric modellers were used to design the samples' geometry that was, for the additive manufacturing, exported to STL format, while the FE meshes were generated from IGS format files.

2.2.1 Production methods and materials

Multi-jet modelling

The polymeric specimens for the quasi-static testing were manufactured from a VisiJet EX200 (3D Systems, USA) UV curable acrylic material suitable for high-resolution 3D printing. The physical properties of the material are summarised in Table 2.1.

Material property	Label	Value	Unit
Mass density	ρ	1.02	g/cm^3
Glass transition temperature	T_g	52.5	$^{\circ}\text{C}$
Young's modulus	E	1283	MPa
Poisson's ratio	ν	0.2	-
Yield stress	σ_Y	42.4	MPa
Tangent stiffness	E_t	12.8	MPa

Table 2.1: Properties of the VisiJet EX200 material.

For the specimen production, a Pro Jet HD3000 3D printer (3D Systems, USA) set to the high-definition mode was used. The manufacturing principle is based on the multi-jet modelling technology, where a special printing head covers the whole working area ($198 \times 185 \text{ mm}$) and builds up the model by adding individual layers of the produced geometry (up to the maximum height of 203 mm). Simultaneously to the modelling material, a supporting wax material is automatically added to the construct to enable the production of very complex geometries. Thanks to its low melting point (approx. $55\text{--}65^{\circ}\text{C}$), all the supporting wax material can be simply removed from the products by heating in a water bath to approx. 80°C without any potential mechanical damage to the products. The final samples were produced with a resolution of $328 \times 328 \times 606 \text{ DPI}$ (x, y, z direction) with layer thickness of 0.036 mm. In this mode, the accuracy of the printing was approximately $0.025\text{--}0.05 \text{ mm}$ and the production process took 11 hours. The visualisation of the specimens is depicted in Figure 2.1.

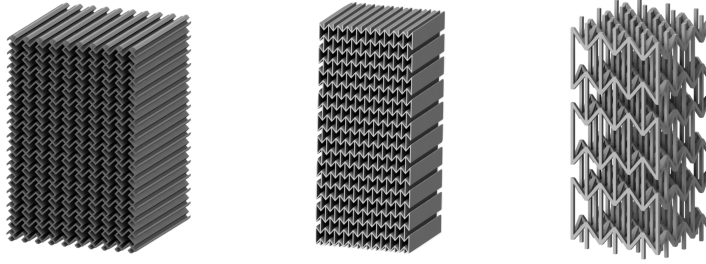


Figure 2.1: Multi-jet modelling printed specimens for quasi-static testing: 2D missing-rib (left), 2D re-entrant honeycomb (middle), 3D re-entrant honeycomb (right).

■ SLS

The specimens for the dynamic testing were printed with an AM 250 device (Renishaw, UK) using the SLS method by sintering powdered SS316L-0407 austenitic stainless steel composed of iron alloyed by 16 – 18 wt% of chromium, 10 – 14 wt% of nickel, and 2 – 3 wt% of molybdenum. The maximum permissible content of carbon is up to 0.03 wt% making this material an extra-low carbon modification of a standard SS316L alloy. The melting range of the material is 1371 – 1399 °C and the density of the wrought solid is 7990 kg · m⁻³. The mechanical properties of the additively manufactured components (according to the manufacturer of the sintering device) are summarised in Table 2.2. The visualisation of the specimens is depicted in Figures 2.2 and 2.3.

Parameter	Horizontal direction	Vertical direction	Unit
Compressive strength	662 ± 2	574 ± 10	MPa
Yield strength	518 ± 5	440 ± 10	MPa
Modulus of elasticity	167 ± 8	134 ± 17	GPa
Elongation at break	43 ± 2	35 ± 8	%

Table 2.2: Properties of the wrought SS316L-0407 steel.

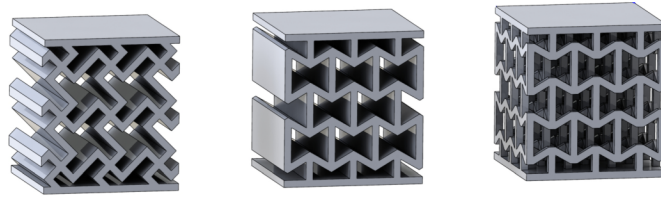


Figure 2.2: SLS printed specimens for dynamic testing: 2D missing-rib (left), 2D re-entrant honeycomb (middle), 3D re-entrant honeycomb (right).

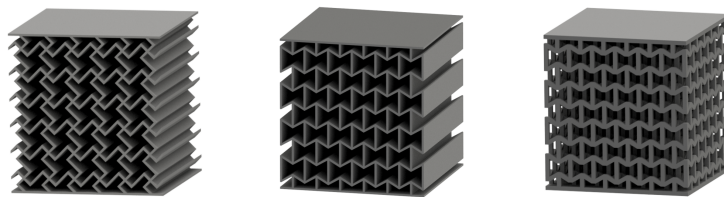


Figure 2.3: SLS printed specimens with RVE number of unit-cells for dynamic testing: 2D missing-rib (left), 2D re-entrant honeycomb (middle), 3D re-entrant honeycomb (right).

■ 2.2.2 Specimen geometry

■ Missing-rib

The missing-rib model is formed by removing selected ribs (elements forming the unit-cell) from a periodical arrangement of squares and by rotating the construct by 45° to the direction of loading [98]. The auxetic behaviour of such a construct depends on the unit-cell dimensions and the angles between the individual ribs.

Polymeric samples. The dimensions of the polymeric constructs were $25.05 \times 25.40 \times 37.75$ mm (width, depth, height), the overall porosity was 72.8%, and the construct consisted of 10×15 cells with a nominal strut thickness of 0.25 mm.

Steel samples. The SLS produced samples with 3×3 unit-cells (9 unit-cells in total) had the nominal dimensions of $11.7 \times 12.0 \times 13.0$ mm and a nominal porosity of 53.1% at a nominal strut thickness of 0.6 mm. The samples having 6×6 unit-cells for a total of 36 unit-cells had the dimensions of $14 \times 14 \times 14.8$ mm and a nominal porosity 74.37% at a nominal strut thickness of 0.2 mm.

■ Re-entrant honeycomb

The re-entrant mesh is generated by changing the four side angles between the ribs in a six-sided honeycomb [131]. The magnitude of Poisson's ratio at a given strain is here primarily given by the length ratio of the individual ribs forming the unit-cell.

Polymeric samples. The dimensions of the 2D polymeric assemblies were $25.65 \times 25.40 \times 58.89$ mm, the overall porosity was 73.2% and the construct consisted of 10×15 cells with a nominal strut thickness of 0.25 mm. The dimensions of the 3D polymeric assemblies were $7.87 \times 7.87 \times 18$ mm, the overall porosity was 91.7% and the construct consisted of 3 cells in every spatial direction.

Steel samples. The SLS manufactured 2D re-entrant honeycomb with 3×3 unit-cells (8 unit-cells in total) had the nominal dimensions of $12.0 \times 12.0 \times 13.0$ mm and a nominal porosity 72.3% at a nominal strut thickness of 0.6 mm. The samples having 6×7 unit-cells for a total of 42 unit-cells had the dimensions of $14.0 \times 14.0 \times 14.5$ mm and a nominal porosity 73.43% at a nominal strut thickness of 0.2 mm. The SLS manufactured 3D re-entrant honeycomb with 3×3 unit-cells (22 unit-cells in total) had the dimensions of $12.1 \times 12.0 \times 13.0$ mm and a nominal porosity 74.0% at nominal strut thickness of 0.6 mm. The samples having 6×7 unit-cells for a total of 252 unit-cells had the dimensions of $14.0 \times 14.0 \times 14.5$ mm and a nominal porosity 72.36% at nominal strut thickness of 0.2 mm.



Chapter 3

Quasi-static response



3.1 Introduction

This chapter is devoted to the investigation of the compressive response of the studied auxetic structures to loading in a quasi-static regime using both experimental and numerical methods. In the experimental part, the description of the loading setup and its optical instrumentation is given together with the method for the digital image correlation of the displacement and strain fields, which is also utilised in the chapter describing the dynamic response of the lattices. Consequently, the evaluation of the stress, the strain, and Poisson's ratio is provided. The experimental results acquired for the polymeric samples are then used as a basis for the development of the numerical methods for the inverse estimation of the compressive characteristics.

The results section in this chapter is divided according to the base material used for the production of the lattices. For the polymeric samples, the comparison of the experimental and numerical results, in terms of the elastic part and the yield characteristics of the effective material response to the compression, is shown. Then, the influence of the numerical aspects such as a

small deformation or the finite strain formulation and the constitutive material model are discussed to show factors that have to be taken into account during optimisation of the auxetic structures using parametric simulations. The experimental results acquired for the SLS printed lattices are then further divided into the stress-strain response and the analysis of the function of Poisson's ratio.

■ 3.2 Experimental methods

■ 3.2.1 Experimental setups

In the case of polymeric samples, the experiments were carried out using an in-house designed loading setup based on a modular compression/tension loading device suitable for both optical and X-ray observations of the deformation processes [132] equipped with an U9B force transducer (HBM, Germany) with a nominal force capacity of 2 kN. A signal from the load-cell was read-out using an OM502T (Orbit Merret, CZ) load-cell indicator at a sampling rate of 50 Hz. The loading of the samples was performed as a displacement driven uni-axial compression. The maximum displacement was set to 8 mm with a loading rate $20 \mu\text{m} \cdot \text{s}^{-1}$. A detailed description of the loading setup is shown in Figure 3.1.

The response of the SLS printed specimens to the uni-axial compression was performed using an electromechanical loading device (Instron 3382, Instron, USA) due to higher load-bearing capacity of the stainless steel constructs. The cross-head speed was set to $0.5 \text{ mm} \cdot \text{min}^{-1}$ (strain-rate of 0.006 s^{-1}) up to 50 % of the overall deformation defined by the cross-head displacement. A detailed description of the loading setup is shown in Figure 3.2.

The deforming microstructure of the samples was during all the experiments observed by a CCD digital camera to enable the optical evaluation of the displacement and strain fields of the investigated microstructures, which was necessary for the evaluation of the stress-strain diagrams and the functions of

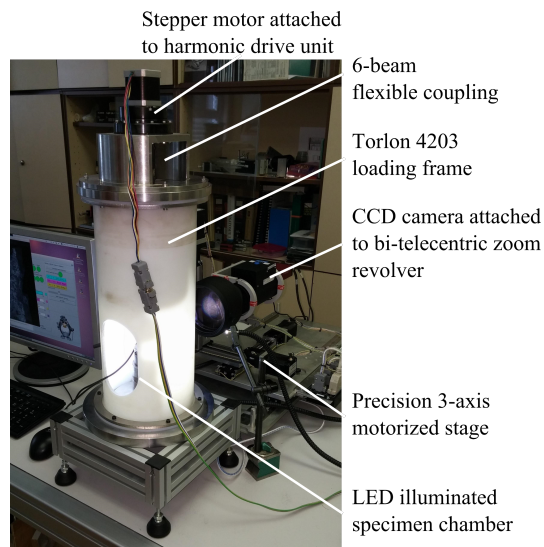


Figure 3.1: Loading setup used in the experiments with the polymeric samples.

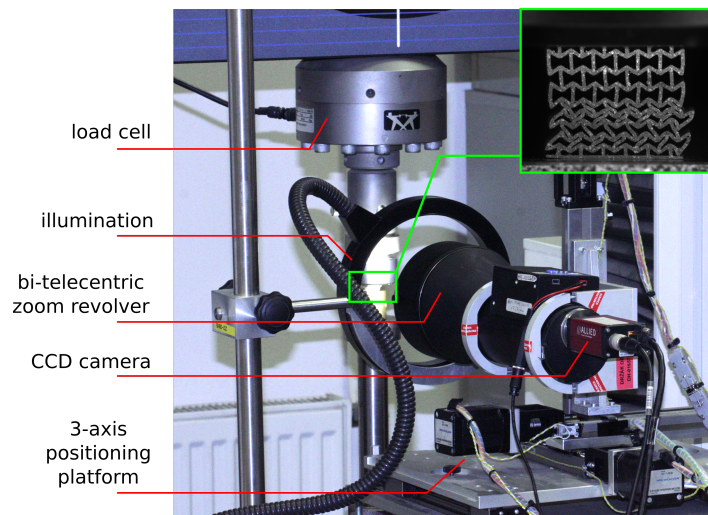


Figure 3.2: Loading setup used in the experiments of the SLS printed samples.

Poisson’s ratio. The optical instrumentation of the experimental setup was composed of a monochromatic camera (Manta G-504B, AVT, Germany) with a resolution of 2452×2056 px operated at 3 fps and attached to a bi-telecentric zoom revolver (TCZR072, OptoEngineering, Italy). The lens uses a stepper motor controlled zoom revolver to set 4 different scene magnifications in the range of 0.125 – 1 with very high image centre stability, parfocality, and no

need for re-calibration after zooming to guarantee the high reliability of the correlation procedure and accuracy of the computed strains. The specimens were illuminated using a KL2500 (Schott, Germany) high-power cold-light LED source. The acquisition of the projections was controlled with custom-developed software based on the OpenCV library and Python programming language [133]. The observed faces of the specimens were sprayed using a granite paint to generate a random pattern to enable the reliable optical deformation tracking.

■ 3.2.2 Digital Image Correlation of the Quasi-Static Experiments

The acquired series of images were exported to a PNG format using a lossless compression algorithm and subjected to a custom DIC procedure implemented in Matlab (Mathworks, USA). The procedure, based on the Lucas-Kanade tracking algorithm [134], uses a zero-mean normalised sum-of-square differences (ZNSSD) criterion to compute the similarity in the pixel intensity between the reference and the deformed image subsets, which is then followed by the optimisation of the received displacement by the Newton-Raphson iterative algorithm to achieve a sub-pixel accuracy of the results. Thus, a periodic grid of correlation points is generated for every investigated sample, where the location and distance between the individual correlation points were selected to track the deformation of the joints between the individual struts to enable the reliable evaluation of the function of Poisson's ratio. Each marker was then tracked throughout the acquired series of projections by searching for the highest correlation coefficient between two consequent projections. As a result, the in-plane displacement and strain fields of the deforming microstructures were obtained and averaged over all the measurements comprising the respective auxetic microarchitecture. Particular attention has to be paid to the treatment of noise in the data to achieve the high reliability of the correlation procedure. For this reason, a correlation window was set to 25 px and its neighbourhood, where the correlation was sought around a centroid of the correlation window in two consequent projections, was set to 30 px and kept constant in all the evaluated quasi-static experiments.

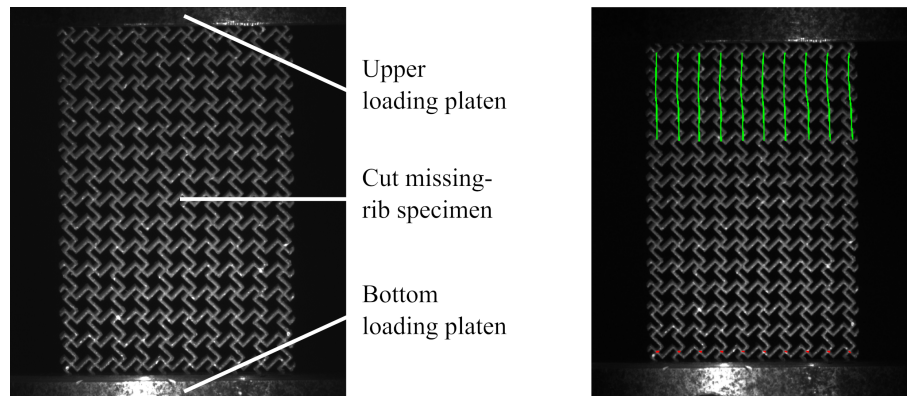


Figure 3.3: Loading scene captured using a CCD camera during the experiment - missing-rib specimen with a sprayed surface for the DIC strain evaluation (left), visualisation of the optically determined displacements (right).

■ Stress and strain evaluation

The engineering stress (σ_{eng}) and strain (ε_{eng}) values were determined from the geometrical properties of the tested specimens and the optically measured displacements of the markers. Then, the true stress (σ_{true}) and true strain ($\varepsilon_{\text{true}}$) were calculated according to Equations (3.1a) and (3.1b)

$$\sigma_{\text{true}} = \sigma_{\text{eng}} \cdot (1 + \varepsilon_{\text{eng}}), \quad (3.1a)$$

$$\varepsilon_{\text{true}} = \ln(1 + \varepsilon_{\text{eng}}). \quad (3.1b)$$

■ Evaluation of Poisson's ratio

From the strain fields assessed by DIC, Poisson's ratio ν_{12} was calculated using the formula

$$\nu_{12} = -\frac{\varepsilon_2}{\varepsilon_1}, \quad (3.2)$$

where ε_2 is the lateral strain in the direction perpendicular to the loading direction and ε_1 is the strain in the loading direction.

In the case of the 3×3 unit-cell samples, the deformation perpendicular to the loading direction was evaluated from the middle parts of the specimens' microstructure, where the concentration of the lateral strain occurred during both the quasi-static and dynamic experiments. Different methods were used for determining the function of Poisson's ratio for both the quasi-static and dynamic experiments of the RVE sized samples as described in detail in [12]. The methods for calculating Poisson's ratio were based on the different sets of correlation markers selected for the analysis. In this thesis, the "inner-inner" method based on the analysis of the inner part of the specimens' microstructure, where the concentration of the lateral strain occurred (see the red markers of the correlation points in Figure 3.4), was used to determine both the deformation parallel and perpendicular to the loading direction. Three specimens of each microarchitecture were tested in the quasi-static experiments and five specimens were tested at each strain-rate during the SHPB experiments, the mean curves, and standard deviation envelopes of the functions of Poisson's ratio for each type of experiment were calculated.

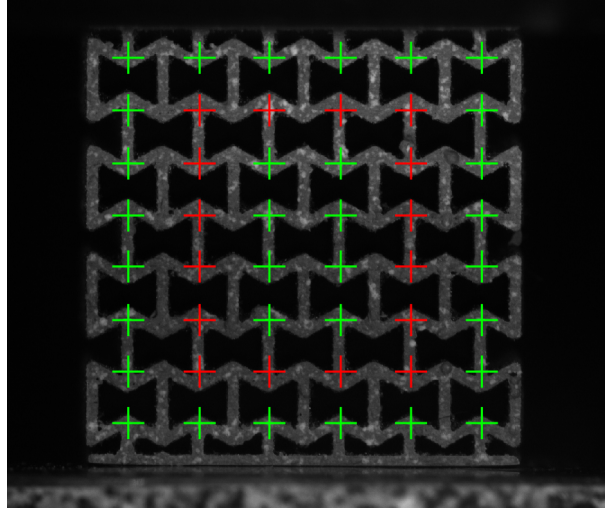


Figure 3.4: Example of the correlation pattern (green colour) generated on the 2D re-entrant honeycomb specimen showing the inner (red) and outer part used for the DIC evaluation of the results.

3.3 Numerical methods

Apart from the experimental methods, analytical and FE models can be used to describe the deformation behaviour of auxetic constructs, allowing the prediction and optimisation of the effective mechanical characteristics that facilitate the material design for a specific application. Most of the analytical models assume small deflections, neglecting the axial deformation of the struts. Thus, the analytical approach can be used to prove the concept of the NPR, optimise the parameters of a structure (e.g., the re-entrant angle, relative density, strut thickness), and maximise the effective parameters of the resulting constructs (i.e., deformation energy per unit volume, yield strength of the structure, compressive strength) according to the specific requirements. Typically, for the unit-cells considered in this work, the derived Poisson's ratio depends on the magnitude of the re-entrant angle governing the topology of the unit-cell and/or the strut length ratio. Using the Timoshenko beam theory and the elastic-behaviour assumption, it is possible to calculate the overall elastic modulus E and critical-yield compressive force F_m based on the yield strength σ_m of the bulk solid material. From the yield compressive force, the compressive strength of the structure can be then expressed.

However, these analytical models are effective only when simplifying assumptions such as when the small deflection theory and linear elastic-material properties are used. Consequently, these models only give satisfactory results for small deformations and are limited to the calculation of the overall elastic properties or the estimation of the yield point of a structure. When large strains with non-linear material properties are to be considered, FE models have to be used instead. Thus, FE models of the tested auxetic structures were developed and subjected to the same loading conditions as during the compression tests. The deformation behaviour of the tested samples under large strains (up to 10% or 20% strain) was then compared with the predictions obtained from the numerical models to verify their suitability for the representation of such microarchitectures. The stress-strain curves were inversely assessed from the FE simulations, i.e., from the reaction forces calculated at the restrained side of a sample. Using such inverse FE simulations, it is relatively easy not only to obtain the stress-strain curves for each

considered sample, but also to establish the stresses and strains arising at the individual struts from the deformation of the structure. Hence, these strains can be easily compared to the values experimentally obtained from the digital image correlation at the same positions (i.e., individual markers).

The parametric FE model of each auxetic structure has been then developed. The geometries have been discretised with beam elements having 6 degrees of freedom at every nodal point. The elements were based on the Timoshenko beam theory, which considers a first-order shear deformation theory, where the transverse shear strain is constant through the cross-section; that is, the cross-sections remain planar and undistorted after deformation. The material model set in the simulations was elasto-plastic, combining von Mises yield criteria and bilinear isotropic work hardening. The material properties of the EX200 material are summarised in Table 3.1.

Parameter	Value	Unit
Young's modulus	1.159	GPa
Yield stress	42.4	MPa
Poisson's ratio	0.2	–
Hardening tangent modulus	12.8	MPa

Table 3.1: Material properties of the EX200 material used in the FE simulations.

To inversely calculate the stress-strain relationship of the structures, the models included both geometric and material nonlinearities. The loading was prescribed in 100 loading steps, i.e., in each step a 0.1% or 0.2% deformation was applied. In the case of such a large-strain analysis, a highly deformed geometry has an important effect on the strain and, therefore, geometric nonlinearities must be considered. To consider the post-buckling behaviour of thin beams subjected to a large compression, strain measures have to account for higher-order terms. Thus, in the analyses, the material stress-strain properties were input in terms of the true stress versus the logarithmic strain. In every loading step, the reaction forces originating from the supports were calculated and the true stresses and strains were established using Equations (3.1a) and (3.1b). The visualisations of the FE models for the individual unit-cells can be seen in Figure 3.5, the visualisation of the planar auxetic lattices is shown in Figure 3.6, and the visualisation of the 3D re-entrant

honeycomb is shown in Figure 3.7.

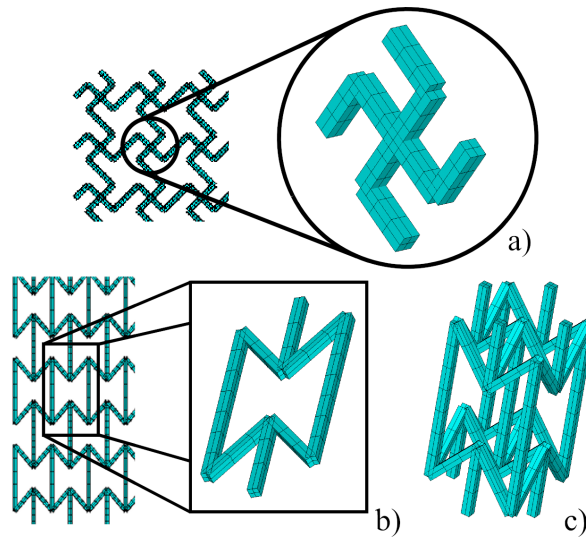


Figure 3.5: Visualisation of the FE-model unit-cells used in the numerical simulations with details of the unit-cells: a) missing-rib structure, b) 2D re-entrant honeycomb, and c) 3D re-entrant honeycomb.

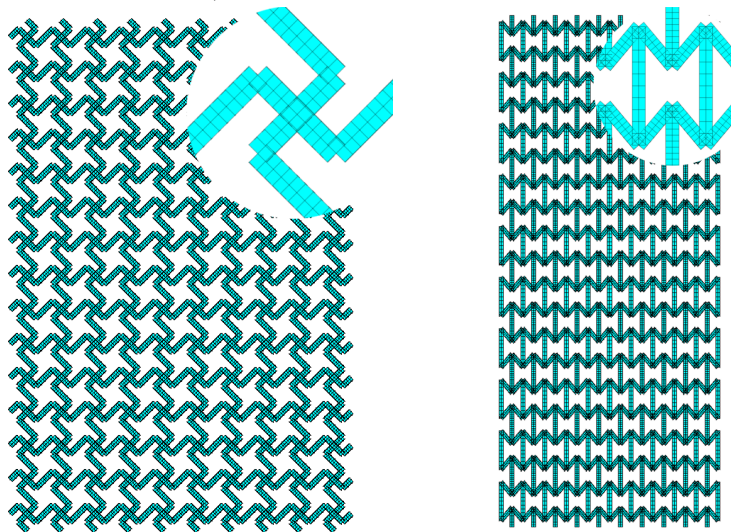


Figure 3.6: FE model of the missing-rib structure and the 2D re-entrant honeycomb. Detailed view of the elements inside the periodic unit-cell in the upper right corner.

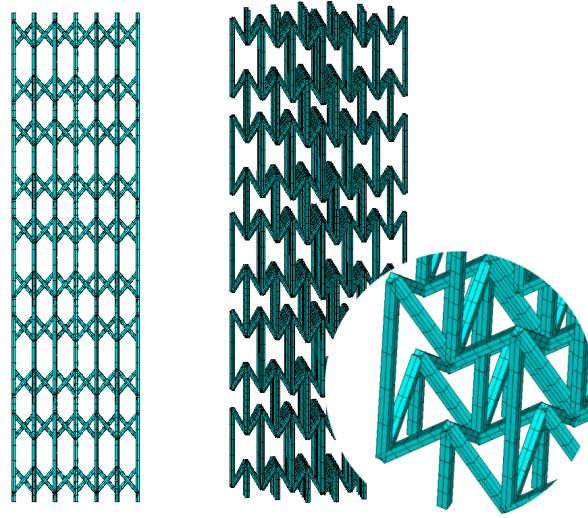


Figure 3.7: FE model of the 3D re-entrant structure: side view of the FE mesh (left), isometric view (right) with a detailed view of the elements inside the periodic unit-cell in the lower right corner.

■ 3.4 Results

■ 3.4.1 Polymeric samples

Using the values for the parameters of the considered material model listed in Table 2.1, the numerical stress-strain diagrams have been obtained for the polymeric samples. The comparison of the numerical and experimental curves is provided in Figures 3.8 - 3.10.

It can be seen that the missing-rib lattice exhibits a similar initial compressive behaviour to a typical closed-cell foam. The initial linear elastic part is followed by an apparent yield point and a compaction region with a constant stress plateau. These regions are then at approximately 17.5% of the strain followed by a localised densification due to the NPR of the unit-cell and repeated decreases in the stress that can be attributed to the beams ruptures due to the excessive bending and brittle behaviour of the material used for the production. Importantly, a good correlation of the numerical and

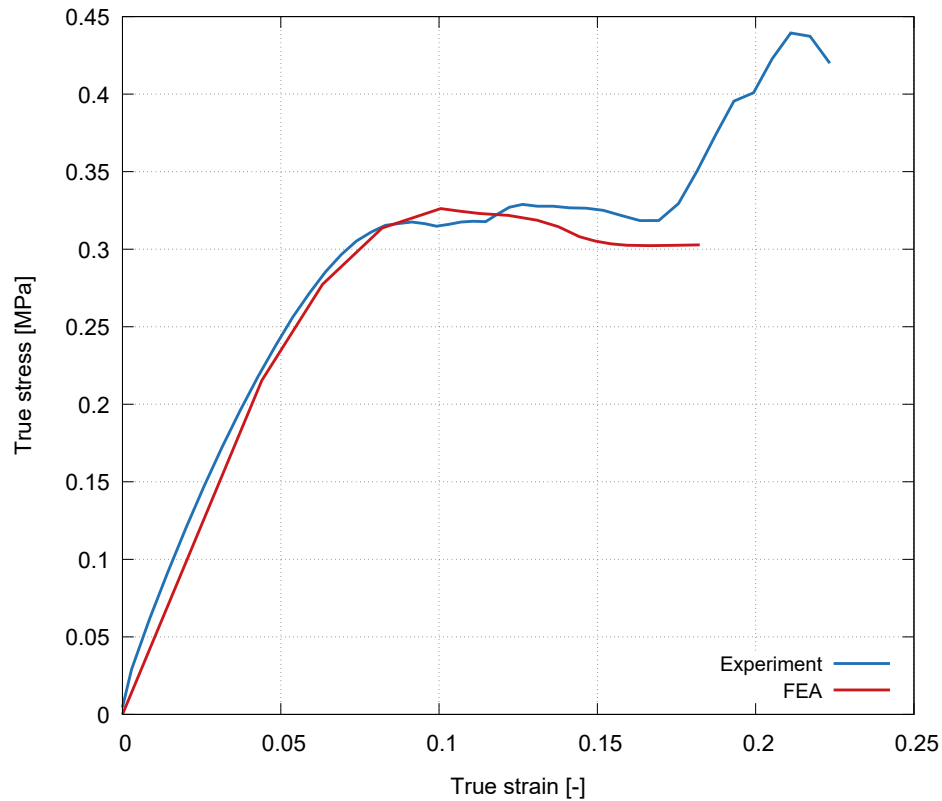


Figure 3.8: Comparison of the experimental stress-strain curve and the numerically calculated curve for the missing-rib structure.

experimental results was obtained in terms of the stiffness, yield point, and plateau stress up to a 15 % strain.

The inspection of the stress-strain diagrams of both the 2D and the 3D re-entrant honeycomb lattices reveals that such a construct exhibits a significantly different deformation behaviour than the missing-rib structure. After the initial linear elastic region, a drop of stress is followed by cyclic increasing and decreasing stress levels in the specimens with an apparent progressive trend. Following the visual inspection of individual projections during the deformation, the occurrence of cycles can be attributed to the collapse of individual layers of unit-cells in the microstructure, which is further facilitated by cracking in the highly stressed regions in the vicinity of the strut joints caused by the characteristics of the printed PMMA material. The FE simulations yield, in this case, a reasonable prediction in terms of the yield stress of the structure and the overall shape of the stress-strain response during the

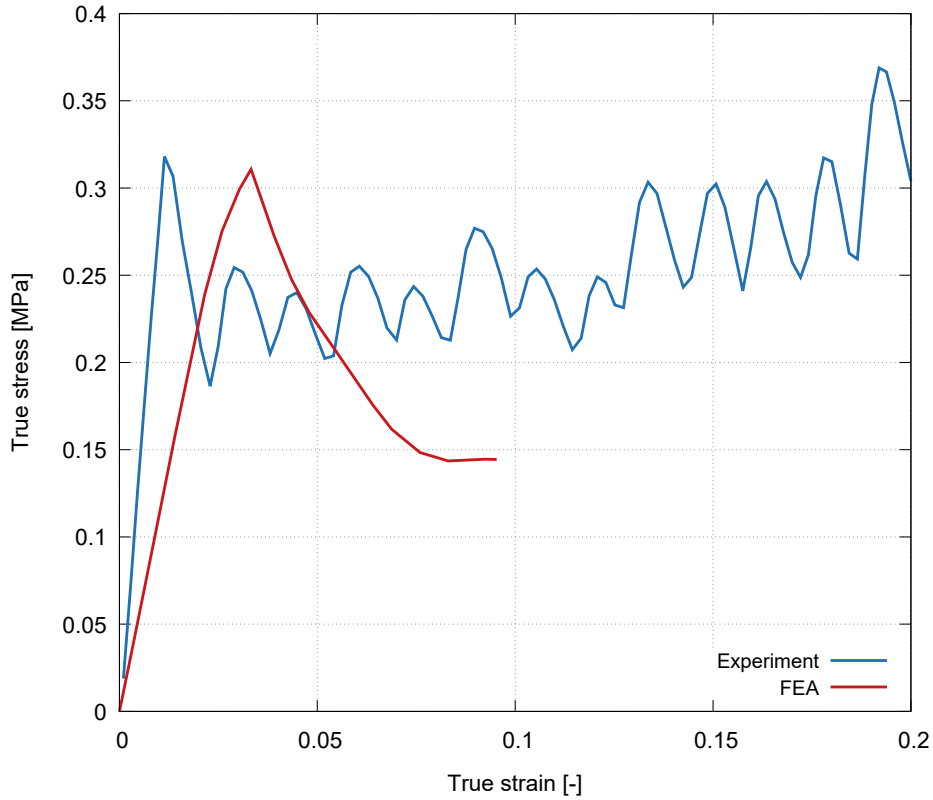


Figure 3.9: Comparison of the experimental stress-strain curve and the numerically calculated curve for the 2D re-entrant structure.

collapse of the first layer of the unit-cells in the lattice. However, the FE simulations of the re-entrant structures predict a smaller overall stiffness, which is apparent from the comparison between the experimental stress-strain curves and the numerically obtained responses. Since the trend of the stress-strain curve obtained from the experimental and numerical analysis is identical and the yield stress is also similar, this difference in the effective stiffness of the lattices can be attributed to the mechanical properties of the wrought EX200 material, which are different from the available nominal values and to non-conformity of the printed samples to the beam analogy considered in the FE simulations.

For this reason, a set of three-point-bending experiments was carried out using prismatic beams with rectangular cross-sections that were carefully cut from the printed specimens using a micro-lathe. Based on the DIC strain evaluation using the same method utilised for the uniaxial compression tests,

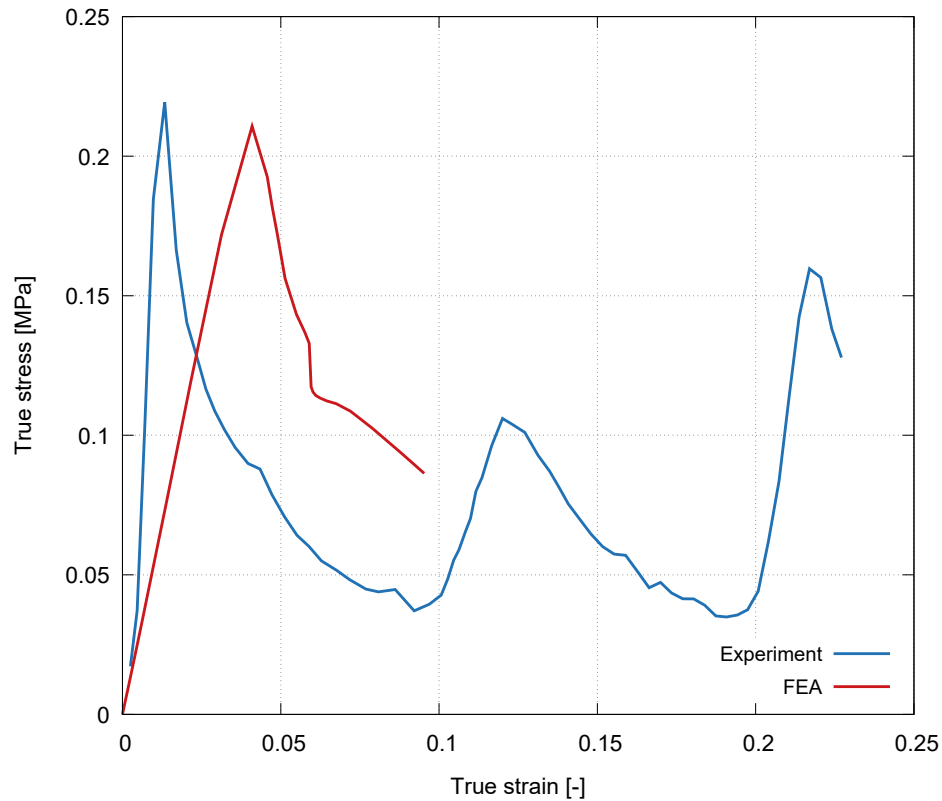


Figure 3.10: Comparison of the experimental stress-strain curve and the numerically calculated curve for the 3D re-entrant honeycomb structure.

a bending modulus of approximately 1.5 GPa was calculated on the basis of the Euler-Bernoulli theory. This value is close to the nominal flexural modulus of 1.5 GPa provided by the manufacturer that was also used in the FE simulations. Thus, the discrepancies between the numerically and the experimentally evaluated stiffness might have been caused on the material-model level by properties that were different from the predicted properties of the joints between the individual struts, influencing the bending characteristics of individual layers, which formed the principal mode of deformation of the re-entrant structures. Additionally, by comparing Figures 3.5 and 3.25, it is evident that the discrepancy between the discretised and real geometry of the samples in the region of strut-joints is also an important contributing factor (see, particularly, the fillet acting as a reinforcement in the joint).

Hence, a parametric FE study was performed to investigate the required compensation measures for the proper calibration of the discretised numerical

models. Here, Young's modulus prescribed by the material model to the elements of struts was varied in the numerical simulations until a smaller than 5% difference between the numerical and experimental yield strain was reached. This measure was selected since the visual inspection of the deforming re-entrant honeycombs during experiments revealed the rigid-like behaviour of the strut joints, while the bending of the struts themselves is the principal mode of deformation of the unit-cells. Using this approach, Young's modulus of 3.3 GPa (increased by a factor of 2.85) for the 2D re-entrant honeycomb and 3.57 GPa (increased by a factor of 3.08) for the 3D re-entrant honeycomb were identified to satisfy the 5% yield strain difference criterion. Figures 3.11 and 3.12 then show a comparison of the experimentally and numerically acquired stress-strain diagrams for both the re-entrant structures with the modified stiffness of the strut joints.

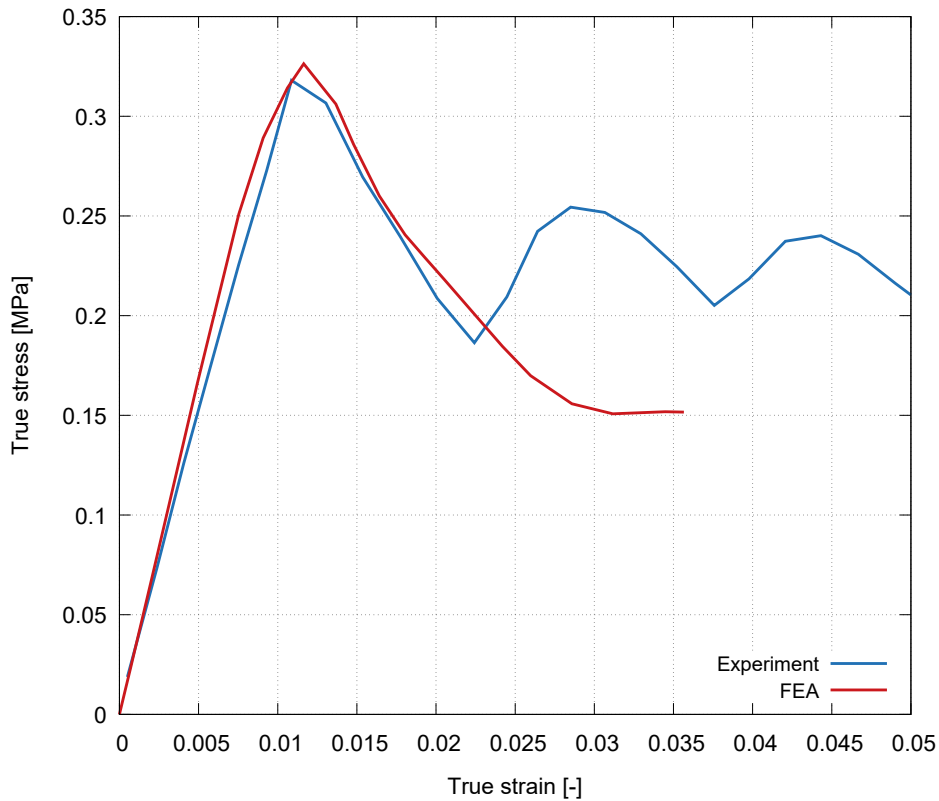


Figure 3.11: Comparison of the experimental stress-strain curve and the numerically calculated curve for the 2D re-entrant structure.

It was possible to perform the FE analysis up to 20% strain only for the missing-rib auxetic structure. Larger strain values could not be calculated as

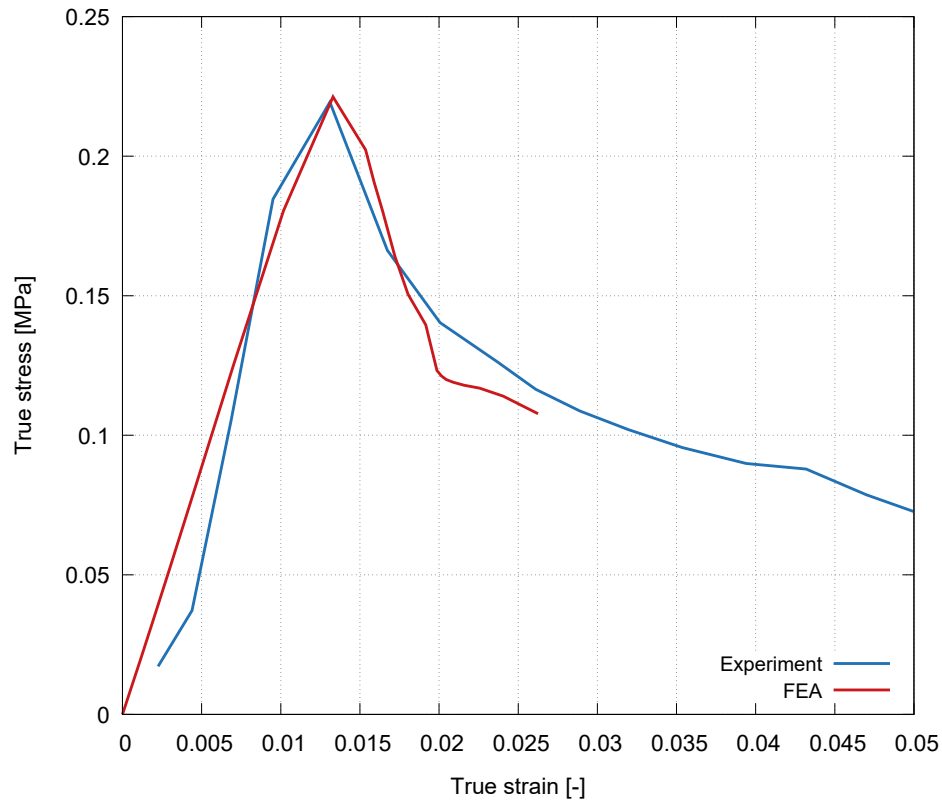


Figure 3.12: Comparison of the experimental stress-strain curve and the numerically calculated curve for the 3D re-entrant honeycomb structure.

the elements become extremely distorted yielding to the instability and convergence issues in the simulations. Furthermore, to capture the stiffening during compaction, it would have been necessary to include the self-contact between the individual struts, which would significantly increase the complexity and computational costs of the simulations.

After verification of the the FE models of selected geometries against the experimental data, the FE models were fully parametrised to enable the fast calculation of the dependencies between the design parameters (strut thickness, orientation angle, strut length) and the overall mechanical properties (stiffness, Poisson's ratio, yield stress). For each structure, calculations were performed in a repetitive manner, while the selected design parameter was varied and the effective properties were established. This enables one to use the FE models for the description of the deformation behaviour of auxetic structures and allows for the effortless and fast prediction (optimisation) of the effective

mechanical characteristics that facilitates the material's design for a specific application. Although there are many analytical models available in the literature, here, only a numerical approach was used. One reason is that the analytical models assume small deflections neglecting the axial deformation of the struts. The other reason is that, for the investigation of very large deformations, one must analyse the self-contact between the individual struts. The analytical models are effective only when simplifying assumptions such as when the small deflection theory and linear elastic material properties are used. In contrast, the FE approach can be used to prove not only the concept of the NPR and/or to optimise the parameters of the structure (e.g., the re-entrant angle, relative density, struts' thickness), but also to maximise the effective parameters of the resulting constructs (i.e., deformation energy per unit volume, yield strength of the structure, compressive strength) according to the specific requirements.

First, only elastic material properties were applied and the basic properties of the structure were determined. This approach was used for all the FE models, in which the following parameters were varied: (i) strut thickness ($b \times h$), (ii) strut length, and (iii) re-entrant angle. Then, the elasto-plastic material properties were applied and the stress-strain curves were assessed from the FE simulations inversely, i.e., from reaction forces calculated at the restrained side of the sample. Such inverse FE simulations provide not only the stress-strain curves for each considered sample, but it is also possible to map the stresses and strains arising at the individual struts from the deformation of the structure. Hence, the strains can be easily compared to the experimentally obtained values from the DIC at the same positions. To demonstrate the importance of nonlinear material properties and finite strain theory in the FE analyses, comparative FE simulations were performed. These simulations were carried out for a variable strut thickness and the results were plotted against the calculated relative density of the FE model. The following graphs show the dependency of the overall stiffness on the relative density. The relative density of the FE models is varied by changing the cross-sectional area of the struts. The relative density is then calculated from the known strut thickness t and the dimensions of the periodic unit-cell.

An important property of an auxetic structure is its overall stiffness. To

calculate the stiffness of each designed auxetics, the FE models were loaded in a longitudinal direction. Instead of using force, the upper side of the model was loaded by a vertical displacement corresponding to 10%. All degrees of freedom corresponding to the bottom plane of the model were removed. The stiffness was calculated as the normal stress σ_n (calculated as the reaction force at the lower support divided by the cross-sectional area A) divided by the applied strain $\varepsilon = 0.1$. Figures 3.13 - 3.15 show the effective stiffness (the reaction force divided by the cross-sectional area) of the studied auxetic lattices plotted against the relative density as computed by the parametric model. The influence of the material models, the linear elastic and von Mises plasticity with isotropic hardening, and also the strain formulation in terms of the small deformation theory and finite strain theory are also compared.

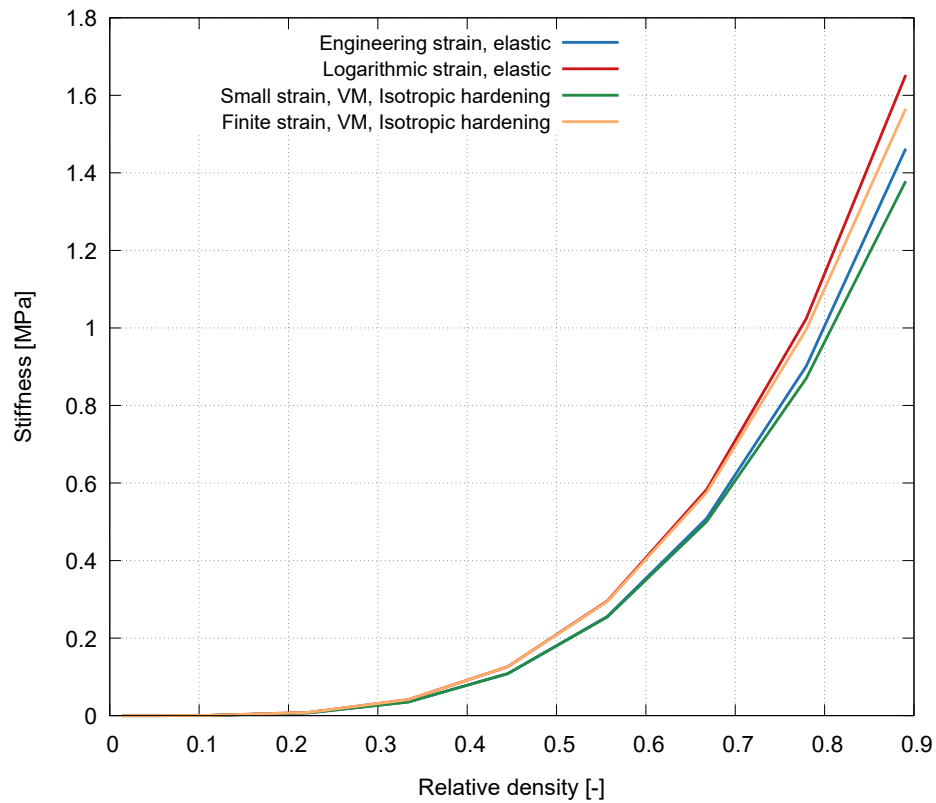


Figure 3.13: Overall stiffness plotted against the relative density for the *missing-rib structure* - the difference in the small/finite strain theory and the elastic/elasto-plastic material models.

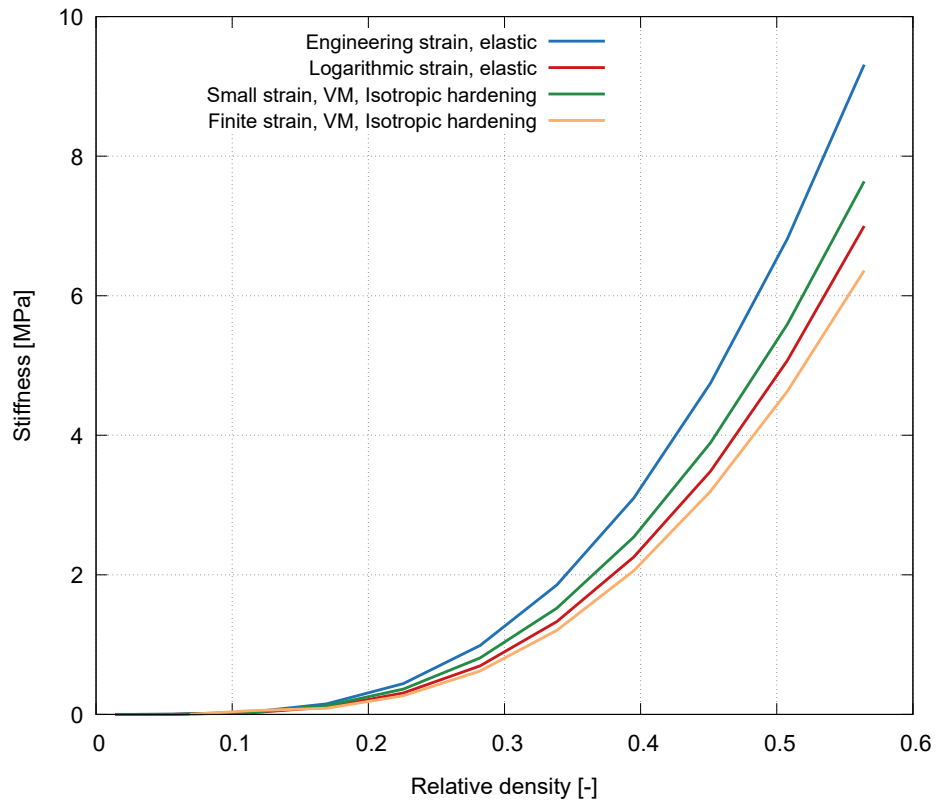


Figure 3.14: Overall stiffness plotted against the relative density for the *2D re-entrant structure* - the difference in the small/finite strain theory and the elastic/elasto-plastic material models.

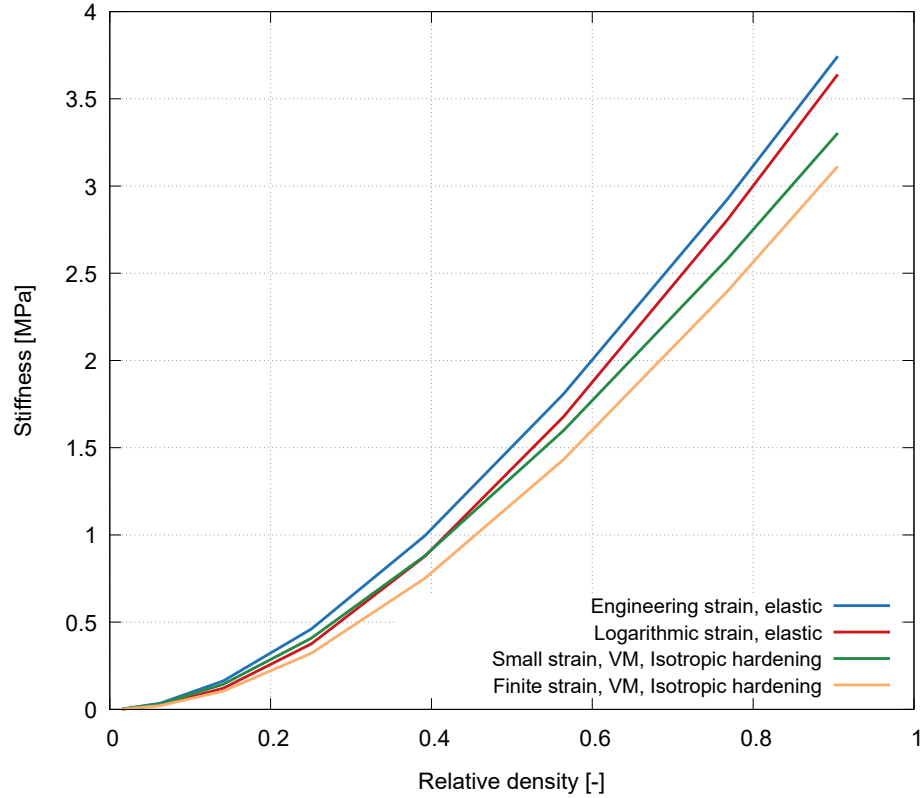


Figure 3.15: Overall stiffness plotted against the relative density for the *3D re-entrant structure* - the difference in the small/finite strain theory and the elastic/elasto-plastic material models.

To show the applicability and the important differences in the small deformation versus the finite strain formulations, the dependency of the calculated Poisson's ratio on the relative density of the structure is plotted in Figures 3.16 - 3.18. Poisson's ratio is calculated from the transversal nodal displacements in the mid-cross-section of the model (i.e., $\varepsilon_{x,y}$ in the middle of the sample divided by applied ε_z). Here, in the finite strain formulations, the Green-Lagrange strain tensor $G = \frac{1}{2} (\mathbf{F}^T \mathbf{F} - \mathbf{I})$, which is based on the deformation gradient $\mathbf{F} = \frac{\partial x}{\partial \mathbf{X}}$ (derivatives of the deformed coordinates with respect to the original coordinates \mathbf{X}), is used. As the work-conjugate stress measure to the Green-Lagrange strain tensor, the second Piola-Kirchhoff stresses are then used.

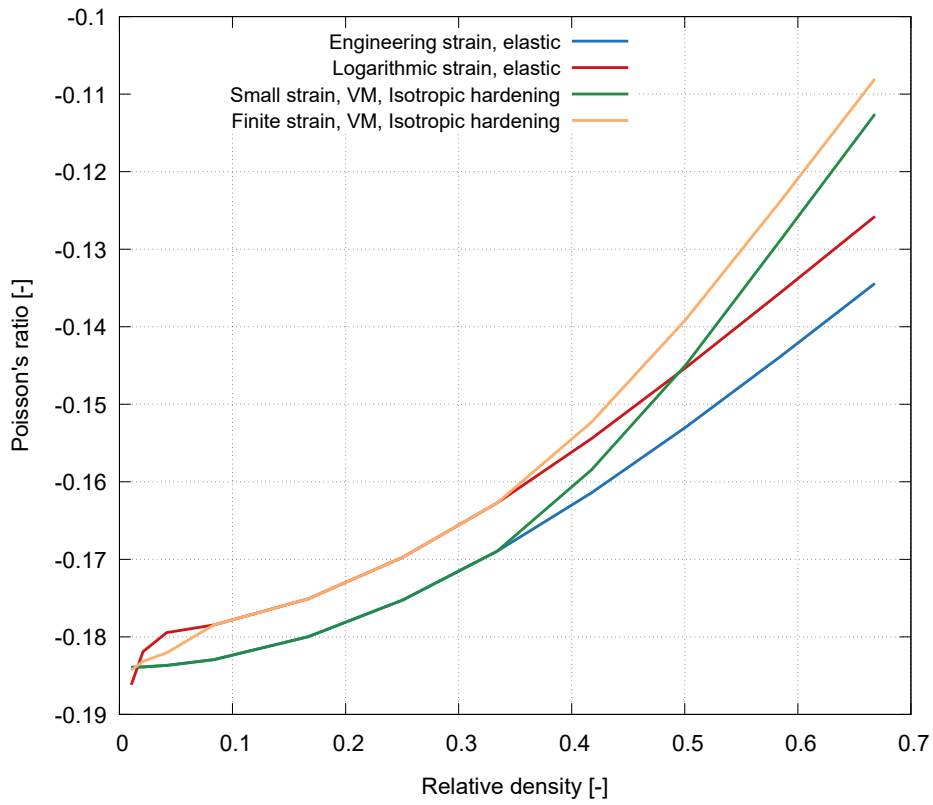


Figure 3.16: Calculated Poisson's ratio plotted against the relative density for the *missing-rib structure* showing the importance of taking geometrical non-linearity into account.

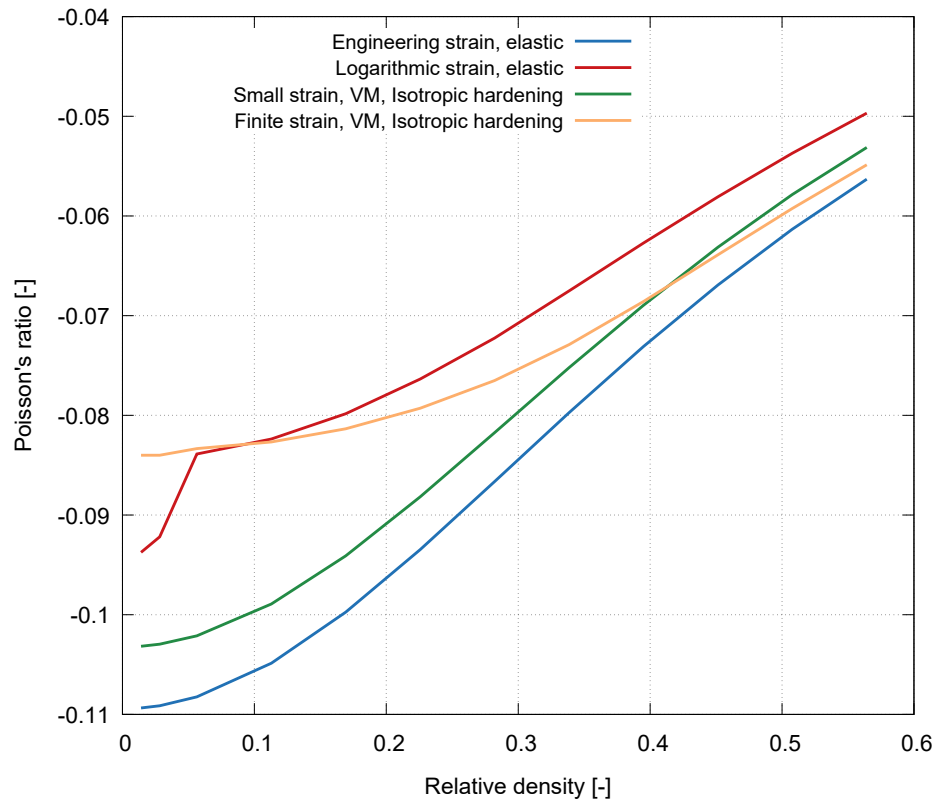


Figure 3.17: Calculated Poisson's ratio plotted against the relative density for the *2D re-entrant structure* showing the importance of taking geometrical non-linearity into account.

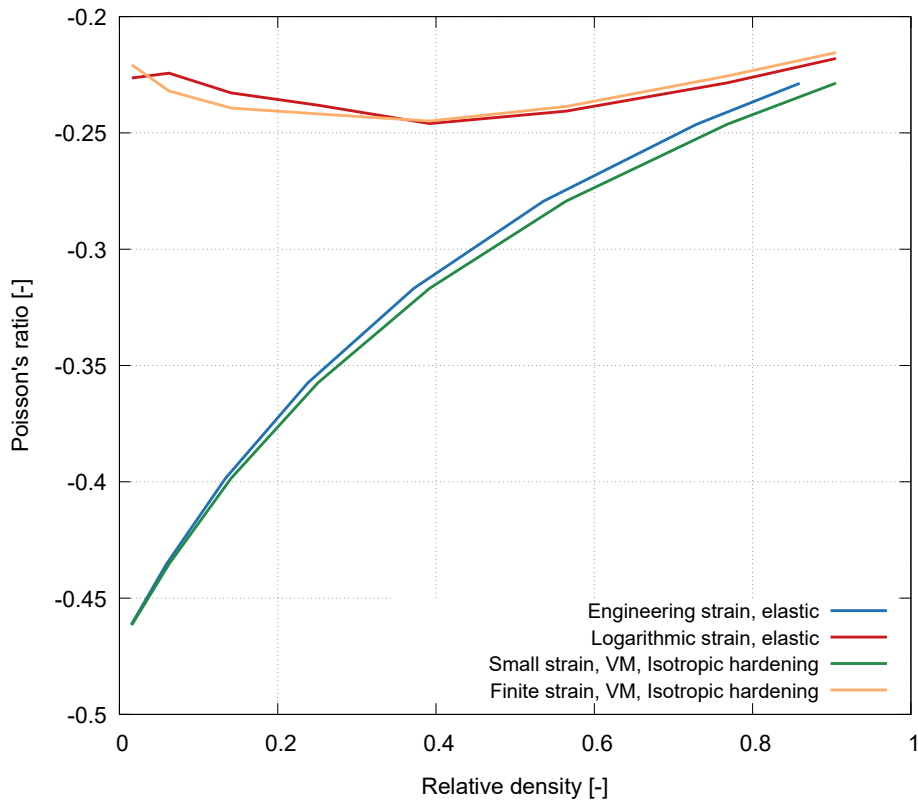


Figure 3.18: Calculated Poisson's ratio plotted against the relative density for the *3D re-entrant structure* showing the importance of taking geometrical non-linearity into account.

3.4.2 Steel samples

Stress-strain response

The stress-strain diagrams of the auxetic lattices having 3×3 unit-cells and the comparison with the RVE sized assemblies are depicted in Figures 3.19 - 3.21. It can be seen that the quasi-static response of the samples with twice the number of unit-cells in every relevant spatial direction is very similar to the previous set even though the overall size of the unit-cells and, consequently, the cross-sectional dimensions of the constituting geometrical elements have been lowered significantly.

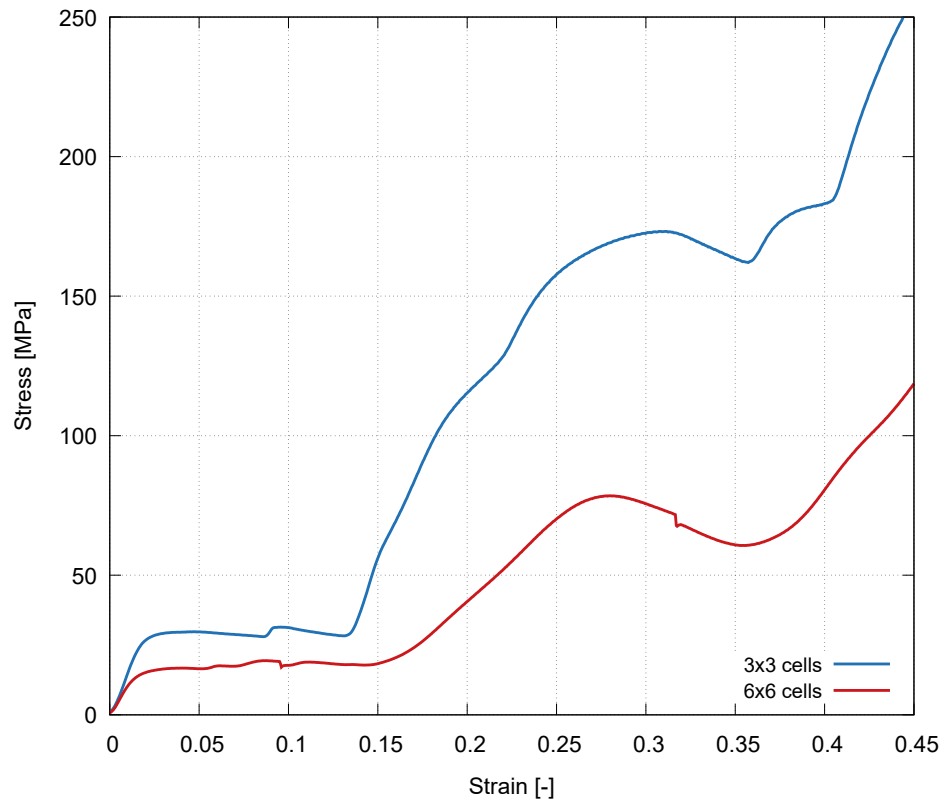


Figure 3.19: Comparison of the experimental quasi-static stress-strain curve - 2D missing-rib lattice with a different number of unit-cells.

The 2D missing-rib lattice is typical for its plateau of constant stress up to 15 % of the compressive strain due to uniform compression in all the unit-cells and their negligible rotations. According to the orientation of the unit-cells in

the lattice, one or more layers of the unit-cells exhibit lateral movement until the collapse of the struts in one layer causes a significant increase in the stress visible at strains over 15%. This process then repeatedly continues until the densification of the whole structure occurs and due to the quasi-static strain-rate, a significant difference in the lateral positions of the upper and bottom layer of the unit-cells can be observed. The increase in the number of unit-cells to the RVE dimensions resulted in a 0.5 times reduction of the apparent yield stress and a 30% lower average plateau stress together with the lower slope of the densification part of the response that also reaches 50% stress at the end of the experiment at the compressive strain of 0.45. The transfer between the plateau region and the densification part is sharper in the case of the 3×3 lattice, but the strain levels of the oscillations in the densification region are interestingly the same indicating that the number of layers is not the dominant factor influencing the overall compressive response of the missing-rib structure, when quasi-static loading is applied.

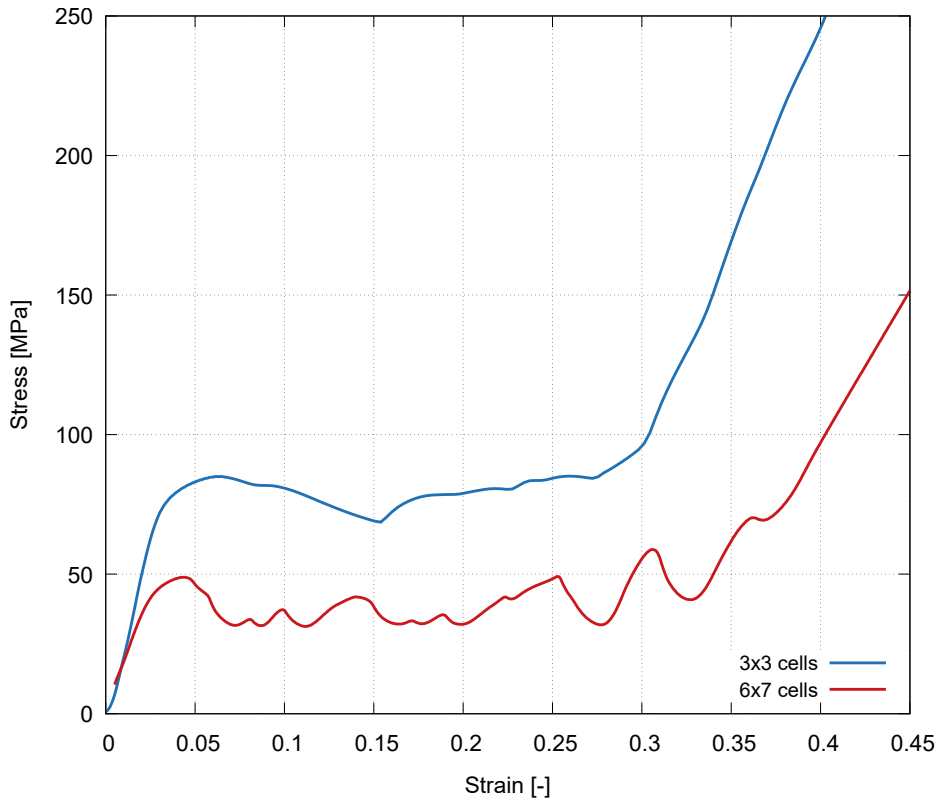


Figure 3.20: Comparison of the experimental quasi-static stress-strain curve - 2D re-entrant honeycomb lattice with a different number of unit-cells.

Both the 2D and the 3D re-entrant honeycomb lattices exhibit compressive

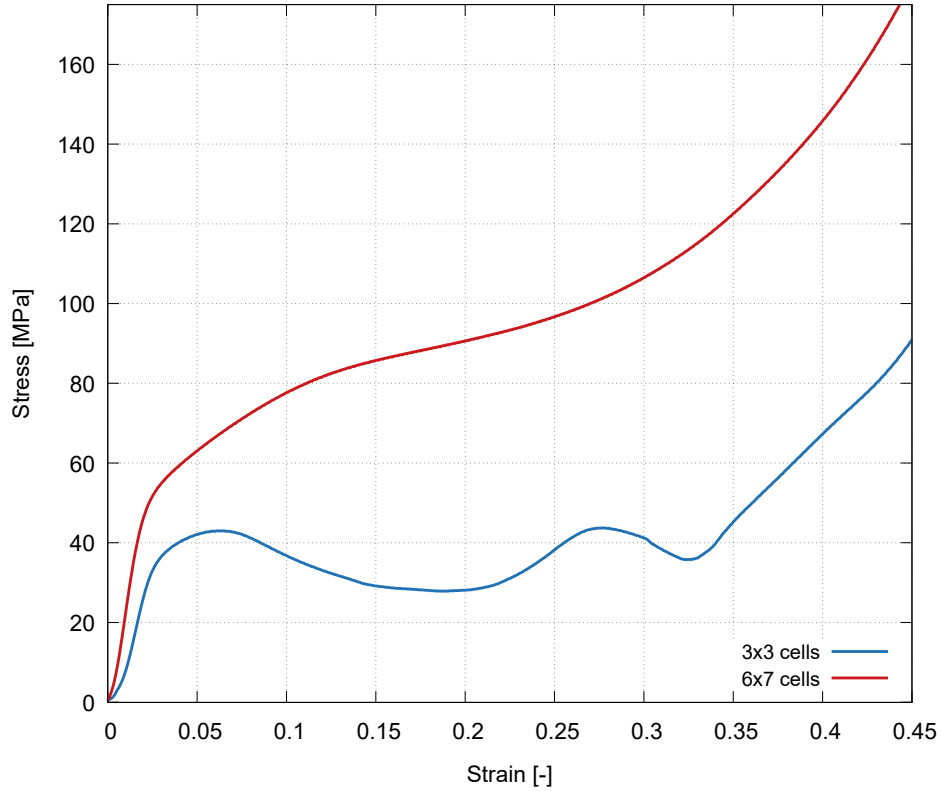


Figure 3.21: Comparison of the experimental quasi-static stress-strain curve - 3D re-entrant honeycomb lattice with a different number of unit-cells.

behaviour very similar to the response of closed-cell metal foams, where the initial elastic part is followed by a relatively wide plateau of constant stress until the self-contact of the microstructural elements occurs and densification, represented by an approximately linear increase of stress, is observed. The difference between the 2D and 3D lattice consists particularly in the shape of the plateau stress as the 3D lattice is prone to a stability loss of the individual struts resulting in an easier collapse of the layers, which then yields a repeated increase and decrease in the overall stress. In the case of the 3×3 lattices, the apparent yield of the 3D lattice also takes place at a stress below 45 MPa, approximately 30% lower than the 2D assembly, due to its higher porosity and lower stiffness of the struts. The same findings can be attributed to the 2D re-entrant honeycomb structure with the difference in the influence of the number of layers in the lattice. When comparing the shape of the plateau stress curve, the 6×7 unit-cell lattice exhibits repetitive oscillations with the number of local maxima correlating with the number of layers in the structure. Consequently, when the last layer undergoes self-contact of

the geometrical elements, the densification part of the specimen response is started. However, the yield point and the plateau stress is decreased by approximately 50% due to decrease in the cross-section of the struts that are then prone to an earlier loss of stability.

A different behaviour can be seen in the case of the 3D re-entrant honeycomb. Here, the lattice with a larger number of unit-cells not only reaches a higher apparent yield strength, but the increase of the stress level is monotonic and gradual from 10% of the strain without any oscillations typical for a structure composed of 3×3 unit-cells. The resulting stress-strain curve is analogous to the compressive response of low-porosity closed-cell metal foams. Similarity can also be found in the compressive behaviour of the open-cell cubic elementary cells forming the constituting elements of the beam analogies for the simulation of closed-cell metal foams [2], when the elasto-plastic material model is used for the inverse estimation of the effective mechanical properties. Probably due to the lower unit-cell dimensions and lower void space within the microstructure of the lattice, the stress levels of the RVE sized lattice are two times higher than in the case of the 3×3 lattice.

■ Strain-dependent Poisson's ratio

Both the compressive and lateral strains were calculated using the DIC method by tracking the deformation of the strut joints. The lateral strains were calculated from the displacements in the central layer of the printed lattices, where the deformation is not affected by the boundary conditions influencing the response of the cells neighbouring the free faces of the specimens. In all the cases, the values of Poisson's ratio reach positive and/or negative extreme values for a compressive strain close to 0 as a result of the division by very low numbers. Figures 3.22 - 3.24 depict Poisson's ratio plotted against the compressive strain of the lattices subjected to the quasi-static loading as a comparison of the assemblies with a different number of cells.

Poisson's ratio of the 2D missing-rib structure is negative only in a narrow deformation range up to approximately 4% of the compressive strain. The

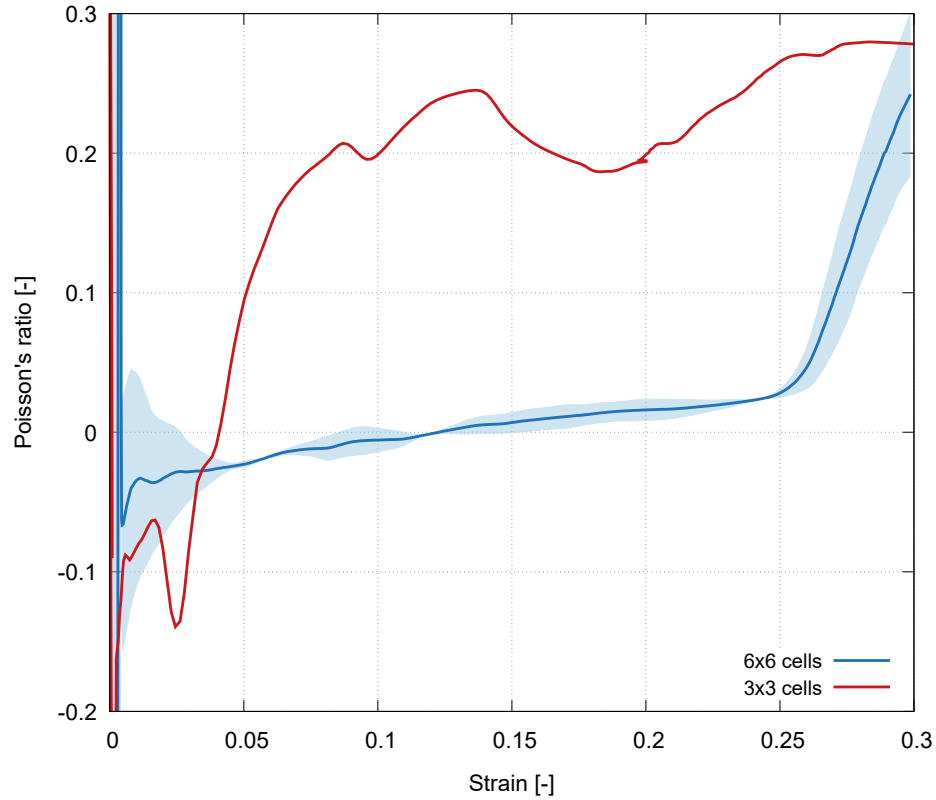


Figure 3.22: Comparison of the experimental quasi-static function of Poisson's ratio - 2D missing-rib lattice with a different number of unit-cells and the standard deviation for the 6×6 lattice.

minimum reliably identified Poisson's ratio of -0.13 is reached at 3% of the compressive strain. From this value, Poisson's ratio gradually increases to 0.25 and oscillates around this value until the end of the experiment. It is apparent that the low number of unit-cells in the lattice and evaluation of Poisson's ratio from the displacement of the outer unit-cells (in the lateral direction) yields unreliable and unrepresentative results. The functions of Poisson's ratio calculated from all three layers were, for this reason, studied and significant discrepancies have been found, supporting the importance of the RVE dimensions. Here, the RVE sized samples exhibit a smooth monotonic increase in Poisson's ratio from the minimum reliable value of -0.04 at a 2% strain up to zero at a 12% strain, where the auxetic behaviour vanishes and Poisson's ratio remains positive until the end of the experiment. The reason for this behaviour is similar to the 3×3 lattice and is given by the low loading rate causing the lateral displacements of the whole layers, which negates the auxetic character of the whole assembly. Following the visual

inspection of the captured image series' in the late stages of the experiments, such a behaviour can account for the overall loss of stability in the specimens due to excessive rotations of the individual strut joints.

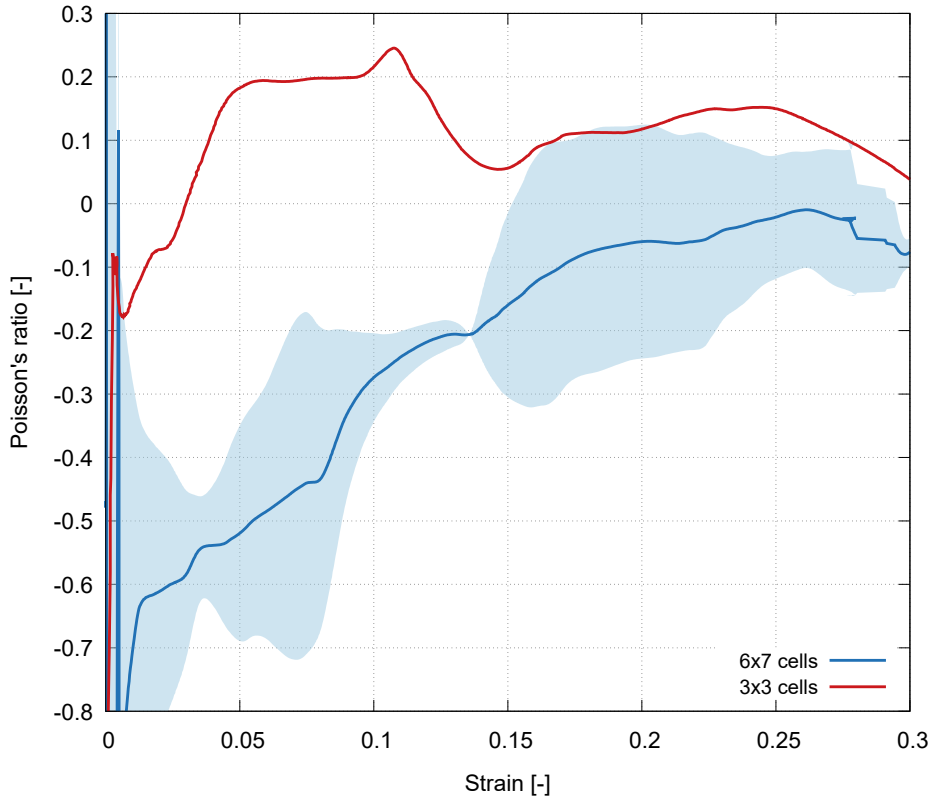


Figure 3.23: Comparison of the experimental quasi-static function of Poisson's ratio - 2D re-entrant honeycomb lattice with a different number of unit-cells and the standard deviation for the 6×7 lattice.

The analogous findings have been made in the case of the 2D re-entrant honeycomb up to the compressive strain of 0.25. Here, Poisson's ratio reaches 0.2 at a 5% strain and remains constant up to 10% of compressive strain. Then, Poisson's ratio repeatedly decreases and increases together with the collapse of the individual layers and the structure regains an auxetic behaviour from 32% of the compressive strain. The comparison of the 2D re-entrant honeycombs, in view of the different number of unit-cells, reveals the conformity of both curves in their general shape, although the influence of the deformation localisation into the particular layer is more significant in the case of the structure with the 3×3 unit-cells. The increase in the number of unit-cells leads to values of Poisson's ratio lower than -0.8 at 1% compressive strain and the average Poisson's ratio from all the experiments

remains negative until the end of the experiments, even though the standard deviations are higher than for the missing-rib structure and reach positive values at strains over 17%.

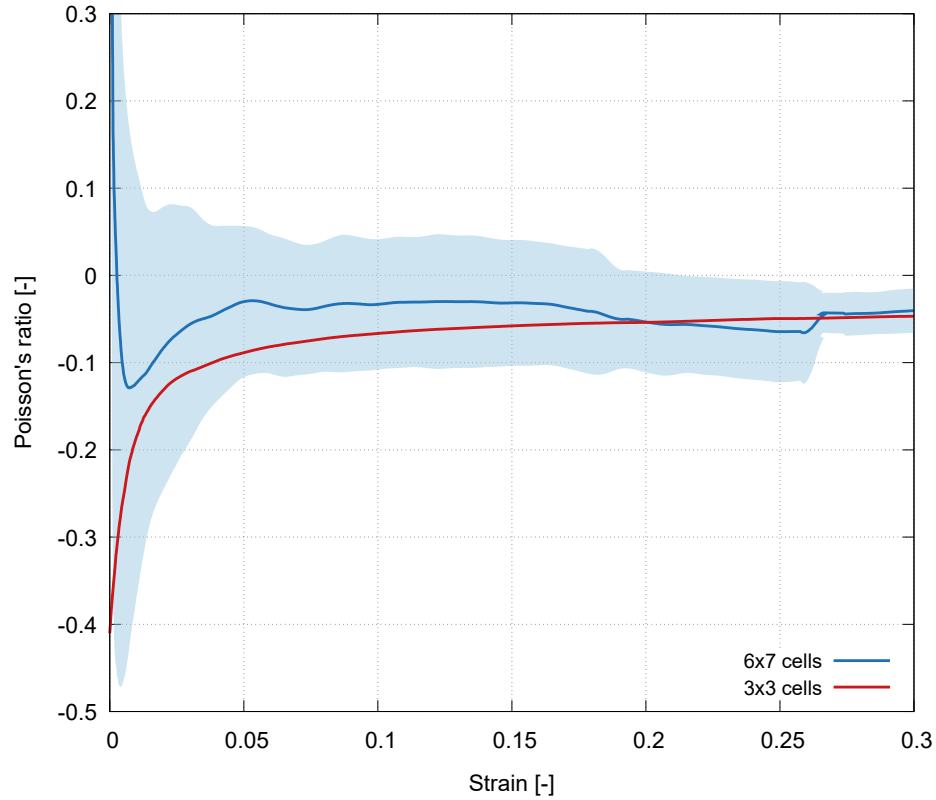


Figure 3.24: Comparison of the experimental quasi-static function of Poisson's ratio - 3D re-entrant honeycomb lattice a with different number of unit-cells and the standard deviation for the 6×7 lattice.

Apparently, a different behaviour was identified for the 3D re-entrant honeycombs, where the highest similarity of the results was obtained for the assemblies with a different number of unit-cells. Apart from the initial region of very small compressive strains, both assemblies not only exhibit auxetic behaviour throughout the quasi-static experiments, but the shape of the curves is analogous and both structures reach the same asymptotic value of -0.05 at compressive strains over 25%. Here, the function of Poisson's ratio of the 3×3 lattice monotonically increases towards zero and the function values are within the standard deviation intervals of the RVE sized lattice in all the stages of the experiment.

3.5 Discussion

The quasi-static compressive response of auxetic lattices with three different porous microarchitectures exhibiting in-plane and volumetric NPR was studied both experimentally and numerically. The samples for the development of the quasi-static FE simulations were printed from PMMA using a multi-jet modelling technology of direct production. Experiments with the optical tracking of the deformation were performed to obtain the true stress - true strain diagrams in compression. The FE models of all the considered polymeric microarchitectures were developed and their ability to predict the mechanical response of the studied constructs were assessed by comparing numerically and experimentally obtained stress-strain diagrams. The presented FE models can be readily used for the optimisation of the auxetic structures for the given overall (desired) mechanical properties and material properties at the level of the struts.

Taking advantage of the direct 3D printing, it was possible to verify the FE models and the overall optimisation methodology against the precise experimental data assessed by the DIC. The results of the study showed the general agreement between the FE simulations, the theoretical models used for the small deformations, and the compressive experiments. However, for larger strain values, one must use the finite strain theory and proper constitutive equations for the material, depending on the geometrical properties (slenderness of the struts). In this work, an elastoplastic material with von Mises plasticity and isotropic linear hardening was used. Combining the plasticity (material nonlinearity) being introduced through stress-strain relations from an incremental plasticity theory with the incremental technique developed to account for the effects of geometric nonlinear behaviour (finite strain and large deflections), the analyses were capable of treating the combined effects of the material and geometric nonlinearity. A parametric study showed that great attention must also be paid to the discretisation of the geometry. It was found, for all the considered FE models, that it was necessary to use a large number of elements per strut to capture the behaviour of the 3D printed specimens with sufficient precision.

Due to the initial disagreement of the simulated and experimentally obtained stress-strain curves in terms of effective stiffness of re-entrant structures, bending experiments of the single struts extracted from the printed specimens were performed. The derived constants of the FE material model were found to be insufficient and the dominant deformation modes of the unit-cells were studied. Then, the stiffness of the base material was varied in a parametric study to reach conformity between the numerically and experimentally obtained stress-strain curves. As a contributing factor, the disagreement between the geometrical model of the lattices, the 3D printed specimens, and the method of the strut-joining in the beam analogy used in the simulations was identified, as the 3D printing performed even at 600 DPI still produces significant fillets instead of sharp edges (see the SEM-SE images of the strut-joint region depicted in Figure 3.25).

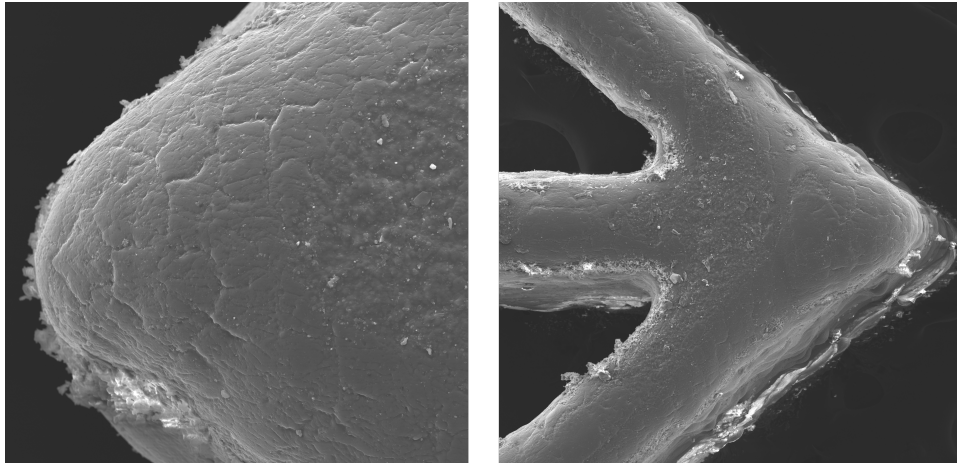


Figure 3.25: Details of the strut joints of the re-entrant lattice acquired using the SEM-SE imaging.

Still, the quasi-static simulations were predominantly used to obtain a framework for the evaluation of the influence of the different geometric parameters of the unit-cells on the resulting compressive response of the lattices, particularly the unit-cell size, strut cross-section dimensions, and re-entrant angle. For this reason, simulations capturing only a limited part of the stress-strain response up to approximately 10 % to 20 % of the compressive strain were sufficient. However, a further increase in the prescribed compression was found to be problematic for several reasons. The large localised deformation and rotation of the individual geometrical elements cause a difficult convergence of the simulations, which is hard to treat in the quasi-static formulation of the problem. Furthermore, the material properties of the wrought PMMA are

significantly more complex than the description provided by the elastoplastic material models with a hardening rule and would require the introduction of a damage model into the FE simulations since the re-entrant honeycombs are particularly typical cases for cracking at the strut-joints yielding typical oscillating stress response. Moreover, a self-contact definition of the problem is required to capture the collapse of the cell layers bringing further problematic factors into the simulations.

One of the disadvantages of the studied auxetic structures was also the overloading at the joints. To demonstrate a possible solution to this problem while maintaining the general topology of the unit-cell, one of the structures was modified to remove this limitation. This modification consisted of adding additional material in the joints between the struts. This has been achieved by modelling a sphere of variable radius (see Figure 3.26).

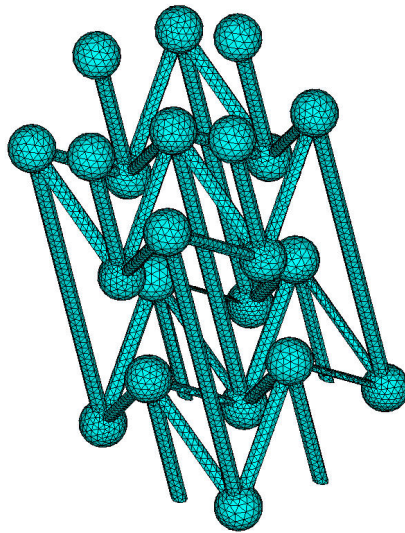


Figure 3.26: Unit-cell of a 3D re-entrant honeycomb with spheres generated at the strut-joints.

Because direct 3D printing is used for the production of such structures, this modification could be theoretically easily achieved in real geometries. However, this type of treatment of the overloading also brings a trade-off in terms of the simulation costs. Here, the relatively computationally cheap beam-analogy has to be exchanged for a costly solid formulation with FE mesh refined so that the sphere is represented with sufficient precision. The problem of the computational costs would be in this case further manifested in

the explicit dynamics simulations. The spheres generated at the strut-joints solve the problem of the stress-overloading as shown in Figure 3.27.

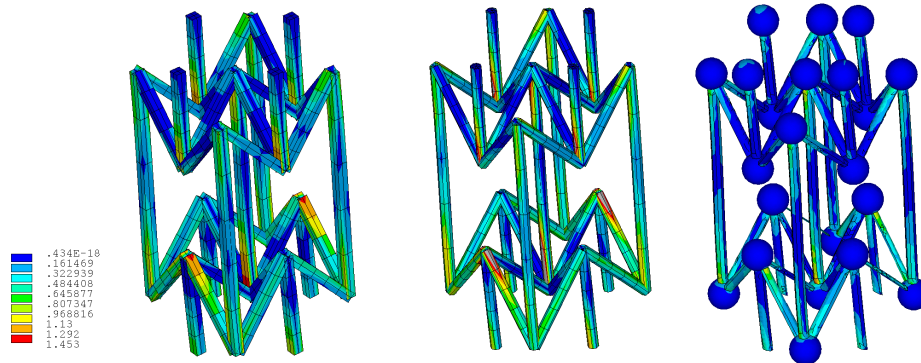


Figure 3.27: Comparison of the stress concentrations inside one unit-cell of the 3D re-entrant structure: a beam model with a rectangular cross-section (left), a beam model with a circular cross-section (middle), and an enhanced model with solid spheres at the joints (right).

In the experimental study on the influence of the strut-joint reinforcement [9], the enhanced 3D re-entrant honeycombs with differently sized spheres placed in the intersections of the struts were studied. Three different sphere radii were selected to control the joint stiffness with the upper limit of 1.125 mm, a medium radius of 0.9375 mm, and the lower limit of 0.75 mm were used to avoid contact between the neighbouring spheres, while a control group of specimens was manufactured to obtain reference data. 3D printing using PMMA in high-definition with a resolution $387 \times 387 \times 300$ dpi was selected for the production of the samples. An identical DIC strain-evaluation was utilised and the obtained curves exhibited consistent behaviour among each group (i.e., sphere radius) in terms of the stiffness in the linear part, the ultimate compressive strength and strain at the first collapse. It was found out that the stress at the collapse of the first-row unit-cells increases proportionally to the stiffness of the joints, while the strain remains unchanged. The magnitude of the auxetic effect also exhibits a marginal increase, when the spheres with the lowest radius are used in the lattice. Then, with an increasing sphere radius, the auxetic behaviour gradually becomes less significant. These results, thus, show the promising possibility of optimising the cellular structures based on a controlled stiffness in the strut joints. In further studies, this knowledge will be employed for the optimisation of the auxetics using different materials in the interconnection regions.

Even more pronounced imperfections can be observed on the SEM micrographs of the SLS printed lattices as shown in Figure 3.28. The images show the surface of the specimens in the region of the strut joint in the 2D re-entrant honeycomb in the as-delivered state, i.e., without any surface treatment such as grinding and polishing. The micrographs highlight similar problems with the conformity of the prescribed geometry and the produced specimens consisting of the apparent fillet radii in the strut joints. Furthermore, the surface quality of the SLS printing procedure is significantly lower due to the imperfect sintering of the powder particles resulting in significant roughness, loose unmelted particles with single point-like connectivity to the surface, and probable cracks in the microstructure.

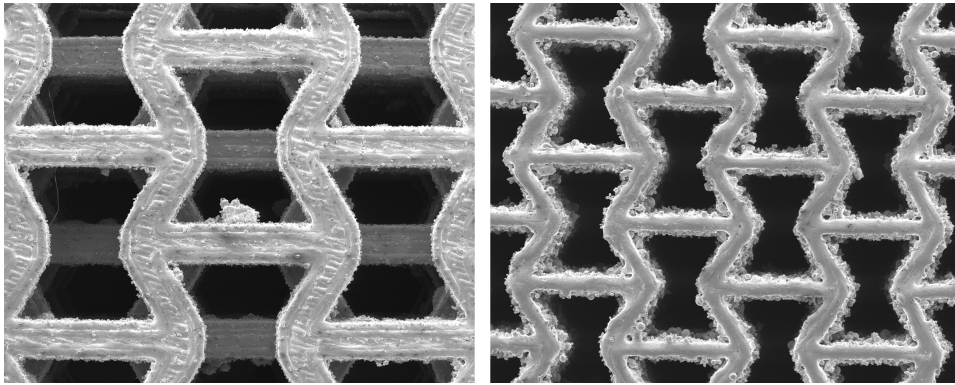


Figure 3.28: SEM-SE micrographs of the SLS printed re-entrant lattices: 3D assembly with the 3×3 cells (left), 2D assembly with RVE dimensions (right).

■ 3.6 Summary - quasi-static regime

In the quasi-static part, uni-axial compressive experiments with all the PMMA samples and two groups of SLS printed steel samples (having a different number of unit-cells in the lattice) were performed to obtain their stress-strain response and the strain-dependent Poisson's ratio characteristics under quasi-static strain rate loading. Beam analogy FE simulations were developed and validated against the PMMA results to investigate its suitability for the optimisation of the structures due to its easy parametrisation and relatively low computational costs. Simultaneously, the influence of the strain formulation and material model selection on the stiffness and the predicted Poisson's ratio was shown. The influence of the printing quality on the agreement between the experimental and numerical results, together with the overloading in the strut joints causing cracking in the PMMA samples were discussed and a possible solution has been outlined. The SLS printed steel samples were experimentally tested for a consecutive comparison with the dynamic response of the lattices during the SHPB testing.



Chapter 4

Dynamic response



4.1 Introduction

The chapter is concentrated on the assessment of the compressive behaviour of the studied auxetic constructs under dynamic loading conditions using experimental testing and numerical simulations. The experimental part contains a description of the SHPB setup used for the testing, as well as the instrumentation used for the optical deformation measurement for the calculation of the strain-dependent Poisson's ratio. This section also covers the method for the calibration of the SHPB setup and strain-gauge data processing together with the DIC of the displacement fields. Since the numerical part is emphasised in this chapter according to the main goal of the thesis, only a brief description of the experimental methods is provided and further details can be found in the related papers [8,12] and dissertation [135]. The numerical part is introduced by a general description of the virtual SHPB developed in LS-DYNA including the element type selection, hourglass stabilisation methods, contact definitions, constitutive material models of the bars and the specimen, and the computational costs of the simulations. To further orient the reader, fundamentals of the numerical dynamics using explicit time integration are provided in terms of the governing equations and methods important for the precision and reliability of the simulations. Because

extensive sensitivity analyses had to be performed during the development of the virtual SHPB, the following subsections discuss the mesh development of the bars in view of its frequency response, the mesh development for the auxetic lattices, and calibration of the 316L sintered austenitic steel material model. The results section is then divided into two subsections concentrated on the experimental and numerical results, respectively, and the numerical results also show a comparison with the experimental data. In each case, the sections are divided into parts related to the stress-strain response of the lattices and the analysis of the function of Poisson's ratio.

■ 4.2 Experimental methods

■ 4.2.1 SHPB setup

A modified Kolsky SHPB setup was used in the study to evaluate the response of the auxetic structures under dynamic conditions. The incident, transmission, and striker bars had the same nominal diameter of 20 mm with a solid cross-section and were made of a high-strength aluminium alloy (EN-AW-7075) to match the mechanical impedance of the specimens as close as possible. A gas-gun system with a 16 bar maximum pressure was used to accelerate the striker bar. The gas-gun system consisted of a 20 l air reservoir, a pressure gauge, a high-flow fast release solenoid valve (366531, Parker, USA), a steel barrel with a maximal stroke of 500 mm, and other peripherals (compressor unit, safety elements, piping etc.). The incident bar and the transmission bar had the same length of 1600 mm and were supported by eight low-friction polymer-liner slide bearings with an aluminium housing (Drylin FJUM housing, IGUS, Germany). A striker bar with a length of 500 mm was used for the generation of the incident wave. A fixed aluminium rod and a hydraulic damper were used as the absorbers of the residual kinetic energy of the experiment. The experiments were carried out without the momentum trap as the damping elements were not in initial contact with the transmission bar. The experimental setup was carefully adjusted to reduce the negative effects of an improper geometrical alignment. Selected high precision extruded

rods with a tight diameter tolerance were used for the experiments. The surfaces of the bars were ground and polished. The position of the bars was adjusted in the bearing housings to achieve a system axis straightness better than $1 \text{ mm} \cdot \text{m}^{-1}$ and the friction effects of the slider bearings were minimised. The impact faces of the bars were finished using high-precision grinding and polishing and were adjusted to be in full contact at the interfaces (striker to incident bar interface and bars to specimen interface). The precision of the contact was measured by a feeler gauge and the maximal distortion of the in-plane contact was in the order of tens of micrometres. As the experiments with the auxetic structures required a high impact velocity, it was necessary to use a pulse shaper at the striker to the incident bar interface to reduce the spurious effects of wave dispersion, while the wave shape was not significantly influenced. This allowed for constant strain rates in the plateau region with no wave interference in the bars. The overall dimensions of the steel samples were chosen to fit in the SHPB setup and, based on the SHPB performance, to reach the densification region in the impact experiment. The cross-section to specimen height ratio was approximately 1 to minimise the frictional and inertia effects in the SHPB experiment.

■ SHPB instrumentation

For the strain wave measurement during the test, the incident and transmission bars of the SHPB setup were equipped with foil strain gauges (3/120 LY61, HBM, Germany) having an active length of 3 mm. Foil strain gauges were selected despite their lower sensitivity in comparison to semiconductor strain gauges (approximately a hundred times lower), because of their linearity and ability to measure higher strain values ($50000 \mu\epsilon$ compared to $2500 \mu\epsilon$ in the case of semiconductor gauges) expected during the experiments and also for their higher service-life. A relatively small length of selected strain gauges enabled the reliable strain measurement (integration of the strain wave along the length of the strain gauge) concerning the wavelength of the strain wave. Two strain gauges were applied on each measurement point using a single component low-viscosity cyanoacrylate adhesive (Cyberbond 2003, Cyberbond Europe GmbH, Germany) in a Wheatstone half-bridge arrangement to eliminate the potential influence of bending, and cured for

at least 24 h. This solution enabled one to compensate for the possible minor bending of the bars during the impact test and to amplify the output signal two times in comparison with a quarter-bridge arrangement. One measurement point in the middle of both the incident and transmission bars was selected in the case of the 3×3 unit-cell specimens. For the measurement of the RVE sized samples, three measurement points were used on the incident bar (one point in the middle of the bar and the other two points 200 mm from each of the bars' faces), while the transmission bar was equipped with one measurement point located 200 mm from the impact face of the bar. To maximise the signal-to-noise ratio, each strain gauge circuit was powered using a battery pack (with an excitation voltage of 3 V) to decrease the noise of the strain gauge signal to a minimum. Due to the small sensitivity of the foil strain gauges, it was necessary to use an active differential low noise amplifier (EL-LNA-2, Elsys AG, Switzerland) with a gain of 10 (bandwidth: 20 MHz) or 100 (bandwidth: 15 MHz). The amplified strain gauge signals were digitised and recorded using a high-speed 16-bit digitiser (PCI-9826H, ADLINK Technology, Inc., Taiwan) with a maximal 20 MHz sample rate. A laser through-beam photoelectric sensor (FS/FE 10-RL-PS-E4, Sensopart, Germany) was employed for the measurement triggering. Two pairs of these sensors were installed on the barrel of the SHPB at a fixed distance from each other. The laser beam interruption of the first pair (closer to the air tank) was used to start the data acquisition (signal from strain gauges, image data from the high-speed camera, etc.), while the interrupt signals from both sensors enabled one to assess the speed of the projectile. The deformation process of the samples was observed using a high-speed digital camera (FASTCAM SA5, Photron, Japan) with a 20 mm square CMOS sensor. Due to the hardware configuration of the camera, the value of the maximal frame rate depends on the image resolution and vice versa. As a compromise between the frame rate and the image resolution with respect to the DIC analysis, a 100 kfps and 320×192 px image resolution were selected for the imaging of the 3×3 unit-cell samples and a 256×168 px image resolution at approximately 130 kfps was used in the case of the RVE sized samples. Because high-speed imaging is very sensitive to the proper illumination of the scene, a pair of high intensity LED lights was used for illumination of the sample during the deformation process. The triggering of the camera was performed using the same photoelectric sensor used for the triggering of the data acquisition system. Thus, the image sequence was synchronised with the strain-gauge measurement. A custom

virtual instrument was designed in LabView (National Instruments, USA) and used to control the instruments, data acquisition, and source synchronisation during the SHPB test. The overall view of the SHPB experimental setup is shown in Figure 4.1.

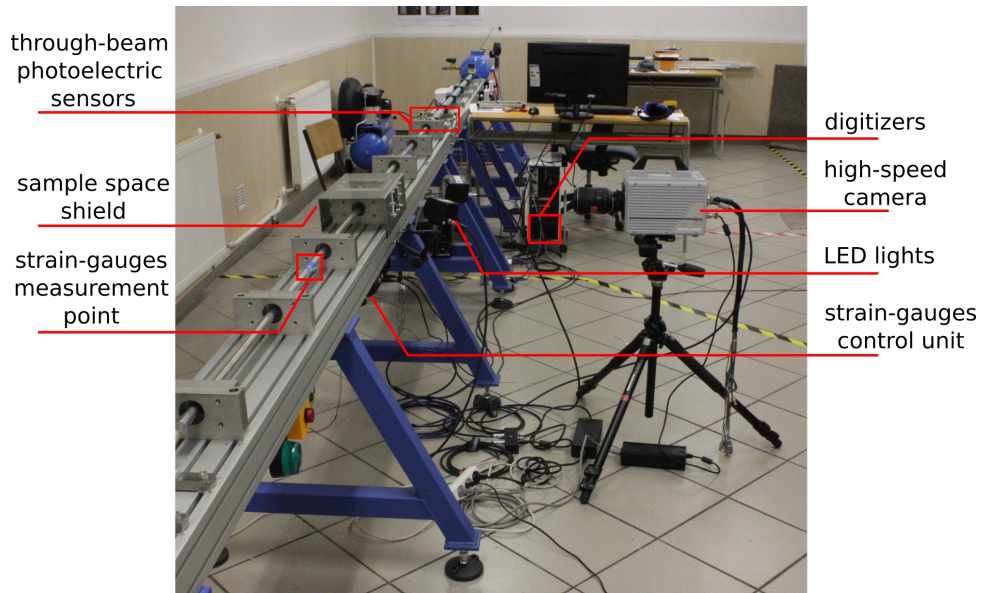


Figure 4.1: Hopkinson bar experimental setup used for the dynamic compression of the specimens. [14]

■ 4.2.2 SHPB experiments

A prepared sample was placed into the SHPB setup between the incident bar and the transmission bar. The faces of the bars were carefully aligned on the faces of the sample to eliminate the distortion of the strain pulse. The ends of both bars (adjacent to the sample) were covered by an artificial speckle pattern to increase the contrast for the image tracking algorithm.

The impact velocity of the striker bar for the 3×3 unit-cell samples was $33 \text{ m} \cdot \text{s}^{-1}$, which resulted from an optimisation procedure to achieve the maximal deformation in the specimen and a constant strain-rate during the experiment. Based on the results from the calibration experiments that were carried out prior to the experiments with the auxetics, a thick cellulose paper ($2 \times 0.25 \text{ mm}$) pulse shaper was placed on the impact face of the incident bar.

To reach two different strain-rates in the RVE sized specimens, two impact velocities of the striker bar were used. A lower striker impact velocity of approximately $21 \text{ m} \cdot \text{s}^{-1}$ was used to compress the specimens at a strain-rate of approximately 1500 s^{-1} (referred to as 'low-rate' in the following text). A higher striker impact velocity of approximately $43 \text{ m} \cdot \text{s}^{-1}$ was used to compress the specimens at a strain-rate of approximately 3000 s^{-1} (referred to as 'high-rate' in the following text). The maximum reachable strain in the SHPB method is dependent on the striker impact velocity and the striker length. However, a longer striker bar could not be used in the low-rate experiments due to the superposition of the forward-propagating and backwards-propagating waves in the strain-gauge signals. Depending on the type of the auxetic structure, the specimens in the low-rate experiments were compressed to a maximum overall strain of approximately 25 – 30 %. The specimens in the experiments conducted at the high-rate reached a significantly higher overall strain of approximately 40 – 50 %. For the minimisation of the wave dispersion effects, cylindrical soft copper pulse-shapers were placed on the incident bar's impact face in this set of experiments. Depending on the type of auxetic structure and strain-rate, the diameter and the thickness of the pulse-shapers varied between 7 – 8 mm and 0.5 – 1 mm, respectively. The pulse-shapers were very effective in filtering out the high frequencies causing the Pochhammer-Chree oscillations and in the reduction of the ramp-in effect during the initial phase of the wave impact on the specimen. A sufficient quality of the dynamic equilibrium was reached in all the experiments at all strain-rates. Using the pulse-shaping technique, it was possible to maintain a constant strain-rate during the impact up to the densification of the auxetic structure. All the methods used for the evaluation of the stress-strain curves exhibited good convergence after the initial phase of the impact, representing a good quality dynamic equilibrium during the experiment. The strain-rate-strain curve showed constant values of the strain-rate up to the densification of the structures. Approximately 35 images of the deforming specimen during the first deformation pulse were captured using the high-speed camera and processed using the DIC technique.

■ SHPB Data Processing

As the mechanical impedance of the bars and specimen was significantly different, a number of calibration and correction methods was utilised to evaluate the results. A series of calibration experiments and void tests were carried out at different impact velocities to obtain the correction data. The data from void tests were used to evaluate the actual mechanical properties of the aluminium bars and to correct the signals from the strain-gauges. Two types of void tests were performed: an 'incident bar apart' void test and a 'bars together' void test. The 'incident bar apart' void test was carried out to analyse the impact velocity, the elastic properties of the bar, the wave propagation velocity, the damping characteristics, the wave shape, the strain-gauge position error, and the linearity of the incident bar. The 'bars together' void test was carried out to analyse the same properties valid for the transmission bar, the quality of the contact between the bars, the wave transfer parameters, the strain-gauge signals equilibrium, and the friction losses of the system. All the evaluated parameters were consistent and the experimental setup was evaluated as being suitable for the measurements of auxetic structures with adequate precision. Void tests with a 50 mm short striker bar and no pulse shaper were performed to record the wave dispersion effects in the bars. The data were used to calculate the experimentally determined wave transfer function and wave propagation coefficient in the frequency domain, according to Bacon's method and its modification [136,137]. The wave propagation coefficient was calculated separately for the incident and transmission bars using the 'bars together' and 'incident bar apart' void tests. Fourier transforms of the first measured pulse in the bar $\tilde{\epsilon}_1(\omega)$ and its reflection $\tilde{\epsilon}_2(\omega)$ on the free end of the bar were used to calculate the wave transfer function $H^*(\omega)$ of the system in the frequency domain. The propagation coefficient was obtained using the equation

$$H^*(\omega) = -\frac{\tilde{\epsilon}_2(\omega)}{\tilde{\epsilon}_1(\omega)} = \exp^{-\gamma(\omega)2d} \quad (4.1)$$

where $\gamma(\omega)$ is the propagation coefficient and d is the distance between the strain-gauge and the free end of the bar [138]. The recorded incident,

a zero normalised sum-of-squares difference (ZNSSD) criterion to compute the similarity in the pixel intensity between the reference and deformed image subsets [142]. In this manner, displacements with a pixel accuracy are obtained. Then, to obtain deformation with sub-pixel accuracy, the above-mentioned ZNSSD criterion is iteratively optimised using the classic Newton-Raphson iterative algorithm. From the displacement fields, the full-field strains were calculated as Green-Lagrange strain tensors. This involves differentiation of the displacements fields, which is sensitive to noise and one must be careful that the displacement fields are not excessively noisy prior to the differentiation. Attention was paid to keep the smoothing window as low as possible not to oversmooth the resulting strain fields. In all the experiments, the smoothing window was 15 pixels. The set of parameters used for the calculation of the results (displacements, strains, Poisson's ratios) were kept constant for all the experiments performed. The only smoothing procedure used in the DIC was the initial displacement smoothing using a 2×2 pixel Gaussian kernel. Since the position and settings for the camera used in the experiments did not change, all the experiments were processed using the same Matlab scripts. This enabled an easy and reliable result evaluation and comparison.

4.3 Numerical methods

To be able to calibrate the numerical simulations and to compare the numerical results with the experimental data, the approach based on the development of a virtual SHPB apparatus used in the experiments was selected. For this reason, a fully three-dimensional model of the SHPB apparatus was developed in LS-DYNA. The experimental arrangement (i.e., the striker, incident, and transmission bars with the specimen placed in contact with both the incident and transmission bars) and the dimensions of the individual components was considered including the geometry of the specimens directly derived from the parametric models used for the SLS production of the samples. Any of the possible analogies for the representation of the auxetic lattices (i.e., beam analogy, solid representation with the homogenised material model, etc.) was not used due to the need to include all the potential phenomena

in the simulations to have the numerical and experimental results directly comparable in terms of the stress wave propagation, the resulting overall stress-strain diagrams of the lattices, the strain-dependent Poisson's ratio, and the influence of the strain-rate on these quantities. Obviously, such an approach effectively prevented the axisymmetric formulation of the problems with the implications of the computational costs as the topology of the lattices does not allow the dimensional reduction of the problem. The arrangement of the virtual SHPB apparatus is depicted in Figure 4.2.

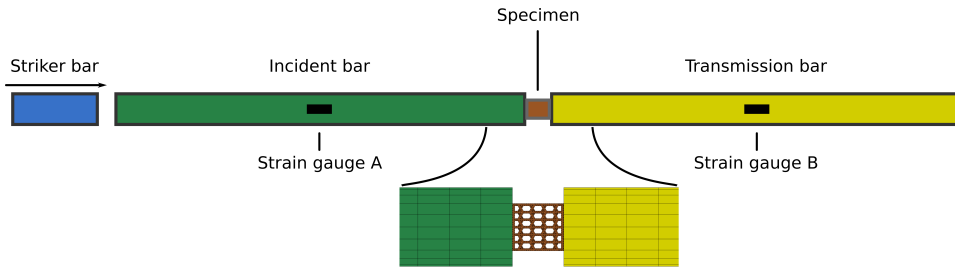


Figure 4.2: Principle of the virtual SHPB.

In the simulations, the initial conditions, in terms of the translational velocity of the striker bar, were imposed with the velocity value measured in the respective SHPB experiment. No body forces nor boundary conditions reflecting the slide bearings carrying the bars of the SHPB apparatus were considered. The geometry of the bars and the auxetic lattices was considered to be ideal, without imperfections in plane-parallelism, surface roughness, defects, or deviations from the geometry prescribed for the SLS testing. The mechanical results from the numerical simulations were extracted by defining the virtual strain gauges on the same location, where the measurement points were established in the SHPB experiments. At the virtual strain-gauges, the strain versus time data was acquired and used in the further post-processing using the same mathematical methods utilised for the experimental evaluation. The geometrical characteristics of the studied auxetic lattices were extracted at the locations equivalent to the full-field DIC evaluation of the high-speed camera data and from the nodal coordinates, the strain-dependent function of Poisson's ratio was established. The bars were represented by under-integrated single-point constant-stress hexahedral elements (ELFORM 1). For the auxetic lattices, 10-noded composite tetrahedral elements (ELFORM 17) were selected.

The FE representation of the bars was selected based on a parametric sensitivity study, where the virtual void-test without a pulse-shaper (i.e., the impact of the striker bar on the incident bar without any other components) was used to reveal an optimal set of parameters representing the experimentally observed stress wave propagation. In the sensitivity studies, the mesh generating pre-processors and algorithms, element size, element formulation, hourglass control algorithm, and time step size were varied. The stability of the simulations together with the shape of strain waves propagating through the incident bar were evaluated. Taking the computational costs into account, the best performing set of parameters was achieved for the ELFORM 1 element formulation with the element edge length of 5 mm in the direction of the SHPB longitudinal axis. Further considerations on the bar FE mesh development with respect to the meshing algorithms and frequency characteristics are included in Section 4.3.2.

Analogously, a parametric sensitivity study was performed to identify the most suitable representation of the auxetic lattices. In this case, the studies were performed with the full virtual SHPB apparatus significantly increasing the computational costs of the calculations. Because of the topology and design of the strut joints, only tetrahedral meshes were considered due to sharp angles present in the geometry of the lattices. Again, the element size, element formulation, hourglass control algorithm, and time step size were varied in the parametric study. From the acquired results, the 10-noded composite tetrahedral element formulation was selected as the best option for an accurate representation of the deformation response of the auxetic lattices. Further information on the FE mesh formulation and influence of the mesh density is included in Section 4.3.3.

For the hourglass mode stabilisation, all the solid control methods were analysed. Since the deformation of the bars is purely elastic and a constant-stress element formulation was used, no influence of the invoked hourglass control algorithm on the results was identified. As a result, when a simple type 1 hourglass stabilisation is sufficient thanks to the regular mesh and offers advantages in terms of the computational costs as the type 1 hourglass viscosity requires approximately 130 additions or multiplications per hexahedron, compared to 620 and 680 for the algorithms of Flanagan-Belytschko and

Wilkins. Since the fully integrated tetrahedral element formulation was used for auxetic lattices, it was not necessary to treat the hourglass modes, which arises from the definition of this effect. Still, every simulation was checked for an energy balance and the hourglass energy was included in the global energy balance due to possible volumetric locking of the elements on the specimen-bar boundary in the densification region of the specimen response.

A sensitivity study on the influence of the numerical damping was performed using simulated void tests. In the study, both the global and the interval damping were evaluated showing that the global damping enables one to filter out the high frequencies in the stress waves, while preserving the fundamental characteristics of the modelled physical process, such as the speed of the wave propagation, etc. However, it is difficult to transfer the results of the sensitivity study to simulations of the auxetic lattices due to the inability to primarily verify the frequency characteristics from the real experiments. For this reason, the numerical damping was omitted in the simulations.

The automatic two-way surface-to-surface contact type was used for all the interfaces between the SHPB components and the specimen, i.e., the striker-incident bar, incident bar - specimen, and specimen-transmission bar contacts were established. This approach was selected even though it is a rather expensive contact-interface definition in terms of the computational costs, but the reason for such a choice was the contact-interface damping performance superior to other contact definitions (particularly the node-to-surface contact), which proved to be crucial due to the oscillations in the rising-edge of the incident stress wave occurring when no pulse-shaping is used. Due to the relatively low mechanical impedance of the auxetic lattices, it was necessary to use the 'soft' option for the bar-specimen interfaces. In this formulation, the contact stiffness is based on the stability considerations taking the time step size into account, as the contact is similar in this formulation to a group of spring-mass systems, each with a Courant time step matched to the actual time step used in the simulation. A single-surface self contact was defined for the auxetic lattices, which was required by the large compressive deformations induced by the stress waves at all strain-rates. A frictionless interface was defined on the striker-incident bar interface, whereas the static coefficient of friction of 0.61 and sliding coefficient of friction of 0.8

was used on the incident bar - specimen and specimen - transmission bar interfaces according to the values reported for aluminium on steel frictional characteristics. On a single-surface self-contact of the auxetic lattices, the static coefficient of friction of 0.65 and the sliding coefficient of friction of 0.42 was used according to values reported for steel on steel friction [143], which improved the simulated deformation behaviour of all the lattices in the plateau-densification transition.

The material model MAT 1 - ELASTIC was selected for the bars of the virtual SHPB based on a fundamental assumption that the bars have to be subjected to elastic deformation only. Here, the MAT 1 not only fulfils the physics of SHPB testing, but it is also the most efficient formulation. The constants of the model were calibrated from the void-tests with the SHPB apparatus yielding a mass density of $2.75 \text{ kg} \cdot \text{cm}^{-3}$ and a Young's modulus of 70 GPa. The Poisson's ratio used in the simulations was 0.3. The material model MAT 12 - ISOTROPIC_ELASTIC_PLASTIC was used for the modelling of the auxetic lattices. The selection of this material model was primarily motivated by the problems encountered with the SLS printing of the powdered austenitic steel and the inability to properly evaluate its characteristics either on a micro- or macroscopic level. Furthermore, this material model is the most effective material model from the computational point of view as only one history variable $\varepsilon_{\text{eff}}^{\text{P}}$ is stored. The details regarding the development of the 316L stainless steel material model are provided in Section 4.3.4.

The simulations were performed using a high-performance workstation equipped with a 16-thread CPU Xeon-W 2145 (Intel, USA). The typical CPU time needed for simulation of the SHPB experiment with a duration of 1.5 ms and the 3×3 auxetic lattice was approximately 6.5 hours using 12 threads, whereas the same simulation of the RVE sized lattice approximately required 20.5 hours of CPU time for the same number of threads. Regarding the distribution of the CPU time, 40 % of the resources was used for the element processing procedures, while 55 % used by the the contact algorithm, where 20 % was used by the striker-incident bar contact and incident bar to the specimen contact, while the remaining time was used by the specimen-transmission bar contact.

4.3.1 Explicit dynamics

The following paragraphs briefly review some important theoretical assumptions of the finite element explicit dynamics relevant for the FEA of the auxetic lattices. The text is adopted primarily from the LS-DYNA manual Vol. IV - Theory so that the specifics of the implementation are covered in the provided theoretical fundamentals.

Governing equations - structural dynamics

The system of governing equations for a transient dynamic problem at time t is generally written as

$$\mathbf{M}\ddot{\mathbf{u}}(t) + \mathbf{C}\dot{\mathbf{u}}(t) + \mathbf{f}_{\text{int}}(u, \dot{u}, \varepsilon, \sigma, t, \dots) = \mathbf{f}_{\text{ext}}(t), \quad (4.2)$$

where \mathbf{M} is the mass matrix, \mathbf{C} is the damping matrix, \mathbf{f}_{int} is the vector of internal forces, \mathbf{f}_{ext} is the vector of external forces, \mathbf{u} are the displacements, $\dot{\mathbf{u}}$ are the velocities, $\ddot{\mathbf{u}}$ are the accelerations, and ε and σ are the strain and stress fields.

For the linear problem, where $\mathbf{f}_{\text{int}} = \mathbf{K}\mathbf{u}(t)$, Equation (4.2) becomes

$$\mathbf{M}\ddot{\mathbf{u}}(t) + \mathbf{C}\dot{\mathbf{u}}(t) + \mathbf{K}\mathbf{u}(t) = \mathbf{f}_{\text{ext}}(t), \quad (4.3)$$

where \mathbf{K} is the stiffness matrix. Even in the case of linear elasticity, i.e., if the relationship between the stress and strain tensor is linear, we obtain in the strong form a system of partial differential equations that does not have a general analytic solution except for the case of a very simple geometry case and linear elasticity. Here, the difficulties primarily arise from the fact that the solution must be as smooth as required by the strong form of the

differential equations. For instance, if the investigated system arises from a geometrical body with a low-order of continuity or the multi-material object is considered, the discontinuous functions are substituted into the equations of motion with the resulting problem of differentiability.

Instead, the original dynamic equation of motion may be reformulated and solved by a numerical integration scheme in the so called weak (weighted-integral) form. Here, the geometric discretisation of the problem is followed by a time discretisation such that a finite difference approximation is used to replace the time derivatives, i.e., the velocities and accelerations are approximated by differences of displacements at particular instants of time. Hence, for a time step $\Delta t = t_{k+1} - t_k$,

$$\mathbf{M}\ddot{\mathbf{u}}_{t+\Delta t} + \mathbf{C}\dot{\mathbf{u}}_{t+\Delta t} + \mathbf{K}\mathbf{u}_{t+\Delta t} = \mathbf{f}_{\text{ext},t+\Delta t}, \quad (4.4)$$

$$\mathbf{u}(t_0) = \mathbf{u}_0, \quad (4.5)$$

$$\dot{\mathbf{u}}(t_0) = \dot{\mathbf{u}}_0. \quad (4.6)$$

Then, various direct integration methods, where the equations are solved in their original form, may be used to solve the problem. Depending on the type of variables on the right side of the discretised equations of motion, these methods can be categorised as explicit or implicit. The implicit methods have the form

$$\mathbf{u}_{t+\Delta t} = f(\mathbf{u}_t, \dot{\mathbf{u}}_{t+\Delta t}, \ddot{\mathbf{u}}_{t+\Delta t}, \dots) \quad (4.7)$$

and the computation of $\mathbf{u}_{t+\Delta t}$ requires knowledge of its unknown time derivatives. In contrast, the explicit methods have the form

$$\mathbf{u}_{t+\Delta t} = f(\mathbf{u}_t, \dot{\mathbf{u}}_t, \ddot{\mathbf{u}}_t, \mathbf{u}_t, \mathbf{u}_{t-\Delta t}, \dots) \quad (4.8)$$

and the determination of $\mathbf{u}_{t+\Delta t}$ can be performed solely on the basis of the historical information comprising the displacements and derivatives of displacements.

Typical direct integration methods are the Central Difference Method and the Newmark method. Using the Central Difference Method, the velocities and accelerations are approximated as

$$\ddot{\mathbf{u}}_t = \frac{1}{\Delta t^2} (\mathbf{u}_{t+\Delta t} - 2\mathbf{u}_t + \mathbf{u}_{t-\Delta t}), \quad (4.9)$$

$$\dot{\mathbf{u}}_t = \frac{1}{2\Delta t} (\mathbf{u}_{t+\Delta t} - \mathbf{u}_{t-\Delta t}). \quad (4.10)$$

If we consider the the equation of motion at time t , i.e.,

$$\mathbf{M}\ddot{\mathbf{u}}_t + \mathbf{C}\dot{\mathbf{u}}_t + \mathbf{K}\mathbf{u}_t = \mathbf{f}_{\text{ext},t}, \quad (4.11)$$

the displacement solution for the time $t + \Delta t$ is obtained by substituting Equations (4.9) and (4.10) yielding

$$\begin{aligned} \left[\frac{1}{\Delta t^2} \mathbf{M} + \frac{1}{2\Delta t} \mathbf{C} \right] \mathbf{u}_{t+\Delta t} &= \\ &= \mathbf{F}_t - \left[\mathbf{K} - \frac{2}{\Delta t^2} \mathbf{M} \right] \mathbf{u}_t - \left[\frac{1}{\Delta t^2} \mathbf{M} - \frac{1}{2\Delta t} \mathbf{C} \right] \mathbf{u}_{t-\Delta t}, \end{aligned} \quad (4.12)$$

from which it is possible to solve for $\mathbf{u}_{t+\Delta t}$ in an explicit time integration procedure. The solution is, thus, based on the equilibrium conditions at time t and such a integration scheme does not require a factorisation of the stiffness matrix in the step-by-step solution.

Using the Newmark method with a time step $\Delta t = t_{k+1} - t_k$, the discretisation of Equations (4.4) - (4.6) is performed using interpolation equations

$$\dot{\mathbf{u}}_{t+\Delta t} = \dot{\mathbf{u}}_t + \Delta t [(1 - \gamma) \ddot{\mathbf{u}}_t + \gamma \ddot{\mathbf{u}}_{t+\Delta t}], \quad (4.13)$$

$$\mathbf{u}_{t+\Delta t} = \mathbf{u}_t + \Delta t \dot{\mathbf{u}}_t + \frac{\Delta t^2}{2} [(1 - 2\beta) \ddot{\mathbf{u}}_t + 2\beta \ddot{\mathbf{u}}_{t+\Delta t}], \quad (4.14)$$

where β and γ are the parameters of the time integration algorithm that act as weights for calculating the acceleration approximation. It can be noted that upon setting $\beta = 0$, the Newmark algorithm becomes explicit and equivalent to the Central Difference Method.

Now, let us reformulate the problem in a different notation using the numbering of time steps such that the difference between the time steps k and $k + 1$ is $t_{k+1} - t_k = t + \Delta t$. For a linear problem, it is possible to formulate the dynamic equilibrium at each time step $k + 1$ using the equation

$$\mathbf{M}\ddot{\mathbf{u}}_{k+1} + \mathbf{C}(\dot{\tilde{\mathbf{u}}}_{k+1} + \ddot{\mathbf{u}}_{k+1}\gamma\Delta t) + \mathbf{K}(\tilde{\mathbf{u}}_{k+1} + \ddot{\mathbf{u}}_{k+1}\beta\Delta t^2) = \mathbf{f}_{\text{ext},k+1}. \quad (4.15)$$

The predictors $\tilde{\mathbf{u}}_{k+1}$ and $\dot{\tilde{\mathbf{u}}}_{k+1}$ depend on the solutions in the previous time step k

$$\tilde{\mathbf{u}}_{k+1} = \mathbf{u}_k + \dot{\mathbf{u}}_k\Delta t + \ddot{\mathbf{u}}_k\left(\frac{1}{2} - \beta\right)\Delta t^2, \quad (4.16)$$

$$\dot{\tilde{\mathbf{u}}}_{k+1} = \dot{\mathbf{u}}_k + \ddot{\mathbf{u}}_k(1 - \gamma)\Delta t, \quad (4.17)$$

while the solution in the current time step $k + 1$ is determined using the correctors \mathbf{u}_{k+1} and $\dot{\mathbf{u}}_{k+1}$ as

$$\mathbf{u}_{k+1} = \tilde{\mathbf{u}}_{k+1} + \ddot{\mathbf{u}}_{k+1}\beta\Delta t^2, \quad (4.18)$$

$$\dot{\mathbf{u}}_{k+1} = \dot{\tilde{\mathbf{u}}}_{k+1} + \ddot{\mathbf{u}}_{k+1}\gamma\Delta t. \quad (4.19)$$

If the problem is nonlinear, then we can reformulate it in a general form using

$$\mathbf{M}\ddot{\mathbf{u}}_t + \mathbf{r}(\mathbf{u}_t, \dot{\mathbf{u}}_t) = \mathbf{f}_{\text{ext},t}, \quad (4.20)$$

$$\mathbf{u}(t_0) = \mathbf{u}_0, \quad (4.21)$$

$$\dot{\mathbf{u}}(t_0) = \dot{\mathbf{u}}_0, \quad (4.22)$$

where \mathbf{r} is the restoring force. Discretization using a time step $\Delta t = t_{k+1} - t_k$ yields

$$\mathbf{M}\ddot{\mathbf{u}}_{k+1} + \mathbf{r}(\mathbf{u}_{k+1}, \dot{\mathbf{u}}_{k+1}) = \mathbf{f}_{\text{ext},k+1}, \quad (4.23)$$

$$\mathbf{u}(t_0) = \mathbf{u}_0, \quad (4.24)$$

$$\dot{\mathbf{u}}(t_0) = \dot{\mathbf{u}}_0. \quad (4.25)$$

A nonlinear problem is solved at each time step $k + 1$ from the equation

$$\mathbf{M}\ddot{\mathbf{u}}_{k+1} + \mathbf{r}\left(\tilde{\mathbf{u}}_{k+1} + \ddot{\mathbf{u}}_{k+1}\beta\Delta t^2, \dot{\tilde{\mathbf{u}}}_{k+1} + \ddot{\mathbf{u}}_{k+1}\gamma\Delta t\right) = \mathbf{f}_{\text{ext},k+1}, \quad (4.26)$$

with the predictors defined using Equations (4.16) - (4.17) and correctors defined using Equations (4.18) - (4.19).

Implementation can be performed using the Newton-Raphson iteration method (see the corresponding paragraph at the end of Section 4.3.1). After that, the restoring force matrix itself is in the solution assembled in a loop over the elements and the update step in each iteration becomes for the explicit time integration

$$\Delta\ddot{\mathbf{u}}_{k+1} \leftarrow (\mathbf{M} + \mathbf{C}\gamma\Delta t)^{-1} \varepsilon, \quad (4.27)$$

where the term $(\mathbf{M} + \mathbf{C}\gamma\Delta t)$ is a matrix to be inverted. Since this matrix remains constant during the iterations, its factorization can be performed once and then followed only by backward substitutions. If we further consider \mathbf{M} to be lumped and \mathbf{C} to be either lumped or zero, the solution of the system is trivial, which is true for all the explicit time integration schemes.

To summarise the differences between the explicit and implicit time-integration, the explicit scheme does not require inversion of a tangent stiffness matrix at each time step, but the conditional stability limits the time stepping to relatively small steps only. Thus, the explicit time-integration is a preferred method for analysis of short-duration problems involving high-frequencies, such as the wave propagation problems investigated in this work.

Newton-Raphson iterations. Newton-Raphson iterative approach, which is one of the most widely used methods for root finding that can be easily generalized to the problem of finding solutions of a system of non-linear equations. To demonstrate its principle on a function of one variable, we rewrite the function $f(x)$ using a Taylor series expansion in $(x - x_0)$

$$f(x) = f(x_0) + f'(x_0)(x - x_0) + \frac{1}{2}f''(x_0)(x - x_0)^2 + \dots = 0, \quad (4.28)$$

where x_0 is an initial value referred to as the initial guess for the root. By truncating the series at the second term, we obtain the Newton-Raphson iteration formula for getting an estimate of the true root as

$$x_1 = x_0 - \frac{f(x_0)}{f'(x_0)}. \quad (4.29)$$

Thus, the tangent to the function $f(x)$ at $x = x_0$ is found and then extrapolated it to intersect the x axis to get x_1 . This point of intersection is taken as the new approximation to the root and the procedure is repeated until a

convergence condition is satisfied, i.e., given the value of $x = x_i$ at the end of the i -th iteration, we obtain x_{i+1} from

$$x_{i+1} = x_i - \frac{f(x_i)}{f'(x_i)}. \quad (4.30)$$

State-space formulation. The order of the investigated mechanical system with its second order equation of motion (4.3) can be reduced using a state-space form of the problem by defining

$$\dot{\mathbf{z}}(t) = \mathbf{A}^* \mathbf{z}(t) + \mathbf{B}^* \mathbf{f}(t), \quad \dot{\mathbf{z}}(t) = \begin{Bmatrix} \dot{\mathbf{x}} \\ \dot{\mathbf{x}} \end{Bmatrix}, \quad (4.31)$$

where the matrices \mathbf{A}^* and \mathbf{B}^* are

$$\mathbf{A}^* = \begin{bmatrix} 0 & \mathbf{I} \\ -\mathbf{M}^{-1}\mathbf{K} & -\mathbf{M}^{-1}\mathbf{C} \end{bmatrix}, \quad \mathbf{B}^* = \begin{Bmatrix} 0 \\ -\mathbf{M}^{-1} \end{Bmatrix}, \quad (4.32)$$

$\dot{\mathbf{z}}(t)$ is the state vector and \mathbf{A}^* is the behaviour matrix of the state-space formulation. For a nonlinear case, it is possible to write

$$\mathbf{M}\dot{\mathbf{x}} + \mathbf{R}(\mathbf{x}) = \mathbf{F}(t), \quad (4.33)$$

$$\dot{\mathbf{x}} = \mathbf{M}^{-1}[\mathbf{F}(t) - \mathbf{R}(\mathbf{x})] = \mathbf{H}(\mathbf{x}, t), \quad (4.34)$$

where

$$\mathbf{M} = \begin{bmatrix} \mathbf{I} & 0 & 0 \\ 0 & \mathbf{m} & 0 \\ 0 & 0 & \mathbf{I} \end{bmatrix}, \quad \mathbf{x} = \begin{Bmatrix} \mathbf{u} \\ \dot{\mathbf{u}} \\ \mathbf{s} \end{Bmatrix}, \quad \mathbf{R} = \begin{Bmatrix} -\dot{\mathbf{u}} \\ \mathbf{r}(\mathbf{u}, \dot{\mathbf{u}}, \mathbf{s}) \\ \mathbf{g}(\mathbf{u}, \dot{\mathbf{u}}, \mathbf{s}) \end{Bmatrix}, \quad \mathbf{F} = \begin{Bmatrix} 0 \\ \mathbf{f}(t) \\ 0 \end{Bmatrix}, \quad (4.35)$$

\mathbf{r} is the nonlinear restoring force vector that depends on displacement \mathbf{u} , velocity $\dot{\mathbf{u}}$ and additional state variables \mathbf{s} , while \mathbf{g} is a nonlinear function that determines the evolution of the additional state variables \mathbf{s} . Thus, the system of second order ordinary differential equations has been converted to a first order system and an arbitrary integration method can be used to obtain its approximate solution. If we assume

$$\frac{d\mathbf{x}}{dt} = \mathbf{H}(\mathbf{x}(t), t), \quad \mathbf{x}(t_0) = \mathbf{0}, \quad (4.36)$$

explicit expression

$$\mathbf{x}_{k+1} = \mathbf{x}_k + \mathbf{H}(\mathbf{x}_k, t_k) \Delta t \quad (4.37)$$

can be obtained for the integration time step Δt using the forward Euler method from the truncated Taylor expansion of $\mathbf{x}(t_{k+\Delta t})$.

■ Governing equations - structural dynamics in FEA

For the following considerations, the general problem of structural dynamics and weak formulation of equilibrium equation is recalled in order to introduce mathematical background and notation of the FEA implementation relevant for this thesis.

Let a point in b initially at X_α ($\alpha = 1, 2, 3$) in a fixed rectangular Cartesian coordinate system move to point x_i ($i = 1, 2, 3$) in the same coordinate system. If a Lagrangian formulation is considered, the deformation can be expressed in terms of the convected coordinates X_α and time t as

$$x_i = x_i(X_\alpha, t) \quad (4.38)$$

At time $t = 0$, the initial conditions are

$$x_i(\mathbf{X}_\alpha, 0) = X_i, \quad (4.39)$$

$$\dot{x}_i(\mathbf{X}_\alpha, 0) = V_i(\mathbf{X}), \quad (4.40)$$

where \mathbf{V} is the initial velocity.

The process of calculation comprises finding a solution for the momentum equation

$$\sigma_{ij,j} + \rho f_i = \rho \ddot{x}_i \quad (4.41)$$

satisfying the traction boundary conditions

$$\sigma_{ij} n_j = t_i(t) \quad (4.42)$$

on boundary ∂b_1 , the displacement boundary conditions

$$x_i(\mathbf{X}_\alpha, t) = D_i(t) \quad (4.43)$$

on boundary ∂b_2 , and the contact discontinuity condition

$$\left(\sigma_{ij}^+ - \sigma_{ij}^- \right) n_j = 0 \quad (4.44)$$

along an interior boundary ∂b_3 , when $x_i^+ = x_i^-$, while σ_{ij}^+ and σ_{ij}^- denote the Cauchy stress in the direction of the inward and outward pointing normal

on the interior boundary. Here, ρ is the current density, \mathbf{f} is the body force density, and \ddot{x} is the acceleration. The comma on $\sigma_{ij,j}$ denotes the covariant differentiation, and n_j is a unit outward normal to a boundary element on ∂b .

The mass conservation can be written as

$$\rho J = \rho_0, \quad (4.45)$$

where J is the the relative volume calculated as a determinant of the deformation gradient matrix F_{ij} ,

$$F_{ij} = \frac{\partial x_i}{\partial X_j} \quad (4.46)$$

and ρ_0 is the reference density.

The energy equation

$$\dot{E} = V s_{ij} \dot{\epsilon}_{ij} - (p + q) \dot{V} \quad (4.47)$$

is integrated in time and is used for evaluating the equations of state and to track the global energy balance. Here, s_{ij} and p represent the deviatoric stresses and pressure according to

$$s_{ij} = \sigma_{ij} + (p + q) \delta_{ij}, \quad (4.48)$$

$$p = -\frac{1}{3} \sigma_{ij} \delta_{ij} - q, \quad (4.49)$$

where q is the bulk viscosity, δ_{ij} is the Kronecker delta, and $\dot{\epsilon}_{ij}$ is the strain rate tensor.

It is possible to write

$$\int_{\mathcal{V}} (\rho \ddot{x}_i - \sigma_{ij,j} - \rho f) \delta x_i dv + \int_{\partial b_1} (\sigma_{ij} n_j - t_i) \delta x_i ds + \int_{\partial b_3} (\sigma_{ij}^+ - \sigma_{ij}^-) n_j \delta x_i ds = 0 \quad (4.50)$$

where the integrations are over the current geometry and δx_i satisfies all the boundary conditions on ∂b_2 . By applying the divergence theorem and noting that

$$(\sigma_{ij} \delta x_i)_{,j} - \sigma_{ij,j} \delta x_i = \sigma_{ij} \delta x_{i,j}, \quad (4.51)$$

weak form of the equilibrium equation can be obtained such that

$$\delta \Pi = \int_{\mathcal{V}} \rho \ddot{x}_i \delta x_i dv + \int_{\mathcal{V}} \sigma_{ij} \delta x_{i,j} dv - \int_{\mathcal{V}} \rho f_i \delta x_i dv - \int_{\partial b_1} t_i \delta x_i ds = 0, \quad (4.52)$$

which is the formulation of the principle of virtual work.

A mesh of finite elements interconnected at the nodal points is superimposed on the reference configuration and the particles are tracked through time, which yields

$$x_i(X_\alpha, t) = x_i(X_\alpha(\xi, \eta, \xi), t) = \sum_{j=1}^k N_j(\xi, \eta, \xi) x_i^j(t), \quad (4.53)$$

where N_j are the shape functions in the natural coordinates (ξ, η, ξ) , k is the number of nodal points defining the element, and x_i^j is the nodal coordinate of the j -th node in the i -th direction.

The condition $\delta\pi = 0$ holds for all variations δx_i and, in particular, holds for variations along the shape functions. In each of the three Cartesian directions upon setting the variation to one of the shape functions, the weak form reduces to a necessary (but not sufficient) condition that must be satisfied by any solution so that the number of equations = $3 \times$ number of nodes.

Since the body is discretised into n elements, it is possible to write the integral (4.52) into n terms using the spatial additivity of integration

$$\delta\pi = \sum_{m=1}^n \delta\pi_m = 0. \quad (4.54)$$

By defining the contribution from each element and assembling the element contributions back into a system of equations leads to

$$\sum_{m=1}^n \left\{ \int_{v_m} \rho \ddot{x}_i (e_i \otimes \nu^m) dv + \int_{v_m} \sigma_{ij}^m (e_i \otimes \nu_j^m) dv - \int_{v_m} \rho f_i (e_i \otimes \nu^m) dv - \int_{\partial b_1 \cap \partial v_m} t_i (e_i \otimes \nu^m) ds \right\} = 0, \quad (4.55)$$

in which

$$v_m = \sum_{i=1}^k N_i e_{n_m}(i)', \quad (4.56)$$

where $n_m(i)$ is the global node number. By applying the approximation scheme of (4.53) to the dependent variables and substituting into (4.55) yields

$$\sum_{m=1}^n \left\{ \int_{v_m} \rho \mathbf{N}_m^T \mathbf{N}_m \mathbf{a} dv + \int_{v_m} \mathbf{B}_m^T \boldsymbol{\sigma} dv - \int_{v_m} \rho \mathbf{N}_m^T \mathbf{b} dv - \int_{\partial b_1} \mathbf{N}_m^T \mathbf{t} ds \right\} = 0, \quad (4.57)$$

where \mathbf{N} is an interpolation matrix, $\boldsymbol{\sigma}$ is the stress vector, \mathbf{B} is the strain-displacement matrix, \mathbf{a} is the nodal acceleration vector, \mathbf{b} is the body force load vector, and \mathbf{t} is the applied traction load.

■ Time step calculation

For solid elements, a critical time step is given by

$$\Delta t_e = \frac{L_e}{Q^2 + (Q^2 + c^2)^{1/2}} \approx \frac{L_e}{c}, \quad (4.58)$$

where L_e is the characteristic element edge length and Q is a function of the bulk viscosity coefficients

$$Q = \begin{cases} C_1 c + C_0 L_e |\epsilon_{kk} \dot{\epsilon}_{kk}| & \text{for } \epsilon_{kk} \leq 0 \\ 0 & \text{for } \epsilon_{kk} > 0 \end{cases}$$

The term c is the adiabatic speed of sound that can be derived from the material properties according to

$$c = \left[\frac{4G}{3\rho_0} + \left(\frac{\partial p}{\partial \rho} \right)_s \right]^{1/2}, \quad (4.59)$$

where ρ is the specific mass density.

If

$$\left(\frac{\partial p}{\partial \rho}\right)_s = \left(\frac{\partial p}{\partial \rho}\right)_U + \left(\frac{\partial p}{\partial U}\right)_\rho \left(\frac{\partial U}{\partial \rho}\right)_s \quad (4.60)$$

and if along an isentrope the incremental energy U in the units of pressure is the product of pressure p and the incremental relative volume dv

$$dU = -p dv, \quad (4.61)$$

it is possible to obtain

$$c = \left[\left(\frac{4G}{3\rho_0}\right)_U + \frac{pv^2}{\rho_0} \left(\frac{\partial p}{\partial U}\right)_\rho \right]^{1/2}. \quad (4.62)$$

For elastic materials with a constant bulk modulus, the adiabatic speed of sound is given by

$$c = \sqrt{\frac{E(1-\nu)}{(1+\nu)(1-2\nu)\rho}} = \sqrt{\frac{K + \frac{4}{3}G}{\rho}}. \quad (4.63)$$

As a result, it can be stated that the time step size Δt_e is limited by a single (smallest) element in the finite element mesh. To decrease the computational costs of the simulations, a mixed time integration based on subcycling routines is implemented in LS-DYNA. The elements are sorted based on their time step size into groups, where the time step size is a multiple of the smallest element time step size $2(n-1)\Delta t$ for integer values of $n \geq 1$. The routine is based on the linear nodal interpolation partition-subcycling algorithm [144, 145]. In the implementation, the grouped elements are subjected to a vectorisation process so that constant length vectors are preferably used even at the cost

of updating the large elements incrementally with the small time step size as this process has been proved overall less computationally expensive, while the stability is preserved.

An aspect of the numerical simulations closely related to the time step size is the Courant number arising from the Courant–Friedrichs–Lewy (CFL) condition [146]. It is a necessary convergence condition for the numerical solution of partial differential equations stating that the time step of the simulations has to be equal or less than a certain value to yield correct results. Effectively, the numerical domain of dependence of any point in space and time (as determined by the initial conditions and the parameters of the approximation scheme) must then include the analytical domain of dependence (wherein the initial conditions have an effect on the exact value of the solution at that point) to assure that the scheme can access the information required to form the solution. As such, the CFL condition relates the length of the time step to a function of the interval lengths of each spatial coordinate and of the maximum speed that the information can travel in the physical space. We can write, for the general n -dimensional case, that

$$C = \Delta t \left(\sum_{i=1}^n \frac{v_{x_i}}{\Delta x_i} \right) \leq C_{\max}, \quad (4.64)$$

where C is the dimensionless Courant number, v_{x_i} is the magnitude of the velocity in the i -th direction, Δt is the time step, and Δx_i is the length interval in the i -th direction. The interval length Δx_i is allowed to be different for each spatial variable $\Delta x_i, i \in \{1, \dots, n\}$. The value of C_{\max} then depends on the method used to solve the discretised equations and particularly the integration scheme, where $C_{\max} = 1$ is typically considered in the explicit time integration.

■ Hourglass control

One of the aspects that has to be carefully treated in the explicit FEA is the hourglass effect originating from the zero-energy modes of the elements.

These undesirable hourglass modes tend to have periods typically significantly shorter than the periods of the structural response and are often observed to be oscillatory. However, hourglass modes that have periods comparable to the structural response may be a stable kinematic component of the global deformation modes and must be admissible. One way of resisting the undesirable hourglass effect is with a viscous damping or small elastic stiffness capable of stopping the formation of the anomalous modes, but having a negligible effect on the stable global modes. Since the hourglass deformation modes are orthogonal to the strain calculations, work done by the hourglass resistance is neglected in the energy equation. Even though this may lead to a small loss of energy, the invoked control of the hourglass should always be used for the under integrated (i.e., one-point) solid elements. Simultaneously, the energy dissipated by the hourglass forces reacting against the formations of the hourglass modes has to be tracked and evaluated against the energy balance in the simulations.

Several options based on different formulations or implementations are available in the LS-DYNA database. The type 1 hourglass control is based on an equation defining the hourglass resisting force vectors

$$f_{i\alpha}^k = a_h h_{i\alpha} \Gamma_{\alpha k}, \quad (4.65)$$

where $h_{i\alpha}$ is the element velocity field, α denotes indices of the hourglass base vectors of the possible zero-energy modes according to element type and

$$a_h = Q_{HG} \rho v_e^{frac{23}{4}} \frac{c}{4}, \quad (4.66)$$

where v_e is the element volume, c is the material speed of sound, and Q_{HG} is a defined constant. Here, the resisting forces are not orthogonal to the linear velocity field when the elements are not in the shape of parallelepipeds. As a consequence, such elements can generate hourglass energy with a constant strain field or rigid body rotation.

To overcome this effect, an hourglass control that is orthogonal to all modes except the zero energy hourglass modes was implemented [147]. Instead of resisting the components of the bilinear velocity field that are orthogonal to the strain calculation, the components of the velocity field that are not part of a fully linear field are being resisted. In the hourglass velocity field, the geometry-dependent hourglass shape vectors that are orthogonal to the fully linear velocity field and the rigid body field are used to resist the hourglass velocity deformations. Hourglass shape vectors can be defined with the use of the base vectors as

$$\gamma_{\alpha k} = \Gamma_{\alpha k} - \phi_{k,i} \sum_{n=1}^8 x_i^n \Gamma_{\alpha k} \quad (4.67)$$

yielding

$$f_{i\alpha}^k = a_h g_{i\alpha} \gamma_{\alpha k}, \quad (4.68)$$

which is a formulation of the type 2 hourglass control, where $g_{i\alpha} = \sum_{n=1}^8 \dot{x}_i^n \gamma_{\alpha k}$.

The type 3 hourglass control is identical to type 2, except that the shape function derivatives are evaluated at the centroid of the element rather than at the origin of the referential coordinate system and the exact element volume is produced.

The remaining hourglass control types calculate the hourglass forces proportional to total hourglass deformation rather than the hourglass viscosity. A stiffness form of hourglass control allows the elements to spring back and will absorb less energy than the viscous forms. Type 4 and 5 hourglass control are similar to type 2 and 3, except that the hourglass stiffness is evaluated rather than the viscosity. The hourglass rates are multiplied by the solution time step to produce increments of the hourglass deformation. The hourglass stiffness is scaled by the element maximum frequency so that stability can be maintained as long as the hourglass scale factor a_h is sufficiently small.

The type 6 hourglass control improves the type 5 by scaling the stiffness so that the hourglass forces match those generated by a fully integrated element control by doing a closed-form integration over the element volume.

■ Prescribed velocity

To introduce the process of establishing the initial velocity condition (i.e., the initial condition prescribed to the striker bar in the simulations), it is convenient to define the imposing displacement constraints. Here, the translational and rotational boundary constraints are imposed either globally or locally by setting the constrained acceleration components to zero. If nodal single point constraints are employed, the constraints are imposed in a local system. Let the local system be defined by specifying a vector \mathbf{u}_1 in the direction of the local x-axis \mathbf{x}_1 and a local in-plane vector \mathbf{v}_1 . After normalisation of \mathbf{u}_1 , the local \mathbf{x}_1 , \mathbf{y}_1 , and \mathbf{z}_1 axes are given by

$$\mathbf{x}_1 = \frac{\mathbf{u}_1}{\|\mathbf{u}_1\|}, \quad (4.69)$$

$$\mathbf{z}_1 = \frac{\mathbf{x}_1 \times \mathbf{v}_1}{\|\mathbf{x}_1 \times \mathbf{v}_1\|}, \quad (4.70)$$

$$\mathbf{y}_1 = \mathbf{z}_1 \times \mathbf{v}_1. \quad (4.71)$$

To transform the acceleration components into the local system, it is possible to write a transformation matrix

$$\mathbf{q} = \begin{bmatrix} \mathbf{x}_1^T \\ \mathbf{y}_1^T \\ \mathbf{z}_1^T \end{bmatrix} \quad (4.72)$$

and the transformation of the nodal translational and rotational acceleration vectors \mathbf{a}_I , $\dot{\mathbf{w}}_I$ for node I to the local system as

$$\mathbf{a}_{I_1} = \mathbf{q}\mathbf{a}_I, \quad (4.73)$$

$$\dot{\mathbf{w}}_1 = \mathbf{q}\dot{\mathbf{a}}_I. \quad (4.74)$$

The constrained components are then zeroed. In the next step, the modified vectors are transformed back to the global system such that

$$\mathbf{a}_{I_1} = \mathbf{q}^T \mathbf{a}_{I_1}, \quad (4.75)$$

$$\dot{\mathbf{w}}_1 = \mathbf{q}^T \dot{\mathbf{a}}_{I_1}. \quad (4.76)$$

Similarly, the prescribed nodal velocities are treated in a nearly identical way. Here, the velocities are prescribed at time $t^{n+1/2}$ after imposing the zero displacement constraints. The acceleration against the time curve is integrated or the displacement against the time curve is differentiated to generate the velocity against the time curve. The prescribed nodal components are then set. Similarly, any prescribed displacements or accelerations are imposed by the transformation into velocity components.

■ Contacts

Among the established approaches for treating contact problems, the method usually referred to as a kinematic constraint method is used in LS-DYNA for tying interfaces. To define the interface in three dimensions, triangular and quadrilateral segments comprising each side of the interface can be listed (in arbitrary order). For future considerations, one side of the interface is denoted as the master side and the other as the slave side, while the nodes located on these surfaces are referred to as master and slave nodes. The slave nodes are constrained to slide on the master surface after impact and must remain on the master surface until a tensile force develops between the node and the surface. In the automatic contact definition used in this work, the slave and master surfaces are generated internally in the software routines.

The kinematic constraint method uses the impact and release conditions of Hughes et al [148], which is imposed to ensure momentum conservation, while the release conditions are not currently implemented. The constraints are imposed on the global equations by transforming the nodal displacement components of the slave nodes along with the contact interface. This transformation eliminates the normal degree of freedom of the nodes. To preserve the efficiency of the explicit time integration, the mass is lumped so that only the global degrees of freedom of each master node are coupled. A known disadvantage of this approach is a state, when some master nodes may penetrate through the slave surface without resistance and create a kink in the slide line. This arises when the master surface zoning is finer than the slave surface zoning. Provided that the interface pressures are high enough, these kinks occur if one or more quadrature points are used in the element integration.

Let us consider the time-dependent motion of two bodies occupying regions B^1 and B^2 in their undeformed configuration at time $t = 0$. Assuming that the intersection

$$B^1 \cap B^2 = \emptyset \tag{4.77}$$

is satisfied, ∂B^1 and ∂B^2 denote the boundaries of B^1 and B^2 and in a given time t , these bodies occupy regions b^1 and b^2 bounded by ∂b^1 and ∂b^2 . Because the deformed configurations cannot penetrate,

$$(b^1 - \partial b^1) \cap b^2 = \emptyset, \tag{4.78}$$

the equations of motion remain uncoupled as long as $(\partial b^1 \cap \partial b^2) \cap b^2 = \emptyset$.

If $(\partial b^1 \cap \partial b^2) \cap b^2 \leq \emptyset$, the constraints are imposed to prevent the interpenetration of the discretised bodies. In these relations, the surfaces ∂b^1 and ∂b^2 of the bodies b^1 and b^2 denote the master and slave surfaces. Unless the

symmetric penalty treatment is employed and the selection of master and slave surfaces is arbitrary, the more coarsely meshed surface should be chosen as the master surface. Additionally, for a large difference in mass densities, the side corresponding to the material with the highest density should be used as the master surface.

The slave search routine finds, for each slave node, its nearest point on the master surface. Assuming that a master segment has been located for slave node n_s and that the slave node is not identified to be lying on the intersection of two master segments, then the identification of the contact point nearest to n_s on the master segment is non-trivial. For each master surface segment s_1 , the parametric representation is

$$\mathbf{r} = f_1(\xi, \eta) \mathbf{i}_1 + f_2(\xi, \eta) \mathbf{i}_2 + f_3(\xi, \eta) \mathbf{i}_3, \quad (4.79)$$

where

$$f_i(\xi, \eta) = \sum_{j=1}^4 \phi_j x_1^j. \quad (4.80)$$

Since r_1 is at least once continuously differentiable and

$$\frac{\partial \mathbf{r}}{\partial \xi} \times \frac{\partial \mathbf{r}}{\partial \eta} \leq 0, \quad (4.81)$$

\mathbf{r} represents the master segment that has a unique normal with a direction depending continuously on the points of s_1 .

Let \mathbf{p} denote a position vector drawn to slave node n_s . Considering that the master surface segment s_1 has been identified with n_s , the contact point coordinates (ξ_c, η_c) on s_1 must satisfy the equations

$$\frac{\partial \mathbf{r}}{\partial \xi}(\xi_c, \eta_c) \cdot [\mathbf{p} - \mathbf{r}(\xi_c, \eta_c)] = 0, \quad (4.82)$$

$$\frac{\partial \mathbf{r}}{\partial \eta}(\xi_c, \eta_c) \cdot [\mathbf{p} - \mathbf{r}(\xi_c, \eta_c)] = 0. \quad (4.83)$$

This system of equations is solved for ξ_c and η_c by solving Equation (4.82) for ξ_c in terms of η_c , substituting the result into (4.83), which yields a numerically solved cubic equation in η_c . Here, a problem in the solution may arise, when two nodes of a bilinear quadrilateral are collapsed into a single node for a triangle as the Jacobian of the minimisation problem is singular at the collapsed node. To overcome this consequence, an analytical solution for triangular segments is sought since the three points define a plane. For the solution of the non-linear equations, the Newton-Raphson iterative approach is used.

Viscous contact damping can be used in removing the high-frequency noise in problems involving impact. The natural frequency of the slave node is calculated from

$$\omega_n = \sqrt{\frac{k(m_{\text{master}} + m_{\text{slave}})}{m_{\text{master}}m_{\text{slave}}}}, m = \min\{m_{\text{master}}; m_{\text{slave}}\}. \quad (4.84)$$

In this equation, ω_n is the natural frequency, m_i is the mass, and k is the interface stiffness. The master node mass m_{master} is interpolated from the master nodes of the segment containing the slave node using the basis functions evaluated at the contact point of the slave node. The viscous contact damping is invoked in the simulations by setting a damping value as a percentage of critical damping $c_c = 2m\omega_n$.

Friction on the contact interfaces is, in LS-DYNA, based on a Coulomb formulation and the frictional algorithm uses the equivalent of an elastic-plastic spring. An exponential interpolation function smooths the transition between the static coefficient of friction μ_s and the dynamic coefficient of friction μ_d according to

$$\mu = \mu_d + (\mu_s - \mu_d) \exp^{-c|\mathbf{v}|}, \quad (4.85)$$

where the relative velocity between the master and the slave node is

$$\mathbf{v} = \frac{\Delta \mathbf{e}}{\Delta t'}. \quad (4.86)$$

The term Δt is the time step size, c is the decay constant, and

$$\Delta \mathbf{e} = \mathbf{r}^{n+1} (\xi_c^{n+1}, \eta_c^{n+1}) - \mathbf{r}^n (\xi_c^n, \eta_c^n). \quad (4.87)$$

The interface shear stress calculated from the Coulomb friction direction may exceed the bearing capacity of the material and another limit is, therefore, placed on the value of the calculated tangential force according to

$$f^{n+1} = \min \left(f_{\text{def}}^{n+1}, \kappa A_{\text{master}} \right), \quad (4.88)$$

where f^{n+1} is the frictional force at time step $n + 1$, f_{def}^{n+1} is the Coulomb's frictional force at time step $n + 1$, A_{master} is the area of the master segment, and κ is the viscous coefficient.

The surface to surface constraint used in this work for all the contacts between the bars and the specimen-bar contact is based on the algorithm developed by Taylor and Flanagan [149]. The algorithm involves a two-pass symmetric approach with a partitioning parameter β set between the negative and positive unity corresponding to one-way treatments with the master surface accumulating the mass and forces from the slave surface ($\beta = 1$) and vice versa ($\beta = -1$). In this constraint approach, the accelerations, velocities, and displacements are updated to a trial configuration without accounting for

the interface interactions and the penetration force is computed for the slave node as a function of the penetration distance ΔL after the update

$$f_p = \frac{m_s \Delta L}{\Delta t^2} \mathbf{n}, \quad (4.89)$$

where \mathbf{n} is the normal vector to the master surface. For each slave node in contact with the master surface and penetrating through it in its trial configuration, the nodal mass and the penetration force is accumulated to a global master surface mass and force vector. When Equation (4.89) is solved for the acceleration vector, the acceleration correction for the slave node is obtained and the process is repeated after reversing the master and slave definitions. The averaged final correction to the acceleration vector is found as

$$\mathbf{a}_n^{\text{final}} = \frac{1}{2} (1 - \beta) \mathbf{a}_n^{\text{pass } 1} + \frac{1}{2} (1 + \beta) \mathbf{a}_n^{\text{pass } 2}. \quad (4.90)$$

Friction is included in the implementation by calculating the frictional force resisting the relative tangential velocity of the slave node with respect to the master surface. Its magnitude is limited by the magnitude of the product of the Coulomb friction constant with the normal force. The modification to the tangential acceleration component of the slave node is given by

$$\mathbf{a}_t = \min \left(\mu \mathbf{a}_{nt} \cdot \mathbf{n}, \frac{|\mathbf{v}_s|}{\Delta t} \right). \quad (4.91)$$

The corrections to both the slave and master node acceleration components are

$$\mathbf{a}_{ts} = \mathbf{a}_t \mathbf{n}_t, \quad (4.92)$$

$$\mathbf{a}_{tk} = -\phi_{tk} \frac{\mathbf{a}_s m_s}{m_s} \mathbf{n}_t, \quad (4.93)$$

where $\mathbf{n}_t = \frac{\mathbf{v}_t}{v_t}$ is the tangential vector parallel to the direction of the tangential acceleration component and \mathbf{a}_s is the slave node acceleration vector.

Again, the process is repeated after reversing the master and slave definitions to obtain the averaged final correction to the acceleration vector

$$\mathbf{a}_t^{\text{final}} = \frac{1}{2} (1 - \beta) \mathbf{a}_t^{\text{pass } 1} + \frac{1}{2} (1 + \beta) \mathbf{a}_t^{\text{pass } 2}. \quad (4.94)$$

The final acceleration at time $n + 1$ is finally found according to

$$\mathbf{a}^{n+1} = \mathbf{a}^{\text{trial}} + \mathbf{a}_n^{\text{final}} + \mathbf{a}_t^{\text{final}}. \quad (4.95)$$

Concerning the topic investigated in this work, the biggest advantage of the constraint algorithm is that the interface nodes remain directly on or very close to the surfaces they are supposed to be in contact. Moreover, the elastic vibrations that can often occur in penalty formulations are insignificant with the constraint technique, which is crucial for the investigation of the stress wave propagation.

The single surface contact algorithm is an evolution of the surface to surface contact algorithm and the post-contact searching follows the procedures employed for the surface to surface contact by the introduction of a bucket sorting procedure. Additionally, the normal nodal vector projection step is superseded using the segment normal vector allowing for an arbitrary segment numbering within the contact surface. At the segment intersections, where nodes may approach undetected in certain cases, an additional logic that puts a cylindrical cap at the segment intersections has been introduced.

■ 4.3.2 Mesh development - bars

In all the cases, including the final simulations with the auxetic lattices, the ELFORM 1 hexahedral elements were used to represent the elastically deforming bars. This element type is an under integrated single-point constant stress element well suited for large deformations also. The characteristic element edge length is given by $L_e = V/A_{\max}$. The direct mesh generation in LS PrePost using the best quality approach algorithm was used to develop the numerical models of the bars, which were then calibrated according to the experimental data. Here, the irregularities are placed between the boundary and the centre by using a 5 block part. Hence, there are 4 irregularities in the mesh, located where only three elements are in contact. These irregularities are not as severe for the mechanical simulations since the average angle at these nodes is 120° , which is only 33% away from the ideal 90 degrees. A series of simulated void tests, impacts of the striker bar on the incident bar in direct contact with the transmission bar without a specimen, using the virtual SHPB was performed and the experimentally measured signals were compared with the signals from the FE model having a different mesh density. According to the results, a sensitivity study on the element sizing was performed since the non-physical behaviour of the stress signal was identified in the selected models [10].

It is well known that FEM can produce very unreliable outputs particularly in the analysis of the stress wave propagation using explicit numerical methods. Here, the mesh acts effectively as a low-pass filter, where smaller elements let the higher frequencies pass through the material in the model and this effect has to be studied to guarantee reliable results. The striker and incident bars with an average element size in the range 1 – 10 mm was then considered. Also, it is a well-known fact that the ability of the mesh to transfer high frequencies of the signal is proportional to the element size and this fact has to be taken into account, when modelling the stress wave propagation events, such as during the SHPB measurements. However, when the results are interpreted with respect to the element size only, very misleading conclusions can be made due to various phenomena, e.g., the non-physical amplitude of spurious oscillations at the face of the propagating stress waves. Thus, the sensitivity analysis in question is a multi-parametric problem and all the

assessed data have to be analysed contextually in consideration of the other properties of the FEA such as the numerical frequency damping, time step sizing, computational costs, etc. The numerical results were compared against the analytical assumptions from the wave propagation theory represented in this case by ideal quadrature signals and aside from the comparison of the stress waves, a frequency analysis was performed to evaluate the frequency and amplitude characteristics in the simulations. Instead of the simulated void tests, where the striker bar impacts the incident bar, a constant velocity was prescribed to one face of the incident bar for a given time interval simulating the analytical initial conditions.

In general, the smoothest mesh approaches the analytical solution with the highest precision, while the slope of the wave increase is inversely proportional to the mesh size. After the prescribed loading of the bar stops, considerations regarding the residual behaviour of the mesh can be made on the frequency-dependent damping of the mesh and the shape of the oscillations. Here, the coarsening of the mesh leads to a slow-down in the damping of low frequencies. The first extremum after initiation of the loading is proportional to the element size, i.e., exceeds the analytical prediction, but the amplitudes of the stress-oscillations may, in certain combinations of FEA parameters, increase in the bar even after removal of the loading. However, a similar behaviour of the first amplitude in the oscillations after the initiation of loading can be observed also in the case of the smoothest mesh. This effect was identified to be related with the time step value, where the default value of a 0.9 multiple of the critical time step has to be lowered to a range of approximately 0.5 multiple, where the FEA captures the real behaviour with sufficient precision.

Unlike the experimental SHPB testing, where the frequency range of the measurement is given by the hardware instrumentation, the FEA is only limited by Nyquist-Shannon sampling theorem in dependence on the element size, time step size and readout rate of the numerical results. The studies showed that the considered element size has only a negligible influence on the results up to approximately 125 kHz, which is still in the evaluated range in the experiments. Thus, a simple comparison with the experimental data may lead to the conclusion that the coarse mesh fits the experiments with the

highest precision as the smooth mesh is able to capture MHz-range frequencies not considered in the evaluation of experimental data. More specifically, the smoothing of the mesh leads to its ability to precisely capture the frequencies in the range of 125 – 500 kHz with the resulting readout of the stress during the numerical experiments yielding apparent spurious oscillations. These oscillations are, however, not present in the experimental data, but the reason is a combination of the numerical aspects of the simulations and the evaluated frequency range in the experiments.

As the FE mesh acts as a low-pass frequency filter, its properties can be quantified from the simulations by analyzing the amplitude and damping characteristics. Here, the analysis of the element-size dependent amplitude characteristics in the area close the applied initial conditions showed that a significant decrease in the signal-amplitude can be observed in the range of 500 kHz (10 mm coarse mesh) and 2 MHz (1 mm smoothest mesh) supporting the previous findings. However, significantly different results are obtained, when the same analysis is performed near the opposite face of the bar. The element size-dependent characteristics related to the stress wave propagation after the removal of the initial conditions cause, in general, decrease in the frequency range towards lower frequencies with a different shape of the amplitude characteristics. What is more important than the pure transferable frequency range, in this case, is the fact that with the coarsening of the mesh, the higher frequencies may even be amplified as the amplitude characteristics in the 0.6 – 4 MHz are near the value of the 0.5 multiple of the intensity of the driving signal.

As a result, the parameters listed in Table 4.1 were used to generate the FE-mesh of the striker, incident, and the transmission bars as the resulting ratio between the computational costs of the simulations and primarily frequency characteristics of the mesh were optimal. The cross-section of such a generated FE mesh of the bar is depicted in Figure 4.3.

Parameter	Value	Unit
Element-edge length parallel to bar axis	5	mm
Element-edge length - radial direction	≈ 1.2	mm
Element-edge length - outer circle	≈ 2	mm
Element count in circumferential direction	32	-
Pass-band - transfer	0.4	MHz
Specific number of elements	512	elem \cdot cm ⁻¹
Element count		
Striker bar	25,600	-
Incident + Transmission bar	81,920	-

Table 4.1: Properties of the FE-mesh representing the SHPB bars in the numerical simulations.

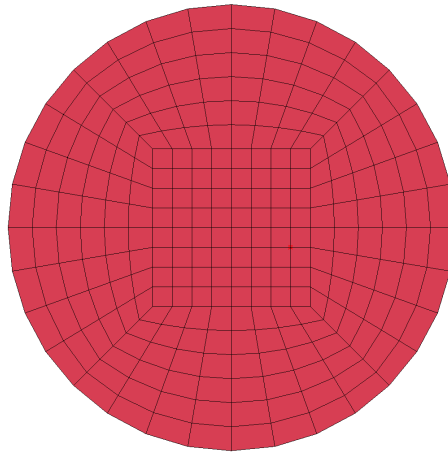


Figure 4.3: Meshed cross-section of the bar used in the FEA.

■ 4.3.3 Mesh development - auxetic lattices

Since the physical nature of the problems studied using FEA consisted of the stress wave propagation through a porous solid, where the microinertia and exact geometry have a critical influence on the comparability of the experimental and numerical deformation modes, a solid modelling approach was selected for the numerical representation of the auxetic lattices. In contrast with the modelling of the bars, a tetrahedral FE representation was selected due to the expected large deformation of the samples. This allowed the modelling of the complex solid bodies by direct conversion from the parametric models used for the additive manufacturing without any a priori geometric simplification. Importantly, such an approach requires no geometric, loading, and constitutive assumptions, and simultaneously, the boundary conditions are treated more realistically compared to the beam or shell discretisations. However, the clear disadvantage of solid modelling in explicit dynamics is its high computational cost in all the tasks from the mesh preparation to the post-processing, including the amount of disk space required. Concerning the ability of the tetrahedral mesh to discretise the whole geometry of the samples including all the details, particularly the geometry of the strut joints, the process of remeshing/mesh refinement to occasionally treat poorly shaped elements was computationally intensive. In all the cases, a mesher integrated into the LS PrePost suite was used to generate the FE mesh of the lattices.

From the database available in LS-DYNA, it is possible to use several different formulations of the tetrahedral elements that have to be evaluated in a parametric study for their suitability to represent the studied processes with the required precision and reliability. However, it is rather difficult to even define a quantitative criterion for such an evaluation as the parametric studies have to be performed in this case with the whole virtual SHPB apparatus including the studied lattice making the dimensionality of the task very high. For this reason, a 3D re-entrant honeycomb lattice having 3×3 unit-cells was selected due to its relatively simple geometry resulting in a conservative number of elements and also due to the volumetric nature of the deformation not limited to the in-plane strains observed in the other studied architectures. The following ELFORM options were studied:

- 10 - 1 point tetrahedron
- 4 - S/R quadratic tetrahedron with nodal rotations
- 16 - 5 point 10-noded tetrahedron
- 17 - 10-noded composite tetrahedron

ELFORM 10. Type 10 tetrahedral element is a 1 point constant stress element usually considered applicable for foams with zero Poisson's ratio and not recommended for general use in simulations except for the transitions in meshes. Even though the limitations are known for this type of element, it was used in the parametric study since the constant stress hexahedrons were successfully used for the representation of the bars. No convergence problems were encountered, but the overall deformation response of the auxetic lattice did not reflect the experiments particularly due to the well-known effect of the volumetric locking resulting in an apparently stiff behaviour and checkerboard mode in certain circumstances. The characteristic element edge length is given as $L_e = 0.85 h_{\min}$, where h_{\min} is the minimum height of the tetrahedron.

ELFORM 4. Type 4 is an element type derived from a 10-node tetrahedron and defined as a 5-node tetrahedron with nodal rotations (i.e., 6 DOFs per node) and selectively reduced integration with generally good accuracy for small strains even though it also has a tendency to have a volumetric locking behaviour. The results for this element formulation are not presented as the convergence of the simulations was difficult due to large strains resulting from the relatively high deformation energy events. The characteristic element edge length is given as $L_e = h_{\min}$.

ELFORM 16 and 17. Type 16 and 17 are fully integrated 5-point tetrahedra with good accuracy for a moderate strain encountered in metals. The type 17 formulation is a composite derivative of type 16, where each tetrahedron is, in fact, an assembly of 12 linear sub-tetrahedra enabling for the correct external force distribution. This is an important property for the stress wave transfer from/to the bars at the impact and distal faces of the specimen and with regards to the deformation behaviour captured only using a limited number

of elements through the cross-section of the geometrical entity. An obvious disadvantage of these element formulations is the high computational cost arising from the CPU costs of the calculations and a high number of elements needed to represent the solid body. The characteristic element edge length for type 16 is given by $L_e = 0.3889 h_{\min}$, while the characteristic element edge length for type 17 is given by $L_e = V/A_{\max}$, where A_{\max} is the maximum area of the constituting triangle.

Before the optimisation of the material model, it was necessary to perform a mesh-related sensitivity study to find an optimum combination of the parameters, so that the numerical experiment reflects the experimentally observed behaviour of the auxetic lattices. Besides the selection of the element formulation itself, the number of elements generated across the thinnest geometrical element of the lattice was selected and identified to have the most significant influence on the deformation response. To demonstrate the influence of the element formulation and the number of elements used to represent the cross-section of the structure, Figures 4.4 and 4.5 show a comparison of the numerical strain waves captured at half of the transmission bar's length for the 3D re-entrant honeycomb lattice discretised using various parameters and subjected to the same initial conditions used in the experiments with a material model calibrated using the experiments with the bulk samples.

It can be clearly seen that the considered parameters are influencing the simulated deformation response of the lattice. However, the sensitivity on the individual parameters cannot be studied by the simple isolation of one parameter at a time in a parametric study due to the synergistic effects encountered in such complex scenarios. For this reason, the influence of the selected factors was studied on the 3D re-entrant honeycomb having 3×3 unit-cells due to its more complex volumetric deformation response, which includes stability problems of the compressed struts. To evaluate the influence of the number of elements across the thinnest dimension of the geometrical elements constituting the auxetic lattice, the geometrical model was discretised with either 1, 2, or 3 elements through the cross-section of the struts constituting the unit-cell. The mesh generation was controlled by prescribing the characteristic element dimension as a fraction of the thickness in the parametric model of the specimen. This task was performed for all the

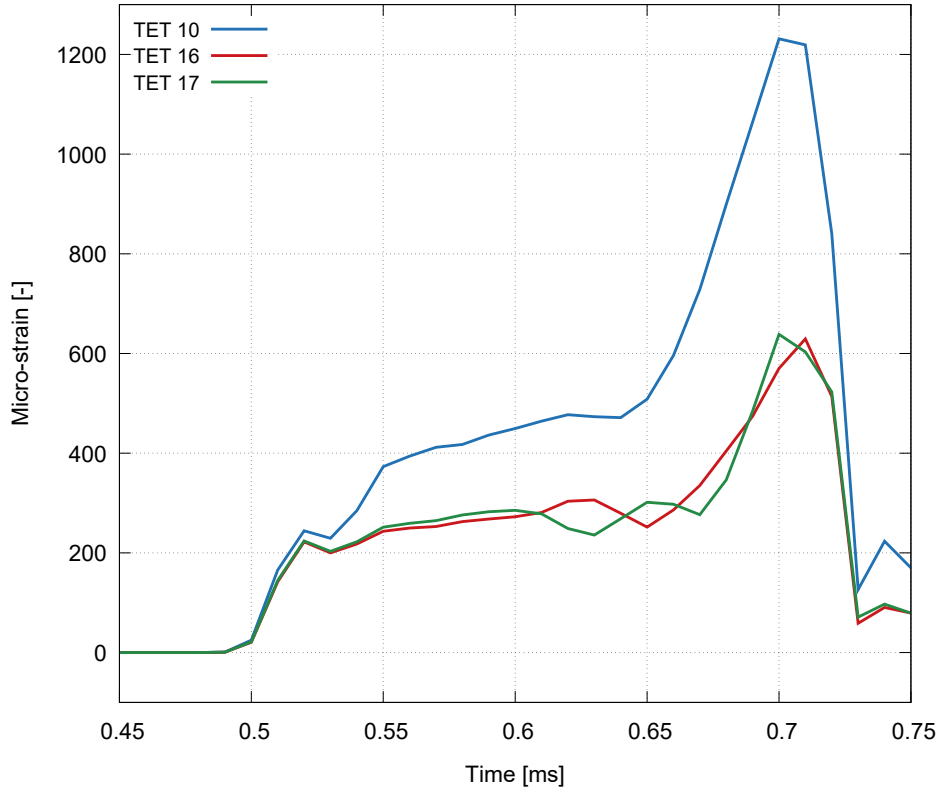


Figure 4.4: Strain plotted against time showing the numerical strain waves for the different element formulations representing the auxetic lattice.

element formulation options exhibiting a successful convergence during the whole duration of the simulated experiments, i.e., for ELFORM 10, 16, and 17. The conformity of the simulated and experimental transmission waves was analysed and according to the acquired results, all the 3×3 unit-cell structures have then been discretised using the ELFORM 17 composite tetrahedra and two elements across the thickness of the struts. Even though the sensitivity study showed the best conformity with the experimental data of the mesh with two elements in the cross-section of the struts, this approach could not be currently used due to the excessive computational costs in the case of the RVE sized lattices. Here, the difference in the CPU time between the 1 and 2 elements generated through the thickness of the struts was 10-fold not only due to the number of elements, but also due to their lower characteristic length arising from the lower thickness of the struts influencing the time step size. As an example, this led to 290 hours of CPU time using 12 threads of the high-performance workstation used in the simulations. Considering the high required number of simulations to obtain the final results (i.e., hundreds

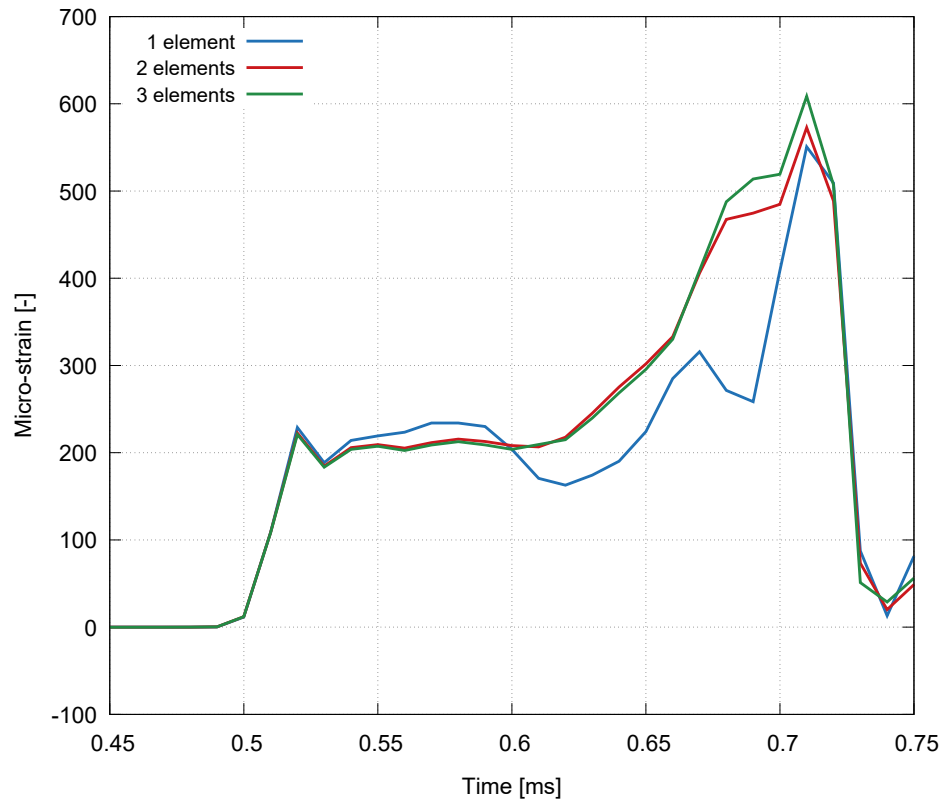


Figure 4.5: Strain plotted against time showing the numerical strain waves for the different number of elements within the cross-section of the microstructure.

for all the RVE sized lattices), it would not be feasible to perform all the tasks in a realistic time-frame and a supercomputer will be used in the future work instead. Table 4.2 summarises the number of elements and nodes in the discretised lattices.

■ 4.3.4 SS316L material model

The auxetic lattices were simulated using the MAT 12 isotropic elastic-plastic material model for its computational efficiency, numerical stability, and the possibility of an easy calibration. In the formulation of this material model, the von Mises yield condition is given by

Structure	Elements across thickness	Elements	Nodes
3 × 3 lattices			
3D re-entrant honeycomb	1	39,614	80,467
3D re-entrant honeycomb	2	196,275	348,521
3D re-entrant honeycomb	3	556,253	906,919
2D re-entrant honeycomb	2	96,550	168,508
2D missing-rib	2	110,556	189,970
RVE sized lattices			
3D re-entrant honeycomb	1	99,066	211,960
3D re-entrant honeycomb	2	372,740	680,701
2D re-entrant honeycomb	1	215,790	415,953
2D missing-rib	1	230,974	442,551

Table 4.2: Number of elements and nodes required for the numerical representation of the studied auxetic lattices.

$$\phi = I_2 - \frac{\sigma_y^2}{3}, \quad (4.96)$$

where the second stress invariant I_2 is defined in terms of the deviatoric stress components as

$$I_2 = \frac{1}{2} s_{ij} s_{ij}. \quad (4.97)$$

The yield stress σ_y is a function of the effective plastic strain $\varepsilon_{\text{eff}}^p$ and the plastic hardening modulus E_p such that

$$\sigma_y = \sigma_0 + E_p \varepsilon_{\text{eff}}^p. \quad (4.98)$$

The effective plastic strain is defined as

$$\varepsilon_{\text{eff}}^{\text{p}} = \int_0^t d\varepsilon_{\text{eff}}^{\text{p}}, \quad (4.99)$$

where

$$d\varepsilon_{\text{eff}}^{\text{p}} = \sqrt{\frac{2}{3} d\varepsilon_{ij}^{\text{p}} d\varepsilon_{ij}^{\text{p}}} \quad (4.100)$$

and the plastic tangent modulus is defined using the tangent modulus E_t as

$$E_p = \frac{EE_t}{E - E_t}. \quad (4.101)$$

The pressure is given by

$$p^{n+1} = K \left(\frac{1}{V^{n+1}} - 1 \right), \quad (4.102)$$

where K is the bulk modulus and the pressure is integrated in time from

$$\dot{p} = -K\dot{\varepsilon}_{ii}, \quad (4.103)$$

where $\dot{\varepsilon}_{ii}$ is the volumetric strain rate.

Before the optimisation of the material model using the parametric numerical simulations, the values of the constants were determined using a combination of data-sheet values from the manufacturer of the SLS device and using the experimental testing of the bulk SLS printed samples [11]. For the properties of the wrought SS316L steel, the company Renishaw provided the following data:

Parameter	Horizontal direction	Vertical direction	Unit
Young's modulus	197± 4	190± 10	GPa
Yield strength	547± 3	494± 14	MPa
Upper tensile strength	676± 2	624± 17	–

Table 4.3: Relevant mechanical properties of the components additively manufactured from SS316L-0407 provided by Renishaw.

Naturally, these values were derived from the quasi-static testing of the bulk samples printed using the SLS technology according to ASTM mechanical standards. Although several papers concentrated on the dynamic testing of printed stainless steels are available (e.g., [150, 151]), the approach based on performing one's own SHPB experiments was selected due to the nature of the SLS additive manufacturing technology. Here, the resulting mechanical properties of the objects are strongly dependent on the specific parameters used during the manufacturing procedure as a result of the know-how of the staff operating the printer and also on the orientation of the objects with respect to the powder bed plane. Thus, no data taken from the literature can be reliably used without verification. Besides the dynamic yield strength of the printed material, the most important unknown parameter strongly influencing the numerical simulations was the tangential modulus. For instance, this property can be estimated from, e.g., the Ramberg-Osgood power-law relation describing the non-linear stress-strain relationship. This model is particularly suited to strain hardening metals showing a smooth elastic-plastic transition. In the classical form, the model can be formulated such that

$$\varepsilon = \frac{\sigma}{E} + \left(\frac{\sigma}{H}\right)^{1/n}, \quad (4.104)$$

$$\sigma = H\varepsilon_p^n, \quad (4.105)$$

where

$$n = \frac{\log\left(\frac{\sigma_m}{\sigma_0}\right)}{\log\left(\frac{\varepsilon_f}{0.002}\right)}, \quad (4.106)$$

$$H = \frac{\sigma_0}{0.002^n}, \quad (4.107)$$

σ_0 is the yield strength, σ_m is the ultimate strength, ε_f is the failure strain, E is the elastic modulus, ε_p is the plastic strain, and constants H and n describe the hardening behaviour of the material considering the 0.002 yield offset. However, the transition beyond the yield point is of too low a curvature when the constants of the printed 316L steel are used in the calculation.

Thus, the strain-rate and printing direction dependency of the compressive behaviour of the 3D printed material of the specimens was investigated. To assess the strain-rate sensitivity as well as the effect of the printing direction on the compressive behaviour of the investigated material, three different sets of specimens, each with a different printing orientation, were tested at various strain-rates using the SHPB apparatus and under the quasi-static loading conditions. The specimens for the quasi-static experiments had a cylindrical shape with a diameter of 5 mm and a height of 10 mm. Therefore, the height to diameter ratio was 2. The specimens were printed with three different orientations - vertically, at the angle of 0 degrees, horizontally, at the angle of 90 degrees and tilted, at the angle of 45 degrees in every case related to the powder bed plane (see Figure 4.6).

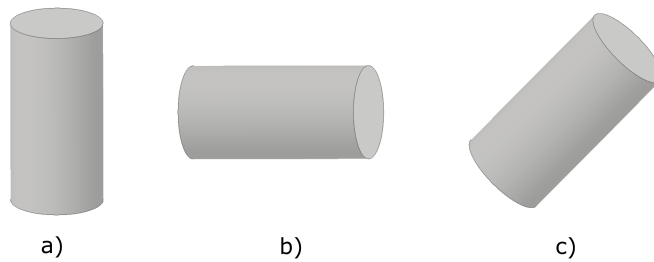


Figure 4.6: Orientation of the specimens during production: a) vertical, b) horizontal, and c) tilted.

Dog-bone shaped specimens with overall dimensions of 18×16 mm were used for the dynamic experiments. The particular design of the specimens for the

dynamic tests (see Figure 4.7) was selected due to the parameters of the used SHPB apparatus. The contact faces of the specimens needed to have a wider diameter to achieve a similar material impedance as has the material of the bars. In this regard, the deformation wave is not reflected at the bar-specimen interference, but is transmitted into the specimen without any significant loss. However, the centre part of the specimen needed to be thinner to achieve a sufficient deformation during the dynamic experiments. The specimens were also 3D printed with the same three different orientations relative to the powder bed plane (see Figure 4.8).

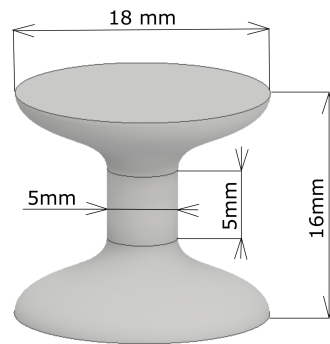


Figure 4.7: Dimensions of the dog bone shaped specimen used for the dynamic experiments.

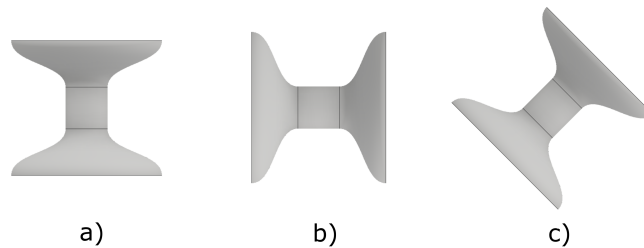


Figure 4.8: Orientation of the specimens during production: a) vertical, b) horizontal, and c) tilted.

An Instron 3382 electro-mechanical loading device was used for the quasi-static experiments. The loading procedure was displacement controlled with the loading velocity of $1 \text{ mm} \cdot \text{min}^{-1}$, resulting in a strain-rate of approximately 0.002 s^{-1} . The dynamic experiments were conducted using the same SHPB apparatus utilised for the measurement of the auxetic lattices. Depending on the required strain-rate, two different striker bars were used in the experiments; for a higher strain-rate (6000 s^{-1}), a striker bar with the length of 500 mm was used and a 650 mm long bar was used for a lower strain-rate (2000 s^{-1}). This enabled one to achieve the same deformation range at both the strain-

rates. To reduce the wave dispersion effects, the pulse-shaping technique was engaged using cylindrical soft copper shapers with a diameter of 7 mm and a thickness of 1 mm.

Figures 4.9 and 4.10 depict the acquired stress-strain curves of the 45 degree rotated specimens relevant for this work as all the auxetic specimens were printed in such an inclined orientation to the powder bed plane due to heat dissipation problems during the printing procedure.

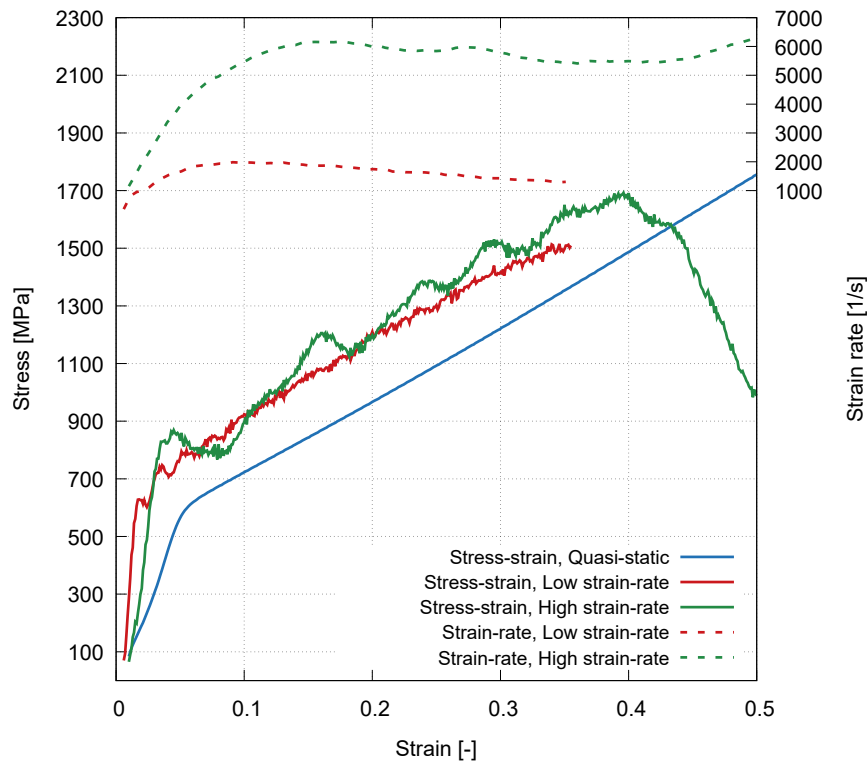


Figure 4.9: Quasi-static averaged stress-strain curves for the cylindrical and dog bone specimens.

From the analysis of the stress-strain relations, the following constants were used in the dynamic FEA before optimisation of the material model:

The mean density of the SLS printed material measured using the set of cylindrical samples was $7.52 \pm 0.17 \text{ g} \cdot \text{cm}^{-3}$ compared to the nominal density of the wrought material of $7.99 \text{ g} \cdot \text{cm}^{-3}$. Hence, a 6% porosity arising from imperfect printing can be assumed. The elastic constants were calculated from the average nominal values according to the established equations for

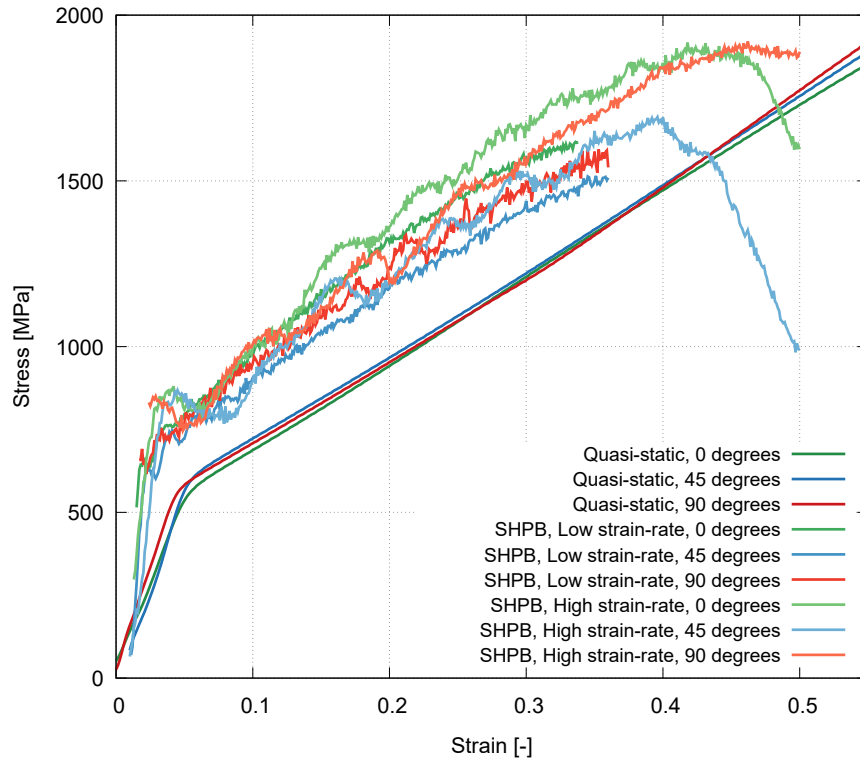


Figure 4.10: Averaged results for the specimens printed at an angle of 45 degrees.

Parameter	Value	Unit
Mass density	7.52	g/cm ³
Yield stress	520	MPa
Plastic hardening modulus	2.32	GPa
Bulk modulus	171.8	GPa
Shear modulus	79.3	GPa

Table 4.4: Constants of the MAT 12 material model of the SLS printed steel used for the initial study of the dynamic FEA.

homogeneous isotropic linear elastic materials considering $\nu = 0.3$ Poisson's ratio. The elastic constants were, from Young's modulus and Poisson's ratio, calculated as

$$K = \frac{E}{3(1-2\nu)}, \quad (4.108)$$

$$G = \frac{E}{2(1+\nu)}. \quad (4.109)$$

For each auxetic lattice and strain-rate, the constants of the material model were optimised in an iterative parametric FE study, where the yield stress σ_y and the plastic hardening modulus E_t were consecutively varied. This was enabled by the nature of the deformation response of the lattices, which in every case reflects the compressive characteristics of the metal foams in terms of the apparent yield point followed by the plateau stress region. Thus, the yield stress set in the material model definition was determined so that the resulting simulated response of a given lattice matches the respective experimental data. Then, the value of the plastic hardening modulus was updated until the conformity of the plateau stress and the shape of the plateau stress curve was found. This, in the majority of cases, also guaranteed the correct densification strain in the virtual experiments. In the remaining cases, the values of the yield stress and plastic hardening modulus were varied together to find the best possible compliance between the experimental and numerical data in terms of the densification strain, the densification modulus, and the ultimate stress induced by the propagation of the first stress wave. Figure 4.11 depicts both the yield stress and plastic hardening modulus plotted against the strain-rate for all the numerical simulations.

Figure 4.11 depicts the results for both the lattices with 3×3 unit-cells and the RVE sized lattices. This is the reason for the distortion of the trends in the strain-rate dependent yield stress of the missing-rib structures and the plastic hardening modulus of both the two-dimensional lattices. However, when only the data for the RVE sized samples are evaluated (strain-rate 1500 s^{-1} and 3000 s^{-1}), clear strain-rate dependencies can be identified in the data. It can be seen that, to correctly reflect the strain-rate dependent characteristics of the SLS printed specimens in the FEA, the yield stress had to be increased in all the simulations by 33 % (missing-rib structure), 17 % (2D re-entrant honeycomb), and 33 % (3D re-entrant honeycomb). Simultaneously, a decreasing tendency in the plastic hardening modulus consisted of 57 % (missing-rib structure), 0 % (2D re-entrant honeycomb), and 8 % (3D re-

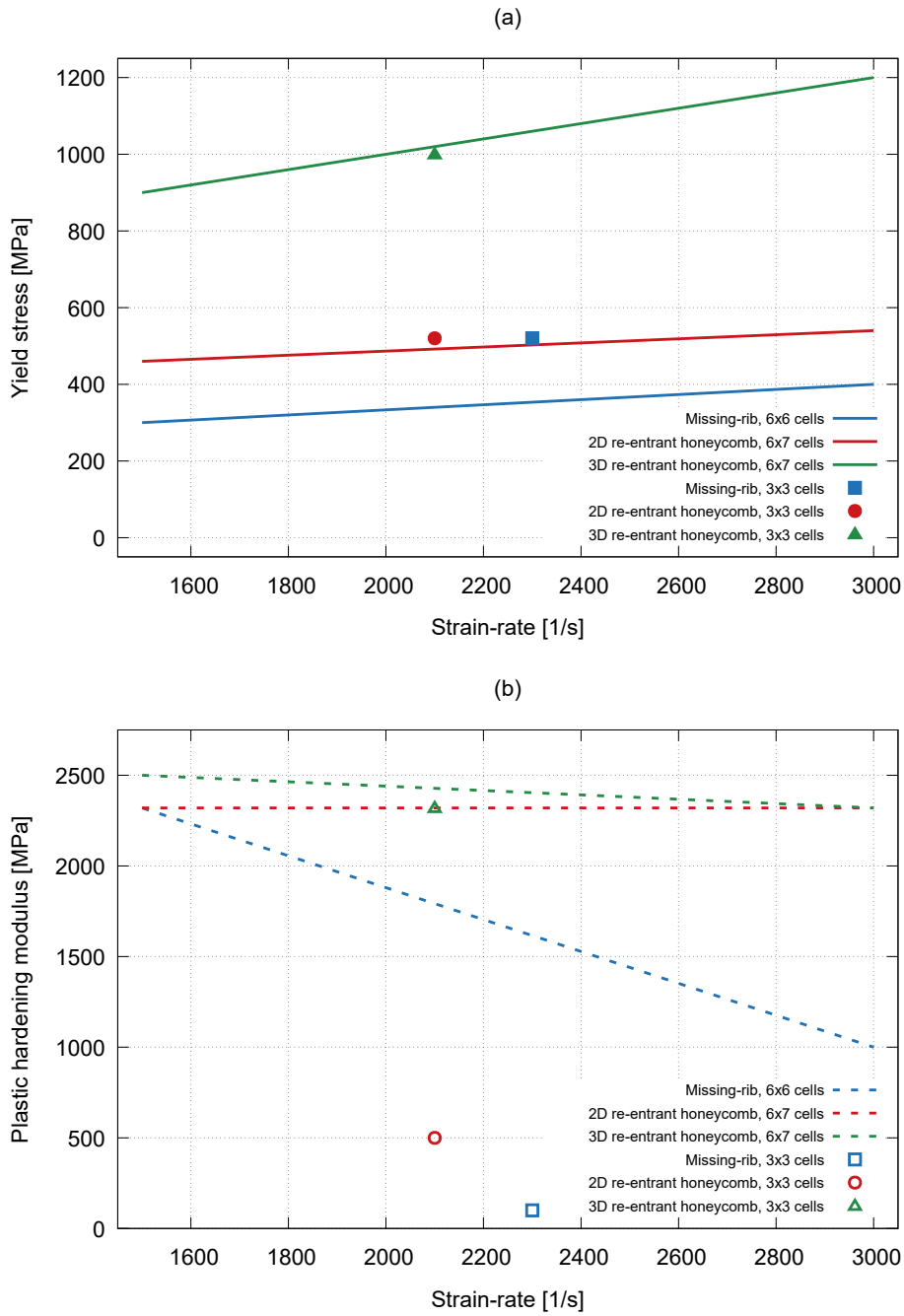


Figure 4.11: The yield stress (a) and the plastic hardening modulus (b) used in the MAT 12 material model plotted against the strain-rate.

entrant honeycomb) can be quantified.

4.4 Results

4.4.1 Experimental results

The employed SHPB setup was suitable to measure the dynamic response of the auxetic structures. Foil strain gauges were successfully employed instead of semiconductor strain gauges. The increased noise and lower sensitivity were compensated for by the linearity of the foil gauge and its extensive working range. The values of the measured strain in the incident bar were significantly above the measurable limit of a semiconductor gauge type. A digitiser sample rate of 20 MHz and a high-speed camera frame rate of 100 kfps were sufficient to capture the deformation of the specimen. The stress-strain curves and strain-dependent Poisson's ratio were evaluated. The results for the RVE sized lattices were obtained at two strain rates denoted in the following figures as low-rate (1500 s^{-1}) and high-rate (3000 s^{-1}). Figures 4.12 and 4.13 depict the microstructure of the specimens during the uniaxial compression.

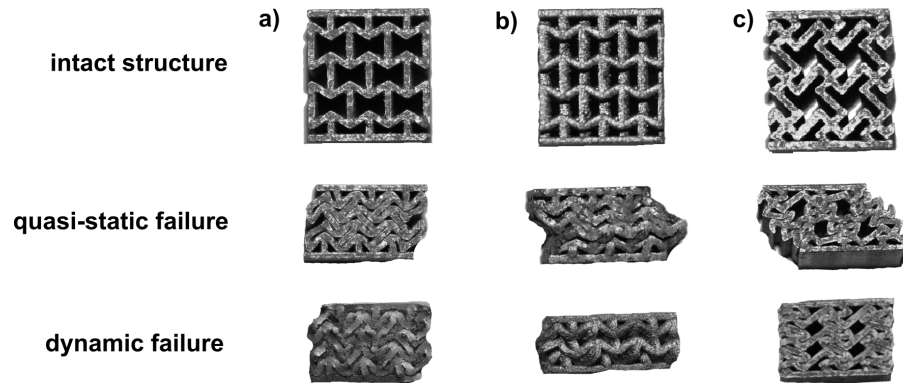


Figure 4.12: Comparison of the 3×3 samples in an intact state, structures collapsed in the quasi-static experiment, and structures collapsed in the SHPB experiments, (a) 2D re-entrant honeycomb, (b) 3D re-entrant honeycomb, (c) 2D missing rib.

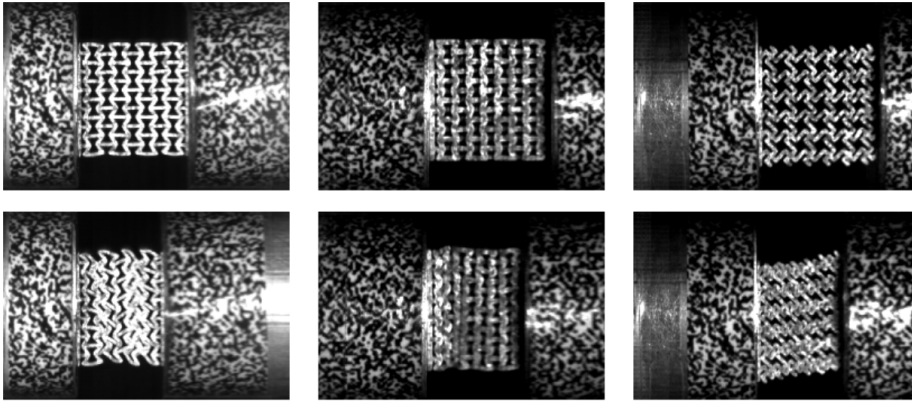


Figure 4.13: Comparison of the RVE sized samples during the dynamic crushing in the SHPB experiments, (a) 2D re-entrant honeycomb, (b) 3D re-entrant honeycomb, (c) 2D missing rib.

■ Stress-strain response

The stress-strain diagrams of the auxetic lattices having 3×3 unit-cells subjected to the dynamic loading are depicted in Figures 4.14 - 4.16 together with the quasi-static curves for the comparison of the strain-rate effect on the compressive response. The dynamic experiments of the 3×3 lattices were conducted with a lower quality compared to the RVE sized samples resulting in a lower precision and repeatability of the results.

The dynamic response of such a 2D missing-rib lattice at the strain-rate of 2100 s^{-1} is very similar to the quasi-static test plateau-stress, the strain of the densification related to the collapse of the first layer, and the slope of the densification part of the response. A difference was identified in the strain value, where the structure reached the plateau stress, which is connected to the delay of the signal during the SHPB measurement and the development of the strain rate in the sample. According to the parameters of the SHPB setup and operation parameters selected for the measurement, the maximum achieved compressive strain was 0.325 constraining the ability for the comparison with the quasi-static results measured throughout the compressive response of the structure. Still, the higher stress values in the dynamic experiments at a strain over 0.28 indicate the strain-rate sensitivity of these samples at later stages of the deformation response. The visual inspection of the high-speed camera data and the samples after the experiment also showed the uni-axial

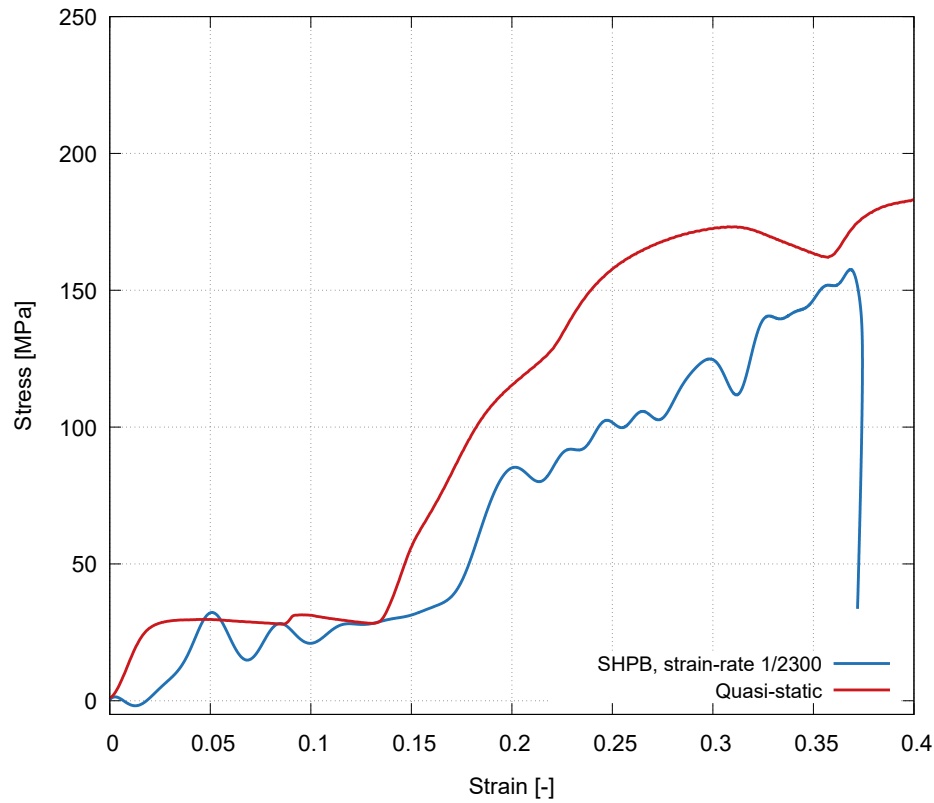


Figure 4.14: Experimental stress-strain curves - 2D missing-rib lattice composed of the 3×3 unit-cells, the dynamic and quasi-static response.

character of the deformation without any significant lateral movement of the upper and bottom layer of the unit-cells present in the quasi-static loading.

In the stress-strain diagrams of both the 2D and the 3D re-entrant honeycomb lattices, it can be seen that their compressive behaviour is very similar to the response of closed-cell metal foams even during dynamic compression. In contrast with the missing-rib structure, however, the strain-rate effect is clearly apparent and leads to a notable increase in the effective yield stress of the structures together with the increase of the plateau stress and lower densification strain.

In the case of the 2D re-entrant structure, the yield stress increased by 40% from 75 MPa to 105 MPa and the average plateau stress increased by 50% from 80 MPa to 120 MPa, while densification occurs at a 0.25 strain compared to a 0.3 strain during the quasi-static loading. The observed decrease in

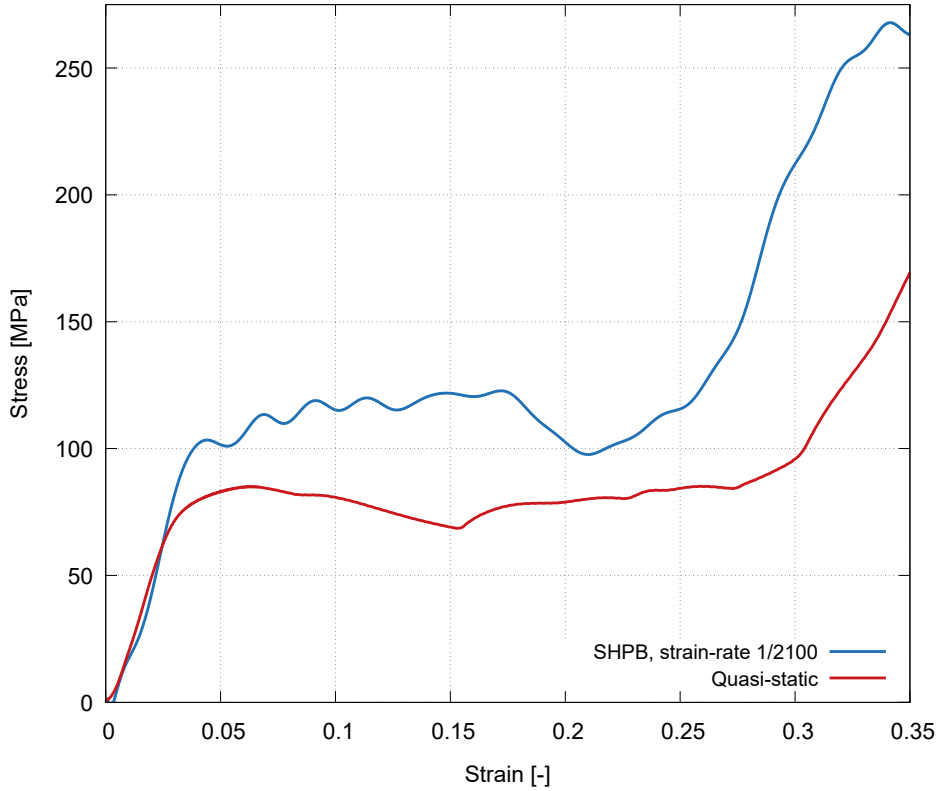


Figure 4.15: Experimental stress-strain curves - 2D re-entrant honeycomb lattice composed of the 3×3 unit-cells, dynamic and the quasi-static response.

the stress at the plateau region caused by the temporary localisation of deformation also occurs at a different point with the local minimum at a 0.05 higher compressive strain in the case of the dynamic tests.

Similar observations have been made in the case of the 3D re-entrant structures. The apparent yield stress (partially hidden in the oscillations and evaluated from the analysis of their amplitudes) increased in this case by 35% from 42.5 MPa to 57.5 MPa and the densification strain decreased to 0.3 from the quasi-static value of 0.325. Unlike the dynamic response, the quasi-static tests showed one local stress maximum after the initial yielding of the structure, which was not present in the dynamic results. Similarly to the 2D re-entrant structure, the decrease in the plateau regions occurs during the dynamic tests at a higher compressive strain (0.175 versus 0.07) and the gradient of the decrease is significantly steeper. Compared to the quasi-static tests, the acquired stress-strain diagrams of the 2D and 3D re-entrant structures show

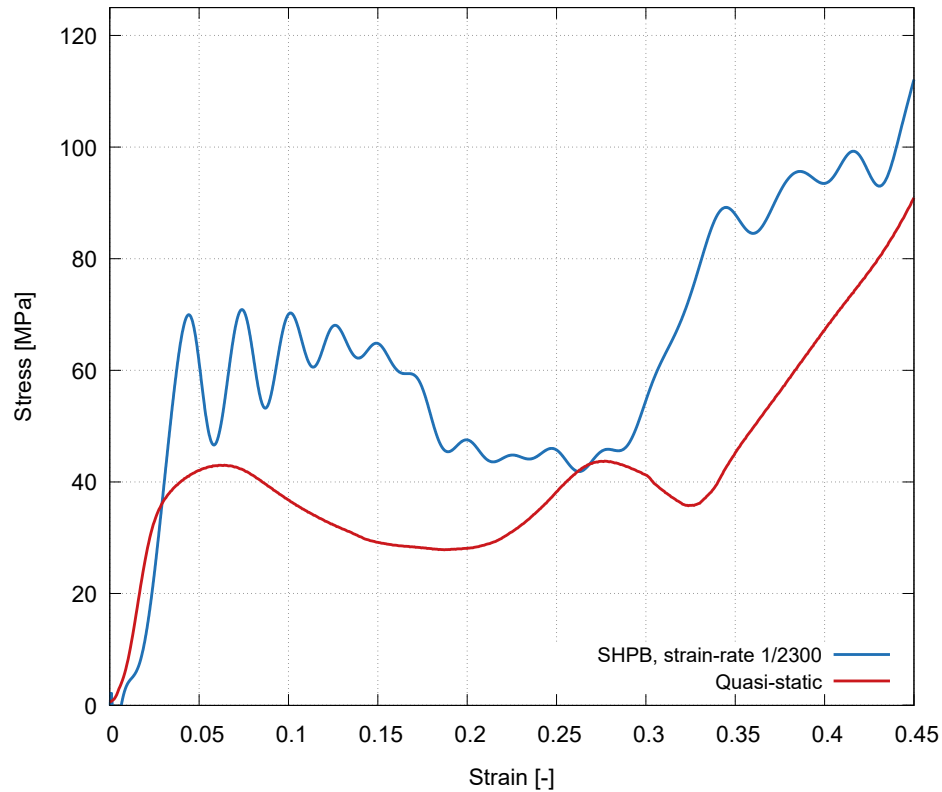


Figure 4.16: Experimental stress-strain curves - 3D re-entrant honeycomb lattice composed of the 3×3 unit-cells, the dynamic and quasi-static response.

a higher similarity in terms of the plateau stress region. Nevertheless, the 3D re-entrant lattice remains weaker than the planar assembly of the re-entrant unit-cells also in the dynamic compression.

Figures 4.17 - 4.19 depict the comparison of the stress-strain diagrams for the auxetic lattices with an RVE number of unit-cells calculated from the quasi-static and dynamic loading at both strain-rates.

In the plot of the stress-strain diagram for the 2D missing-rib structure, the difference between the quasi-static and dynamic compression is clearly apparent. The yield stress and plateau stress increased from 20 MPa to 30 MPa and the level of stress remains at higher levels throughout the deformation range of the experiments. The most significant difference between the quasi-static and dynamic response at strains above 0.225, where the stress calculated from the high strain-rate experiments increases steeply resulting in a 100 %

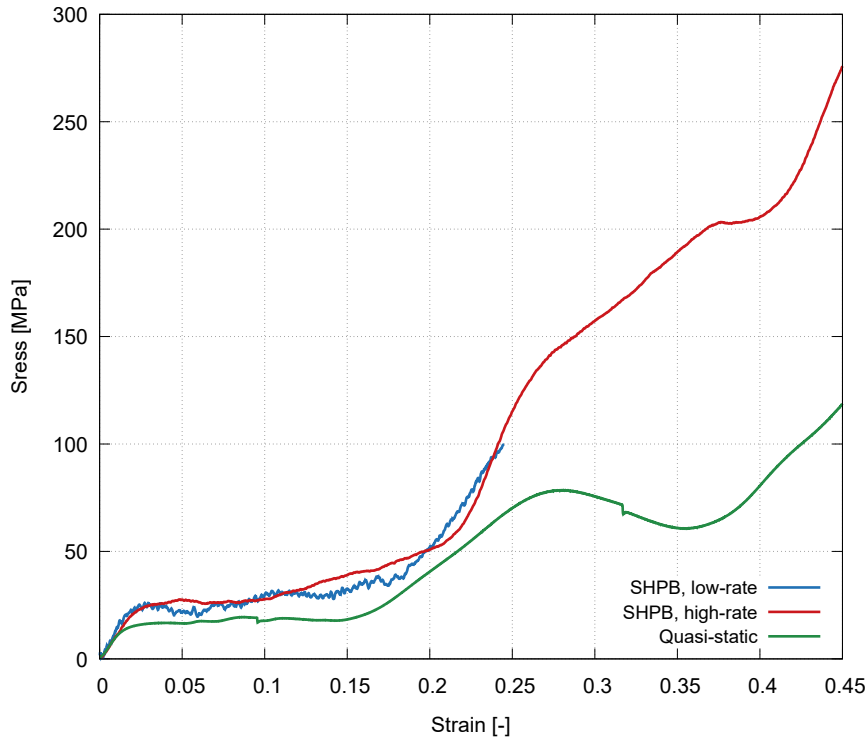


Figure 4.17: Comparison of the experimental stress-strain curves - the RVE sized 2D missing-rib lattice, the dynamic and quasi-static response.

difference at a 0.45 strain. From the visual inspection of the deforming structures, this effect can be attributed to the different deformation mode of the dynamically loaded lattices resulting in a uni-axial response without any lateral movements of the layers induced by the orientation of the unit-cells. The differences in the deformation response to the low and high-strain rate loading resulted in a consistently higher and monotonic increase in the stress for the higher strain-rate. However, due to the characteristics of the low strain-rate experiment, the comparison can be made only up to 0.25 of the compressive strain, and the remaining part of the densification region could not be assessed.

Similarly, the strong strain-rate effect in terms of the difference between the quasi-static and dynamic effect was assessed for the 2D re-entrant honeycomb structure. Here, the yield strength increased by 50 % from 50 MPa to 75 MPa for both the dynamic strain-rates, while the stress level at 0.45 of the compressive strain resulted in a 55 % increase between the high strain-rate SHPB measurement and the quasi-static loading. In the dynamic response,

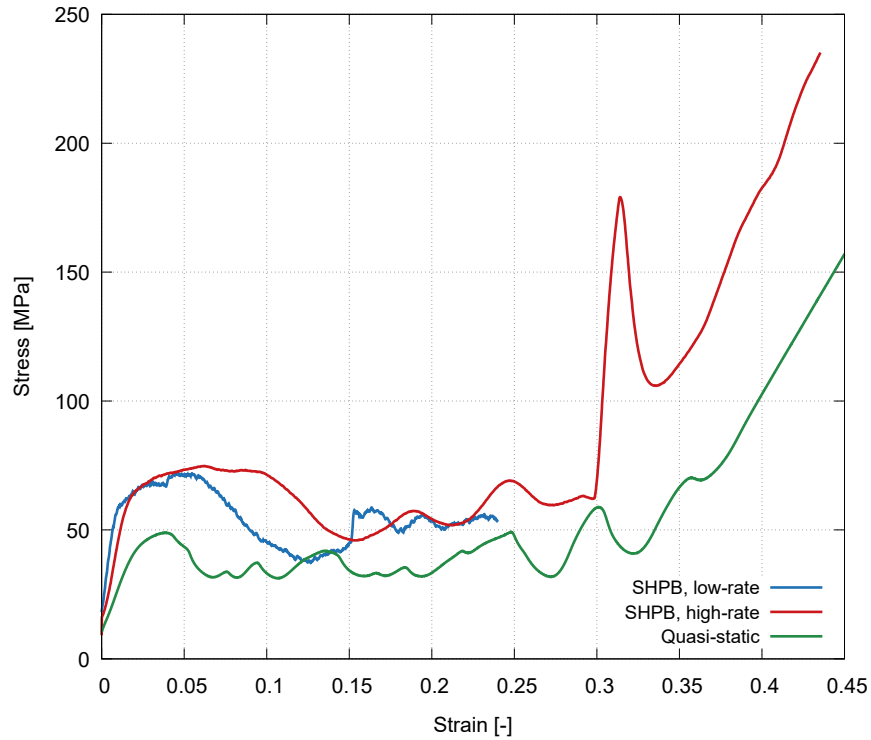


Figure 4.18: Comparison of the experimental stress-strain curves - the RVE sized 2D re-entrant honeycomb, the dynamic and quasi-static response.

the amplitude of the stress oscillations in the plateau region is significantly pronounced (with the low-rate loading reaching a local minimum under the corresponding level of the quasi-static test), but the number of oscillations is reduced in comparison with the quasi-static loading. Interestingly, an increase of strain-rate in the SHPB test leads to the identical apparent yield stress of the structure and a decrease in the plateau stress at a higher strain suggesting that micro-inertia effects are the driving force of the strain-rate dependence in this case.

The strain-rate sensitivity of the deformation response of the 3D re-entrant structure shows trends analogous to the planar assembly of the re-entrant honeycomb unit-cells except for the oscillations at the plateau region. Approximately the same increase of the apparent yield stress and ultimate stress at the end of the experiment (a compressive strain of 0.4) by a factor of 1.5 was assessed for the high strain-rate experiments, when compared to the quasi-static loading. The apparent yield stress in this case is identical for both the SHPB strain-rates, while no difference in the plateau region was

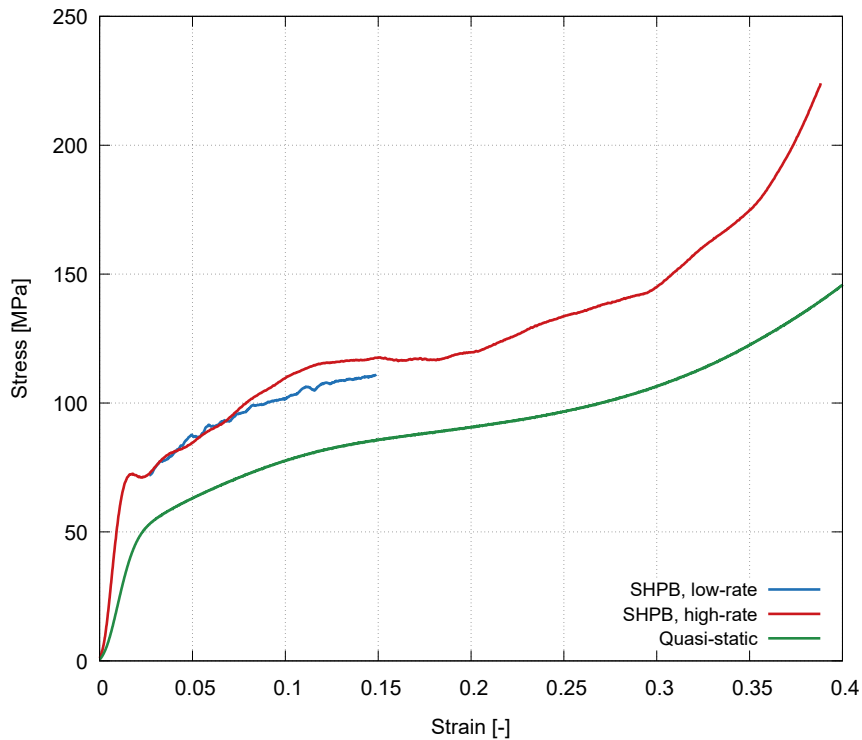


Figure 4.19: Comparison of the experimental stress-strain curves - the RVE sized 3D re-entrant honeycomb, the dynamic and quasi-static response.

reliably identified as the trends and absolute values are nearly identical up to the maximum strain achieved during the low strain-rate loading.

■ Strain-dependent Poisson's ratio

For every investigated microarchitecture, the DIC-based evaluation of the function of Poisson's ratio was performed and the resulting curves were compared to reveal the strain-dependent characteristics of the microarchitectures. Figures 4.20 - 4.22 depict Poisson's ratio plotted against the compressive strain of the lattices subjected to the quasi-static and dynamic loading.

By comparing the graphs for the function of Poisson's ratio for the 2D missing-rib structure, a significant strain-rate effect arising from the differing deformation responses of the structure to the quasi-static and dynamic loading is clearly apparent. Here, the quasi-static loading resulted in an NPR only in a

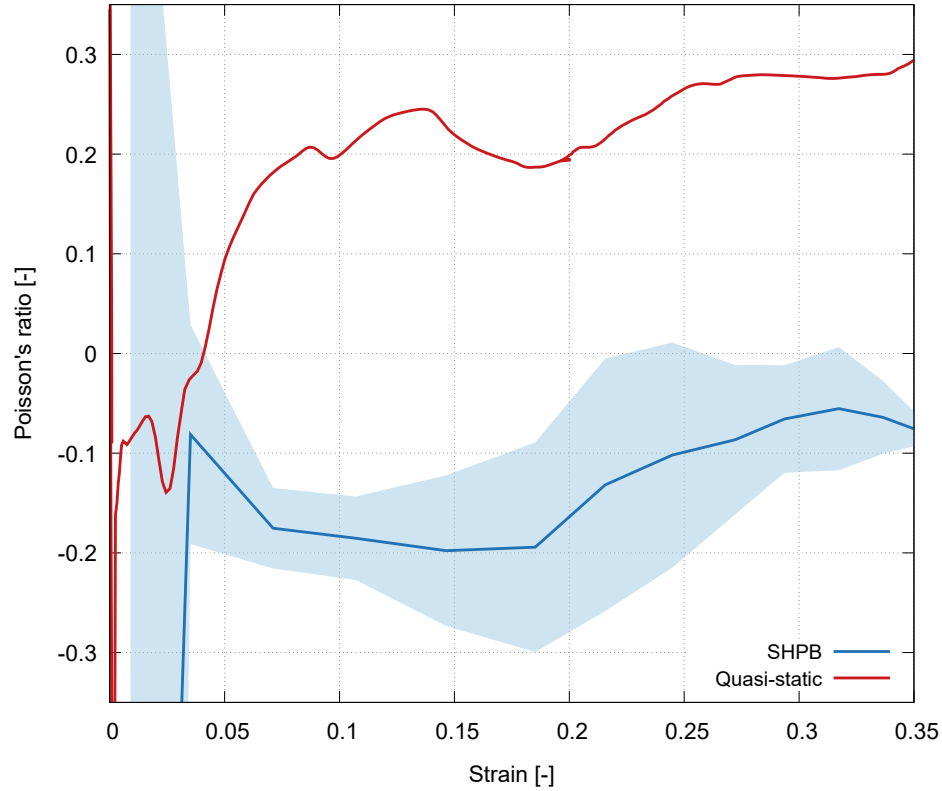


Figure 4.20: Experimental function of Poisson’s ratio - 2D missing-rib lattice composed of the 3×3 unit-cells, the dynamic and quasi-static response.

narrow deformation range up to approximately 4% of the compressive strain, while the dynamic loading of the lattice resulted in an auxetic response throughout the observed deformation range with the minimum value of Poisson’s ratio of -0.2 with the function oscillating around the value of -0.15 . The plotted interval of the standard deviation also shows a reasonable variability in the results, when a low number of unit-cells in the lattice is taken into account, as the non-auxetic behaviour can be, in the variability of results, observed only at two compressive deformation levels.

Similar trends have been revealed in the case of the strain-rate sensitivity of the 2D re-entrant honeycomb structure. Again, the quasi-static response yields an auxetic character of the lattice only in a limited range of deformation at the beginning of the experiment followed by a non-auxetic character in a wide range of deformation up to 32% of the compressive strain, where the values of Poisson’s ratio are lower than zero and remain negative up to

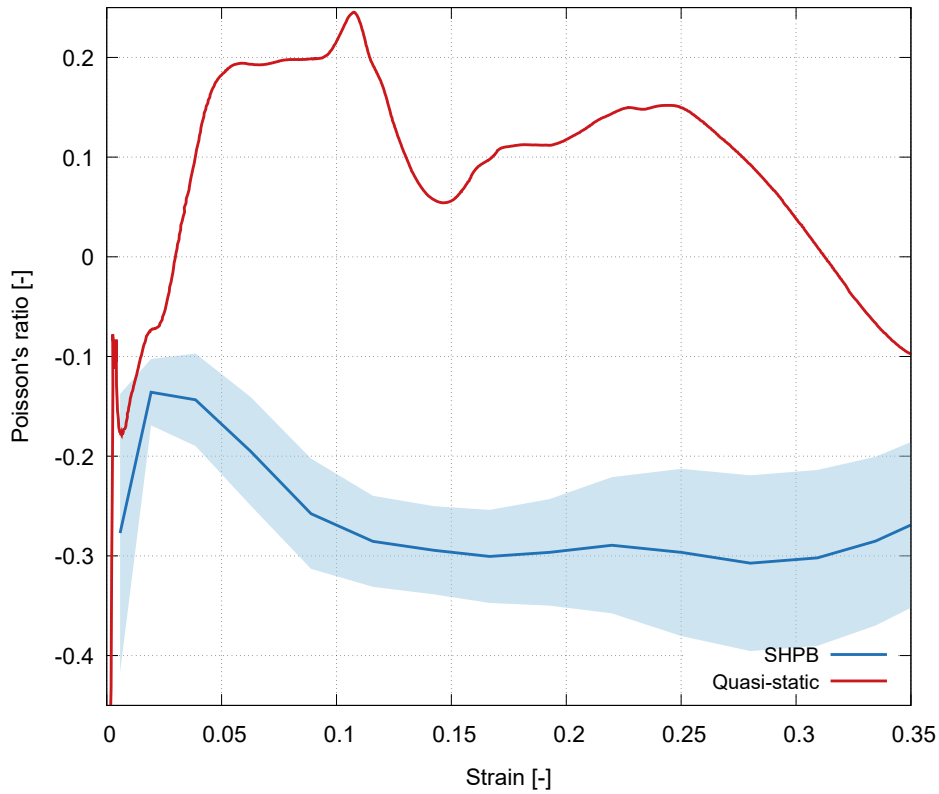


Figure 4.21: Experimental function of Poisson's ratio - 2D re-entrant honeycomb lattice composed of the 3×3 unit-cells, the dynamic and quasi-static response.

the end of the experiment. In contrast, an auxetic behaviour was identified during the dynamic compression of these specimens with the minimum value of -0.3 achieved at 0.275 of the compressive strain. The interval of the standard deviations is also narrower showing negative values in all stages of the experiments. The equivalent difference in the response of the structure to the quasi-static and dynamic loading was revealed after inspection of the high-speed camera data as the dynamic compression is purely uni-axial without any lateral movement of the individual unit-cell layers.

The 3D re-entrant honeycomb subjected to dynamic compression exhibited a consistently negative function of Poisson's ratio over the whole range of the compressive deformation. As the quasi-static response of this structure also resulted in a purely auxetic behaviour, the strain-rate dependence here pronounces the magnitude of auxetic behaviour as the dynamic Poisson's ratio reaches approximately a 45% lower value at a compressive strain of 0.2 . Due

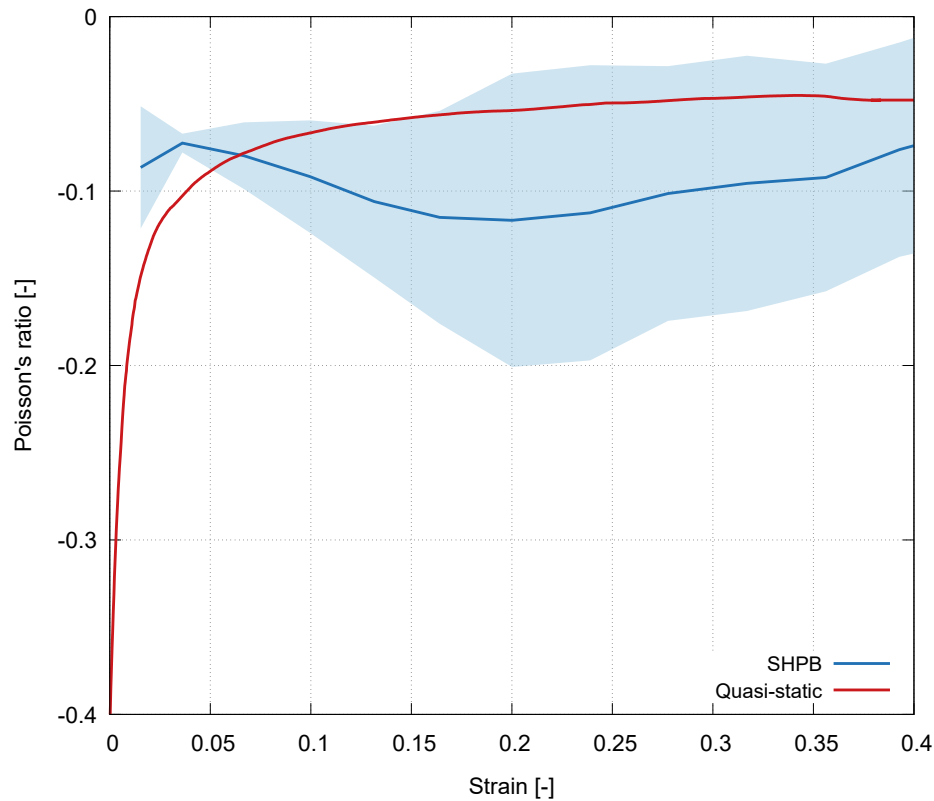


Figure 4.22: Experimental function of Poisson's ratio - 3D re-entrant honeycomb lattice composed of the 3×3 unit-cells, the dynamic and quasi-static response.

to the three-dimensional assembly of the unit-cells, where the compression causes loss of stability of the unit-cell struts in the cross-sectional plane and the bifurcation effects follow the stochastic nature of the SLS printed solids, larger standard deviations were calculated for the identified Poisson's ratio. From the plot of the comparison between the quasi-static and dynamic response, it is evident that the quasi-static function of Poisson's ratio lies within the standard deviation of the dynamic measurements.

The DIC determined functions of Poisson's ratio for the RVE sized specimens are shown in Figures 4.23 - 4.25.

The most profound strain-rate dependence was revealed in the case of the 2D missing-rib structure. At both considered strain-rates, Poisson's ratio decreased to one local and a global minimum located between 2% and 10% of the compressive strain. The global minimum was, in both cases, followed by

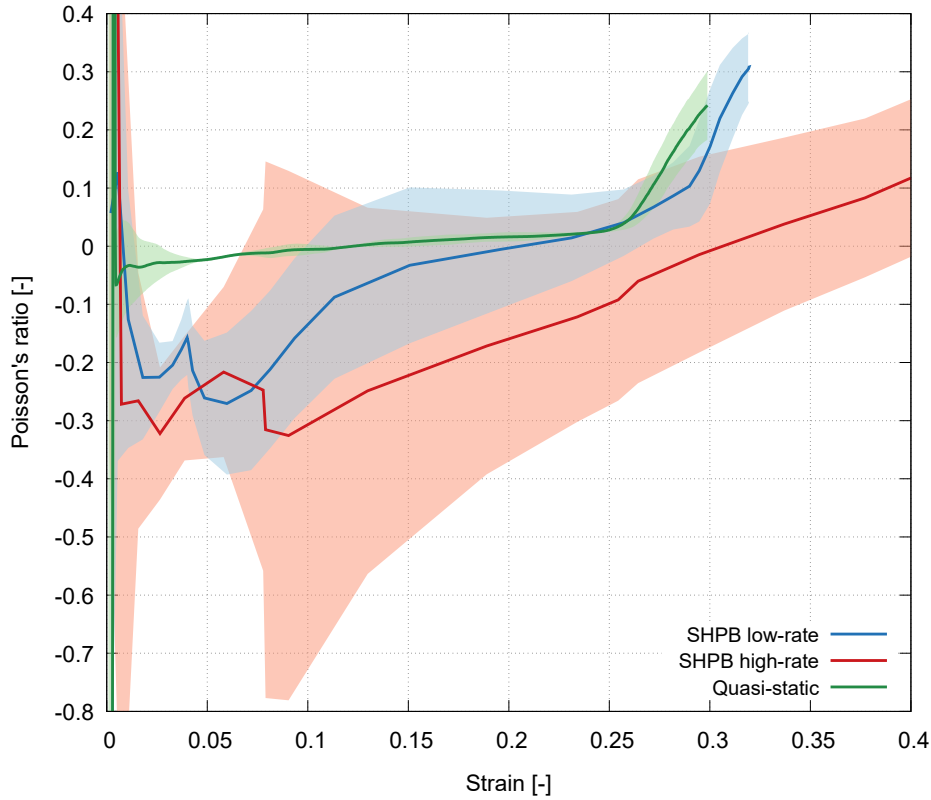


Figure 4.23: Experimental function of Poisson's ratio - 2D missing-rib lattice composed of the 6×6 unit-cells, the dynamic and quasi-static response.

a gradual increase to positive values while a zero Poisson's ratio was reached at 20% of the compressive strain in the case of the low strain-rate and 30% in the case of the high strain-rate, respectively. Both strain-rates produced insignificantly different values of the lowest achieved Poisson's ratio of -0.28 during the lower strain-rate and -0.33 during the high strain-rate experiments. Interestingly, this trend is inverse to the other dynamic experiments. A visual inspection of the deforming structures also showed that the two observable local extrema of the function of Poisson's ratio can be accounted for the initial collapse of the two layers of the microstructure. The comparison with the quasi-static curve reveals that the SHPB experiments at the lower strain-rate yield results converge to the same trend for compressive strains over 25%.

From the comparison of the strain-dependent function of Poisson's ratio of the 2D re-entrant honeycomb structure, it can be seen that the overall shape of the curve is very similar for both the considered SHPB strain-rates. Poisson's

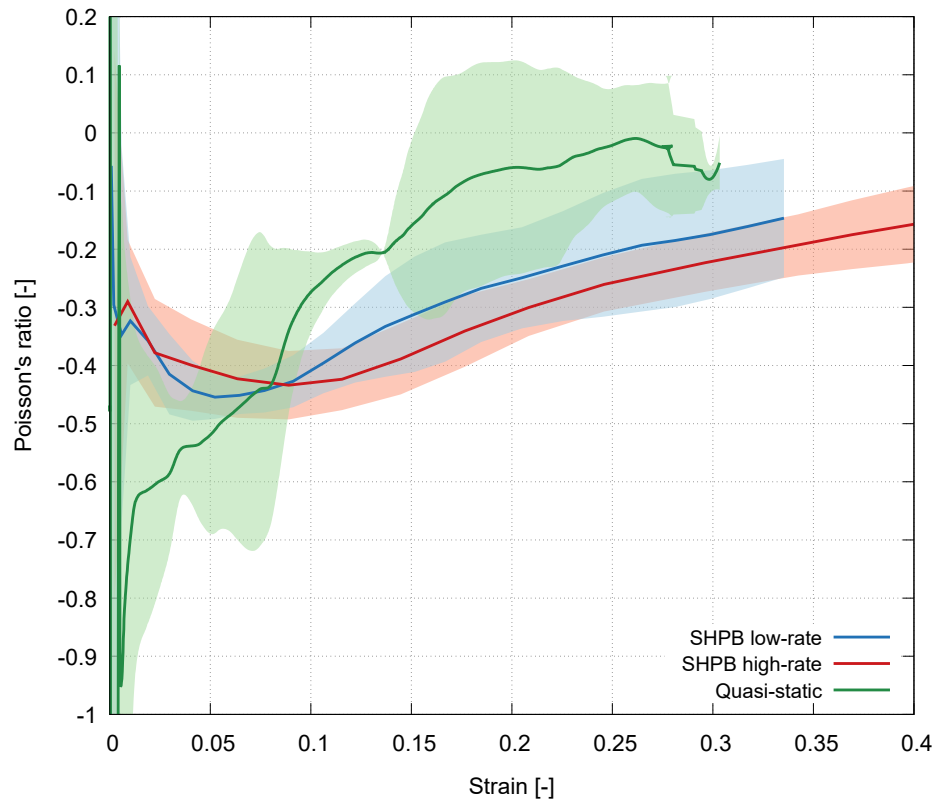


Figure 4.24: Experimental function of Poisson's ratio - 2D re-entrant honeycomb lattice composed of the 6×7 unit-cells, the dynamic and quasi-static response.

ratio reaches its global minimum in the initial stages of the deformation and then gradually increases up to positive values. The difference between the high and the low strain-rate is the magnitude of the auxetic effect. The extremum of Poisson's ratio in the case of the lower strain-rate was also reached at the lower compressive strain (5% compared to 8%). The overall trend of the dynamic response is similar to the quasi-static response at compressive strains over 10% and represented by a monotonic increase in Poisson's ratio towards positive values.

Similar to the quasi-static results, the 3D re-entrant honeycomb structures exhibited a significantly different response than the periodical assembly of the two-dimensional re-entrant honeycombs. As can be seen, the results from the dynamic testing at both strain-rates are very similar to each other and the results of the quasi-static test. During the dynamic experiments, Poisson's ratio increased from the values of approximately -0.1 at very small

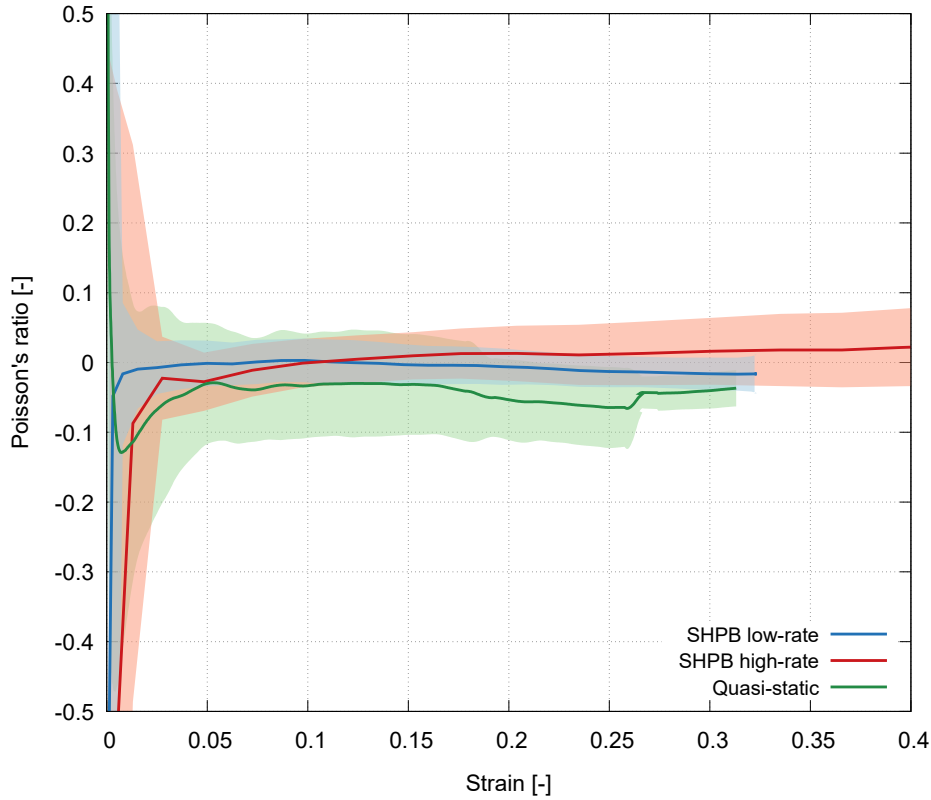


Figure 4.25: Experimental function of Poisson's ratio - 3D re-entrant honeycomb lattice composed of the 6×7 unit-cells, the dynamic and quasi-static response.

strains and then formed the plateau-like region similar to the specimens subjected to the quasi-static loading. A comparison of the low and the high strain-rate experiments shows that the values of Poisson's ratio at the plateau region increase with a higher strain-rate. At a lower strain-rate, Poisson's ratio remains constantly negative (approximately -0.02) beyond the 30% compressive strain. However, with an increase of the applied strain-rate, the plateau region reaches positive values at 10% of the compressive strain and further increases at a 40% strain.

4.4.2 Numerical results

The framework for the numerical simulations comprising the virtual SHPB device utilised for the calibration and verification measurements was used for the development of the simulations of the investigated auxetic lattices

subjected to dynamic compressive loading. The virtual experiments were, in all cases, performed with boundary and initial conditions (particularly the striker bar velocity) identical to the SHPB experiments except the use of pulse shapers in the real tests. Virtual strain-gauges were used to capture the transmission of the strain waves in the simulated bars and the same mathematical methods were used to derive the stress-strain diagrams of the investigated lattices. From the geometrical coordinates of the finite element nodes used for the discretisation of the lattices, the functions of Poisson's ratio were evaluated using the same methodology as during the experiments. Figures 4.26 and 4.27 depict the microstructure of the specimens during simulated compression using the virtual SHPB apparatus.

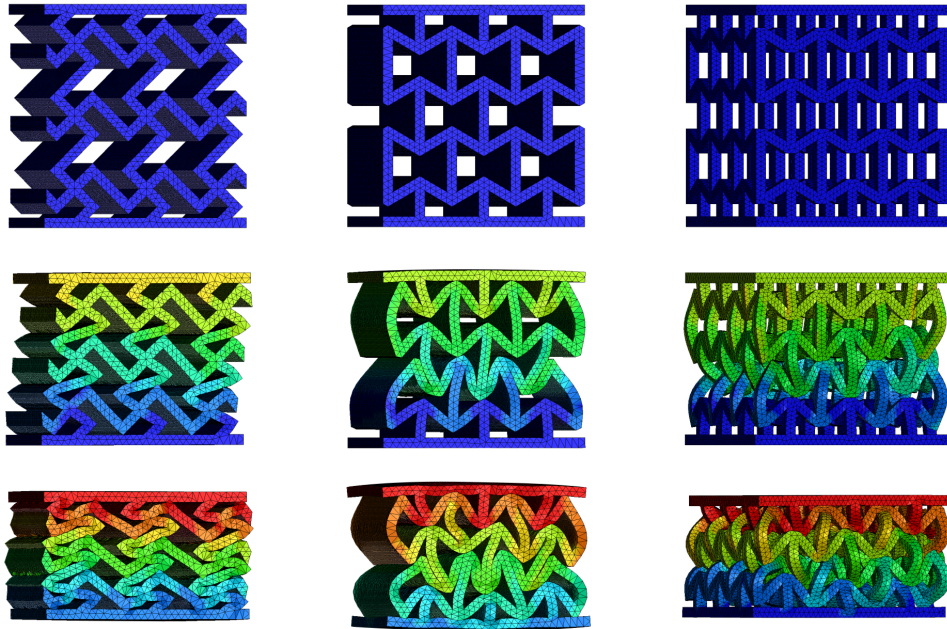


Figure 4.26: Comparison of the 3×3 samples - visualisation of the FE results using the resultant displacement showing the intact specimens (first row), the plateau stress region (middle row), and the maximum achieved compression (bottom row).

■ Stress-strain response

The numerical stress-strain diagrams of the auxetic lattices having 3×3 unit-cells subjected to dynamic loading using the virtual SHPB are depicted in Figures 4.28 - 4.30 together with the experimental quasi-static and dy-

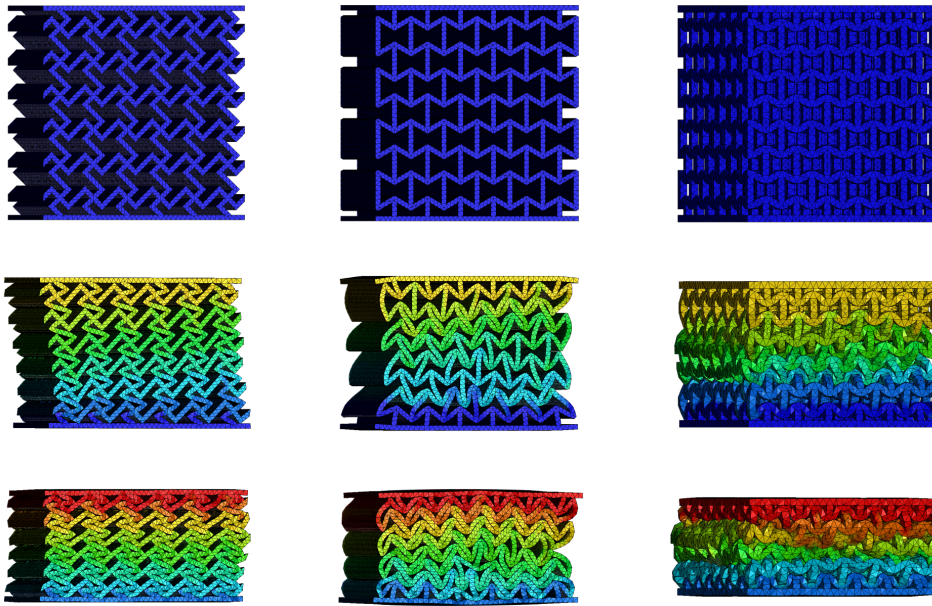


Figure 4.27: Comparison of the RVE sized samples during high strain rate loading - visualisation of the FE results using the resultant displacement showing the intact specimens (first row), the plateau stress region (middle row), and the maximum achieved compression (bottom row).

dynamic curves for the comparison of the FEA precision. Since the dynamic experiments of the 3×3 lattices were conducted with lower quality compared to the RVE sized samples, the results exhibit lower precision and repeatability, which complicated both the development and validation of the numerical simulations.

It can be seen in Figure 4.28 that the numerical model captures the measured behaviour of the sample in all parts of its deformation response. Notable differences arise from the absence of the pulse shaping measures in the simulated events apparent from the differences in the initial and terminal stages of the numerical stress-strain diagrams common to all the performed numerical simulations. In contrast to the SHPB experiments, the simulated response of the lattice yield increase in the overall stress from zero compressive strain. Then, the simulated plateau stress reaches the same value observed during the quasi-static loading of the samples and matches the SHPB experimental data at strains from 0.1. The numerically obtained densification strain and the slope of the initial part of the densification region are also both very similar. Differences can then be seen at a higher stress at the point of the

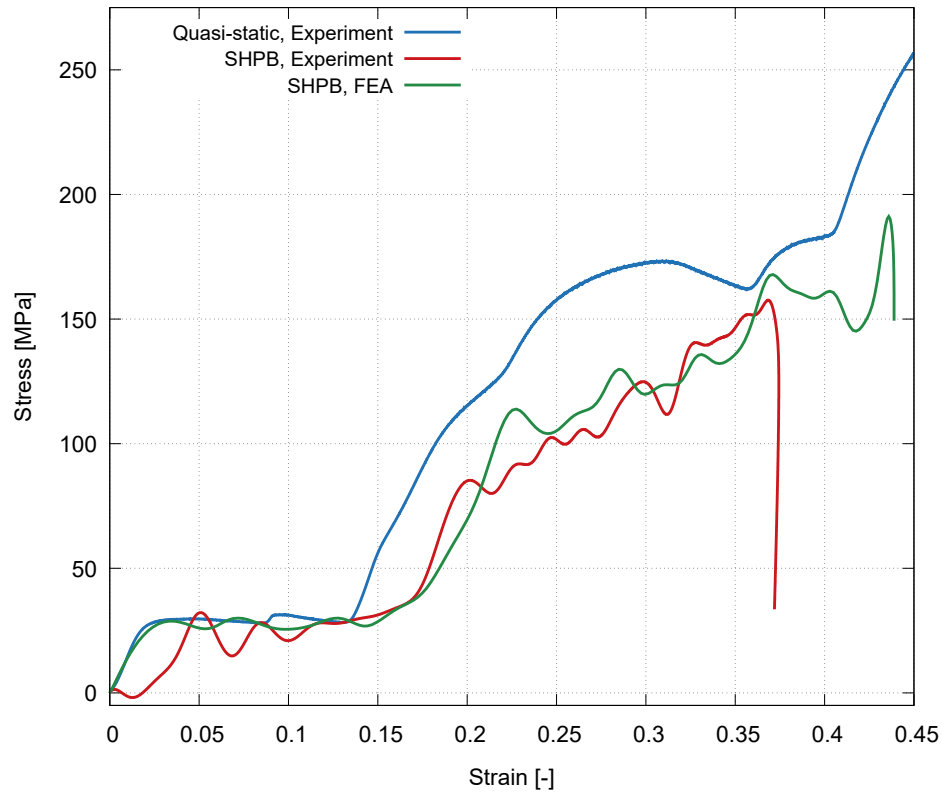


Figure 4.28: Comparison of the numerical and experimental stress-strain curves - 2D missing-rib lattice composed of the 3×3 unit-cells, dynamic and quasi-static response.

slope change in the densification region, but the subsequent numerical and experimental curves are approximately parallel. From the comparison of the terminal parts of the curves, the apparent discrepancy in the maximum achieved compression of the samples arising from the different conditions during the simulations and experiments can be seen.

From the comparison of the numerical and experimental stress-strain curves of the 2D re-entrant honeycomb shown in Figure 4.29, it can be seen that the numerical simulations also predict the strain-rate sensitivity of the lattice in terms of a stress-strain diagram. The apparent yield of the lattice predicted by the numerical simulations occurred at approximately the same stress and strain as calculated from the experiments. Then, the compression of the lattice in the simulation leads to a plateau of constant stress, whereas the SHPB experiments resulted in a gradual increase in the stress up to a

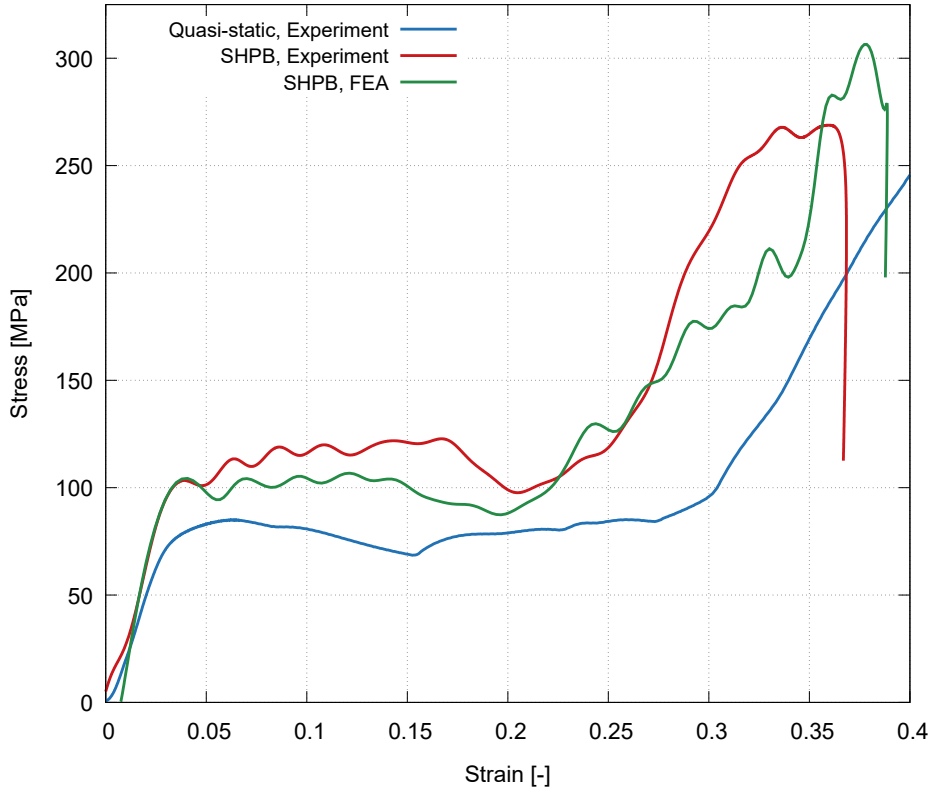


Figure 4.29: Comparison of the numerical and experimental stress-strain curves - 2D re-entrant honeycomb lattice composed of the 3×3 unit-cells, the dynamic and quasi-static response.

local maximum at a 0.175 strain followed by a drop in the stress due to the deformation response of the microstructure. This leads to an approximately 16% underestimation of the absorbed energy by the FEA. However, the local maximum followed by the decrease in the stress was numerically predicted and the point of the local minimum before the densification of the structure is also very similar in terms of both the stress and strain. In the densification region of the deformation response, the experimentally tested lattices exhibited a higher slope of the stress-strain curve, while the maximum calculated stress was 13% lower together with insignificantly lower maximum achieved compressive strain.

Better conformity between the numerical and experimental results was achieved in the case of the 3D re-entrant honeycomb structure (see Figure 4.30). Even without the pulse-shaping measures in the simulations, the

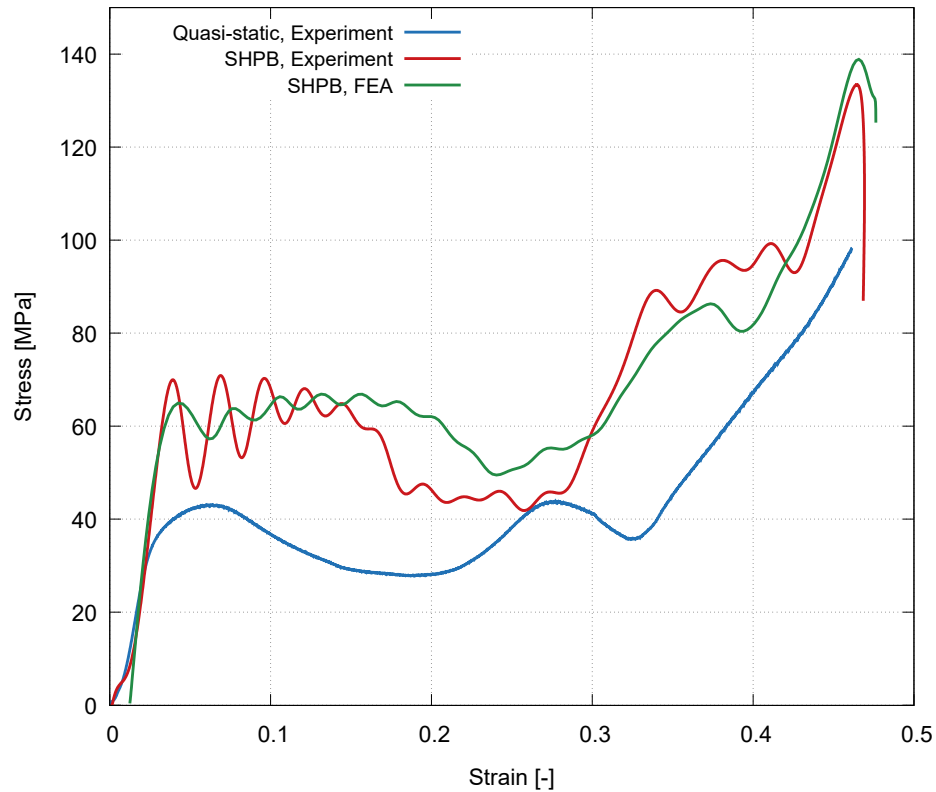


Figure 4.30: Comparison of the numerical and experimental stress-strain curves - 3D re-entrant honeycomb lattice composed of the 3×3 unit-cells, the dynamic and quasi-static response.

oscillations in the region of the yield point and the plateau region are significantly lower. The yield of the structure occurred at the same compressive strain during the simulations and the plateau stress up to 15% of the compressive strain was well captured by the FEA. Both the numerically and experimentally compressed lattices exhibit an apparent decrease in the stress before the densification of the structure, where the simulations predict approximately a 15% higher energy absorption. Nevertheless, the densification part is captured with significantly higher precision as the shape, maximum stress and maximum compressive strain are nearly identical.

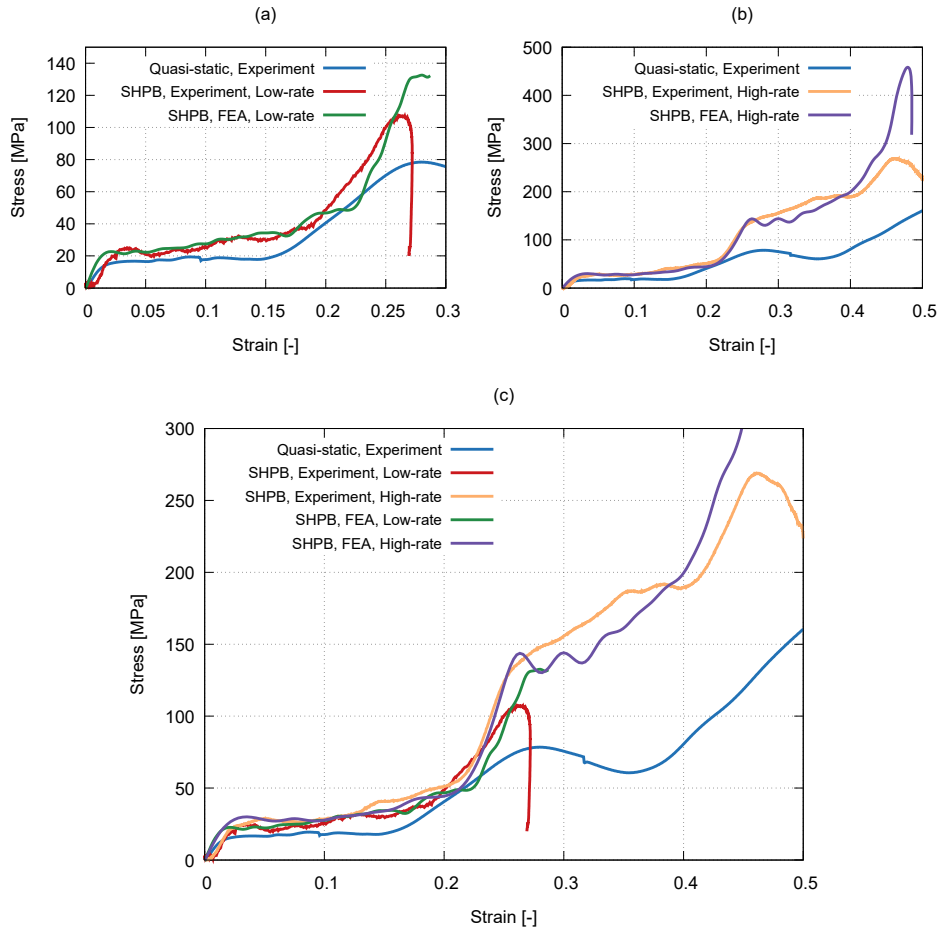


Figure 4.31: Comparison of the numerical and experimental stress-strain curves for the RVE sized 2D missing-rib lattice: (a) low strain rate, (b) high strain rate, (c) all the experiments and the FE results.

Figures 4.31 - 4.33 depict the numerical and experimental stress-strain diagrams for the auxetic lattices with the RVE number of unit-cells calculated from the dynamic loading at both strain-rates and a comparison with the quasi-static results.

In the plots of the stress-strain diagrams for the 2D missing-rib structure at the different strain-rates (Figure 4.31), the effect of the strain-rate on the stress-strain curve captured by the FEA is clearly apparent. At both strain-rates, the FE simulations showed very high precision in terms of the prediction of the yield characteristics of the lattices, the behaviour of the microstructures in the plateau region, and in the majority of the densification region. In

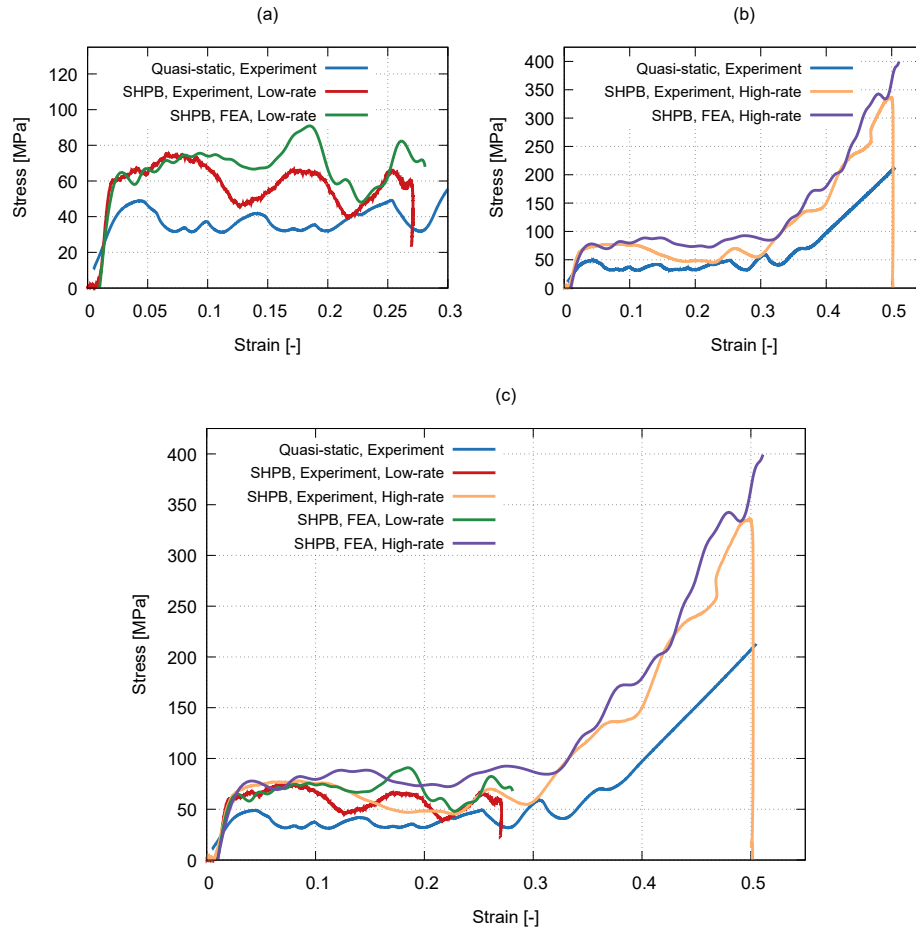


Figure 4.32: Comparison of the numerical and experimental stress-strain curves for the RVE sized 2D re-entrant honeycomb: (a) low strain rate, (b) high strain rate, (c) all the experiments and the FE results.

the case of the low-strain rate loading, the main difference is the later start in the densification occurring at a 4% higher compressive strain, while the slope of the numerical densification part is significantly higher together with the maximum calculated strain at 135 MPa compared to the experimental value of 105 MPa. Except for the delayed beginning of the densification, the simulation also yielded a higher stress level than the values from the quasi-static loading. The high-strain rate simulations resulted in the highly precise prediction of the yield point, the plateau region, and the initial part of the densification. Due to the absent pulse shaping measures and presumably due to mesh density reasons, the maximum numerical stress deviated by 60% forming a sharp peak in the stress at the end of the experiment.

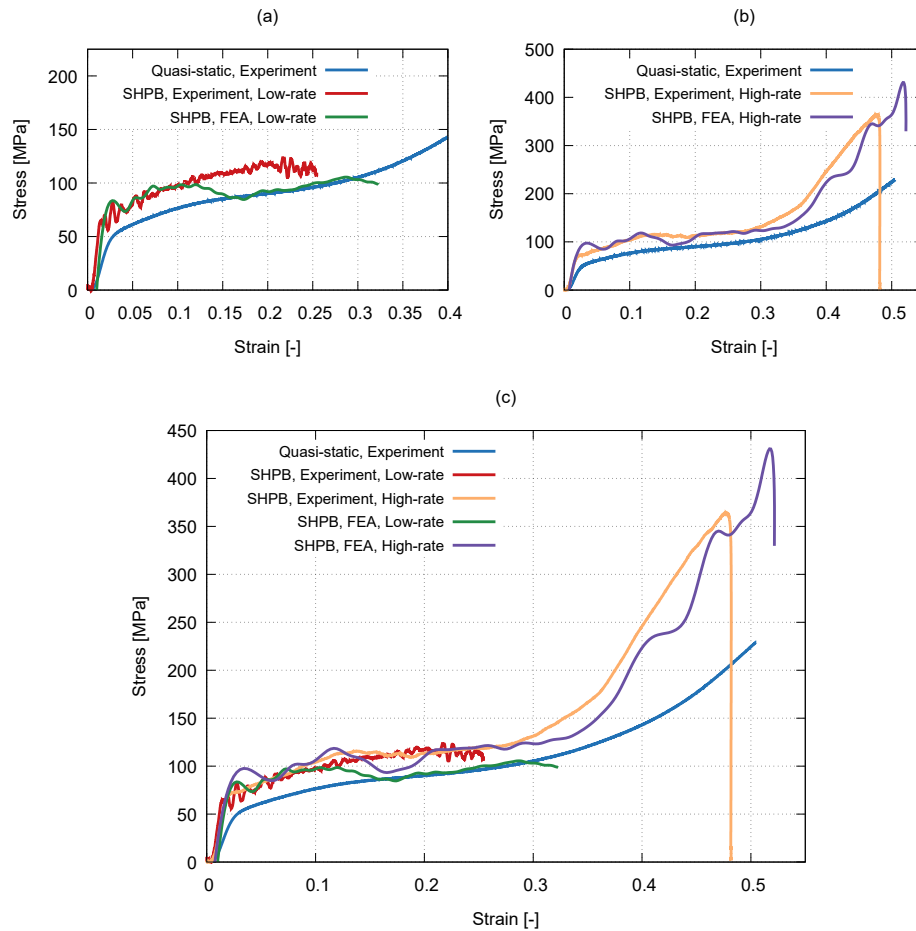


Figure 4.33: Comparison of the numerical and experimental stress-strain curves for the RVE sized 3D re-entrant honeycomb: (a) low strain rate, (b) high strain rate, (c) all the experiments and the FE results.

Strain-dependent Poisson's ratio

For every investigated microarchitecture, the evaluation of the function of Poisson's ratio based on the DIC-data postprocessing of the experimental measurements was performed. Instead of the DIC method for the analysis of the displacements and strains on the deforming lattices, the time-dependent characteristics of the FE mesh (i.e., the location of the selected nodes) were extracted from the databases and subjected to analysis. The acquired curves were compared to the experimental results to evaluate the ability of FEA to predict Poisson's ratio of the dynamically loaded auxetic lattices in question.

Figures 4.34 - 4.36 depict the numerically and experimentally assessed Poisson's ratio plotted against the compressive strain of the lattices subjected to the quasi-static and dynamic loading.

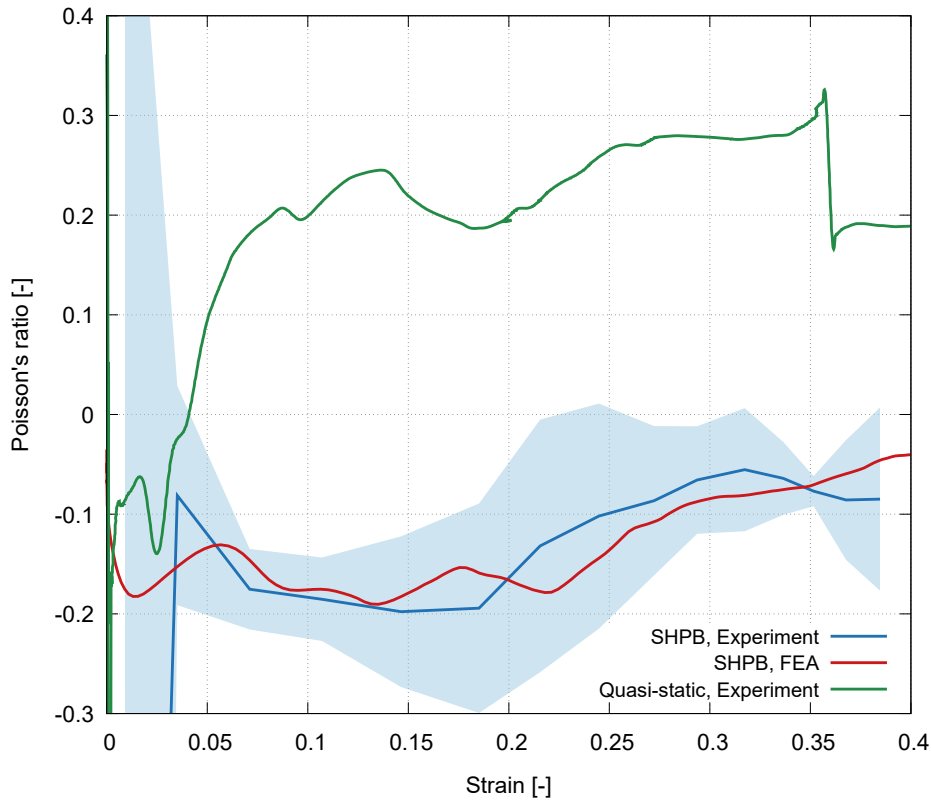


Figure 4.34: Numerical and experimental function of Poisson's ratio - 2D missing-rib lattice composed of the 3×3 unit-cells, the dynamic and quasi-static response.

Interestingly, the highest agreement between the FEA and experimentally evaluated function of Poisson's ratio was obtained for the missing-rib structure having 3×3 unit-cells in the assembly (Figure 4.34). Here, the numerical values of Poisson's ratio not only lie within the standard deviation intervals of the experimental curve, but, starting at the compressive strain of 0.05, the FEA results almost precisely follow the experimental results up to a compressive strain of 0.35.

In the case of the 2D re-entrant honeycomb (Figure 4.35), the numerical simulations predict a consistently lower Poisson's ratio throughout the deformation range used in the experiments. The values of the numerical curve

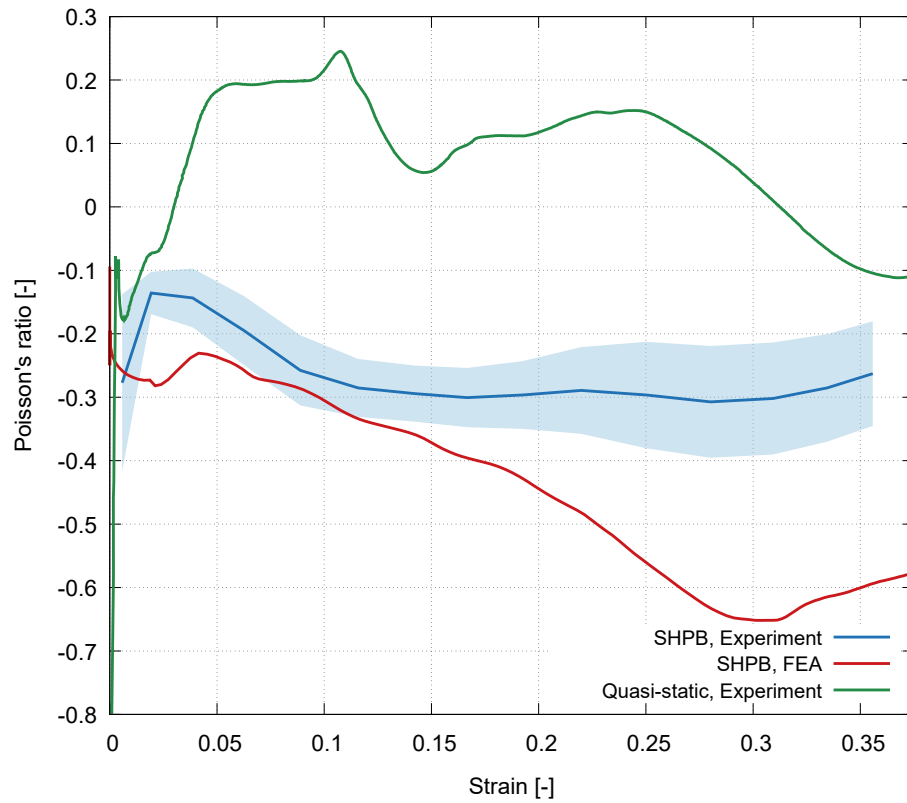


Figure 4.35: Numerical and experimental function of Poisson’s ratio - 2D re-entrant honeycomb lattice composed of the 3×3 unit-cells, the dynamic and quasi-static response.

are outside the standard deviation envelope of the SHPB experiments except for the compressive strain range of 0.05 – 0.1 reaching a global minimum of -0.65 at a 0.3 compressive strain. The discrepancy between the experimental and numerical extremum, thus, amounts to 100%. It can be seen that similarly to the experiments, the numerical Poisson’s ratio decreases up to a 0.3 compressive strain, but the slope of the curve increases between the 0.2 and 0.3 compressive strain, which does not reflect the theoretical assumptions for the response of re-entrant honeycomb auxetic lattices.

The numerical deformation response of the 3D re-entrant lattice also shows significant discrepancies between the experiments and the simulations (Figure 4.36), although in this case, the overall shape of the curves is similarly convex during the majority of the compression. The calculated minimum of Poisson’s ratio in the simulations was -0.38 , whereas the minimum value

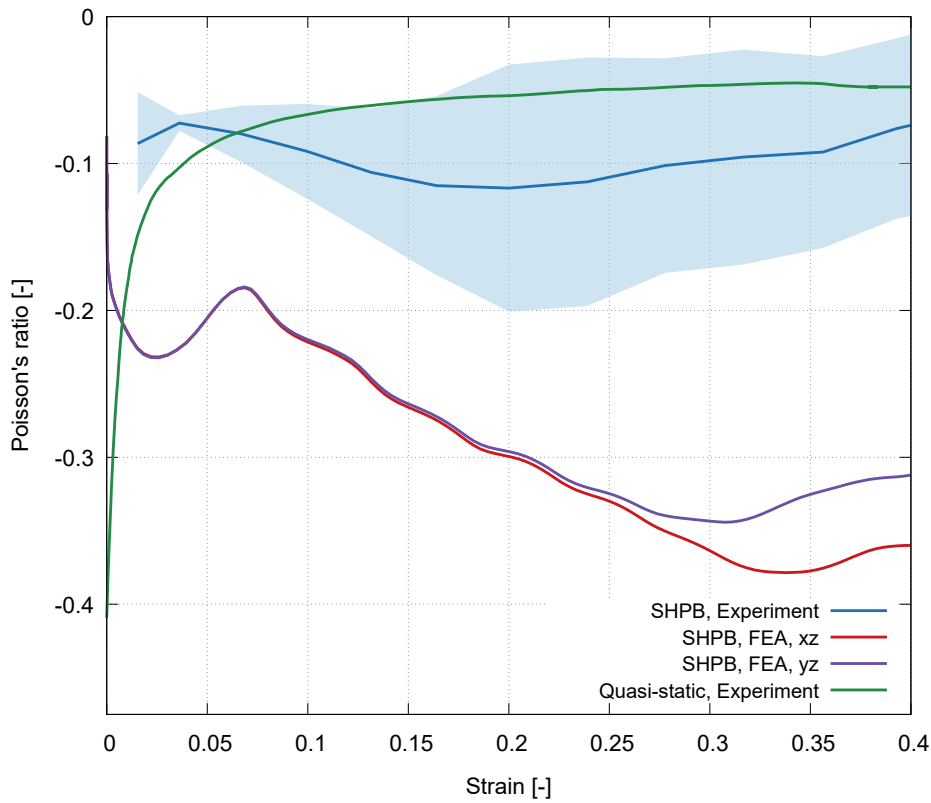


Figure 4.36: Numerical and experimental function of Poisson’s ratio - 3D re-entrant honeycomb lattice composed of the 3×3 unit-cells, the dynamic and quasi-static response.

in the simulations was -0.12 . The numerical Poisson’s ratio evaluated from the two perpendicular faces of the lattice was identical up to approximately 20% of the compressive strain. At higher strains, the face denoted yz yielded approximately 10% higher values of Poisson’s ratio. For Poisson’s ratio calculated from both the faces, a trend similar to the 2D re-entrant honeycomb consisting in the decrease of Poisson’s ratio beyond a 0.3 compressive strain can be observed, which also does not correspond to the theory of re-entrant honeycomb NPR lattices.

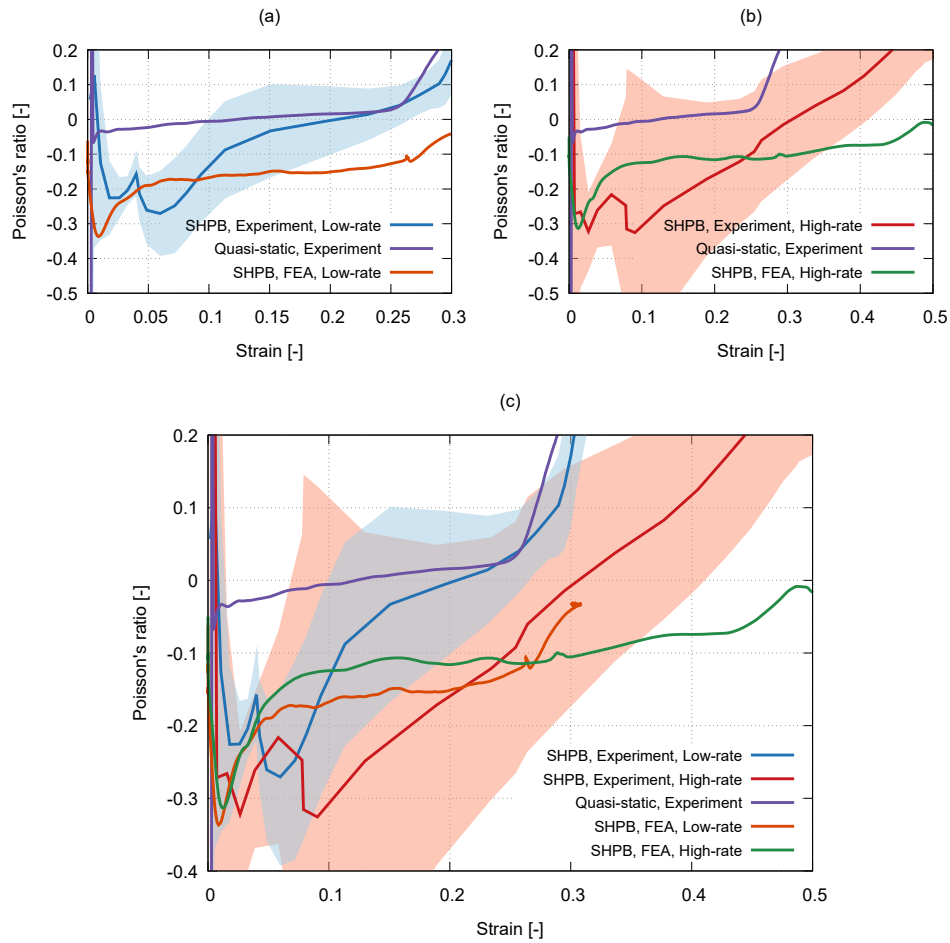


Figure 4.37: Comparison of the numerical and experimental function of Poisson's ratio for the RVE sized 2D missing-rib lattice: (a) low strain rate, (b) high strain rate, (c) all the experiments and the FE results.

The numerically and experimentally determined functions of Poisson's ratio for the RVE sized specimens are shown in Figures 4.37 - 4.39.

From the plots of the strain-dependent Poisson's ratio, it can be seen that the precision of the numerical simulation is proportional to the strain-rate in the case of the missing-rib structure (Figure 4.37). In the low strain-rate loading, the results of the numerical simulations show an increase in Poisson's ratio from -0.33 to -0.18 within 1% and 7% of the compressive strain followed by a gradual increase to -0.125 at 25% of the compressive strain, where the gradient of Poisson's ratio increases significantly. In the interval of the compressive strain between 1% and 17%, the numerical Poisson's ratio lies

within the standard deviation band of the SHPB experiments. Although the overall shape of the numerical and experimental curves is different, the two curves are approximately parallel at strains over 20%. The numerically determined Poisson's ratio at the high-strain rate then exhibits a similar shape to the low strain-rate loading, except for the gradient increase at a 25% strain that is not present at the high strain-rate loading. Unlike the SHPB data, the numerical Poisson's ratio is constant at a value of -0.15 in a wide range of deformation throughout the experiment, while the DIC determined behaviour of the samples shows an approximately linear increase in Poisson's ratio from the global minimum of -0.33 at 9% strain up to a zero value. However, the numerical simulations predict an inverse proportionality of the strain-dependent Poisson's ratio to the strain-rate than the SHPB experiments as the auxetic behaviour of the lattice was decreasing with the strain-rate. Nevertheless, it is difficult to draw conclusions on the reliability and precision of the simulations in this case as the standard deviations in the SHPB experiments were very high resulting in an overlap of the statistically evaluated Poisson's ratios at a high and low strain rate.

The simulations of the 2D re-entrant honeycomb (Figure 4.38) resulted in approximately a 75% lower predicted minimum of Poisson's ratio, while closely maintaining a similar shape during the whole range of deformation. The comparison of the low-strain rate experiments and the simulations shows, besides the different absolute values, that the global minimum of Poisson's ratio was obtained at a 0.025 strain in the simulations and 0.05 in the experiments. On the contrary, the high strain-rate loading yields the global minimum identically at a 0.05 strain. Interestingly, the strain-rate effect during the SHPB experiments showed a higher Poisson's ratio at a higher strain-rate up to a 0.08 strain and the inverse behaviour at higher strains, which was also captured in the numerical simulations including the compressive strain of the intersection point between the curves of the two strain-rates.

The numerical Poisson's ratio was, in the case of the 3D re-entrant honeycomb lattice, evaluated from two perpendicular faces (Figure 4.39), while only one direction was observed by the high-speed camera during the SHPB experiments and thus subjected to the DIC-based analysis. From the experimental curves, it can be seen that the strain-rate dependence of this lattice

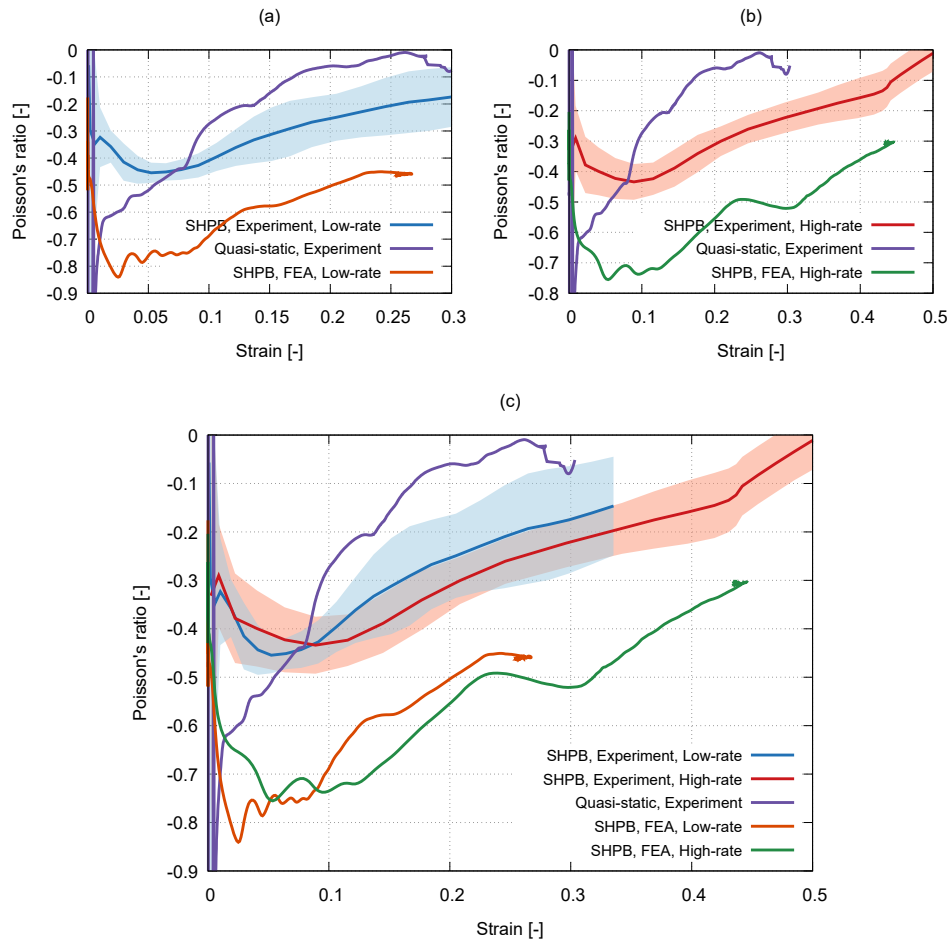


Figure 4.38: Comparison of the numerical and experimental function of Poisson's ratio for the RVE sized 2D re-entrant honeycomb: (a) low strain rate, (b) high strain rate, (c) all the experiments and the FE results.

is represented by an inverse proportionality as the magnitude of the auxetic behaviour decreases with the considered strain-rate towards positive Poisson's ratio and closely resembles a compressive response typical for closed-cell metal foams. In the numerical simulations at both strain-rates, interesting results were acquired in terms of the difference in Poisson's ratio derived from the two perpendicular faces. It can be seen that the results calculated from the face denoted yz are both within the standard deviation interval of the SHPB experiments although the predicted strain-rate effect is negligible. Simultaneously, Poisson's ratio calculated from faces denoted xz predict the same strain-rate dependence as evaluated from the SHPB experiments, but the auxetic behaviour increases with the compressive strain and the curves

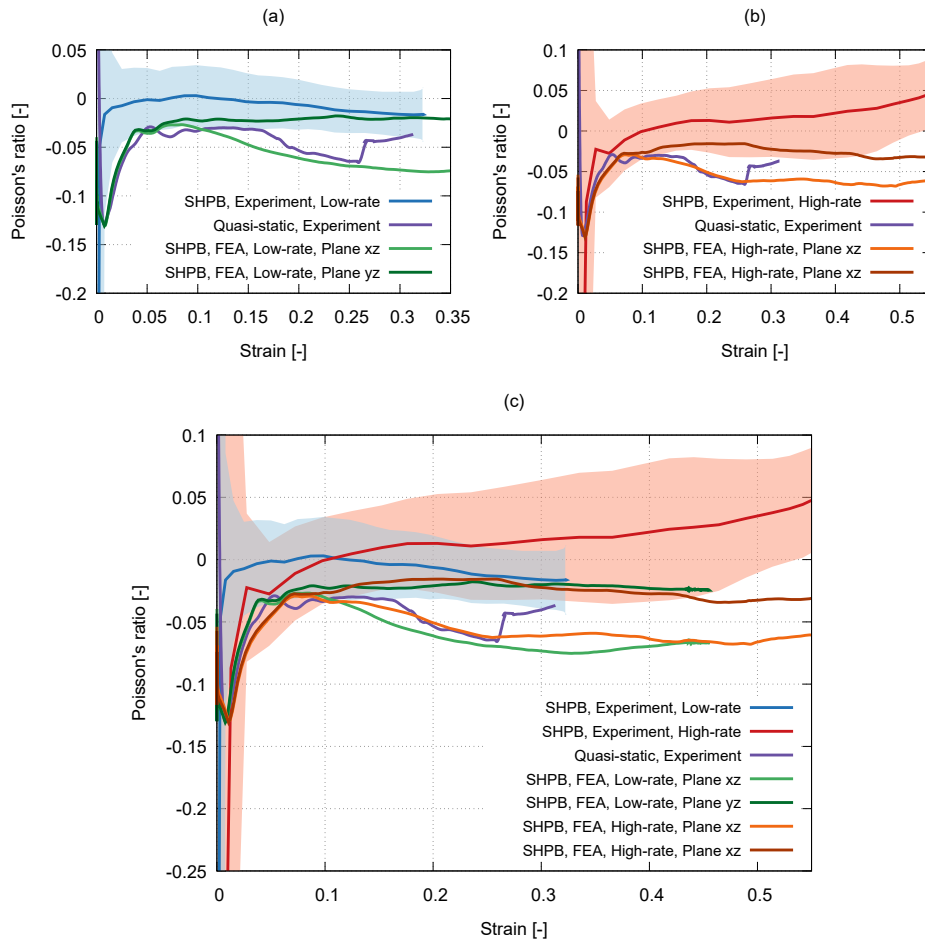


Figure 4.39: Comparison of the numerical and experimental function of Poisson's ratio for the RVE sized 3D re-entrant honeycomb: (a) low strain rate, (b) high strain rate, (c) all the experiments and the FE results.

lie outside the standard deviations of the experiments at a strain higher than 0.1.

4.5 Discussion

Experimental part

The employed SHPB experimental setup and its instrumentation were suitable for the measurement of the SLS printed auxetic structures with a different number of unit-cells in the lattice under all strain rates. The setup calibration, pulse shaping techniques, and data correction methods were used for the evaluation of the dynamic material characteristics. Dynamic equilibrium was achieved shortly after the arrival of the incident wave to the impact face of the specimen. The evaluated stress-strain curves were valid and were successfully used for the analysis of the effect of the number of unit-cells in the structure and strain-rate on the stress-strain response of the structures and the function of Poisson's ratio. Furthermore, the results of the SHPB experiments were used for the calibration and verification of the FE simulations.

The identified strain rate sensitivity of the sintered structures was comparable to the results summarised in the literature, where additively manufactured bulk specimens from sintered material were studied using SHPB [152, 153]. The quasi-static compression tests showed a similar deformation behaviour of the auxetic lattices, as can be seen in the quasi-static compression study concerning sintered metallic re-entrant lattices of a similar geometry. Significant buckling effects and a loss of stability of single layers in quasi-static compression were observed during the loading of all the investigated lattices resulting in significant lateral displacements affecting the calculated Poisson's ratio. These effects were reduced significantly in dynamic compression in SHPB, where the lateral distortion was minimised and the structures exhibited a homogeneous deformation. The densification of the structures occurred at lower strains in dynamic compression as well.

DIC was successfully used for the evaluation of the displacement and strain fields to be used as a basis for the calculation of the function of Poisson's ratio. The important finding is that the auxetic behaviour of the structures under quasi-static loading is not very strong, but it is very profound under dynamic

loading. From the DIC, it was found out that the nearly homogeneous compression in the loading direction was maintained for all the samples. For all the experiments, it was possible to compute the strain fields from the recorded images and derive the function of Poisson's ratio for a compressive strain of at least 30 %. For comparison purposes between the studied lattices, a relatively simple procedure based on the described two-stage DIC algorithm with sub-pixel precision for the evaluation of the displacement was used. Since the strain values in the longitudinal and lateral directions are used to mutually compare the behaviour of the structures and compare Poisson's ratio of the studied lattices, the simplified procedure enables an easy comparison. Improvement of the evaluation of the displacement and strain fields of such experiments using DIC would require taking the incremental strain theory into account or perform a global DIC procedure, where adjusting the shape-function-controlling parameters during minimisation routines affects the displacement field globally. It would be necessary to account for additional effects, e.g., out-of-plane deformation, Lagrangian mesh tracking to follow the strain localisation, and checking for a distorted mesh occurrence. To take these effects into account, it would be necessary to use a two-camera system with a higher frame-rate at a higher resolution together with the appropriate DIC and post-processing algorithms.

■ **Poisson's ratio**

The missing-rib microstructure exhibited NPR behaviour in all the dynamic loading cases. Due to the chiral nature of the unit-cells and the lateral movements of all the layers during the compression, the standard deviations of Poisson's ratio curves in the dynamic compression were higher than in the experiments of the other structures. Nevertheless, the missing-rib structure exhibited a proportional strain-rate sensitivity of the function of Poisson's ratio to the strain rate. With an increasing strain-rate, the structure also exhibited an auxetic behaviour up to higher compressive strains. The 2D re-entrant honeycomb auxetic structure exhibited an NPR response under all dynamic loading conditions and a strain-rate sensitivity of Poisson's ratio. In the dynamic compression of the RVE sized lattices, the global minimum Poisson's ratio did not reach the magnitude observed in the quasi-static

compression, but the microstructure remained auxetic up to significantly higher compressive strains. The 3D re-entrant honeycomb auxetic structure exhibited an NPR effect also in the quasi-static loading of the 3×3 lattice. During the dynamic loading scenarios, the structure exhibited a Poisson's ratio close to zero and the magnitude of the auxetic behaviour was inversely proportional to the strain rate as the higher strain rate loading resulted in approximately a zero average Poisson's ratio. It was not possible to clearly identify the strain-rate sensitivity of the structure due to the high standard deviations of the evaluated Poisson's ratio curves in all the loading cases. The results correspond to the behaviour observed during the visual inspection of the experiments. Such an architecture exhibits not only the highest porosity, but the assembly is based on slender individual struts prone to a loss of stability and with a significantly lower loading capacity than in the case of the structural elements of the other analysed microarchitectures. As a result, the compressive response of such a structure is very similar to the compression of an open-cell or a closed-cell metal foam. In the experiments with the 2D missing-rib structure and the 2D re-entrant honeycomb, Poisson's ratio did not adhere to the theoretical assumptions concerning these lattices as the minimum of Poisson's ratio at very small strains was not followed by its gradual increase towards zero or positive values. This behaviour can be, however, attributed to the low quality of the SLS printing (see Discussion - X-ray micro-CT inspection), which may have substantially changed the deformation response of the lattices.

■ Strain-rate dependence

The discussed effects of the strain-rate on the observed deformation properties are caused by non-linearities at several levels of the hierarchical structure of the material, i.e., from the strain-rate dependence of the printed steel on a microscale to the micro-inertia effects and shock wave propagation on a macroscale. As a result, the mode of deformation of the individual struts and their joints varies in quasi-static and dynamic loading regime. For example, it can be seen in the quasi-static experiments that every layer of the unit-cells moves laterally after its collapse leading to a very high lateral difference in the final position of the lowest and the highest layers. In the dynamic experiments,

however, the mentioned effects are not as significant and exhibit a more uniaxial response of the microstructure, where the pronounced Poisson's ratio effects cause a more uniform compression. As the boundary conditions can be different during the quasi-static experiments and dynamic compression using Hopkinson bar, which can affect the measured data, all the contact faces of the specimens as well as the faces of the loading devices in the contact with the specimens were precisely polished and lubricated with a small amount of grease. Thus, the boundary conditions of the experiments were very similar. Moreover, the bending of the incident and transmission bars (the off axis-movement that can negatively affect the results) was investigated by a high-speed camera. No significant bending of the bars was observed during the impact up to the densification of all types of structures. Considering this analysis, it can be concluded that any changes in the deformation behaviour can be addressed solely with the strain-rate. Friction and shock effects on the specimen's boundaries during the dynamic experiments can be considered consistent and are therefore a part of the specimen's response to the impact loading. The design of the specimen is a trade-off between the specimen's suitability for the high strain-rate dynamic measurements, the actual limits of the manufacturing technology (resolution, printing technique, mechanical properties of the printed specimen), and the representative volume element of the cellular structure. Moreover, a valid SHPB experiment has to be conducted in dynamic equilibrium and attention has to be paid to the friction and inertia effects. The mechanical impedance of the specimen and the wave propagation phenomena are key factors for the relevant results of the test. Thus, the dimensions of the specimens were selected to minimise the friction and inertia effects. Also, the specimen was equipped with the necessary supporting platens on the contact faces to provide good contact with the propagating stress wave on the contact faces. Otherwise, the ramp-in effect of the propagating stress wave would cause a non-ideal contact of the bar with the specimen's struts resulting in the limited wave transfer, long times to reach the dynamic equilibrium, very non-uniform wave propagation through the specimen, or even the sudden collapse of the struts during the initial ramp-in phase. On the other hand, the supporting platens change the boundary conditions of the neighbouring cells [154]. Using the selected geometry of the specimens with the RVE number of unit-cells, it was possible to have at least 3×3 unit-cells in the core surrounded by the other cells. The core of the specimen was of main interest as the behaviour in this region should be

the most representative for the investigated structures. It can be concluded, that the specimens exhibit stress concentrations in the central part (the core of the specimen) and the resulting properties of the auxetic structure itself would be dependent on the array configuration.

■ Numerical part

Finite element simulations of the auxetic lattices subjected to dynamic compression using the virtual SHPB apparatus were developed to create a framework for the prediction of their mechanical and microstructural characteristics, as well as the estimation of the parameters of the SHPB experiments. Here, the experimental results obtained during the dynamic compression of the lattices were used as a basis for the calibration and verification of the numerical simulations. During the development of the simulation framework, sensitivity studies covering several aspects of the FEA were performed to find an optimal, computationally feasible approach for the accurate and reliable numerical estimation of the compressive characteristics of the considered auxetic lattices. The parameters identified in the sensitivity studies were used in the parametric simulations for optimisation of the material model for the SLS printed auxetic lattices by comparing the numerically and experimentally obtained strain histories captured at the incident and transmission bar. The strain versus time data captured at the virtual incident and transmission strain-gauges were then subjected to the same SHPB evaluation methods used in the experiments. For all the considered auxetic lattices and initial conditions, generally, a very good agreement between the experimental and numerical results was found in terms of the apparent yield strength, the plateau region behaviour, and the densification stage of the deformation response. Since the numerical pulse shaping measures were omitted in the simulations due to the additional complexity of the task, the differences of the FEA from the experimental results, the achieved compressive strain and the maximum stress, are primarily a result of the different slope of the strain waves and the resulting development of the strain-rate in the specimen.

By having full access to the location of the FE mesh features in the numerical simulations, the nodes in the locations consistent with the markers generated

in the DIC evaluation of the experiments were used to derive the numerical strain-dependent Poisson's ratio. A significantly lower agreement between the numerical and experimental results was observed particularly in case of the structures having 3×3 unit-cells in the lattice. Here, the problem consists of a combination of several factors influencing the tested and simulated mechanical response of the lattices including insufficient number of unit-cells with respect to the RVE dimensions. This fact, in connection with the generally poor quality of the SLS printing resulting in the localised porosity and anisotropic geometrical changes due to the heat dissipation, which renders the evaluation of FEA precision and reliability particularly difficult. A further factor that has to be taken into account is the sub-RVE size of the lattices. This is one probable factor causing the non-physical strain-dependent behaviour of Poisson's ratio, where the asymptotic decrease towards zero or positive values was not achieved in the case of both the 2D and 3D re-entrant lattices. Furthermore, the Poisson's ratio was evaluated from nodal displacements of the joints of only one row of unit-cells that were, moreover, located near the faces of the lattice. Thus, the both the microstructural and numerical size effect influence the reliability of the simulations in this case. In contrast, the simulations of the RVE sized lattices showed better accuracy, as the numerical and experimental trends were similar and, in certain cases, such as the 3D re-entrant honeycomb, the numerical curves were within the standard deviation bands of the experimental results. Furthermore, an interesting phenomenon was observed in the case of the RVE sized 3D re-entrant honeycomb, where Poisson's ratio calculated from one side of the specimen was almost precisely corresponding to the experimental results, while the perpendicular face showed a different behaviour. This leads to the conclusion that the accuracy of the FEA can not be evaluated without the use of the DIC on both the perpendicular faces of experimentally tested specimens, or using an additional set of experiments with the other face observed by a high-speed camera. Moreover, non-linear out of plane displacements have been observed in the numerical simulations, which is a phenomenon requiring a 3D DIC algorithm being implemented in the experimental evaluation procedures.

■ FEA calibration

Based on the results of the sensitivity studies, it is important to primarily discuss the mesh density and material model selection problems. Even without considering the constitutive material of the SLS printed lattices, the most important problems in the calibration of the FE simulations arise from the multi-variable nature of the investigated compressive response, where it is not possible to isolate and calibrate the individual parameters. Moreover, it is difficult to define the objective function for the calibration procedures, and in this work, the qualitative evaluation of the transmission waves was used as a most suitable approach. When computational costs are also taken into account, the follow-on analyses including additional sensitivity studies will be performed on a supercomputer instead of the high-performance workstation, which will also be necessary for simulations of the RVE sized lattices with a higher mesh density.

For the representation of the SLS printed powdered austenitic stainless steel, the relatively simple MAT 12 isotropic elastic-plastic material model was used. It is a common practice in the explicit dynamic simulations of metals that particularly a certain formulation of the Johnson-Cook material model for the simulation of events comprising temperature-sensitive plasticity, where the strain rates vary over a large range and adiabatic temperature increases due to plastic work-induced heating cause material softening. Here, the complete formulation of MAT 15, or the simplified formulation of MAT 98 can be selected in the LS-DYNA database. The simplification of MAT 98 model is due to the ignored thermal effects (and damage) so that the maximum stress is directly limited since the thermal softening, which is very significant in reducing the yield stress under adiabatic loading, is not available. To compensate for the lack of thermal softening, limiting stress values are used to keep the stresses within reasonable limits and the linear bulk modulus is used to determine the pressure in the elements. Regarding the computational costs, MAT 15 also requires an equation of state and MAT 98 is comparatively 50 % less computationally intensive due to the simplifications related to the thermal softening and damage. By analysing the material model database, other suitable material models can be selected, for instance, MAT 19 strain-rate dependent plasticity or MAT 24 piecewise linear plasticity. However, the

same disadvantages apply for all four constitutive material models regarding the ability of the experimental calibration because of the available methods and instrumentation.

■ Influence of AM quality

In the author's experience, the actual properties of the SLS printed constructs unfortunately strongly depends on the know-how of every supplier, i.e., the resulting microstructural and macroscopic characteristics are always unique to a certain extent and may also vary from batch to batch of the specimens. This is given by the fact that the printing procedure is defined by hundreds of individual arbitrary parameters, where the values almost entirely depend on the operator's experience. This is comprised of several aspects including the rotation of the printed specimen with respect to the bedplate, where it is necessary to define supporting pillars in the reference geometric models to guarantee the stability of the porous construct and proper heat dissipation during printing. The pillars have to be carefully removed by machining after the printing though, because fragments or damage to the construct may have a significant influence on the dynamic properties. Simultaneously, the printing has to produce a homogeneous material at the grain-size level, ideally without voids. It has been shown here that the SLS/SLM AM process induces many imperfections influencing the mechanical properties, such as porosity, cracks, or entrapped gas bubbles as reported in, e.g., [155] for Ti-6Al-4V and [150] for the 316L stainless steel considered in this work. The greatest influence is from the pores or regions of non-processed powder, which primarily form between layers. Many other processes are influencing the quality of the result, such as the thermal/fluid aspects inherent to SLS which are essential for optimizing the printing process and ensuring defect-free, high-quality results. The inherent attribute of the SLS/SLM relevant to this work leading to the degradation of the specimen quality is the porosity. Pores inside the SLM parts drastically influence the deformation behaviour and, therefore, reducing the porosity produced by SLS/SLM and research on the windows of the parameters required to produce high-density parts is essential [151]. Some analyses were performed using purposely produced SLS samples made from a Ti-6Al-4V powder with defects by varying the process parameters from the

factory default settings (see, e.g., [156]). It was concluded that the energy characteristics have a significant effect on defect generation and high energy density causes over-melting of the powder bed leading to a significant defect generation.

■ X-ray micro-CT inspection

As a result, to get, at least, rudimentary information about the investigated constructs, the samples with the RVE number of unit-cells were subjected to metrology and X-ray microtomographic measurements. From the geometrical characterisation, it was surprisingly found out that the strut thickness in the lattices may vary up to 30 % from the prescribed dimensions, but more importantly, the overall dimensions of the constructs were shrunk in all three spatial directions by approximately 10 %. For this reason, the corresponding geometrical models of the constructs had to be reversely engineered according to the actual dimensions of the samples. Despite the strong photon scattering in the reconstructed 3D images of the constructs, caused by the high atomic number of the Ferrum element in the alloy not compensated by sufficient filtering, voids stochastically distributed in the printed solid were identified, while certain inclusions had an effective diameter as high as half of the strut thickness. Figure 4.40 shows slices in the reconstructed volume of the tomographically scanned sample having the 3D re-entrant geometry printed using SLS.

It can be seen, despite the strong beam hardening and photon scatter artefacts, that the printed geometry conforms reasonably to the prescribed model in one plane (upper part of Figure 4.40) except for the surface of the struts on one side (see the middle part of Figure 4.40 and compare with the position of the slice in the bottom part of the same Figure). Here, the SLS printing procedure resulted in a large amount of improperly sintered material, which significantly changed the cross-sectional characteristics of the struts. The lower part of Figure 4.40 also shows a typical region with increasing occurrence of voids in the struts together with the apparent bent-shape of the struts or noncompliance of the printed lattice with the prescribed vertical orientation of struts. Assuming these facts, the material of the construct can be considered

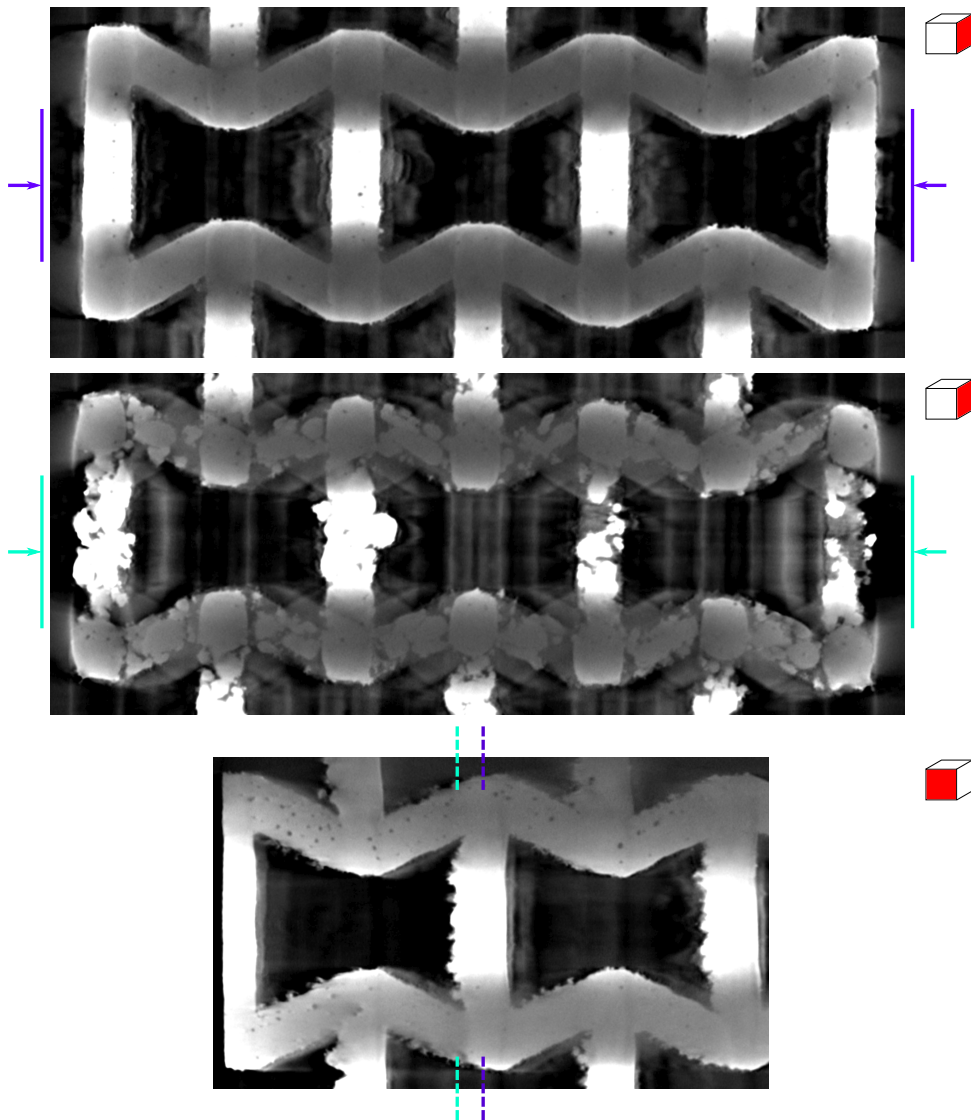


Figure 4.40: Slices in the reconstructed 3D image of the SLS printed 3D re-entrant lattice: front view in the axis of symmetry of the struts (top), front view showing the unsintered surface of the struts (middle), and side view showing the porosity within the struts (bottom).

a porous solid with at least an orthotropic nature rather than a homogeneous isotropic metal. All these factors lead to the motivation to use the simple MAT 12 elastic-plastic material model as it is not possible to reasonably substantiate the use of the Johnson-Cook constants from the literature due to the uniqueness of the printing procedure. The MAT 19 material model requires a definition of yield stress, Young's modulus, and tangential modulus as a function of the strain rate. Similarly, the MAT 24 material model requires

data for the effective stress versus the effective plastic strain for the given strain rate range and strain rate scaling effect on the yield stress together with the strain rate parameters for the constitutive equations. The microstructural characterisation together with the dynamic testing showed that the behaviour of the SLS printed bulk samples represents the characteristics of the specimens only to a limited extent due to differences in the orientation during printing and the different size of the struts in the auxetic lattices. For this reason, the MAT 12 material model was selected as it enables the easy calibration, computational efficiency, and numerical stability. The follow on parametric studies utilizing the supercomputer capabilities will be then concentrated not only on the mesh properties, but also on the alternative constitutive material model selection including the stress hardening properties, thermal softening and possible orthotropy [157], which is currently followed direction of the research.

■ Temperature dependent properties

An experimental investigation into the thermal effects during the SHPB compression of the investigated RVE sized samples has been performed. It is commonly published (see, e.g., [158]) that the strength of the 316L steel decreases rapidly over 400 °C, while the tensile strength and elongation at break remain approximately constant up to 100 °C. For this reason, high-speed thermography during the SHPB testing of the 2D re-entrant auxetic lattices has been performed to evaluate the maximum temperature of the struts in the central part of the lattices, when subjected to loading at two different strain-rates [13]. The same SHPB setup utilised in this work was used also in the thermal experiments, albeit with updated optical instrumentation composed of two high-speed Fastcam SA-Z (Photron, Japan) cameras and two high-performance MULTILED QT (GS Vitec, Germany) LED light sources for the lighting of the scene. One camera was used to record the in-plane auxetic deformation of the specimen at a resolution of 256×168 px and approximately 252 kfps. Images of this camera were used for the DIC analysis to calculate the displacement and strain fields. A speckle pattern was applied on both ends of bars for the DIC of their movement during the experiment. The second camera provided a general overview of the experiment and served

as a means for the inspection of the behaviour of the experimental apparatus at the moment of impact. Its resolution was set to 512×424 px resulting in 80 kfps. Simultaneously, the impacts were observed by the thermal imaging camera to evaluate the thermal effects induced by the rapid compression of the samples. The SC 7600 (FLIR, USA) high-speed thermal imaging camera equipped with an actively cooled focal plane array (FPA) with a full-frame resolution of 640×512 px and pixel pitch $15 \mu\text{m}$ was attached to a 50 mm f/2 lens with anti-reflection coated silicon glass optics. The camera uses a photon counting Indium Antimonide (InSb) detector operating in a $1.5 - 5 \mu\text{m}$ spectral range (SWIR to MWIR band). The lens-camera assembly was calibrated for the temperature range from -20°C to 300°C , where the thermal response of the samples to the loading was anticipated. To achieve the maximum possible frame-rate at a reasonable resolution, FPA windowing to 96×44 px was used to perform imaging at approximately 2 kfps for the room and elevated temperature experiments, while the cooled samples were observed at approximately 1.9 kfps given by the integration time necessary for imaging the samples at such low temperatures. During all the experiments, an MgF_2 infrared-transparent protective window was used to guarantee the safety of the thermal imaging optics. For verification of the cooling procedure and the sensitivity of the high-speed thermal-imaging camera, a microbolometric LWIR thermal imager i7 (FLIR, USA) was used.

At strain-rates of 1150 s^{-1} and 2300 s^{-1} , the specimens were tested at three temperature levels distinguished by different initial temperatures at the moment of the start of the measurement. According to the capabilities of the in-house developed heating/cooling setups (see [13] for details), particularly the achievable speed of the temperature changes, and the thermal conductivity of the samples, the low temperature of -5°C , the room temperature of 25°C , and the elevated temperature of 120°C were selected for the measurement. In total, five specimens were tested at a given strain-rate and temperature.

Stress-strain curves for the individual temperatures and strain rates were evaluated from the strain-gauge signals according to the standard one-dimensional wave propagation theory valid for SHPB. For all the temperatures, the stresses in dynamic compression were considerably higher than in the case of the quasi-static tests (approximately 30 % higher at the room temperature). The

stresses in the experiments with the low temperature were higher than the stresses during the experiments conducted at room temperature. The same trend was observed in the experiments at the elevated temperature, where the stresses were significantly lower than during the room temperature testing and even approached the values of the quasi-static room temperature curve. With the increasing strain rate, the densification of the structure occurred at the lower strain. To quantify the strain rate and temperature-related sensitivity of the lattice structure, the average plateau stress was calculated from the stress-strain diagram in a strain range of 0.05 – 0.25. This range was selected as the strain rate in this interval remained approximately constant and was not affected by the initial ramp-in phase of the strain pulse or rapid strain rate decrease during the densification. Here, the coupled thermo-mechanical behaviour of the lattice structure was very profound as, at the low and room temperature, the average plateau stress was increasing with the strain rate. The rate of its increase was marginally higher for the low temperature. The inverse behaviour was observed in the experiments conducted at the high temperature, where the average plateau stress decreased with the strain rate revealing the thermal related softening of the lattice structure.

A qualitative analysis of the deformation processes was performed by studying the distribution of heat in the acquired thermograms. The data show that the initial temperature of the sample not only trivially influences the highest observable temperature of the deforming microstructure, but, more importantly, affects the difference between the initial and the highest measured temperature during the given experiment. As such, the highest temperature difference was calculated for the room temperature samples, while the lowest difference was assessed for the elevated-temperature samples loaded at a lower strain-rate. Furthermore, the thermograms can be used as a means for the inspection of the concentration of the deformation within the specimen microstructure. Here, it is possible to reveal, e.g., the localised heating in the joints of struts and the overall distribution of the deformation over the microstructure including the possible localisation of deformation to certain layers of the unit-cells.

4.6 Summary - dynamic regime

In the dynamic part, SHPB experiments with all the SLS printed steel samples (having a different number of unit-cells in the lattice) were performed to obtain their strain-rate dependent stress-strain response and the strain-dependent Poisson's ratio characteristics under dynamic loading conditions. A virtual SHPB apparatus was developed in LS-DYNA and precise geometrical models of the investigated structures were used in the numerical modelling to assess their simulated deformation characteristics with. The stress-strain response of the virtual experiments is obtained from the strain versus time histories captured at the virtual strain-gauges that are subjected to the same mathematical evaluation procedures used in the experiments. Using the full access to the nodal displacements in the FEA, the function of Poisson's ratio is derived at the same locations used in the DIC-based evaluation of the experiments. Several aspects of the numerical modelling were addressed, including the constitutive model development, the mesh development of the SHPB bars, and the mesh development of the auxetic lattices. The ability of the numerical simulations to capture the dynamic deformation of the investigated lattices is shown on comparison of the experimental and numerical results in terms of stress-strain diagrams and the function of Poisson's ratio. The influence of the printing quality on the agreement between the experimental and numerical results is commented in the discussion together with the temperature dependent characteristics assessed using the SHPB apparatus equipped with a high-speed thermal imaging camera.



Chapter 5

Summary

In the experimental campaign, three types of auxetic lattices were subjected to uni-axial quasi-static and compressive impact loading in the SHPB. The 2D re-entrant honeycomb, the 3D re-entrant honeycomb, and the 2D missing-rib structures were printed from PMMA using multi-jet modelling technology and sintered from powdered 316L austenitic steel. Furthermore, two different types of SLS printed steel samples with a different number of unit-cells in the lattice were developed and the samples having an RVE number of unit-cells were subjected to dynamic compression at two strain-rates. In all cases, the quasi-static compression was observed using a CCD camera, whereas the dynamic experiments were recorded using a high-speed camera for processing the acquired images of the deforming structures using the DIC technique. The longitudinal and lateral strain fields were calculated and the strain-dependent Poisson's ratio was evaluated for each of the lattices. The derived functions of Poisson's ratio were analysed and the changes in the deformation behaviour induced by the different compressive strain-rates were identified. The 2D re-entrant honeycomb and the 2D missing-rib structures exhibited a significant strain-rate dependency of the auxetic behaviour. The 3D re-entrant structure exhibited auxetic behaviour only in the region of a limited number of the unit-cells close to its centroid and only during the quasi-static compression. Overall, the dynamic experiments with this lattice having an RVE number of unit-cells in the structures yielded a Poisson's ratio close to

zero rendering the deformation response of this microarchitecture very similar to metal foams. The resulting magnitude of the auxetic behaviour remained low, although negative over the whole range of the deformation, while the standard deviation of the experiments reached positive values of Poisson's ratio. Aside from the experiments with the lattice structures, quasi-static and dynamic experiments with bulk samples printed from 316L stainless steel in different orientations were performed during the development of the FE material model. The dependency of the strain-rate sensitivity and the printing direction of the material was clearly apparent from the stress-strain diagrams. The specimens with a horizontal printing orientation exhibited, on average, a 28 % variation between the stresses achieved during the quasi-static and the dynamic loading, while the smallest difference of 14 % was observed as noted for the tilted printing orientation. The average difference of the stress values evaluated from the quasi-static and dynamic testing of the vertically printed specimens was 21 %. It was found out that the values of the yield stress in dynamic compression are lower than the nominal quasi-static data, which can be attributed to the poor surface quality of the specimens and the overall brittle-fracture tendency of the bulk samples. As a part of the experimental campaign, the selected auxetic lattice was also subjected to a micro-CT measurement to inspect its internal structure, which showed a relatively large localised porosity corresponding to the difference in the nominal and measured mass density of the samples. Also, it has to be stated that the quality of the steel AM procedure was questionable with an utmost probability significantly influencing the mechanical and microstructural response of the samples due to the non-compliance of the printed samples with the given geometry in terms of both the overall dimensions and the surface quality.

Based on the testing of the PMMA samples in the quasi-static regime, the corresponding FE simulations were developed in ANSYS using beam-analogy discretisation to investigate the possibilities of the parametrisation of the structures including the influence of the numerical aspects of the simulations. At first, displacement controlled simulations were used to obtain the numerical stress-strain curve of each lattice up to the yield of the structure and the results were compared with the experiments. Then, parametric simulations were performed to reveal the influence of the relative density on the stiffness and Poisson's ratio at the given compression of the structures, while different material models and strain formulations were studied to characterise the

numerical aspects of the simulations. Dynamic FE simulations comprising explicit time integration in LS-DYNA and the exact geometry of the SLS printed lattices were performed to be able to predict the deformation response of the lattices and estimate the SHPB parameters for the measurements of such constructs. For this reason, a virtual SHPB apparatus was developed and calibrated by performing multi-parametric optimisation of the FE mesh of the bars, material models, and numerical properties of the simulations. Experimentally verified void tests were used for the development of the virtual SHPB setup. The simulations concerning the dynamic loading of the auxetic lattices were performed using the same initial conditions as the experiments to assess the reliability of the simulations. Here, the overall compressive response of the lattices and the acquired strain-dependent Poisson's ratio were evaluated and compared against the experimental data. It has been found out that such an approach consisting of the precise modelling of both the experimental apparatus and the geometry of the samples can be successfully employed even if a relatively simple material model of the lattice is considered. Due to the uncertainties caused by the low quality of the printing, it can be reasonably assumed that even a more accurate material model, incorporating thermal effects and damage, could not describe the deformation response of the lattices with higher precision. As a result, the very good precision of the FE simulations was achieved in the case of the predicted stress-strain response of the structures. However, a significantly lower reliability was achieved for the Poisson's ratio, where, in the majority of cases, only a general trend of experimental curves was captured except for the 3D re-entrant honeycomb with an RVE number of unit-cells. Here, the numerical Poisson's ratio was calculated from the deformation of two perpendicular faces yielding function values within the standard deviation of the experiments from one face only. A better evaluation was not possible in this case because only one face was observed by the high-speed camera during experiments.

Using the evaluated results, the following conclusions can be drawn:

1. The SHPB is a suitable method for the investigation of the deformation behaviour of laser-sintered auxetic structures. Dynamic equilibrium was achieved in the experiments and the specimens were compressed at approximately a constant strain rate.

2. The material used for sintering was identified as strain rate sensitive, which added to the strain rate dependency induced by the micro-inertia (to the studied lattices). All the structures exhibited approximately a 40 – 70 % higher plateau stress in dynamic compression.
3. A different deformation behaviour of the specimens was observed during the quasi-static and dynamic experiments. The structures in quasi-static compression exhibited a lateral deformation during compression, in particular the 2D missing rib. The dynamically compressed specimens exhibited a homogeneous deformation without any lateral distortion. Densification of the structures occurred at the lower strain in dynamic compression compared to the quasi-static tests.
4. Poisson's ratio was evaluated in both the quasi-static and dynamic experiments using the DIC. Deformation with a negative Poisson's ratio was identified in all the structures having an RVE number of unit-cells in the lattice in both the quasi-static and dynamic compression. The structures with the reduced number of unit-cells were influenced by this factor in terms of the strain-dependent Poisson's ratio, which resulted in the discrepancy between the dynamic and quasi-static response, including a positive Poisson's ratio.
5. The evaluation of both faces is necessary in the case of the 3D auxetic lattices. In the numerical simulations, the discrepancy of the functions of the strain-dependent Poisson's ratio was assessed, but due to the instrumentation consisting of only one camera observing the deforming structure, the evaluation of the numerical results against the experimental data was not possible.
6. A very high-quality of the SLS printing has to be pursued as the localised voids together with the poor surface quality are the likely cause of discrepancies between the explicit FE simulations and the experiments, particularly in case of Poisson's ratio. Certain aspects of the printing quality, such as the porosity and surface roughness, can only be barely incorporated in the numerical simulations on the level of the constitutive model. Furthermore, the evaluation of these effects is also possible from a statistical point of view.
7. The clear disadvantage of the presented approach to the numerical simulations (i.e., a full-scale model of the SHPB apparatus, the precise

geometry of the samples) is the computational cost that would be further manifested with a higher-order material model of the sintered steel and denser mesh of the RVE sized lattices. As a result, a supercomputer with a high number of CPUs (threads) would be needed to achieve reasonable calculation times, particularly in the case of parametric simulations.

8. The time-history of the strain rate in the virtual SHPB experiments is a source of errors in the numerical simulations causing the discrepancies in the initial and final stages of the dynamic compression of the samples. This is caused by the numerical oscillations in the incident strain waves and different slope of both the rising and falling edges, which is in the experiments, influenced by the pulse shaper. For this reason, it is also advisable to include the numerical pulse shaping measures to achieve a higher agreement in the initial conditions [93].

Further work will be focused on the enhancement of the current modelling schemes to include a higher-order material model of the SLS printed austenitic steel, a higher mesh density of the auxetic lattices with an RVE number of unit-cells, and the use of numerical incident pulse shaping measures. This will enable one to achieve a higher precision in the prediction of the deformation response of the samples to enable the numerical estimation of the SHPB parameters for the testing of the particular lattice as well as the optimisation of the design towards the precise tuning of the energy absorption capabilities. Furthermore, it will also be possible to verify the numerical results for the structures utilizing innovative concepts, such as structures with enhanced strut-joint properties (e.g., a joint formed by a special structural element - a hollow sphere similar to the enhanced re-entrant honeycomb model, where the void inside the sphere enables the joint-like rotation of connected beams) and structures with a tunable micro-inertia influencing their strain-rate dependent response (e.g., structures with a purposefully added mass to tailor the micro-inertia effect). The calibrated SHPB apparatus, or more precisely its components, can also be used in the related dynamic problems, such as the dynamic crushing of porous solids, and to study the phenomena connected with the strain wave propagation in the continuum with the necessary measures being developed for the evaluation of the SHPB measurements including wave separation techniques. Furthermore, with the use of a calibrated framework based on the LS-DYNA code, it will be possible

to support the development of innovative solvers for explicit FEM applied to contact-impact problems, where open doors still exist for primary research on the numerical methods to answer, e.g., the following questions: Is it possible to integrate with an explicit FEM with a larger timestep? How to avoid the sensitivity of the stiffness penalty parameter in penalty methods for enforcing contact constraints? Is it possible to eliminate spurious stress and contact force oscillations? How to efficiently compute self-contact problems? How to use modern computer networks and clouds in impact problems based on the explicit time integration with minimal transfer of data among processors? Is it possible to use tools of artificial intelligence in explicit FEM based on High-Performance Computing for contact-impact problems?



Appendix A

Bibliography

- [1] O. Jiroušek, I. Jandejsek, and D. Vavřík. Evaluation of strain field in microstructures using micro-CT and digital volume correlation. *Journal of Instrumentation*, 6(01):C01039–C01039, 2011.
- [2] P. Koudelka, P. Zlamal, D. Kytýr, T. Doktor, T. Fíla, and O. Jirousek. On the modeling of the compressive behaviour of metal foams: A comparison of discretization schemes. In *Proceedings of the Fourteenth International Conference on Civil, Structural and Environmental Engineering Computing*. Civil-Comp Press, 2013.
- [3] P. Koudelka, T. Doktor, J. Valach, D. Kytýř, and O. Jiroušek. Effective elastic moduli of closed-cell aluminium foams - homogenization method. *UPB Scientific Bulletin, Series D: Mechanical Engineering*, 75(1), 2013.
- [4] T. Doktor, P. Zlámal, T. Fíla, P. Koudelka, D. Kytýř, and O. Jiroušek. Properties of polymer-filled aluminium foams under moderate strain-rate loading conditions. *Materiali in Tehnologije*, 49(4):597–600, 2015.
- [5] A. Jung, M. Larcher, O. Jirousek, P. Koudelka, and G. Solomos. Strain-rate dependence for Ni/Al hybrid foams. *EPJ Web of Conferences*, 94:04030, 2015.

- [6] P. Koudelka, M. Neuhauserova, T. Fíla, and D. Kytýř. Deformation mechanisms of auxetic microstructures for energy absorption applications. *Applied Mechanics and Materials*, 821:428–434, 2016.
- [7] P. Koudelka, O. Jiroušek, T. Fíla, and T. Doktor. Compressive properties of auxetic structures produced with direct 3D printing. *Materiali in Tehnologije*, 50(3):311–317, 2016.
- [8] T. Fíla, P. Zlámal, O. Jiroušek, J. Falta, P. Koudelka, D. Kytýř, T. Doktor, and J. Valach. Impact testing of polymer-filled auxetics using split hopkinson pressure bar. *Advanced Engineering Materials*, 19(10), 2017.
- [9] T. Doktor, T. Fíla, P. Koudelka, D. Kytýř, and O. Jiroušek. Compressive properties of auxetic structures with controlled stiffness of strut joints. *Acta Polytechnica CTU Proceedings*, 25:17–20, 2019.
- [10] R. Dvořák, P. Koudelka, and T. Fíla. Numerical modelling of wave shapes during SHPB measurement. *Acta Polytechnica CTU Proceedings*, 25:25–31, 2019.
- [11] M. Neuhäuserová, P. Koudelka, J. Falta, M. Adorna, T. Fíla, and P. Zlámal. Strain-rate and printing direction dependency of compressive behaviour of 3D printed stainless steel 316L. pages 68–72, 2019.
- [12] T. Fíla, P. Koudelka, P. Zlámal, J. Falta, M. Adorna, M. Neuhäuserová, J. Luksch, and O. Jiroušek. Strain dependency of poisson’s ratio of SLS printed auxetic lattices subjected to quasi-static and dynamic compressive loading. *Advanced Engineering Materials*, 21(8):1900204, 2019.
- [13] P. Koudelka, T. Fíla, J. Falta, J. Šleichrt, P. Zlámal, A. Mauko, M. Adorna, M. Neuhäuserová, and O. Jiroušek. Temperature dependent compressive characteristics of additively manufactured stainless-steel auxetic lattices at high strain-rate. In *Temperature dependence of material behaviour at high strain-rate*, Stresa, 2019. Politecnico di Torino.
- [14] Faculty of Transportation Sciences Czech Technical University in Prague. Dynlab, 2020.
- [15] L. J. Gibson and M. F. Ashby. *Cellular Solids*. Cambridge University Press, 1997.

- [16] L. J. Gibson. Mechanical behavior of metallic foams. *Annual Review of Materials Science*, 30(1):191–227, 2000.
- [17] Y. Sugimura, J. Meyer, M. Y. He, H. Bart-Smith, J. Grenstedt, and A. G. Evans. On the mechanical performance of closed cell Al alloy foams. *Acta Materialia*, 45(12):5245 – 5259, 1997.
- [18] Y. Boonyongmaneerat, C. Schuh, and D. Dunand. Mechanical properties of reticulated aluminum foams with electrodeposited Ni-W coatings. *Scripta Materialia*, 59(3):336–339, August 2008.
- [19] A. Jung, H. Natter, R. Hempelmann, S. Diebels, M. R. Koblischka, U. Hartmann, and E. Lach. Electrodeposition of nanocrystalline metals on open cell metal foams: Improved mechanical properties. volume 25, pages 165–172, 2010.
- [20] A. Jung, H. Natter, S. Diebels, E. Lach, and R. Hempelmann. Nanonickel coated aluminum foam for enhanced impact energy absorption. *Advanced Engineering Materials*, 13:23 – 28, 02 2011.
- [21] A. Jung, M. Koblischka, E. Lach, S. Diebels, and H. Natter. Hybrid metal foams: Mechanical testing and determination of mass flow limitations during electroplating. *Int. J. Mater. Sci.*, 2:97–107, 01 2012.
- [22] G. Xiao-lu, Y. Liu, S. Y. He, and J. Lu. Manufacturing and low-velocity impact response of a new composite material: Metal porous polymer composite (MPPC). *Journal of Materials Science and Technology*, 20:65–68, 12 2004.
- [23] Y. Liu and X-L. Gong. Compressive behavior and energy absorption of metal porous polymer composite with interpenetrating network structure. *Transactions of Nonferrous Metals Society of China*, 16:439 – 443, 2006.
- [24] N. Dukhan, N. Rayess, and J. Hadley. Characterization of aluminum foam-polypropylene interpenetrating phase composites: Flexural test results. *Mechanics of Materials*, 42:134–141, 02 2010.
- [25] Y. Su, Z. Li, X. Gong, Q. Ouyang, Q. Guo, C. Guo, J. Zhang, and D. Zhang. Structural modeling and mechanical behavior of metal-porous-polymer-composites (MPPCs) with different polymer volume fractions. *Composite Structures*, 153, 06 2016.

- B. Yaakobi. Material dynamics under extreme conditions of pressure and strain rate. *Materials Science and Technology*, 22(4):474–488, 2006.
- [37] J. L. Chaboche. A review of some plasticity and viscoplasticity constitutive theories. *International Journal of Plasticity*, 24(10):1642 – 1693, 2008. Special Issue in Honor of Jean-Louis Chaboche.
- [38] Y. C. Lin and X-M. Chen. A critical review of experimental results and constitutive descriptions for metals and alloys in hot working. *Materials & Design*, 32(4):1733–1759, 2011.
- [39] G. R. Johnson and W. H. Cook. Fracture characteristics of three metals subjected to various strains, strain rates, temperatures and pressures. *Engineering Fracture Mechanics*, 21(1):31 – 48, 1985.
- [40] A. S. Khan and S. Huang. Experimental and theoretical study of mechanical behavior of 1100 aluminum. *International Journal of Plasticity*, 8(4):397 – 424, 1992.
- [41] A. S. Khan, Y. S. Suh, and R. Kazmi. Quasi-static and dynamic loading responses and constitutive modeling of titanium alloys. *International Journal of Plasticity*, 20(12):2233–2248, 2004.
- [42] J. H. Sung, J. H. Kim, and R. H. Wagoner. A plastic constitutive equation incorporating strain, strain-rate, and temperature. *International Journal of Plasticity*, 26(12):1746 – 1771, 2010.
- [43] W. Wu, W. Hu, G. Qian, H. Liao, X. Xu, and F. Berto. Mechanical design and multifunctional applications of chiral mechanical metamaterials: A review. *Materials & Design*, 180:107950, 2019.
- [44] A. du Plessis, I. Yadroitsava, and I. Yadroitsev. Effects of defects on mechanical properties in metal additive manufacturing: A review focusing on X-ray tomography insights. *Materials & Design*, 187:108385, 2020.
- [45] X. Yu, J. Zhou, H. Liang, Z. Jiang, and L. Wu. Mechanical metamaterials associated with stiffness, rigidity and compressibility: A brief review. *Progress in Materials Science*, 94:114 – 173, 2018.
- [46] C. S. Lee, S. G. Kim, H. J. Kim, and S. H. Ahn. Measurement of anisotropic compressive strength of rapid prototyping parts. *Journal*

- of Materials Processing Technology*, 187-188:627 – 630, 2007. 3rd International Conference on Advanced Forming and Die Manufacturing Technology.
- [47] I. Gajdos and J. Slota. Influence of printing conditions on structure in fdm prototypes. *Technical Gazette*, 20:231–236, 05 2013.
- [48] J. Torres, J. Cotelo, J. Karl, and A. P. Gordon. Mechanical property optimization of FDM PLA in shear with multiple objectives. *JOM*, 67(5):1183–1193, 2015.
- [49] A. Tsouknidas, M. Pantazopoulos, I. Katsoulis, D. Fasnakis, S. Maropoulos, and N. Michailidis. Impact absorption capacity of 3D-printed components fabricated by fused deposition modelling. *Materials & Design*, 102:41 – 44, 2016.
- [50] S. R. G. Bates, I. R. Farrow, and R. S. Trask. 3D printed polyurethane honeycombs for repeated tailored energy absorption. *Materials & Design*, 112:172 – 183, 2016.
- [51] H. B. Rebelo, D. Lecompte, C. Cismasiu, A. Jonet, B. Belkassam, and A. Maazoun. Experimental and numerical investigation on 3D printed PLA sacrificial honeycomb cladding. *International Journal of Impact Engineering*, 131:162–173, 2019.
- [52] M. Kristoffersen, M. Costas, T. Koenis, V. Brøtan, C. O. Paulsen, and T. Børvik. On the ballistic perforation resistance of additive manufactured AlSi10Mg aluminium plates. *International Journal of Impact Engineering*, 137:103476, 2020.
- [53] Y. Duan, B. Du, X. Shi, B. Hou, and Y. Li. Quasi-static and dynamic compressive properties and deformation mechanisms of 3D printed polymeric cellular structures with kelvin cells. *International Journal of Impact Engineering*, 132:103303, 2019.
- [54] B. Song, E. Nishida, B. Sanborn, M. Maguire, D. Adams, J. Carroll, J. Wise, B. Reedlunn, J. Bishop, and T. Palmer. Compressive and tensile stress–strain responses of additively manufactured (AM) 304l stainless steel at high strain rates. *Journal of Dynamic Behavior of Materials*, 3(3):412–425, 2017.

- [55] G. Mirone, R. Barbagallo, D. Corallo, and S. Di Bella. Static and dynamic response of titanium alloy produced by electron beam melting. *Procedia Structural Integrity*, 2:2355 – 2366, 2016. 21st European Conference on Fracture, ECF21, 20-24 June 2016, Catania, Italy.
- [56] B. Nurel, M. Nahmany, N. Frage, A. Stern, and O. Sadot. Split hopkinson pressure bar tests for investigating dynamic properties of additively manufactured AlSi10Mg alloy by selective laser melting. *Additive Manufacturing*, 22:823–833, 2018.
- [57] E. Zaretsky, A. Stern, and N. Frage. Dynamic response of AlSi10Mg alloy fabricated by selective laser melting. *Materials Science and Engineering: A*, 688:364 – 370, 2017.
- [58] T. Tancogne-Dejean, A. B. Spierings, and D. Mohr. Additively-manufactured metallic micro-lattice materials for high specific energy absorption under static and dynamic loading. *Acta Materialia*, 116:14–28, 2016.
- [59] T. Tancogne-Dejean, X. Li, M. Diamantopoulou, C. C. Roth, and D. Mohr. High strain rate response of additively-manufactured plate-lattices: Experiments and modeling. *Journal of Dynamic Behavior of Materials*, 5(3):361–375, 2019.
- [60] P-H. Li, W-G. Guo, W-D. Huang, Y. Su, X. Lin, and K-B. Yuan. Thermomechanical response of 3D laser-deposited Ti-6Al-4V alloy over a wide range of strain rates and temperatures. *Materials Science and Engineering: A*, 647:34 – 42, 2015.
- [61] T-C. Lim. *Auxetic Materials and Structures*. Springer Singapore, 2015.
- [62] R. Lakes. Foam structures with a negative poisson’s ratio. *Science*, 235(4792):1038–1040, 1987.
- [63] D. Luong, D. Pinisetty, and N. Gupta. Compressive properties of closed-cell polyvinyl chloride foams at low and high strain rates: Experimental investigation and critical review of state of the art. *Composites Part B: Engineering*, 44:403–416, 2013.
- [64] H. Zhao. Testing of polymeric foams at high and medium strain rates. *Polymer Testing*, 16(5):507 – 516, 1997.

- [65] M. Saha, H. Mahfuz, U. Chakravarty, M. Uddin, and S. Jeelani. Effect of density, microstructure, and strain rate on compression behavior of polymeric foams. *Materials Science and Engineering A-structural Materials Properties Microstructure and Processing - MATER SCI ENG A-STRUCT MATER*, 406:328–336, 2005.
- [66] G. Subhash and Q. Liu. Quasistatic and dynamic crushability of polymeric foams in rigid confinement. *International Journal of Impact Engineering - INT J IMPACT ENG*, 36:1303–1311, 2009.
- [67] U. Chakravarty. An investigation on the dynamic response of polymeric, metallic, and biomaterial foams. *Composite Structures - COMPOS STRUCT*, 92:2339–2344, 2010.
- [68] X. Pang and H. Du. Dynamic characteristics of aluminium foams under impact crushing. *Composites Part B: Engineering*, 112:265 – 277, 2017.
- [69] B. Song, W. Chen, S. Dou, N. Winfree, and J. Kang. Strain-rate effects on elastic and early cell-collapse responses of a polystyrene foam. *International Journal of Impact Engineering - INT J IMPACT ENG*, 31:509–521, 2005.
- [70] S. Wu. *Introduction to the explicit finite element method for nonlinear transient dynamics*. Wiley, Hoboken, N.J, 2012.
- [71] T. Belytschko. *Nonlinear finite elements for continua and structures*. Hoboken, New Jersey Wiley, Chichester, West Sussex, UK, 2014.
- [72] R. Kolman, J. Plešek, J. Červ, M. Okrouhlík, and P. Pařík. Temporal-spatial dispersion and stability analysis of finite element method in explicit elastodynamics. *International Journal for Numerical Methods in Engineering*, 106(2):113–128, 2016.
- [73] J. Kopačka, A. Tkachuk, D. Gabriel, R. Kolman, M. Bischoff, and J. Plešek. On stability and reflection-transmission analysis of the bipenalty method in contact-impact problems: A one-dimensional, homogeneous case study. *International Journal for Numerical Methods in Engineering*, 113(10):1607–1629, 2018.
- [74] R. Kolman, S. S. Cho, and K. C. Park. Efficient implementation of an explicit partitioned shear and longitudinal wave propagation algorithm.

- International Journal for Numerical Methods in Engineering*, 107(7):543–579, 2016.
- [75] S. S. Cho, R. Kolman, J. A. González, and K. C. Park. Explicit multistep time integration for discontinuous elastic stress wave propagation in heterogeneous solids. *International Journal for Numerical Methods in Engineering*, 118(5):276–302, 2019.
- [76] K. Peng, K. Gao, J. Liu, Y. Liu, Z. Zhang, X. Fan, X. Yin, Y. Zhang, and G. Huang. Experimental and numerical evaluation of rock dynamic test with split-hopkinson pressure bar. *Advances in Materials Science and Engineering*, 2017:1–12, 2017.
- [77] Z. Xu, H. Hao, and H.N. Li. Mesoscale modelling of fibre reinforced concrete material under compressive impact loading. *Construction and Building Materials*, 26(1):274 – 288, 2012.
- [78] Q.M. Li and H. Meng. About the dynamic strength enhancement of concrete-like materials in a split hopkinson pressure bar test. *International Journal of Solids and Structures*, 40(2):343 – 360, 2003.
- [79] J. K. Dong, K. Sirijaroonchai, S. El-Tawil, and A. E. Naaman. Numerical simulation of the split hopkinson pressure bar test technique for concrete under compression. *International Journal of Impact Engineering*, 37(2):141 – 149, 2010.
- [80] Z. Ozdemir, A. Tyas, R. Goodall, and H. Askes. Energy absorption in lattice structures in dynamics: Nonlinear FE simulations. *International Journal of Impact Engineering*, 102:1 – 15, 2017.
- [81] N. Novak, M. Vesenjak, L. Krstulović-Opara, and Z. Ren. Mechanical characterisation of auxetic cellular structures built from inverted tetrapods. *Composite Structures*, 196:96 – 107, 2018.
- [82] N. Novak, K. Hokamoto, M. Vesenjak, and Z. Ren. Mechanical behaviour of auxetic cellular structures built from inverted tetrapods at high strain rates. *International Journal of Impact Engineering*, 122:83 – 90, 2018.
- [83] J. X. Qiao and C. Q. Chen. Impact resistance of uniform and functionally graded auxetic double arrowhead honeycombs. *International Journal of Impact Engineering*, 83:47 – 58, 2015.

- [84] S. Hou, T. Li, Z. Jia, and L. Wang. Mechanical properties of sandwich composites with 3D-printed auxetic and non-auxetic lattice cores under low velocity impact. *Materials & Design*, 160:1305 – 1321, 2018.
- [85] L. Xiao, W. Song, C. Wang, H. Tang, Q. Fan, N Liu, and J. Wang. Mechanical properties of open-cell rhombic dodecahedron titanium alloy lattice structure manufactured using electron beam melting under dynamic loading. *International Journal of Impact Engineering*, 100:75 – 89, 2017.
- [86] M. S. Chaudhry and A. Czekanski. FE analysis of critical testing parameters in kolsky bar experiments for elastomers at high strain rate. *Materials*, 12(23), 2019.
- [87] S. T. Marais, R. B. Tait, T. J. Cloete, and G. N. Nurick. Material testing at high strain rate using the split hopkinson pressure bar. *Latin American Journal of Solids and Structures*, 1(3):219–339, 2004.
- [88] M. Kucewicz, P. Baranowski, M. Stankiewicz, M. Konarzewski, P. Platek, and J. Malachowski. Modelling and testing of 3D printed cellular structures under quasi-static and dynamic conditions. *Thin-Walled Structures*, 145:106385, 2019.
- [89] J. Liu, B. Zheng, K. Zhang, B. Yang, and X. Yu. Ballistic performance and energy absorption characteristics of thin nickel-based alloy plates at elevated temperatures. *International Journal of Impact Engineering*, 126:160 – 171, 2019.
- [90] Z. Song, L. Hou, D. Whisler, and G. Gao. Mesoscopic numerical investigation of dynamic mechanical properties of ice with entrapped air bubbles based on a stochastic sparse distribution mechanism. *Composite Structures*, 236:111834, 2020.
- [91] C. Shou. Numerical simulation of split-hopkinson pressure bar test on high-density polyethylene. *Chemical Engineering Transactions*, 66:271–276, 2018.
- [92] Imbalzano G., S. Linforth, T. D. Ngo, P. V. S. Lee, and P. Tran. Blast resistance of auxetic and honeycomb sandwich panels: Comparisons and parametric designs. *Composite Structures*, 183:242 – 261, 2018. In honor of Prof. Y. Narita.

- [93] R. Dvořák. Numerické modelování tvaru napěťových pulzů při SHPB měření. Master's thesis, Czech Technical University in Prague, Faculty of Transportation Sciences, 2018.
- [94] A. G. Kolpakov. Determination of the average characteristics of elastic frameworks. *Journal of Applied Mathematics and Mechanics*, 49(6):739 – 745, 1985.
- [95] K. E. Evans, M. A. Nkansah, I. J. Hutchinson, and S. C. Rogers. Molecular network design. *Nature*, 353(6340):124–124, September 1991.
- [96] K. E. Evans. Auxetic polymers: a new range of materials. *Endeavour*, 15(4):170 – 174, 1991.
- [97] D. Prall and R. S. Lakes. Properties of a chiral honeycomb with a poisson's ratio of -1. *International Journal of Mechanical Sciences*, 39(3):305 – 314, 1997.
- [98] C. W. Smith, J. N. Grima, and K. E. Evans. A novel mechanism for generating auxetic behaviour in reticulated foams: missing rib foam model. *Acta Materialia*, 48(17):4349 – 4356, 2000.
- [99] H. M. A. Kolken and A. A. Zadpoor. Auxetic mechanical metamaterials. *RSC Adv.*, 7:5111–5129, 2017.
- [100] N. Novak, M. Vesenjajk, and Z. Ren. Auxetic cellular materials - a review. *Strojniški vestnik – Journal of Mechanical Engineering*, 62(9):485–493, September 2016.
- [101] X. Ren, R. Das, P. Tran, T. D. Ngo, and Y. M. Xie. Auxetic meta-materials and structures: a review. *Smart Materials and Structures*, 27(2):023001, 2018.
- [102] K. Günaydın, Z. Eren, Z. Kazancı, F. Scarpa, A. M. Grande, and H. S. Türkmen. In-plane compression behavior of anti-tetrachiral and re-entrant lattices. *Smart Materials and Structures*, 28(11):115028, oct 2019.
- [103] W. Wu, X. Song, J. Liang, R. Xia, G. Qian, and D. Fang. Mechanical properties of anti-tetrachiral auxetic stents. *Composite Structures*, 185:381 – 392, 2018.

- [104] Y. Jiang and Y. Li. 3D printed chiral cellular solids with amplified auxetic effects due to elevated internal rotation. *Advanced Engineering Materials*, 19(2):1600609, 2017.
- [105] Y. Jiang and Y. Li. Novel 3D-printed hybrid auxetic mechanical metamaterial with chirality-induced sequential cell opening mechanisms. *Advanced Engineering Materials*, 20(2):1700744, 2018.
- [106] T. Li, Y. Chen, X. Hu, Y. Li, and L. Wang. Exploiting negative poisson’s ratio to design 3D-printed composites with enhanced mechanical properties. *Materials & Design*, 142:247 – 258, 2018.
- [107] T. Li, X. Hu, Y. Chen, and L. Wang. Harnessing out-of-plane deformation to design 3D architected lattice metamaterials with tunable poisson’s ratio. *Scientific Reports*, 7(1), August 2017.
- [108] T. Li and L. Wang. Bending behavior of sandwich composite structures with tunable 3D-Printed core materials. *Composite Structures*, 175, 05 2017.
- [109] K. Kuribayashi, K. Tsuchiya, Z. You, D. Tomus, M. Umemoto, T. Ito, and M. Sasaki. Self-deployable origami stent grafts as a biomedical application of ni-rich tini shape memory alloy foil. *Materials Science and Engineering: A*, 419(1):131 – 137, 2006.
- [110] M. N. Ali and I. U. Rehman. An auxetic structure configured as oesophageal stent with potential to be used for palliative treatment of oesophageal cancer: development and in vitro mechanical analysis. *Journal of Materials Science: Materials in Medicine*, 22(11):2573–2581, September 2011.
- [111] L. Jiang and H. Hu. Low-velocity impact response of multilayer orthogonal structural composite with auxetic effect. *Composite Structures*, 169:62 – 68, 2017. In Honor of Prof. Leissa.
- [112] G. Imbalzano, P. Tran, T. D. Ngo, and P. V. S. Lee. Three-dimensional modelling of auxetic sandwich panels for localised impact resistance. *Journal of Sandwich Structures & Materials*, 19(3):291–316, 2017.
- [113] M. I. Khan, J. Akram, M. Umair, S. T. A. Hamdani, K. Shaker, Y. Nawab, and M. Zeeshan. Development of composites, reinforced by

- novel 3D woven orthogonal fabrics with enhanced auxeticity. *Journal of Industrial Textiles*, 49(5):676–690, 2019.
- [114] I. Gibson, D. Rosen, and B. Stucker. *Additive Manufacturing Technologies*. Springer New York, 2015.
- [115] L. Foster, P. Peketi, T. Allen, T. Senior, O. Duncan, and A. Alderson. Application of auxetic foam in sports helmets. *Applied Sciences*, 8(3), 2018.
- [116] L. Yang, O. Harrysson, H. West, and D. Cormier. Mechanical properties of 3D re-entrant honeycomb auxetic structures realized via additive manufacturing. *International Journal of Solids and Structures*, 69-70:475 – 490, 2015.
- [117] K. K. Saxena, R. Das, and E. P. Calius. Three decades of auxetics research - materials with negative poisson’s ratio: A review. *Advanced Engineering Materials*, 18(11):1847–1870, 2016.
- [118] A. Beharic, R. R. Egui, and L. Yang. Drop-weight impact characteristics of additively manufactured sandwich structures with different cellular designs. *Materials & Design*, 145:122 – 134, 2018.
- [119] K. E. Evans and A. Alderson. Auxetic materials: Functional materials and structures from lateral thinking! *Advanced Materials*, 12(9):617–628, 2000.
- [120] Y. Prawoto. Seeing auxetic materials from the mechanics point of view: A structural review on the negative poisson’s ratio. *Computational Materials Science*, 58:140–153, 2012.
- [121] I. I. Argatov, R. Guinovart-Díaz, and F. J. Sabina. On local indentation and impact compliance of isotropic auxetic materials from the continuum mechanics viewpoint. *International Journal of Engineering Science*, 54:42–57, 2012.
- [122] V. L. Coenen and K. L. Alderson. Mechanisms of failure in the static indentation resistance of auxetic carbon fibre laminates. *physica status solidi (b)*, 248(1):66–72, 2011.
- [123] Q. Liu. Literature review: Materials with negative poisson’s ratios and potential applications to aerospace and defence. *Aust. Gov. Dep. Def.*, 2006.

- [124] R. Critchley, I. Corni, J. A. Wharton, F. C. Walsh, R. J. K. Wood, and K. R. Stokes. A review of the manufacture, mechanical properties and potential applications of auxetic foams. *physica status solidi (b)*, 250(10):1963–1982, 2013.
- [125] W. Yang, Z-M. Li, W. Shi, B-H. Xie, and M-B. Yang. Review on auxetic materials. *Journal of Materials Science*, 39(10):3269–3279, 2004.
- [126] S. Xinchun and R. S. Lakes. Stability of elastic material with negative stiffness and negative poisson’s ratio. *physica status solidi (b)*, 244(3):1008–1026, 2007.
- [127] J. B. Choi and R. S. Lakes. Fracture toughness of re-entrant foam materials with a negative poisson’s ratio: experiment and analysis. *International Journal of Fracture*, 80(1):73–83, 1996.
- [128] A. Bezazi, W. Boukharouba, and F. Scarpa. Mechanical properties of auxetic carbon/epoxy composites: static and cyclic fatigue behaviour. *physica status solidi (b)*, 246(9):2102–2110, 2009.
- [129] J. B. Choi and R. S. Lakes. Non-linear properties of metallic cellular materials with a negative poisson’s ratio. *Journal of Materials Science*, 27(19):5375–5381, 1992.
- [130] S. K. Maiti, M. F. Ashby, and L. J. Gibson. Fracture toughness of brittle cellular solids. *Scripta Metallurgica*, 18(3):213 – 217, 1984.
- [131] I. G. Masters and K. E. Evans. Models for the elastic deformation of honeycombs. *Composite Structures*, 35(4):403 – 422, 1996.
- [132] P. Zlámál, O. Jiroušek, and D. Vavřík. A novel compression/tension device for investigation of trabecular bone failure using real-time micro-CT imaging. page 91, 2008.
- [133] V. Rada, T. Fíla, P. Zlámál, D. Kytýř, and P. Koudelka. Multi-channel control system for in-situ laboratory loading devices. In *16th Youth Symposium On Experimental Solid Mechanics*, volume 18, Prague, CZ, 2018. Česká technika - nakladatelství ČVUT, ČVUT v Praze.
- [134] B. Lucas and T. Kanade. An iterative image registration technique with an application to stereo vision (IJCAI). volume 81, 1981.

- [135] D. Fila. *Mechanical Behavior of Materials under High Strain-rates Investigated by SHPB*. PhD thesis, Czech Technical University in Prague, Faculty of Transportation Sciences, 2020.
- [136] C. Bacon. An experimental method for considering dispersion and attenuation in a viscoelastic hopkinson bar. *Experimental Mechanics*, 38(4):242–249, 1998.
- [137] J. Janizewski, W. Buzantowicz, and P. Baranowski. Correction procedure of wave signals for a viscoelastic split hopkinson pressure bar. *Problems of Mechatronics - Armament, Aviation, Safety Engineering*, 23(7):17–30, 2016.
- [138] J. Schwerdtfeger, F. Schury, M. Stingl, F. Wein, R. F. Singer, and C. Körner. Mechanical characterisation of a periodic auxetic structure produced by SEBM. *physica status solidi (b)*, 249(7):1347–1352, 2012.
- [139] S. Montabone. *Beginning Digital Image Processing*. Apress, 2009.
- [140] H. A. Bruck, S. R. McNeill, M. A. Sutton, and W. H. Peters. Digital image correlation using newton-raphson method of partial differential correction. *Experimental Mechanics*, 29(3):261–267, 1989.
- [141] P. Zhou. Subpixel displacement and deformation gradient measurement using digital image/speckle correlation (DISC). *Optical Engineering*, 40(8):1613, 2001.
- [142] W. Tong. An evaluation of digital image correlation criteria for strain mapping applications. *Strain*, 41(4):167–175, 2005.
- [143] Engineering ToolBox. Friction and friction coefficients, 2004.
- [144] T. Belytschko, H-J. Yen, and R. Mullen. Mixed methods for time integration. *Computer Methods in Applied Mechanics and Engineering*, 17-18:259 – 275, 1979.
- [145] T. Belytschko. Partitioned and adaptive algorithms for explicit time integration. In *Nonlinear Finite Element Analysis in Structural Mechanics*, pages 572–584. Springer Berlin Heidelberg, 1981.
- [146] R. Courant, K. Friedrichs, and H. Lewy. Über die partiellen differenzgleichungen der mathematischen physik. *Mathematische Annalen*, 100(1):32–74, 1928.

- [147] D. P. Flanagan and T. Belytschko. A uniform strain hexahedron and quadrilateral with orthogonal hourglass control. *International Journal for Numerical Methods in Engineering*, 17(5):679–706, 1981.
- [148] T. J. R. Hughes, R. L. Taylor, J. L. Sackman, A. Curnier, and W. Kanoknukulchai. A finite element method for a class of contact-impact problems. *Computer Methods in Applied Mechanics and Engineering*, 8(3):249 – 276, 1976.
- [149] L. M. Taylor and D. P. Flanagan. Pronto 3D: A three-dimensional transient solid dynamics program. 1989.
- [150] J. A. Cherry, H. M. Davies, S. Mehmood, N. P. Lavery, S. G. R. Brown, and J. Sienz. Investigation into the effect of process parameters on microstructural and physical properties of 316L stainless steel parts by selective laser melting. *The International Journal of Advanced Manufacturing Technology*, 76(5-8):869–879, 2014.
- [151] J. Kluczyński, L. Śnieżek, K. Grzelak, J. Janiszewski, P. Płatek, J. Torzewski, I. Szachogłuchowicz, and K. Gocman. Influence of selective laser melting technological parameters on the mechanical properties of additively manufactured elements using 316L austenitic steel. *Materials*, 13(6):1449, 2020.
- [152] R. Fadida, D. Rittel, and A. Shirizly. Dynamic mechanical behavior of additively manufactured Ti6Al4V with controlled voids. *Journal of Applied Mechanics*, 82(4), 2015. 041004.
- [153] W-S. Lee and J-K. Chou. The effect of strain rate on the impact behaviour of Fe-2 mass% Ni sintered alloy. *MATERIALS TRANSACTIONS*, 46(4):805–811, 2005.
- [154] Y. Liu, Z. Dong, J. Liang, and J. Ge. Determination of the strength of a multilayer BCC lattice structure with face sheets. *International Journal of Mechanical Sciences*, 152:568 – 575, 2019.
- [155] T. Vilaro, C. Colin, and J. D. Bartout. As-fabricated and heat-treated microstructures of the Ti-6Al-4V alloy processed by selective laser melting. *Metallurgical and Materials Transactions A*, 42(10):3190–3199, 2011.

Appendix B

SEM micrographs - steel constructs

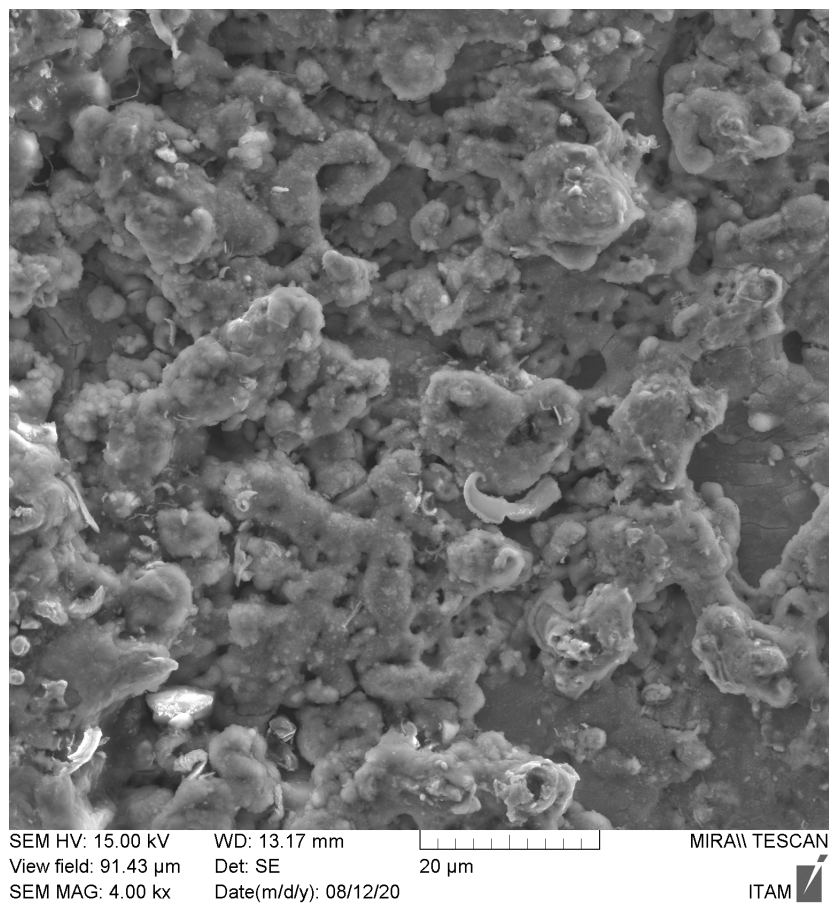
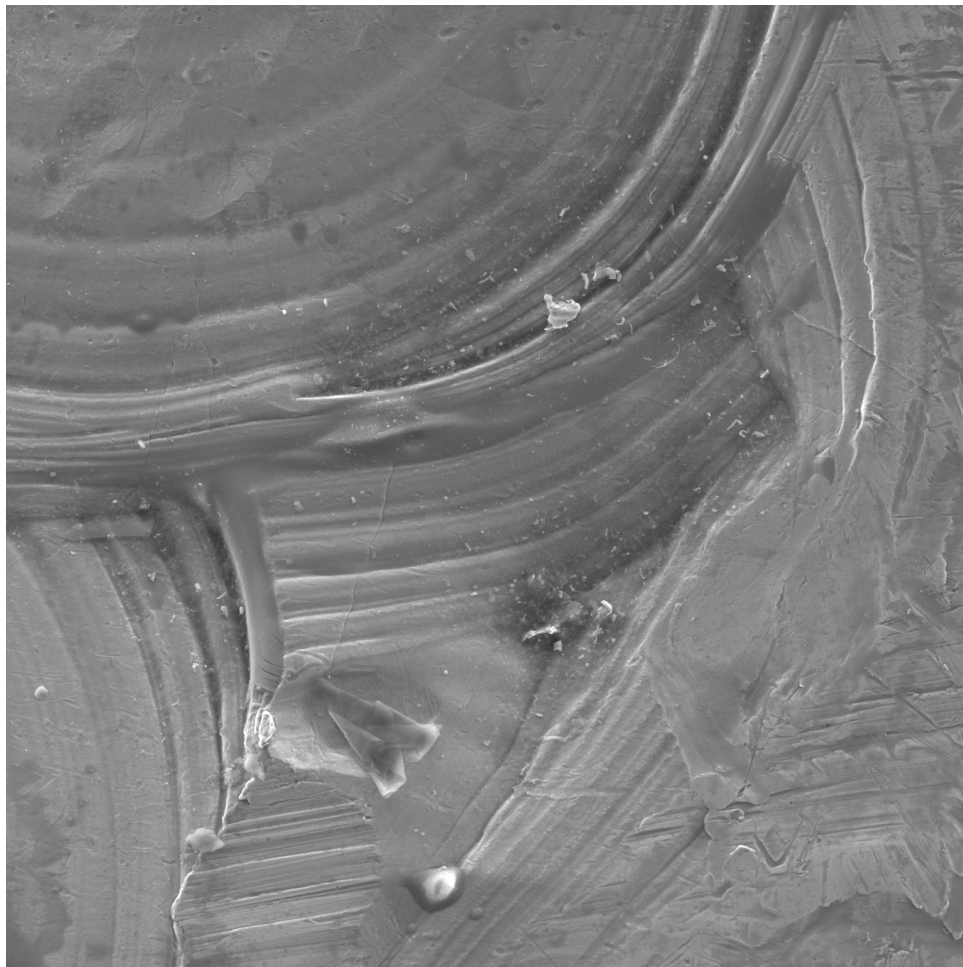


Figure B.1: Microstructure at the printed surface.



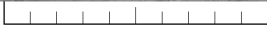

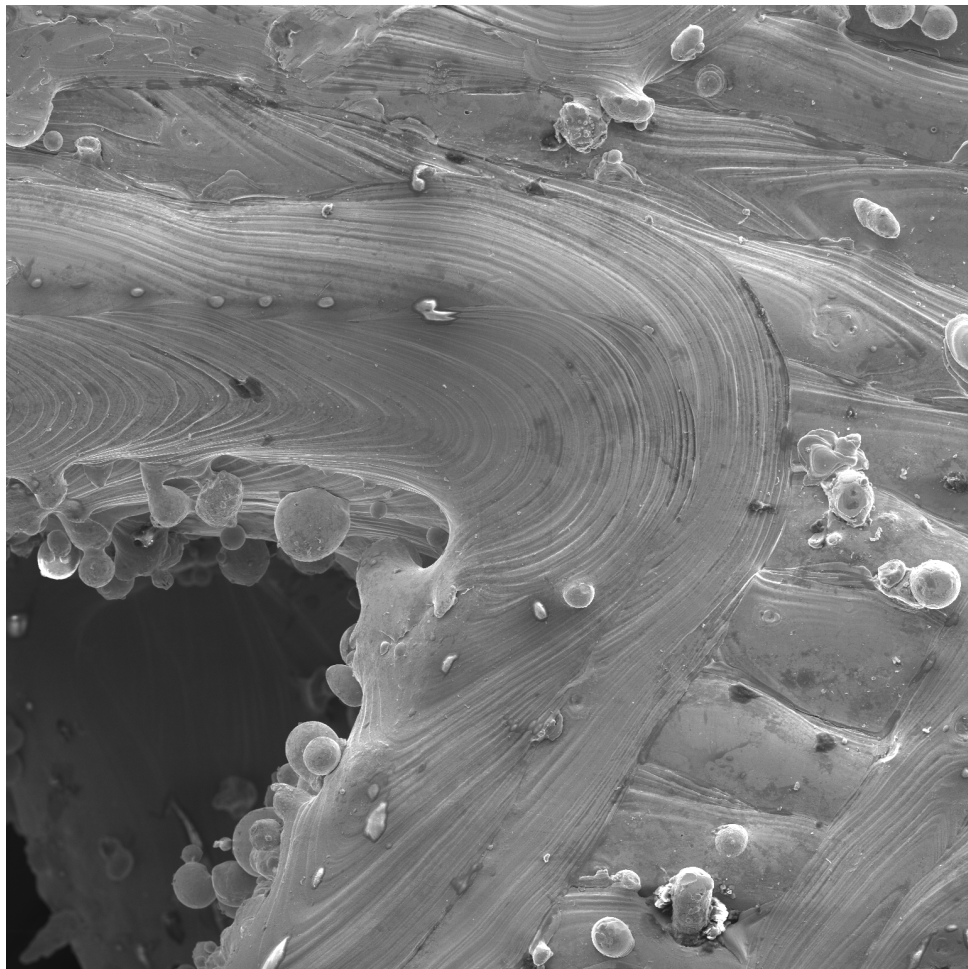
SEM HV: 15.00 kV WD: 15.36 mm  MIRA\\ TESCAN
View field: 182.9 μm Det: SE 50 μm
SEM MAG: 2.00 kx Date(m/d/y): 08/12/20 ITAM 

Figure B.2: Microstructure at the printed surface of the strut joint.





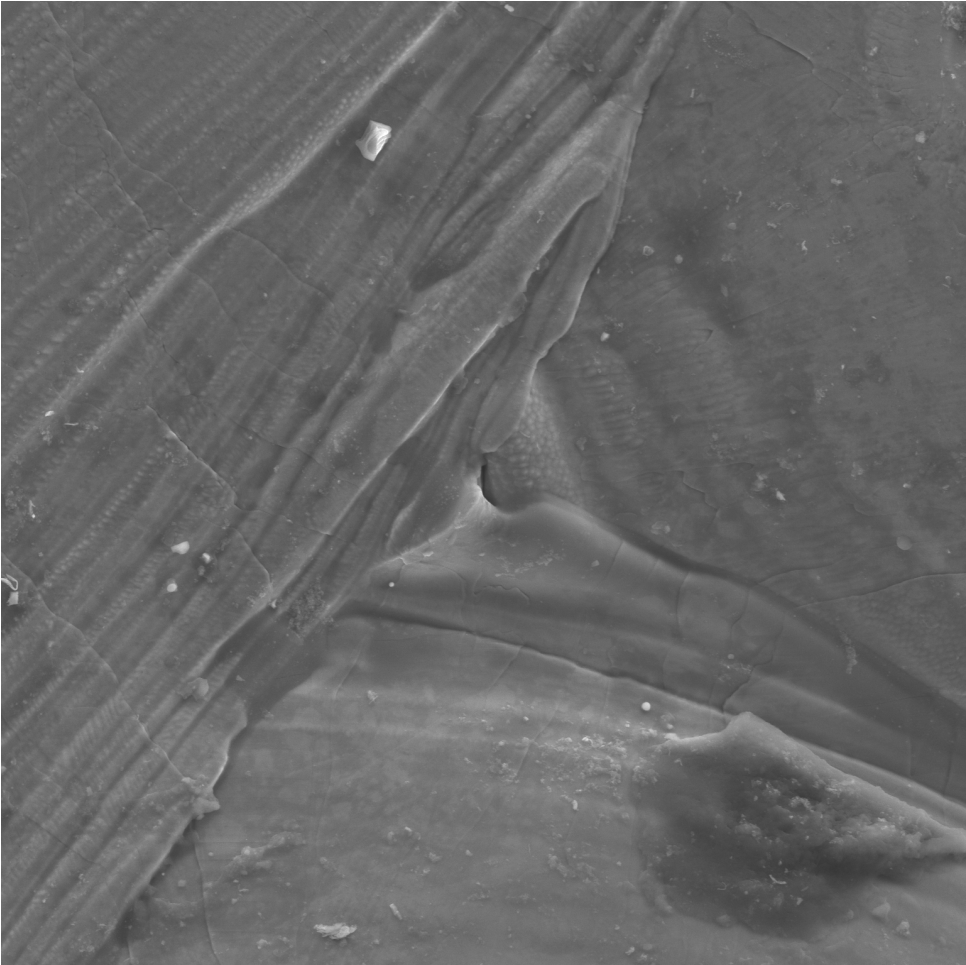
SEM HV: 15.00 kV WD: 33.00 mm  MIRAM TESCAN
View field: 914.3 μ m Det: SE 200 μ m
SEM MAG: 400 x Date(m/d/y): 08/12/20 ITAM 

Figure B.3: Microstructure at the printed surface in the strut joint area.





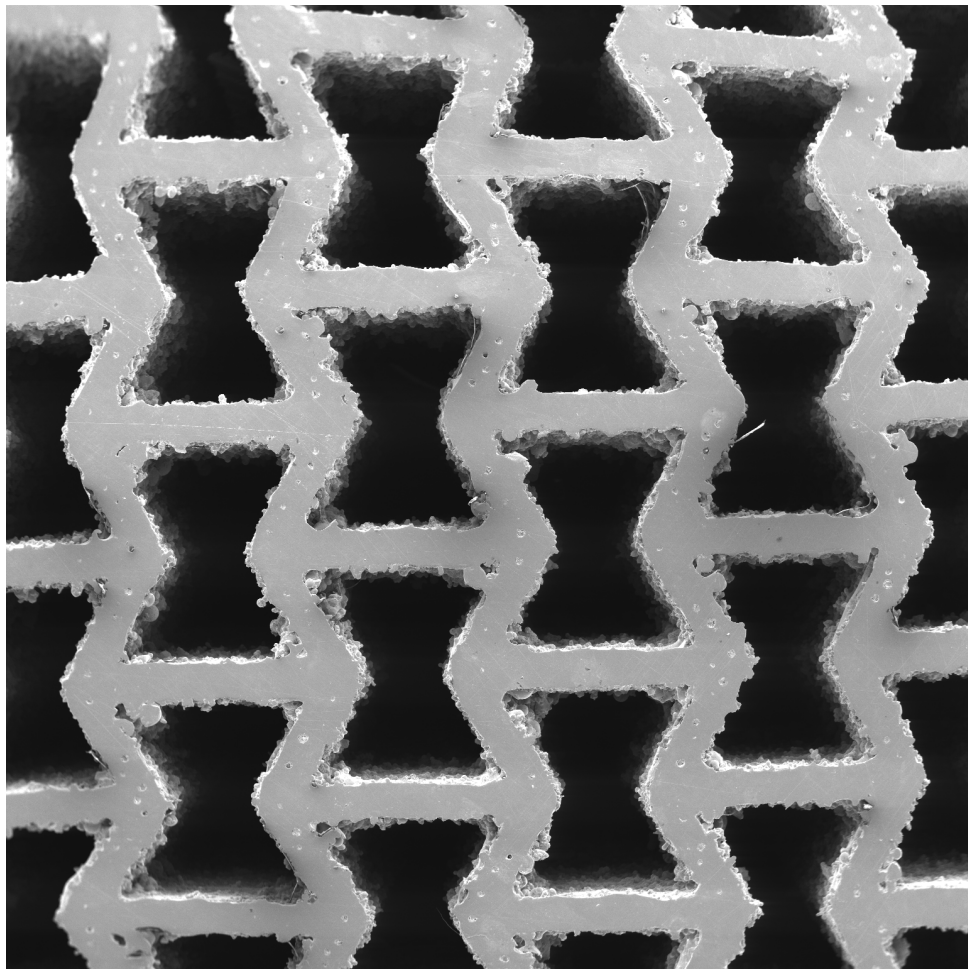
SEM HV: 15.00 kV WD: 15.01 mm  MIRA\\ TESCAN
View field: 91.43 μm Det: SE 20 μm
SEM MAG: 4.00 kx Date(m/d/y): 08/12/20 ITAM 

Figure B.4: Microstructure at the printed surface of the strut joint.





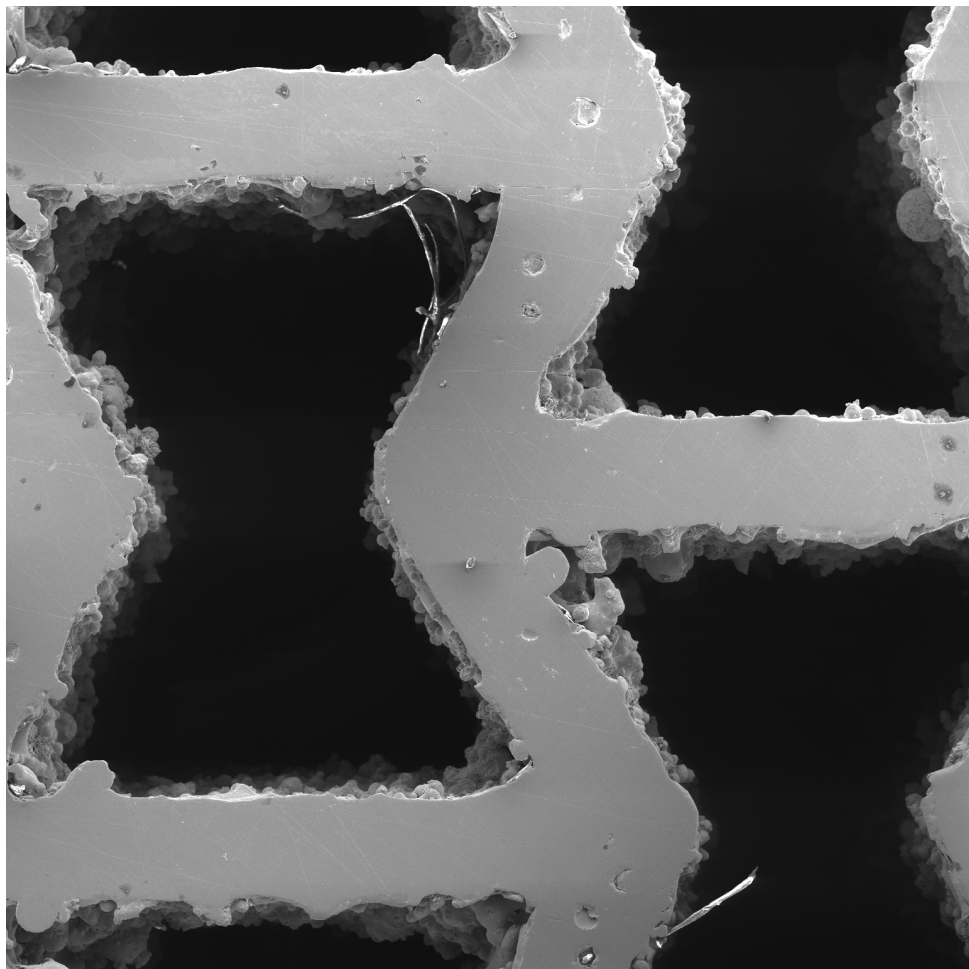
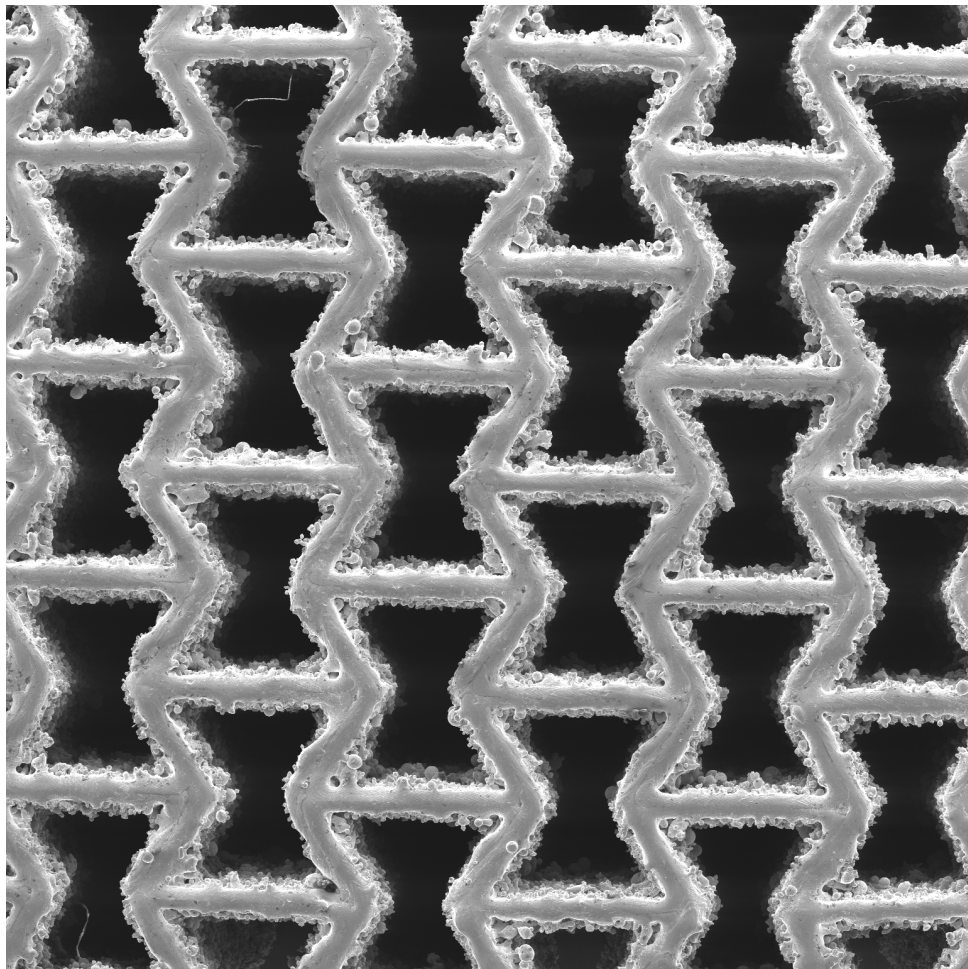
SEM HV: 15.00 kV WD: 33.97 mm  MIRALL TESCAN
View field: 7.31 mm Det: SE 2 mm
SEM MAG: 50 x Date(m/d/y): 08/12/20 ITAM 

Figure B.5: Polished surface of the 6×7 2D re-entrant honeycomb.



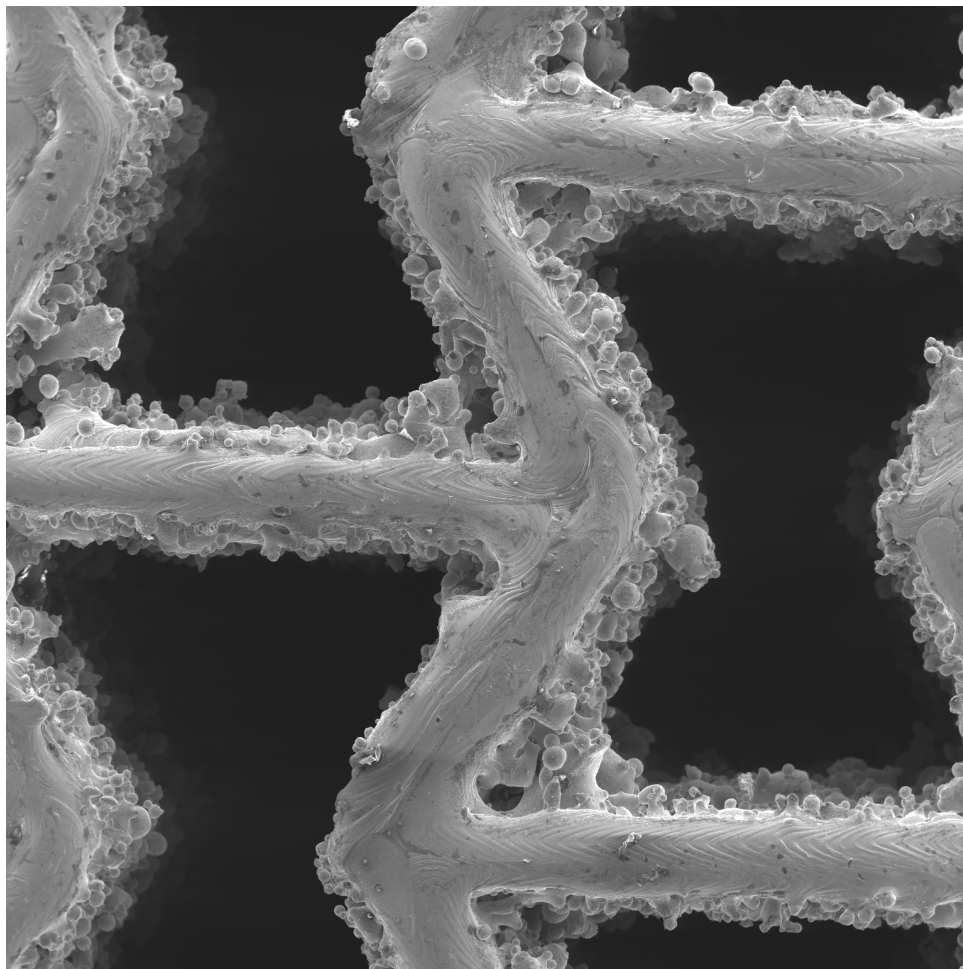
SEM HV: 15.00 kV WD: 33.97 mm 500 μ m MIRAX TESCAN
View field: 2.61 mm Det: SE
SEM MAG: 140 x Date(m/d/y): 08/12/20 ITAM

Figure B.6: Polished surface of the 6×7 2D re-entrant honeycomb - detail of the strut joints.



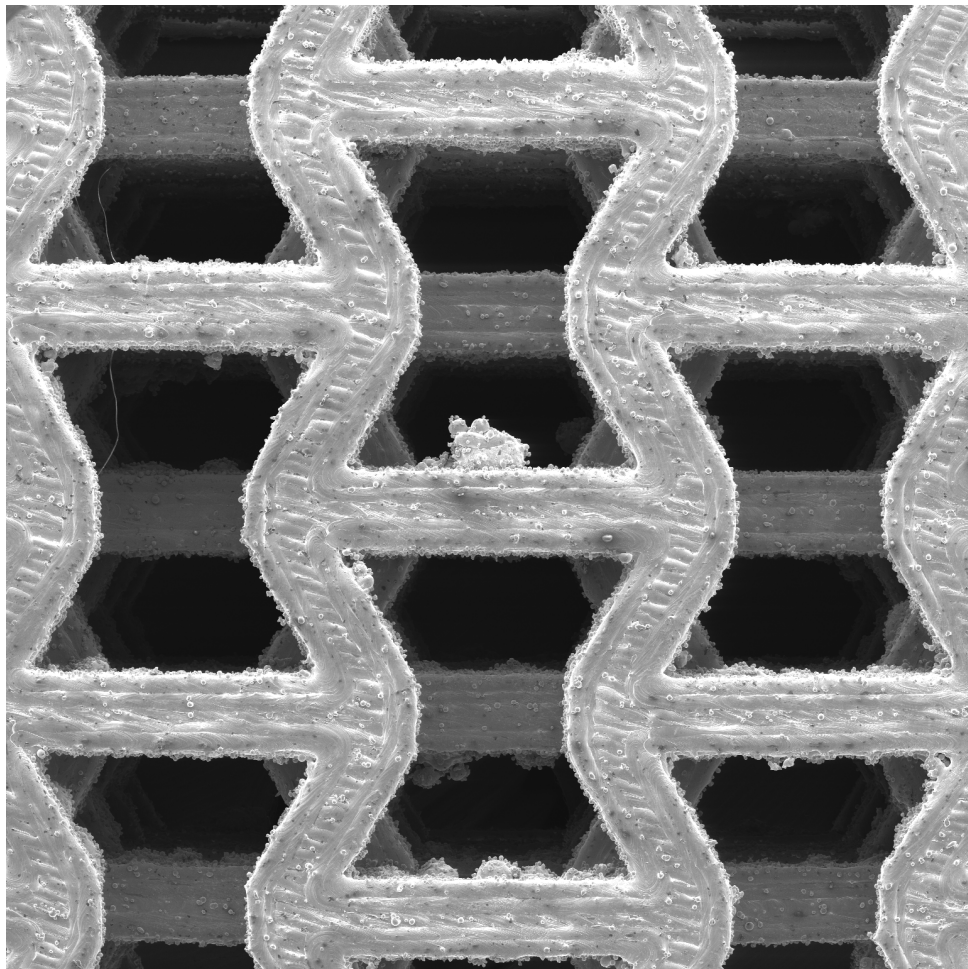
SEM HV: 15.00 kV WD: 38.00 mm  MIRALL TESCAN
View field: 9.14 mm Det: SE 2 mm
SEM MAG: 40 x Date(m/d/y): 08/12/20 ITAM 

Figure B.7: Polished surface of the 6×7 2D re-entrant honeycomb.



SEM HV: 15.00 kV WD: 15.36 mm 500 µm MIRAM TESCAN
View field: 2.61 mm Det: SE
SEM MAG: 140 x Date(m/d/y): 08/12/20 ITAM

Figure B.8: Polished surface of the 6 × 7 2D re-entrant honeycomb - detail of the strut joints.





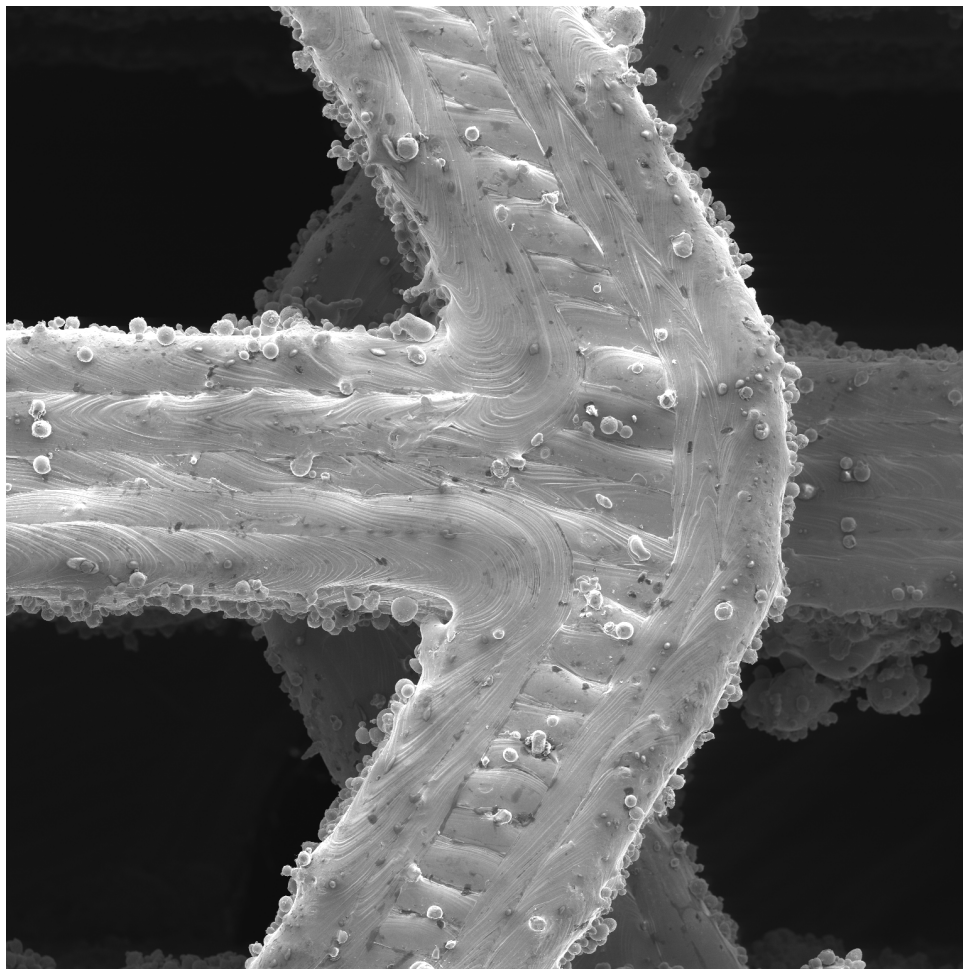
SEM HV: 15.00 kV WD: 36.98 mm  MIRAM TESCAN
View field: 9.14 mm Det: SE 2 mm
SEM MAG: 40 x Date(m/d/y): 08/12/20 ITAM 

Figure B.9: Polished surface of the 3×3 3D re-entrant honeycomb.



SEM HV: 15.00 kV WD: 33.44 mm 500 µm MIRA\\ TESCAN
View field: 2.61 mm Det: SE
SEM MAG: 140 x Date(m/d/y): 08/12/20 ITAM

Figure B.10: Polished surface of the 3×3 3D re-entrant honeycomb - detail of the strut joints.